The Dissertation Committee for Matthew Walter Spencer certifies that this is the approved version of the following dissertation:

Melt Processed Polymer-Organoclay Nanocomposites

Committee:

Donald R. Paul, Supervisor

Benny D. Freeman

Christopher J. Ellison

Isaac C. Sanchez

Desiderio Kovar

Melt Processed Polymer-Organoclay Nanocomposites

by

Matthew Walter Spencer, B.S.; M.S.E.

Dissertation

Presented to the Faculty of the Graduate School of
The University of Texas at Austin
in Partial Fulfillment
of the Requirements
for the Degree of

Doctor of Philosophy

The University of Texas at Austin

December 2011

Dedication

To my loving wife, our sweet daughter, and our baby boy

Acknowledgements

I would like to thank my supervisor Dr. Don Paul for his support, patience, and guidance. I sincerely appreciate all the advice he has given me over the past several years and the confidence expressed in my ability to improve my skills as a researcher. I would also like to thank the other members of my committee: Dr. Benny Freeman, Dr. Christopher Ellison, Dr. Isaac Sanchez, and Dr. Desiderio Kovar for their time and suggestions. Their guidance and instruction, combined with the efforts of other Chemical Engineering faculty, were invaluable to me during my years of graduate study.

I would also like to thank my colleagues, past and present, in Don Paul's research group, especially Dr. Lili Cui, Dr. Youngjae Yoo, and Dr. Rajkiran Tiwari for their training, assistance, and friendship. Special thanks are due to Dr. JiPing Zhou and Dr. Domingo Ferrer for their help with TEM training. I wish to thank other staff members of the Department of Chemical Engineering, including Susan Chapman and 'T' Stockman. I appreciate the friendship and assistance of other colleagues at the University of Texas including Taylor Harvey, Kody Powell, Jeff Easley, and Julie Cushen.

I would also like to express my gratitude to my undergraduate professors at Brigham Young University, especially those I worked with in the Design Institute for Physical Properties (DIPPr), who helped me develop modeling, researching, and evaluating skills.

I am indebted to the people at Southern Clay Products for research collaborations, technical support, and generous donations of clay materials. In particular, I am sincerely appreciative Dr. Doug Hunter for his friendship and collaboration on various nanocomposite investigations. I am also grateful to Mr. Tony Gonzalez for his help on numerous X-ray experiments and to Mr. Ben Knesek for his help on agglomeration investigations.

I am grateful to Dr. Mark Wetzel and Dr. Christina Troeltzsch at E.I. DuPont Co. for donating polymers and for their collaboration on various projects.

Most importantly, I thank all of my family for their unfailing love and support. I am grateful to my parents for all they taught me and for the character they instilled in me. I especially thank my wife, Sandra, for her loyal support and love and for caring for our family. I would also like to thank my daughter and son for providing motivation and perspective.

Melt Processed Polymer-Organoclay Nanocomposites

Matthew Walter Spencer, Ph.D.
The University of Texas at Austin, 2011

Supervisor: Donald R. Paul

Polymer nanocomposites with organoclay fillers offer improved properties and performance, providing opportunities for commercial applications. The key to significant property enhancement is to exfoliate the individual organoclay platelets into the polymer matrix to utilize their high aspect ratio and modulus. The affinity between the polymer matrix and the organoclay is one of the most important factors for determining the exfoliation level.

Although polar polymers, such as nylon 6, exfoliate the organoclay well, hydrophobic matrices, such as polyolefins, generally do not effectively exfoliate the organoclay. Thus, a significant part of this work investigates various routes to improve polyolefin-organoclay interactions and organoclay exfoliation in these systems.

Nanocomposites formed from organoclay and blends of high density polyethylene and maleic anhydride-grafted high density polyethylene over the entire range of compositions were melt processed to obtain further insights into the ‘compatiblizing’ role of maleated polyolefins. The organoclay particle aspect ratio was found to initially increase drastically, reach a maximum, and slightly decrease with increased maleation. As the maleation level increases, the relative modulus increases initially and then levels off at higher loadings.

To a certain extent, the affinity between the polymer and the organoclay can be enhanced by optimizing the organoclay structure for a given polymer matrix. A silanized organoclay was investigated to determine if reduced agglomeration, improved exfoliation, and matrix reinforcement could be achieved in a polypropylene matrix without using a more costly compatibilizer. The silanized organoclay was found to be superior to the non-silanized precursor, but did not achieve the benefits obtained with a compatibilized matrix.

Ionomer matrices have also been used as a means of improving organoclay exfoliation. This study examined the effects of ion type (K^+, Na^+), neutralization level, and melt index on the nanocomposite morphology and properties. The Na^+ ionomers appear to have more favorable interactions with the organoclay. Exfoliation and matrix reinforcement tend to increase with decreased melt index and with increased neutralization, except at high levels. In these cases, it is possible that the additional exfoliation results in particles with lower aspect ratios.

Composite properties are highly dependent on the particle aspect ratio. Several theories were used to predict the modulus and the thermal expansion coefficient of composites based on the filler aspect ratio. Novel two-population approaches were applied to enable the modeling of nanocomposites containing organoclay tactoids and single platelets, organoclay particles and glass fibers, or organoclay and elastomer particles. The quantitative agreement between the values predicted using experimentally determined particle aspect ratios and experimental modulus and thermal expansion was vastly improved using these methods.

Table of Contents

Chapter 6: Effect of acid neutralization on the properties of K^+ and Na^+ poly(ethylene-*co*-methacrylic acid) ionomers 138

List of Tables

List of Figures

Chapter 1: Introduction

Polymer nanocomposites continue to attract interest in both industrial and academic laboratories as a new class of industrially important materials. Compared to conventional composites, very low concentrations (2~5 wt%) of nanometric-sized filler particles can significantly improve many properties, such as strength [1-5], gas permeability [6-10], flammability resistance [11-15], thermal stability [16], ionic conductivity [17, 18], and tunable biodegradability [19], without significantly increasing the density of the polymer or changing its optical properties. For these reasons, polymer nanocomposites have drawn interest in a wide variety of applications, e.g., automotive, electronics, food packaging, biotechnology, and others [20, 21] in recent years.

BACKGROUND

Organoclay

Nanoparticles can be classified based on the number of dimensions with nanometer size: one dimension (platelets), two dimensions (fibers), and three dimensions (spherical particles). This work focuses on polymer-layered silicate nanocomposites using fillers based on sodium montmorillonite (MMT), which consists of layered platelets with thicknesses of 0.94 nm and lateral dimensions as large as hundreds of nanometers. The individual platelets have high aspect ratios (~ 50-500), surface areas (~750 m^2/g), and moduli (~178 GPa).

Sodium montmorillonite is a member of the 2:1 layered smectite family of clays. In the case of montmorillonite, two tetrahedral sheets composed of Si oxide sandwich an octahedral sheet comprised of Al, Mg, and Fe oxides and hydroxides, as shown in Figure 1.1. Montmorillonites are structurally derived from pyrophyllite [$Si_8Al_4O_{20}(OH)_4$] or talc

$[Si_8Mg_6O_{20}(OH)_4]$ by substitutions mainly in the octahedral layers, e.g., trivalent Al can be substituted by divalent Mg or monovalent Li, which results in some excess negative charges [22]. The charge imbalance is compensated by the presence of cations, such as Na^+, Ca^{2+} and K^+, absorbed between the platelets. Though the cations are stoichiometric, they are held relatively loosely and are readily exchanged by other cations. The triple-sheet layers are stacked onto each other with the interlamellar gallery between them, forming bundles of a few microns.

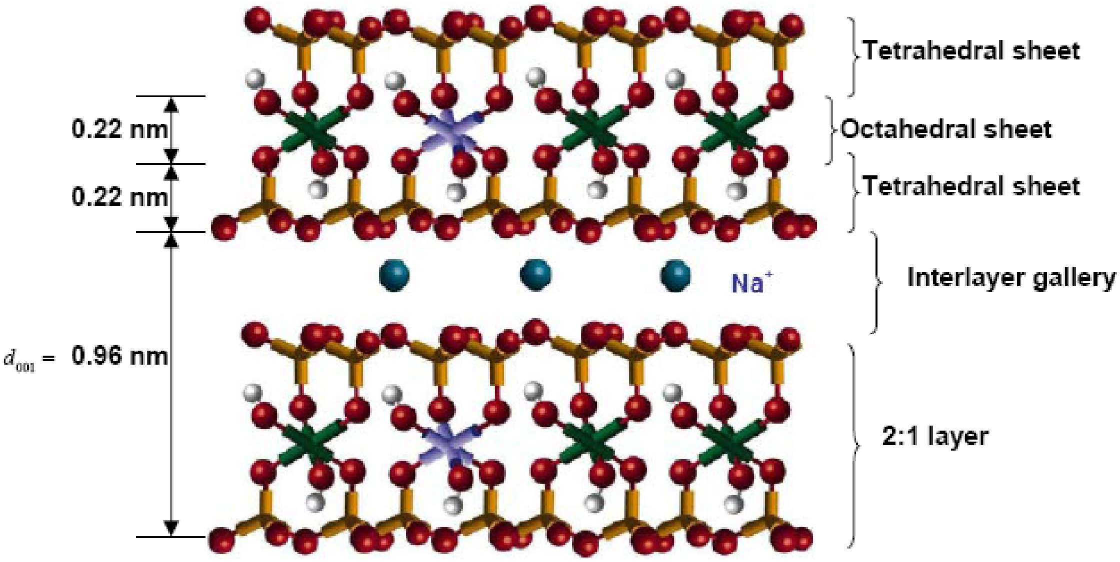

Figure 1.1: Structure of sodium montmorillonite.

Exfoliation of the individual platelets in the polymer matrix leads to the significant improvements in properties due to the high aspect ratio and high surface area of the silicate platelets. In general, the hydrophilic silicate surface can be made relatively organophilic by ion-exchange reactions with cationic surfactants, such as primary, secondary, tertiary, and quaternary alkylammonium cations, facilitating dispersion in many engineering polymers (see Figure 1.2). Alkylammonium cations in the organoclay lower the surface energy of the inorganic silicate, improve the wetting characteristics of the polymer matrix, and increase the interlayer spacing. Some frequently used abbreviations are employed to represent the substituents on the ammonium cation, e.g., M for methyl and HT for long alkyl chains from hydrogenated tallow [23].

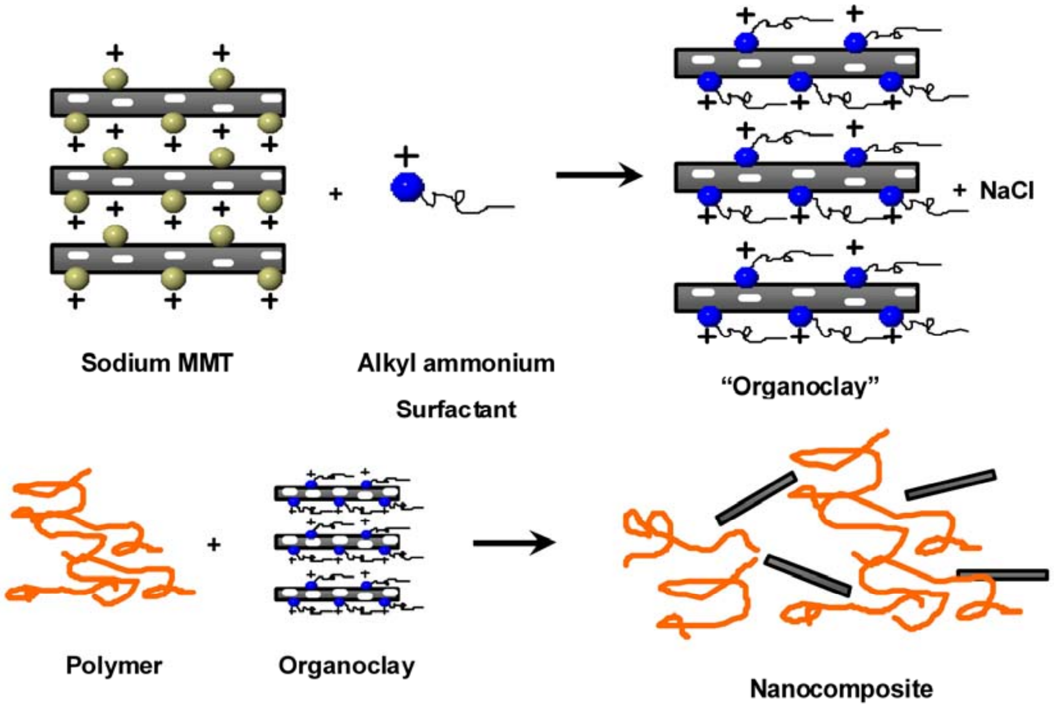

Figure 1.2: Illustrations of organoclay and nanocomposite formation.

Although an organoclay can be exfoliated more readily than native sodium montmorillonite, other issues, such as the processing conditions, the chemical structure of the surfactant used to form the organoclay, and the properties of the polymer matrices must also be considered to form well-exfoliated nanocomposites.

Efforts have been made globally starting from two major findings: first, the report from the Toyota research group of a Nylon-6 /montmorillonite (MMT) nanocomposite [24], in which very small amounts of layered silicate loadings resulted in pronounced improvements of thermal and mechanical properties; second, Vaia et al. [25] found that it is possible to melt blend polymers with layered silicates without using organic solvents. Because then, there have been some advances in these areas, but the process of organoclay exfoliation is still not fully understood.

The structure of the ammonium surfactants used to modify montmorillonite (MMT) clay can be chosen to increase the affinity between the hydrophilic aluminosilicate clay and the organophilic polymer matrix. In our previous studies, nylon 6-based nanocomposites showed the best exfoliation with organoclays formed from a surfactant with only one long alkyl tail, allowing the polar polyamide more access to the silicate surface of the clay [23, 26, 27]. Non-polar polyolefin matrices, such as polypropylene or polyethylene, on the other hand, result in better exfoliation with organoclays modified by a surfactant with two or more long alkyl tails, providing increased alkyl-polyolefin interactions and decreased silicate-polyolefin interaction [28-31].

Preparation of nanocomposites

Various techniques have been used for preparing polymer nanocomposites; including *in-situ* polymerization [9, 32, 33], emulsion polymerization [34-37], sol-gel templating [38-40], and melt processing [27-30, 41-47]. Melt processing is more economic and environmentally friendly than other techniques, yet produces nanocomposites of comparable properties. In addition, nanocomposite formation is shifted closer to the final product manufacture and is well-suited for rapid changes of polymer matrix, organoclay filler, and organoclay loading. Melt processing was used to prepare the nanocomposites studied in this work.

In most cases, the polymer is hand-mixed with the desired amount of organoclay and introduced into a Haake co-rotating twin screw extruder (diameter = 30 mm, L/D =

10) at a temperature slightly above the melting temperature of the polymer. The combined effect of shear and physical and chemical interactions between the polymer and organoclay separates the clay platelets to various degrees and disperses them in the polymer matrix to form the nanocomposite. The resulting nanocomposite pellets are molded into standard tensile (ASTM D638, Type I) and Izod (ASTM D256) bars (0.318 cm thick) using an Arburg Allrounder 305-210-700 injection molding machine. A schematic of the experimental procedure is presented in Figure 1.3.

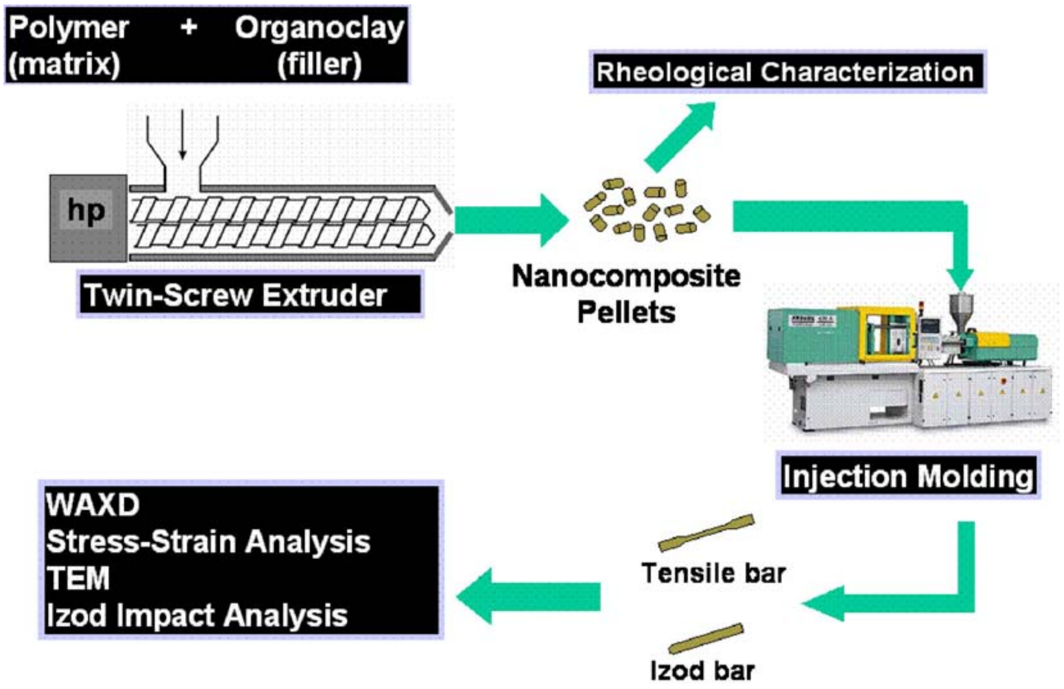

Figure 1.3: Overview of the experimental procedure used for preparing and characterizing nanocomposites.

Characterization

The morphology and properties of the nanocomposites are evaluated using characterization methods such as wide angle X-ray scattering (WAXS), transmission electron microscopy (TEM), and tensile tests. WAXS is commonly used to determine the interlayer spacing, d_{001}, by looking at the arbitrary intensity versus 2θ. The spacing is then calculated from Bragg's law:

$$d_{001} = n\lambda/(2\sin\theta) \tag{1}$$

According to conventional understanding in the literature, shifting of the d_{001} peak to the left, i.e., lower angles, indicates an expanded *d*-spacing caused by intercalation of polymer or low-molecular weight oligomers in the gallery of the clay platelets, while the absence of any characteristic basal reflections suggests a well-exfoliated morphology.

Properly prepared TEM images provide direct visualization of the dispersion of the clay particles in nanocomposites, which usually, but not always, confirm the WAXS results. Figure 1.4 illustrates the typical WAXS patterns and their respective representative morphologies observed by TEM. To have a quantitative assessment of the level of organoclay exfoliation, detailed particle analyses are performed on the TEM images.

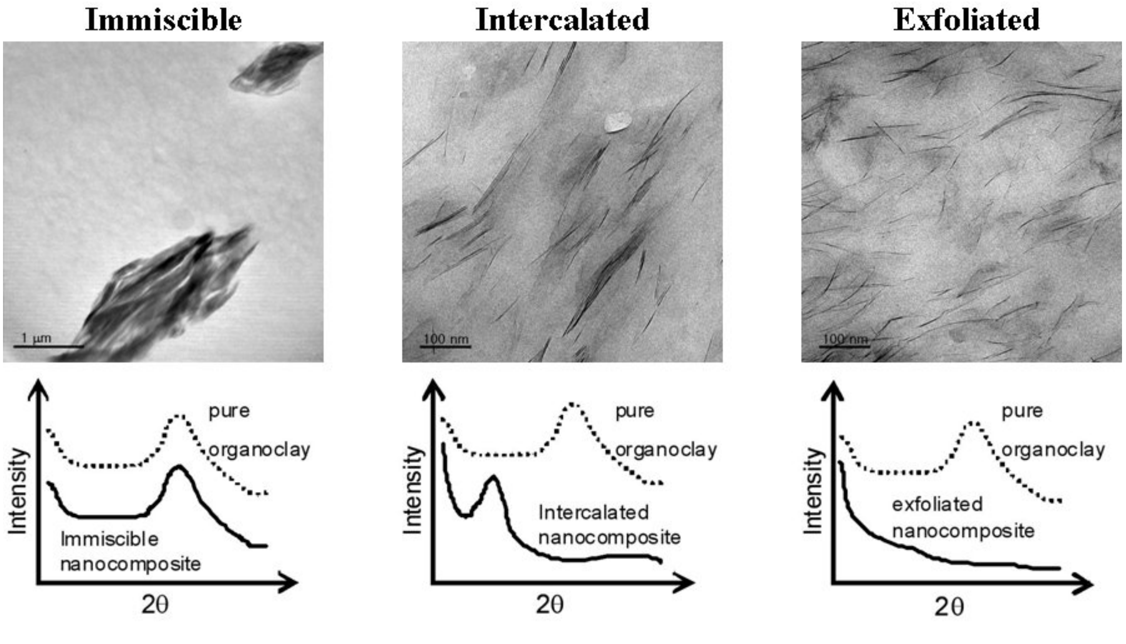

Immiscible

Intercalated

Exfoliated

Figure 1.4: TEM and WAXS illustration of the typical nanocomposite morphologies.

As shown in Figure 1.4, nanocomposites are commonly classified as *immiscible*, *intercalated*, or *exfoliated*. An *immiscible* morphology is formed when the polymer does not intercalate into the galleries of the organoclay, producing a macroscopic mixture composed of regions of pure organoclay and regions of pure polymer. The TEM micrographs show large agglomerates of clay while the resulting WAXS pattern is unchanged from that of the pure organoclay. *Intercalated* morphologies consist of small amounts of intercalated polymer that expand the interlayer distance of the clay platelets but cannot overcome the original ordered structure of the clay. TEM micrographs show small, intercalated agglomerates and WAXS patterns show a broad intense peak corresponding to a basal spacing close to that of the pure organoclay. On the other hand, *exfoliated* nanocomposites consist predominantly of individual delaminated silicate platelets dispersed in the polymer matrix. TEM shows the individual platelets while WAXS show no characteristic basal reflections.

The degree to which addition of organoclay to the polymer matrix alters mechanical properties provides another way to assess the extent of organoclay exfoliation. The increase in tensile modulus is usually a sensitive reflection of organoclay exfoliation and is measured by tensile testing the samples at room temperature according to ASTM D638. An increase in the stiffness of the nanocomposites is usually accompanied by decreases in their ductility and toughness, as characterized by the elongation at break values, and Izod impact tests (ASTM D256), respectively.

DISSERTATION SCOPE AND ORGANIZATION

This Ph.D. project addresses a number of fundamental issues associated with the melt processing of polymer nanocomposites to better understand the exfoliation process.

The major focus of this project is improving the organoclay exfoliation in non-polar polyolefin matrices. Various compatibilizers, such as maleated polyolefins, and various organoclay types are examined. Another major part of this dissertation is modeling these nanocomposites using novel approaches to improve understanding of these systems.

This dissertation is divided into eight chapters. Chapter 2 gives a description of the materials used and an overview of the experimental techniques employed to form and characterize the nanocomposites investigated in this study. Specific details and variations of these experimental techniques to meet specific objectives are described in the corresponding chapters. Chapters 3 deals with nanocomposites based on HDPE/HDPE-*g*-MA blends from 0% to 100% HDPE-*g*-MA to investigate the effect of maleation over the entire range on the morphology and mechanical properties of the nanocomposites. As a part of this work, a novel two-population composite model is discussed. Chapter 4 investigates the possibility of using an edge-silanized organoclay to achieve better exfoliation without using a polar compatibilizer. Chapter 5 is devoted to understanding TPO nanocomposites via composite modeling using novel modeling concepts. Chapters 6 and 7 investigate two series of potassium (K^+) and sodium (Na^+) ionomer nanocomposites based on ethylene methacrylic acid (EMAA) copolymers with various degrees of neutralization and melt indices. Chapter 6 deals with the thermal, rheological, and mechanical properties of the neat ionomers. Chapter 7 discusses the morphological, thermal, rheological, and mechanical properties of the corresponding ionomer nanocomposites. Finally, Chapter 8 summarizes the general conclusions from the research work performed and includes recommendations for future work.

REFERENCES

1. Wang Z and Pinnavaia TJ. Chemistry of Materials 1998;10(12):3769-3771.

2. Usuki A, Koiwai A, Kojima Y, Kawasumi M, Okada A, Kurauchi T, and Kamigaito O. Journal of Applied Polymer Science 1995;55(1):119-123.
3. Giannelis EP. Applied Organometallic Chemistry 1998;12(10-11):675-680.
4. Lan T and Pinnavaia TJ. Chemistry of Materials 2002;6(12):2216-2219.
5. Liu L, Qi Z, and Zhu X. Journal of Applied Polymer Science 1999;71(7):1133-1138.
6. Bharadwaj RK. Macromolecules 2001;34(26):9189-9192.
7. Messersmith PB and Giannelis EP. Journal of Polymer Science Part A: Polymer Chemistry 1995;33(7):1047-1057.
8. Yano K, Usuki A, Okada A, Kurauchi T, and Kamigaito O. Journal of Polymer Science Part A: Polymer Chemistry 1993;31(10):2493-2498.
9. Kojima Y, Usuki A, Kawasumi M, Okada A, Fukushima Y, Kurauchi T, and Kamigaito O. Journal of Materials Research 1993;8(5):1185–1189.
10. Xu R, Manias E, Snyder AJ, and Runt J. Macromolecules 2001;34(2):337-339.
11. Gilman JW. Applied Clay Science 1999;15(1-2):31-49.
12. Bourbigot S, Le Bras M, Dabrowski F, Gilman JW, and Kashiwagi T. Fire and Materials 2000;24(4):201-208.
13. Gilman JW, Kashiwagi T, Brown JET, Lomakin S, Giannelis EP, and Manias E. Int. SAMPE Symp. Exhibit. 1998;43:1053.
14. Malwitz MM, Lin-Gibson S, Hobbie EK, Butler PD, and Schmidt G. Journal of Polymer Science Part B: Polymer Physics 2003;41(24):3237-3248.
15. Hu Y, Wang S, Ling Z, Zhuang Y, Chen Z, and Fan W. Macromolecular Materials and Engineering 2003;288(3):272-276.
16. Yoon PJ, Fornes TD, and Paul DR. Polymer 2002;43(25):6727-6741.
17. Chen W, Xu Q, and Yuan RZ. Materials Science and Engineering B 2000;77(1):15-18.
18. Chen W, Xu Q, and Yuan RZ. Composites Science and Technology 2001;61(7):935-939.
19. Sinha Ray S, Yamada K, Okamoto M, and Ueda K. Polymer 2003;44(3):857-866.
20. Chavarria F and Paul DR. Polymer 2004;45(25):8501-8515.
21. Chavarria F and Paul DR. Polymer 2006;47(22):7760-7773.
22. Utraki LA. Clay-containing polymeric nanocomposites. Shawbury, Shrewsbury, Shropshire, SY4 4NR, UK, 2004.

23. Fornes TD, Yoon PJ, Hunter DL, Keskkula H, and Paul DR. Polymer 2002;43(22):5915-5933.

24. Okada A, Kawasumi M, Usuki A, Kojima Y, Kurauchi T, and Kamigaito O. Materials Research Society Symposium Proceedings 1990;171(Polym. Based Mol. Compos.):45-50.

25. Vaia RA, Ishii H, and Giannelis EP. Chemistry of Materials 1993;5(12):1694-1696.

26. Fornes TD, Hunter DL, and Paul DR. Macromolecules 2004;37(5):1793-1798.

27. Fornes TD, Yoon PJ, Keskkula H, and Paul DR. Polymer 2001;42(25):9929-9940.

28. Hotta S and Paul DR. Polymer 2004;45(22):7639-7654.

29. Kim DH, Fasulo PD, Rodgers WR, and Paul DR. Polymer 2007;48(18):5308-5323.

30. Lee H-S, Fasulo PD, Rodgers WR, and Paul DR. Polymer 2005;46(25):11673-11689.

31. Shah RK, Hunter DL, and Paul DR. Polymer 2005;46(8):2646-2662.

32. Usuki A, Kojima Y, Kawasumi M, Okada A, Fukushima Y, Kurauchi T, and Kamigaito O. Journal of Materials Research 1993;8(5):1179-1184.

33. Weimer MW, Chen H, Giannelis EP, and Sogah DY. Journal of the American Chemical Society 1999;121(7):1615-1616.

34. Lee DC and Jang LW. Journal of Applied Polymer Science 1996;61(7):1117-1122.

35. Lee DC and Jang LW. Journal of Applied Polymer Science 1998;68(12):1997-2005.

36. Wang KH, Choi MH, Koo CM, Choi YS, and Chung IJ. Polymer 2001;42(24):9819-9826.

37. Kim YK, Choi YS, Wang KH, and Chung IJ. Chemistry of Materials 2002;14(12):4990-4995.

38. Ding Y, Zhang X, Xiong R, Wu S, Zha M, and Tang H. European Polymer Journal 2008;44(1):24-31.

39. Carrado KA and Xu L. Chemistry of Materials 1998;10(5):1440-1445.

40. Kotoky T and Dolui SK. Colloid & Polymer Science 2006;284(10):1163-1169.

41. Cho JW and Paul DR. Polymer 2001;42(3):1083-1094.

42. Cui L, Ma X, and Paul DR. Polymer 2007;48(21):6325-6339.

43. Shah RK and Paul DR. Polymer 2004;45(9):2991-3000.

44. Stretz HA, Paul DR, Li R, Keskkula H, and Cassidy PE. Polymer 2005;46(8):2621-2637.

45. Vaia RA, Ishii H, and Giannelis EP. Chemistry of Materials 2002;5(12):1694-1696.

46. Yoo Y, Shah RK, and Paul DR. Polymer 2007;48(16):4867-4873.

47. Yoon PJ, Hunter DL, and Paul DR. Polymer 2003;44(18):5323-5339.

Chapter 2: Experimental procedures

This chapter describes the materials used and the experimental techniques employed to form and characterize the nanocomposites investigated in this work. Each subsequent chapter also includes a brief description of the materials and experimental procedures used in that chapter, as well as any additional information specific to that study.

MATERIALS

Polymers

The major focus of this work was on exploring the morphology and properties of polyolefin nanocomposites. The polymers used in this work are described in Table 2.1. Modeling work was done on some nylon nanocomposites and on blends including an ethylene/octane elastomeric copolymer.

Table 2.1: Polymers used in this work

Polymer class	Designation	Commercial designation	Supplier	Select specification
High density polyethylene	HDPE	Alathon M6020	LyondellBasell	MI = 2 g/10 min $\rho = 0.96$ g/cm^3
Maleic anhydride grafted high density polyethylene	HDPE-*g*-MA	Fusabond E MB100D	DuPont	MI = 2 g/10 min $\rho = 0.96$ g/cm^3 MP = 134 °C MA content = 0.9 wt%
Polypropylene	PP	Pro-Fax PH020	LyondellBasell	MI = 37 g/10 min $\rho = 0.902$ g/cm^3
Maleic anhydride grafted polypropylene	PP-*g*-MA	Polybond 3200	Chemtura	MI = 115 g/10 min $\rho = 0.91$ g/cm^3 MP = 157 °C MA content = 1.0 wt% $\overline{M}_w = 90{,}000$ MWD ≈ 2.7

Sodium ionomers of poly(ethylene-co-methacrylic acid)	Na 1	Experimental	DuPont	MI = 15.3 g/10 min Precursor MI = 60 g/10 min MAA content = 15 wt% Neutralization = 14.2 %
	Na 2	Experimental	DuPont	MI = 5.8 g/10 min Precursor MI = 60 g/10 min MAA content = 15 wt% Neutralization = 27.1 %
	Na 3	Experimental	DuPont	MI = 2.6 g/10 min Precursor MI = 60 g/10 min MAA content = 15 wt% Neutralization = 39.5 %
	Na 4	Experimental	DuPont	MI = 1.2 g/10 min Precursor MI = 60 g/10 min MAA content = 15 wt% Neutralization = 50.7 %
	Na 5	Experimental	DuPont	MI = 0.6 g/10 min Precursor MI = 60 g/10 min MAA content = 15 wt% Neutralization = 58.9 %
	Na 6	Experimental	DuPont	MI = 5.5 g/10 min Precursor MI = 25 g/10 min MAA content = 15 wt% Neutralization = 16.0 %
	Na 7	Experimental	DuPont	MI = 2.3 g/10 min Precursor MI = 25 g/10 min MAA content = 15 wt% Neutralization = 27.8 %
	Na 8	Experimental	DuPont	MI = 1.2 g/10 min Precursor MI = 25 g/10 min MAA content = 15 wt% Neutralization = 40.4 %
	Na 9	Experimental	DuPont	MI = 0.5 g/10 min Precursor MI = 25 g/10 min MAA content = 15 wt% Neutralization = 50.7 %
Potassium ionomers of poly(ethylene-co-methacrylic acid)	K 1	Experimental	DuPont	MI = 47.6 g/10 min Precursor MI = 200 g/10 min MAA content = 15 wt% Neutralization = 20.3 %
	K 2	Experimental	DuPont	MI = 22.4 g/10 min Precursor MI = 200 g/10 min MAA content = 15 wt% Neutralization = 31.7 %

	K 3	Experimental	DuPont	MI = 11 g/10 min Precursor MI = 200 g/10 min MAA content = 15 wt% Neutralization = 43.1 %
	K 4	Experimental	DuPont	MI = 4.8 g/10 min Precursor MI = 200 g/10 min MAA content = 15 wt% Neutralization = 53.6 %
	K 5	Experimental	DuPont	MI = 12.6 g/10 min Precursor MI = 60 g/10 min MAA content = 15 wt% Neutralization = 20.5 %
	K 6	Experimental	DuPont	MI = 5.7 g/10 min Precursor MI = 60 g/10 min MAA content = 15 wt% Neutralization = 30.4 %
	K 7	Experimental	DuPont	MI = 3 g/10 min Precursor MI = 60 g/10 min MAA content = 15 wt% Neutralization = 40.1 %
	K 8	Experimental	DuPont	MI = 1.3 g/10 min Precursor MI = 60 g/10 min MAA content = 15 wt% Neutralization = 52.4 %
	K 9	Experimental	DuPont	MI = 5.4 g/10 min Precursor MI = 25 g/10 min MAA content = 15 wt% Neutralization = 20.4 %
	K 10	Experimental	DuPont	MI = 3.7 g/10 min Precursor MI = 25 g/10 min MAA content = 15 wt% Neutralization = 25.6 %
	K 11	Experimental	DuPont	MI = 1.3 g/10 min Precursor MI = 25 g/10 min MAA content = 15 wt% Neutralization = 38.4 %
	K 12	Experimental	DuPont	MI = 1.2 g/10 min Precursor MI = 25 g/10 min MAA content = 15 wt% Neutralization = 39.9 %

Fillers

Three different types of organoclay, generously donated by Southern Clay Products, were used in this work as described in Table 2.2. The organoclays were prepared by cation exchange reaction between sodium montmorillonite (Na-MMT) and an alkyl ammonium surfactant derived from natural tallow oils provided to Southern Clay Products by Akzo Nobel. A simple nomenclature system has been adopted to describe the structure in a concise manner, i.e., M for methyl and HT for hydrogenated tallow oil (predominantly saturated C18 chains). The level of the surfactants added to the clay is designated by the milliequivalent ratio (MER) defined as the milliequivalents of surfactant per 100 g of clay [1]. Modeling work was done on some composites containing glass fibers.

Table 2.2: Organoclays used in this study

Designation	Commercial designation[1]	Surfactant used[2]	Specification[3]
C20A $M_2(HT)_2$	**Cloisite® 20A:** Dimethyl bis(hydrogenated-tallow) ammonium montmorillonite	$M_2(HT)_2$ 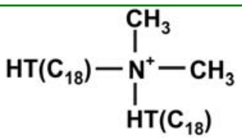 $\mathrm{HT(C_{18})-\overset{\overset{CH_3}{\vert}}{\underset{\underset{HT(C_{18})}{\vert}}{N^+}}-CH_3}$	95 MER Organic content = 31.5 wt% d_{001} = 24.2 Å
C15A $M_2(HT)_2$	**Cloisite® 15A:** Dimethyl bis(hydrogenated-tallow) ammonium montmorillonite	$M_2(HT)_2$	125 MER Organic content = 43 wt% d_{001} = 31.5 Å
s-$M_2(HT)_2$	**Experimental:** Dimethyl bis(hydrogenated-tallow) ammonium montmorillonite	$M_2(HT)_2$	125 MER Organic content = 43 wt% d_{001} = 31.5 Å 6 wt% trimethoxyphenyl silane

Notes:

1. All the organoclays used in this study are generously donated by Southern Clay Products Inc.
2. The symbols are M = methyl and (HT) = hydrogenated tallow.
3. The organic loadings shown here are values reported by Southern Clay Products, Inc.

MELT PROCESSING

The organoclay and the hydrophilic polymers, i.e., HDPE-*g*-MA, PP-*g*-MA, and ionomers, were dried for a minimum of 24 h in a vacuum oven, prior to melt processing.

Most of the nanocomposites were melt compounded in a Haake co-rotating, intermeshing twin screw extruder (diameter = 30 mm, L/D = 10) using a barrel temperature of slightly above the melt temperature of the polymer, a screw speed of 280 rpm , and a feed rate of 1 kg/h. The polymer and the organoclay were hand-mixed prior to extrusion and introduced into the extruder by a single hopper. Additional nanocomposite samples were melt compounded in a Werner and Pfeiderer ZSK 25 (diameter = 25 mm, L/D = 48) extruder.

After drying the pellets from the extrusion process in a vacuum oven, tensile specimens (ASTM D638, Type I) and Izod bars (ASTM D256) were prepared by an Arburg Allrounder 305-210-700 injection-molding machine. After molding, the samples were immediately sealed in a polyethylene bag and placed in a vacuum desiccator for a minimum of 24 hours prior to testing.

The clay concentrations of the nanocomposites are reported in terms of the montmorillonite (MMT) weight percent rather than the amount of organoclay because the silicate is the reinforcing component. The montmorillonite content of the nanocomposite was determined by placing pre-dried nanocomposite pellets in a furnace at 900 °C for 45 min and weighing the remaining MMT ash, correcting for loss of structural water [2-4].

$$MMT\% = MMT_{ash}\% / 0.935 \qquad (1)$$

CHARACTERIZATION

Morphology

Wide angle X-ray scattering (WAXS)

Wide angle X-ray scattering (WAXS) scans were performed using a Bruker-AXS D8 Advance diffractometer in the reflection mode, using an incident X-ray wavelength of 0.1541 nm at a scan rate of 3.0°/min over the range of $2\theta = 1°$ to $12°$. The skin of the major face of the rectangular nanocomposite bars and the organoclay powder were scanned at room temperature. These scans were performed at Southern Clay Products.

Transmission electron microscopy

Morphology was examined primarily via a FEI TECNAI G2 F20 X-TWIN transmission electron microscope (TEM) operating under an accelerating voltage of 200 kV. Some samples were observed using a JEOL 2010F TEM operating under an accelerating voltage of 120 kV. Ultra-thin sections (~50 nm) for morphological analysis were taken from the core portion of an injection-molded bar in the plane defined by the flow direction (FD) and the normal direction (ND) using an RMC PowerTome XL microtome as shown in Figure 2.1.. The nanocomposite samples and the diamond knife were cooled using liquid nitrogen. Cut sections were collected onto 400 mesh grids and dried with filter paper.

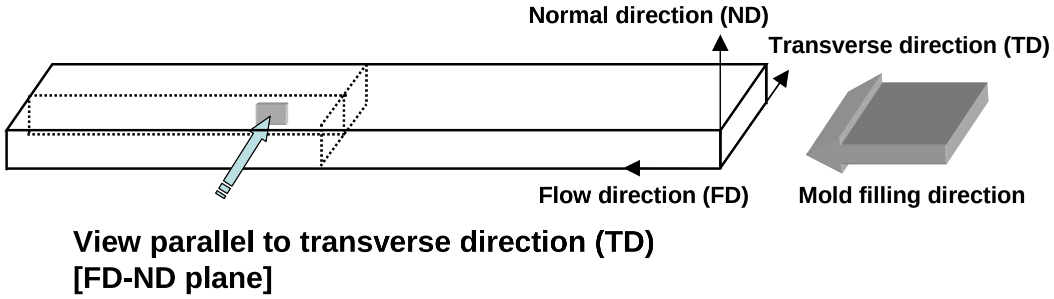

Figure 2.1: Illustrations of TEM sample orientation used in this work.

MMT particle analysis

Particle analyses were performed on TEM micrographs at magnifications of 8–30 K, depending on the extent of exfoliation in the sample. Because of low contrast, TEM images were converted into .jpg format and opened in GIMP (GNU Image Manipulation Program). Two tracings in separate, transparent layers were made of particle lengths and thicknesses. For nanocomposites with single platelets, the thickness of these platelets could not accurately be measured and was assigned a thickness of 0.94 nm corresponding to the known results for MMT platelets [5, 6]. Each tracing was saved separately in .tif format and imported into the image analysis program, SigmaScan Pro, where each particle tracing was assigned a number and their characteristic dimensions were measured. Because the numbers assigned in the tracing of the length and the tracing of the thickness of the particles do not correspond, the particle dimensions must be matched manually. In this work, four different kinds of aspect ratios are calculated, i.e., the number and weight averages of the aspect ratios calculated for individual particles, $\langle l/t \rangle_n$ and $\langle l/t \rangle_w$, and ratios of the number and weight averages of particle lengths and thicknesses, $(\overline{l_n}/\overline{t_n})$ and $(\overline{l_w}/\overline{t_w})$. To ensure statistical validity of the analysis, 200–500 particles were counted to measure the length, thickness, and aspect ratio.

Light microscopy

The extent of agglomeration was examined by performing light microscopy on an Olympus BX51 Cross Polarized Optical Microscope with a 10X lens in the transmission, brightfield mode with a polarizing filter between the light source and the sample and another polarizing filter set at 90º to the first filter located between the sample and the camera. Images were collected on an Olympus DP72 Microscope Digital Camera. Samples were prepared by compression molding thin films (~40μm) above the melting point between two sheets of Mylar for a total of 4.5 minutes (including a 2.5 minute preheat/melting time) in a manual Carver press and quenching the hot films in an ice bath. The films were mounted between a 25 by 75 mm slide and a 22 mm cover slide with low viscosity mineral oil on both sides of the specimen. These agglomeration investigations were conducted at Southern Clay Products.

Properties

Tensile

Tensile tests were performed at room temperature according to ASTM D638 using an Instron model 1137 machine upgraded for computerized data acquisition. Tensile modulus values were determined using an extensometer at a crosshead rate of 0.51 cm/min. Elongation at break and yield strength data were measured at 0.51 cm/min and 5.1 cm/min. Elongations greater than 400% could not be measured due to the limitations of crosshead travel. Typically, at least five specimens were tested and averaged to determine the tensile properties.

Izod impact

Notched Izod impact tests were conducted at room temperature with a 6.8 J hammer at an impact velocity of 3.5 m/s using a TMI Impact tester (model 43-02). Standard notches were made according to ASTM D256. Frequently, as-molded rectangular bars are cut in half (to generate more samples) and the Izod impact strength data from the gate end (the end at which the molten polymer enters the mold during injection molding) and the far end are averaged together. Morphological differences arising from the injection-molding process can result in significant differences between the Izod impact strength measured at the gate end and the far end of the samples. Thus, in some cases, the Izod impact strength data were averaged from four samples each of the gate end, of the middle, and of the far end of the bars. In most cases, however, the impact strength data from the gate and far ends were averaged together because the difference between the two is relatively small.

Melt rheology

Melt rheological characteristics were determined using an AR 2000ex Rheometer using a parallel plate fixture at a fixed temperature under a nitrogen gas flow. Frequency sweep tests were made over a range of 0.1–200 rad/s at a fixed strain within the linear viscoelastic range for each sample. Specimens for rheological testing were taken from the far end of injection molded samples and trimmed after heating on the rheometer plate to a disk with a diameter of 25 mm and a thickness of 1 mm.

Thermal expansion

Thermal expansion tests were conducted according to ASTM D696 using a Perkin–Elmer thermomechanical analyzer (TMA 7). Rectangular specimens were prepared from the central region of Izod bars. The dimensions of the specimens were approximately as follows: thickness = 3.2 mm, width = 6.4 mm, and height = 12.7 mm. Thermal expansion measurements were made in the flow direction (FD). Each specimen was held at −40 °C for 5 min, heated at a rate of 5 °C/min to 125 °C and subsequently held for 30 min, and then quenched to room temperature. In order to assess both reversible and non-reversible effects, each specimen was stored at room temperature for at least 24 h after the first heating and then rescanned from −40 °C to 125 °C at a rate of 5 °C/min. All measurements were done in a nitrogen atmosphere.

Differential scanning calorimetry

Differential scanning calorimetric (DSC) thermograms were recorded using a Perkin Elmer Model DSC-7 at a heating rate of 10 °C/min under an extra dry N_2 atmosphere. The predried samples of 7-10 mg were packed into aluminum pans and heated slightly above the melting point to reset the thermal history. The melting temperature and the heat of fusion were determined from the second heating scan. A number of factors, such as moisture content and room temperature aging, can affect the details of the DSC thermograms [7-9]. Thus, in some cases, the samples were kept in a desiccator for various times before the second scan to assess the effect of room temperature aging time.

Composite theory

Theoretical modeling is an attractive approach for the design of polymer composite systems, and numerous models [10-13] have been proposed for predicting the properties of composites and for correlating experimental data with such predictions. However, numerous assumptions are made when using such models. For example, it is assumed that the polymer matrix is not affected by the presence of the filler, that the filler is of uniform dimensions and is perfectly aligned, that the matrix and filler are isotropic, that the matrix and filler are well bonded, and that there are no particle—particle interactions or agglomerations [14].

These models all treat the fillers as aligned ellipsoidal particles characterized by the ratio of the major to the minor axes, i.e., $a = l/t$ for prolate ellipsoids (fiber-shaped inclusions) and $a = t/l$ for oblate ellipsoids (disk-shaped particles), with the major axis defined as being in the **1** direction (Figure 2.2). Because in an idealized injection-molded composite the major axes of fiber-shaped inclusions are parallel to the flow direction (FD) while the major axes of disk-shaped inclusions are perpendicular to the plane defined by the FD and the transverse direction (TD), the coordinate system depicted in Figure 2.3 is used to describe the composite properties.

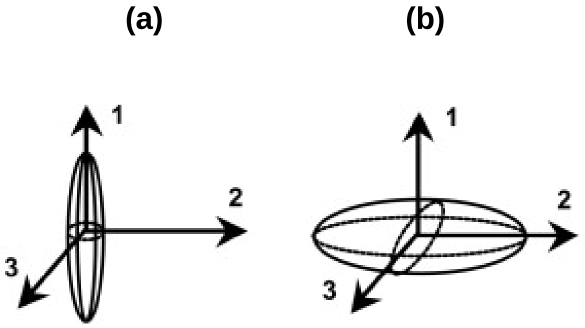

Figure 2.2. Physical representations and coordinate systems for fiber- (a) and disk-shaped (b) particles.

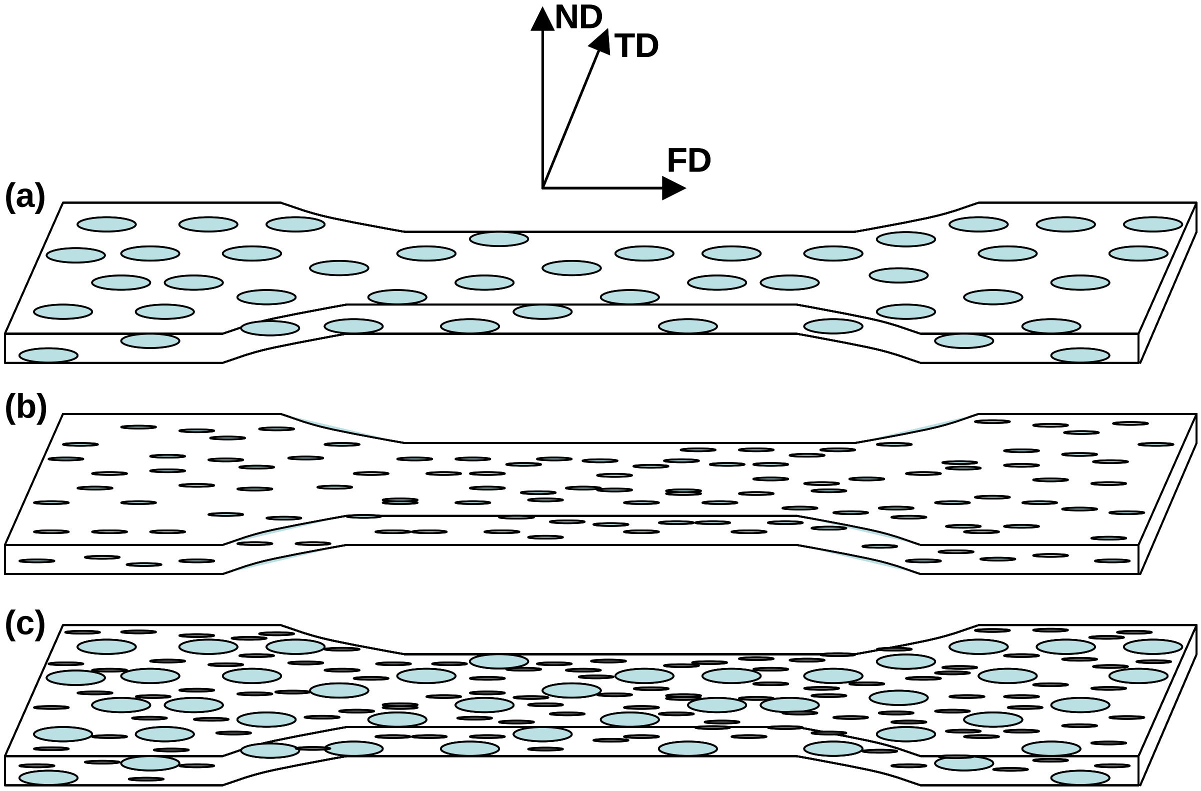

Figure 2.3. Physical representations and coordinate system for elastomer (a), organoclay (b), and elastomer/organoclay (c) composites.

Filler parameters

In the model calculations, there are generally two ways of treating the organoclay particles. One is to assume good exfoliation (method 1) and treat the MMT platelets themselves as the reinforcing filler particles. In this case, $E_{\mathrm{p}} = E_{\mathrm{MMT}} = 178$ GPa [14], $\nu = 0.20$, and $\phi_{\mathrm{p}} = \phi_{\mathrm{MMT}}$.

Another way is to consider the partially exfoliated clay particles as parallel arrangements of MMT platelets and gallery material as described in previous reports [5, 14-18] (method 2). The tensile modulus of such an effective particle is often assumed to be given by the following rule of mixtures

$$E_{\mathrm{p}} = \mathrm{v}_{\mathrm{MMT}} E_{\mathrm{MMT}} + \mathrm{v}_{\mathrm{gallery}} E_{\mathrm{gallery}} \tag{2}$$

where $\mathrm{v}_{\mathrm{MMT}}$ and $\mathrm{v}_{\mathrm{gallery}}$ are the volume fraction of montmorillonite and of the gallery space in the effective particle, while E_{MMT} and E_{gallery} are their corresponding moduli. The volume fraction of MMT platelets in the particle, $\mathrm{v}_{\mathrm{MMT}}$, is calculated as the ratio of the thickness of an individual platelet and the *d*-spacing of the nanocomposite as determined by the WAXS analysis

$$\mathrm{v}_{\mathrm{MMT}} = \frac{t_{\mathrm{platelet}}}{d_{001}} \tag{3}$$

Considering that the modulus of the organic material in the gallery is significantly smaller than the modulus of the MMT platelets, Eq. (19) reduces to

$$E_{\mathrm{p}} = \mathrm{v}_{\mathrm{MMT}} E_{\mathrm{MMT}} \tag{4}$$

The volume fraction of the filler particles in the composites can be estimated as

$$\phi_{\mathrm{p}} = \frac{\text{volume of MMT}}{\text{volume of nanocomposite}} \frac{\text{volume of filler particle}}{\text{volume of MMT}} = \frac{\phi_{\mathrm{MMT}}}{\mathrm{v}_{\mathrm{MMT}}} \tag{5}$$

Halpin-Tsai model

The Halpin-Tsai equations treat the fillers as rectangular platelets and can be used to predict the tensile modulus of nanocomposites from the neat component properties and the particle aspect ratios as determined by quantitative particle analysis of TEM images. The expression for the longitudinal modulus [14-16] is

$$\frac{E^{\mathrm{H-T}}}{E_{\mathrm{m}}} = \frac{1+2(l/t)\phi\eta}{1-\phi\eta} \tag{6}$$

where E_{p} and E_{m} are the modulus values of the filler particle and matrix polymer, respectively, ϕ is the volume fraction of the filler particles, l/t represents the filler aspect ratio, and η is given by

$$\eta = \frac{(E_{\mathrm{p}}/E_{\mathrm{m}})-1}{(E_{\mathrm{p}}/E_{\mathrm{m}})+2(l/t)} \tag{7}$$

Mori-Tanaka model

The Mori-Tanaka average stress theory [19] is based on the principles of Eshelby's inclusion model for predicting an elastic stress field in and around an ellipsoidal particle in an infinite matrix [20]. To account for finite filler concentrations, however, Mori and Tanaka [19], considered a non-dilute composite of many identical ellipsoidal particles that cause the matrix to experience an average stress different from the applied stress. The volume average stress over the entire composite was forced to equal the applied stress to satisfy equilibrium conditions. Tandon and Weng [21] used this assumption together with Eshelby's solution to derive complete analytical solutions for the elastic moduli of an isotropic matrix filled with aligned ellipsoidal inclusions. The relative tensile modulus when the direction of the applied load is parallel to the major axes of the inclusions is

$$\frac{E_{\parallel}^{M-T}}{E_m} = \frac{A}{A+\phi[A_1+2\nu_m A_2]} \tag{8}$$

and the relative modulus when the direction of the applied load is perpendicular to the major axes of the inclusions is

$$\frac{E_{\perp}^{M-T}}{E_m}=\frac{2A}{2A+\phi[-2\nu_{\mathrm{m}}A_3+(1-\nu_{\mathrm{m}})A_4+(1+\nu_{\mathrm{m}})A_5A]} \tag{9}$$

where ϕ is the volume fraction of filler, ν_m is Poisson's ratio of the matrix, and A, A_1, A_2, A_3, A_4, A_5, are functions of Eshelby's tensor and the properties of the filler and the matrix, specifically Young's modulus, Poisson's ratio, filler concentration, and filler aspect ratio (a) (see Appendices A and B) [21].

For composites based on fiber-shaped inclusions, the tensile modulus in the FD is calculated using Eq. (8), $E_{FD} = E_{||}$, and the modulus in the normal direction (ND) and the TD is calculated using Eq. (9), $E_{ND} = E_{TD} = E_{\perp}$. For composites based on disk-shaped inclusions, the tensile modulus in the FD and the TD is calculated using Eq. (9), $E_{FD} = E_{TD} = E_{\perp}$, and the modulus in the ND is calculated using Eq. (8), $E_{ND} = E_{||}$.

Lee model

The Lee method employs the same assumptions and procedures used in the Mori-Tanaka average stress theory to derive the coefficients of thermal expansion (CTE). The linear CTE parallel to the major axis direction is

$$\frac{\alpha_{||}^{L}}{\alpha_{\mathrm{m}}}=1+\phi\frac{D_4(2B_2-B_4-B_5)}{(2B_2B_3-B_1B_4-B_1B_5)} \tag{10}$$

and the CTE perpendicular to the major axes of the inclusions is

$$\frac{\alpha_{\perp}^{L}}{\alpha_{\mathrm{m}}}=1+\phi\frac{D_4(B_3-B_1)}{(2B_2B_3-B_1B_4-B_1B_5)} \tag{11}$$

where ϕ is the volume fraction of filler, and B_1, B_2, B_3, B_4, B_5, and D_4 are functions of Eshelby's tensor and the properties of the filler and the matrix, specifically Young's modulus, Poisson's ratio, filler concentration, and filler aspect ratio (a) (see Appendices A and B) [24].

For composites based on fiber-shaped inclusions, the CTE in the FD is calculated using Eq. (10), $\alpha_{FD} = \alpha_{\parallel}$, and the CTE in the ND and the TD is calculated using Eq. (11), $\alpha_{ND} = \alpha_{TD} = \alpha_{\perp}$. The bulk CTE is

$$\gamma = \alpha_{FD} + 2\alpha_{ND} \tag{12}$$

For composites based on disk-shaped inclusions, the CTE in the FD and the TD is calculated using Eq. (11), $\alpha_{FD} = \alpha_{TD} = \alpha_{\perp}$, and the CTE in the ND is calculated using Eq. (10), $\alpha_{ND} = \alpha_{\parallel}$. The bulk CTE is

$$\gamma = 2\alpha_{FD} + \alpha_{ND} \tag{13}$$

Chow model

The Chow model treats the fillers as aligned ellipsoidal particles characterized by the ratio of the major to the minor axes [25, 26]. The relative tensile modulus when the direction of the applied load is parallel to the major axes of the inclusions is

$$\frac{E_{\parallel}^{C}}{E_{\mathrm{m}}} = 1 + \frac{(k_f/k_m - 1)G_1 + 2(\mu_f/\mu_m - 1)K_1}{2K_1G_3 + G_1K_3}\phi \tag{14}$$

and the relative modulus when the direction of the applied load is perpendicular to the major axes of the inclusions is

$$\frac{E_{\perp}^{C}}{E_{\mathrm{m}}} = 1 + \frac{(k_f/k_m - 1)G_3 + (\mu_f/\mu_m - 1)(G_3\xi + K_1\zeta)}{2K_1G_3 + G_1K_3}\phi \tag{15}$$

where ϕ is the volume fraction of filler, and k_f and k_m are the bulk modulus and μ_f and μ_m are the shear modulus of the filler and matrix, respectively. Other parameters used are defined in Appendix C.

For composites based on fiber-shaped inclusions, the modulus in the FD is calculated using Eq. (14), $E_{\mathrm{FD}} = E_{\parallel}$, and the modulus in the ND and the TD is calculated using Eq. (15), $E_{\mathrm{ND}} = E_{\mathrm{TD}} = E_{\perp}$. For composites based on disk-shaped inclusions, the modulus in the FD and the TD is calculated using Eq. (15), $E_{\mathrm{FD}} = E_{\mathrm{TD}} = E_{\perp}$, and the modulus in the ND is calculated using Eq. (14), $E_{\mathrm{ND}} = E_{\|}$.

The CTE parallel to the major axes of the inclusions is

$$\frac{\alpha_{\|}^{C}}{\alpha_{\mathrm{m}}} = 1 + \frac{k_f}{k_m} \frac{(\gamma_f - \gamma_m)\widetilde{G}_1}{2\widetilde{K}_1\widetilde{G}_3 + \widetilde{G}_1\widetilde{K}_3} \frac{\phi}{\alpha_{\mathrm{m}}} \tag{16}$$

and the CTE perpendicular to the major axes of the inclusions is

$$\frac{\alpha_{\perp}^{C}}{\alpha_{\mathrm{m}}} = 1 + \frac{k_f}{k_m} \frac{(\gamma_f - \gamma_m)\widetilde{G}_3}{2\widetilde{K}_1\widetilde{G}_3 + \widetilde{G}_1\widetilde{K}_3} \frac{\phi}{\alpha_{\mathrm{m}}} \tag{17}$$

where the parameters used are defined in Appendix C.

For composites based on fiber-shaped inclusions, the CTE in the FD is calculated using Eq. (16), $\alpha_{FD} = \alpha_{\|}$, and the CTE in the ND and the TD is calculated using Eq. (17), $\alpha_{ND} = \alpha_{TD} = \alpha_{\perp}$. The bulk CTE is

$$\gamma = \alpha_{FD} + 2\alpha_{ND} \tag{18}$$

For composites based on disk-shaped inclusions, the CTE in the FD and the TD is calculated using Eq. (17), $\alpha_{FD} = \alpha_{TD} = \alpha_{\perp}$, and the CTE in the ND is calculated using Eq. (16), $\alpha_{ND} = \alpha_{\|}$. The bulk CTE is

$$\gamma = 2\alpha_{FD} + \alpha_{ND} \tag{19}$$

Schapery (Voigt) model

The Schapery model describes the theoretical limit of a composite with fillers of infinite aspect ratio [27]. These models are based on the upper bounds described by Voigt [28]. The longitudinal tensile modulus is

$$E_{11}^{S} = E_{\mathrm{m}}(1-\phi) + E_{\mathrm{f}}\phi \tag{20}$$

The longitudinal and transverse CTE are

$$\alpha_{11}^{S} = \frac{E_m \alpha_{\mathrm{m}} (1-\phi) + E_f \alpha_{\mathrm{f}} \phi}{E_m (1-\phi) + E_f \phi} \tag{21}$$

$$\alpha_{33}^{S} = (1+v_m)\alpha_{\mathrm{m}}(1-\phi) + (1+v_f)\alpha_{\mathrm{f}}\phi - \alpha_{11}(v_{\mathrm{m}}(1-\phi) + v_f \phi) \tag{22}$$

REFERENCES

1. Fornes TD, Yoon PJ, Hunter DL, Keskkula H, and Paul DR. Polymer 2002;43(22):5915-5933.
2. Fornes TD, Yoon PJ, Keskkula H, and Paul DR. Polymer 2002;43(7):2121-2122.
3. Fornes TD, Yoon PJ, Keskkula H, and Paul DR. Polymer 2001;42(25):9929-9940.
4. Stretz HA, Paul DR, Li R, Keskkula H, and Cassidy PE. Polymer 2005;46(8):2621-2637.
5. Cui L, Ma X, and Paul DR. Polymer 2007;48(21):6325-6339.
6. Paul DR, Zeng QH, Yu AB, and Lu GQ. Journal of Colloid and Interface Science 2005;292(2):462-468.
7. Tachino H, Hara H, Hirasawa E, Kutsumizu S, and Yano S. Journal of Applied Polymer Science 1995;55(1):131-138.
8. Kutsumizu S, Tadano K, Matsuda Y, Goto M, Tachino H, Hara H, Hirasawa E, Tagawa H, Muroga Y, and Yano S. Macromolecules 2000;33(24):9044-9053.
9. Hirasawa E, Yamamoto Y, Tadano K, and Yano S. Journal of Applied Polymer Science 1991;42(2):351-362.
10. Halpin JC and Kardos JL. Polymer Engineering & Science 1976;16(5):344-352.
11. Hill R. Journal of the Mechanics and Physics of Solids 1965;13(4):213-222.
12. Halpin J. J. Compos. Mater. 1969;3:732.
13. Hill R. Proc. Phys. Soc., London 1952;65A:349-354.
14. Fornes TD and Paul DR. Polymer 2003;44(17):4993-5013.
15. Shah RK, Kim DH, and Paul DR. Polymer 2007;48(4):1047-1057.
16. Sheng N, Boyce MC, Parks DM, Rutledge GC, Abes JI, and Cohen RE. Polymer 2004;45(2):487-506.
17. Brune DA and Bicerano J. Polymer 2002;43(2):369-387.

18. Kim DH, Fasulo PD, Rodgers WR, and Paul DR. Polymer 2007;48(18):5308-5323.

19. Mori T and Tanaka K. Acta Metallurgica 1973;21(5):571-574.

20. Eshelby JD. Proceedings of the Royal Society of London. Series A. Mathematical and Physical Sciences 1957;241(1226):376-396.

21. Tandon GP and Weng GJ. Polymer Composites 1984;5(4):327-333.

22. Hui CY and David S. Polymer Engineering & Science 1998;38(5):774-782.

23. van Es M, Xiqiao F, van Turnhout J, and van der Giessen E. Comparing polymer–clay nanocomposites with conventional composites using composite modeling. In: Al-Malaika S, Golovoy A, and Wilkie C, editors. Specialty polymer additives: principles and applications. London: Blackwell Science, 2001. pp. Chapter 21.

24. Lee KY, Kim KH, Jeoung SK, Ju SI, Shim JH, Kim NH, Lee SG, Lee SM, Lee JK, and Paul DR. Polymer 2007;48(14):4174-4183.

25. Chow TS. Journal of Polymer Science: Polymer Physics Edition 1978;16(6):967-970.

26. Chow TS. Journal of Polymer Science: Polymer Physics Edition 1978;16(6):959-965.

27. Schapery RA. Journal of Composite Materials 1968;2(3):380-404.

28. Voigt, W. Abh.Kgl.Ges.Wiss.Göttingen, Math.Kl. 1887;34: 3-51.

Chapter 3: Morphology and properties of nanocomposites based on HDPE/HDPE-*g*-MA blends

Nanocomposites formed from polyolefin matrices are often modified with a polar compatibilizer to improve exfoliation and enhance properties. The grafting of maleic anhydride to the polyolefin backbone significantly increases the polarity and, thus, improves exfoliation in polypropylene [1-9] and polyethylene [10-20]. Other approaches include the incorporation of polar comonomers like vinyl acetate [12, 21, 22], methacrylic acid [23-26], or methacrylic acid ionomers [27-30].

Maleated polypropylene, PP-*g*-MA, is typically used in relatively low quantities, comparable to the mass of organoclay, to form polypropylene-based nanocomposites and is thought of as a "compatibilizer" [4-9]. Use of small amounts of PP-*g*-MA is advantageous commercially owing to the substantially higher cost of PP-*g*-MA compared to unmodified PP. It would be useful, however, to understand how the morphology and properties of nanocomposites change as the ratio of maleated to unmaleated polyolefin in the matrix changes over a broader range.

It is not practical to explore this question for polypropylene-based nanocomposites because the maleation process leads to significant scission of polypropylene chains, lowering the molecular weight and, therefore, greatly reducing the melt viscosity of PP-*g*-MA compared to the PP precursor [31-33]. Melt rheology is known to play some role in the exfoliation process in melt compounding because this affects the stresses imposed on the organoclay tactoids [34, 35]. However, maleation of linear polyethylene does not lead to significant chain scission, making it possible to obtain commercial high density polyethylene (HDPE) and maleic anhydride-grafted high density polyethylene (HDPE-*g*-MA) with comparable rheological properties.

This chapter explores the extent of organoclay exfoliation and the mechanical properties of melt compounded nanocomposites with matrices consisting of HDPE/HDPE-*g*-MA blends over the full range of compositions. This allows a useful way to explore the relationship between mechanical properties and the degree of exfoliation without dramatically changing the nature of the polymer matrix and to obtain further insights into the "compatibilizing" role of maleated polyolefins for nanocomposite formation.

EXPERIMENTAL

Materials

The high density polyethylene, HDPE, (Alathon® M6020, LyondellBasell) and the maleic anhydride-grafted high density polyethylene, HDPE-*g*-MA, (Fusabond® E MB100D, Du Pont) were chosen because they have the same melt index (MI = 2 g/10 min). It is expected that the HPDE and the HDPE-*g*-MA used are miscible with each other based on prior work with related polyolefins [36, 37]. The organoclay designated as $M_2(HT)_2$, donated by Southern Clay Products, was prepared by a cation exchange reaction between sodium montmorillonite (Na^+ MMT) and a two-tailed quaternary ammonium surfactant, dimethyl bis(hydrogenated-tallow) ammonium chloride (Arquad 2HT-75). Some frequently used abbreviations are employed here to represent the substituents on the ammonium cation, e.g., M for methyl and HT represents long alkyl chains from hydrogenated tallow [28, 38, 39]. Tables 2.1 and 2.2 in Chapter 2 provide further details on the materials used in this study. This organoclay was selected based upon recent studies showing improved organoclay exfoliation in polyethylene using surfactants with two tails on the ammonium ion instead of one tail [10, 21, 24, 28]. The polymers employed have better affinity for the largely aliphatic organic modifier than for the unmodified clay surface. The larger area of the clay surface covered by two tails increases the favorable surfactant-polymer interaction and decreases the unfavorable polymer-clay interaction.

Melt processing

The organoclay and the HDPE-*g*-MA were dried for a minimum of 24 h in a vacuum oven at 80 °C, prior to melt processing. Nanocomposites were melt compounded in a Haake co-rotating, intermeshing twin screw extruder (diameter = 30 mm, L/D = 10) using a barrel temperature of 200 - 205 °C, a screw speed of 280 rpm , and a feed rate of 1 kg/h. The HDPE, the HDPE-*g*-MA, and the organoclay were hand-mixed prior to extrusion and introduced into the extruder by a single hopper.

Tensile specimens (ASTM D638, Type I) and Izod bars (ASTM D256) were prepared by an Arburg Allrounder 305-210-700 injection-molding machine using a barrel temperature of 200 °C (feed) to 205 °C (die), an injection pressure of 75 bar, and a holding pressure of 50 bar. After molding, the samples were immediately sealed in a polyethylene bag and placed in a vacuum desiccator for a minimum of 24 h prior to testing.

The montmorillonite content of the nanocomposite was determined by placing pre-dried nanocomposite pellets in a furnace at 900 °C for 45 min and weighing the remaining MMT ash, correcting for loss of structural water [34, 40-42].

Characterization

Differential scanning calorimetric (DSC) thermograms were recorded using a Perkin-Elmer Model DSC-7 at a heating rate of 10 °C/min under an extra dry N2 atmosphere over a temperature range of 30 °C to 180 °C. The predried neat HDPE and HDPE-*g*-MA samples of 7 mg to 10 mg were packed in aluminum pans, heated to

180 °C, and held there for 5 min to reset the thermal history. The melting temperature and the heat of fusion were determined from the second heating scan. The percent crystallinity was determined by dividing the heat of fusion value by 293 J/g, the heat of fusion of 100% crystalline polyethylene [43].

Morphology was examined primarily via a JEOL 2010F transmission electron microscope (TEM) operating under an accelerating voltage of 120 kV. Some samples were observed using a FEI TECNAI G2 F20 X-TWIN TEM operating under an accelerating voltage of 200 kV. Ultra-thin sections (~50 nm) for morphological analysis were taken from the core portion of an injection molded bar in the plane defined by the flow direction (FD) and the normal direction (ND) using an RMC PowerTome XL microtome [44]. The nanocomposite samples and the diamond knife were cooled to between -75 and -85 °C and -60 °C, respectively, using liquid nitrogen. Cut sections were collected onto 400 mesh grids and dried with filter paper.

Wide angle X-ray scattering (WAXS) scans were performed using a Bruker-AXS D8 Advance diffractometer in the reflection mode, using an incident X-ray wavelength of 0.1541 nm at a scan rate of 3.0°/min over the range of $2\theta = 1°$ to $12°$. The skin of the major face of the rectangular nanocomposite bars and the organoclay powder were scanned [45].

Tensile tests were performed according to ASTM D638 using an Instron model 1137 machine upgraded for computerized data acquisition. Tensile modulus values were determined using an extensometer at a crosshead rate of 0.51 cm/min and averaged from at least five specimens. Elongation at break and yield strength data were taken at 0.51 cm/min and averaged from at least three specimens. Elongations greater than 400% could not be measured, due to the limitations of crosshead travel.

Notched Izod impact tests were conducted at room temperature using a 6.8 J hammer and 3.5 m/s impact velocity using a TMI Impact tester (model 43-02). Standard notches were made according to ASTM D256. Frequently, as-molded rectangular bars are cut in half (to generate more samples) and the Izod impact strength data from the gate end (the end at which the molten polymer enters the mold during injection molding) and the far end are averaged together. Morphological differences arising from the injection molding process can result in significant differences between the Izod impact strength measured at the gate end and the far end of the samples. Thus, in this work, the Izod impact strength data were averaged from four samples each of the gate end, of the middle, and of the far end of the bars.

Particle analysis

Particle analyses were performed on TEM micrographs at magnifications of 8K to 30K, depending on the extent of exfoliation in the sample. Because of low contrast, TEM images were converted into .jpg format and opened in GIMP (GNU Image Manipulation Program). Two tracings in separate, transparent layers were made of particle length and thickness. For nanocomposites with single platelets, the thickness of these platelets could not accurately be measured and was assigned a thickness of 0.94 nm corresponding to the known results for MMT platelets [21, 46]. Each tracing was saved separately in .tif format and imported into the image analysis program, SigmaScan Pro, where each particle tracing was assigned a number and their characteristic dimensions were measured. Because the numbers assigned in the tracing of the length and the tracing of the thickness of the particles do not correspond, the particle dimensions must be matched manually. In this work, four different kinds of aspect ratios are calculated, i.e., the number and weight averages of the aspect ratios calculated for individual particles,

$\langle l/t \rangle_n$ and $\langle l/t \rangle_w$, and ratios of the number and weight averages of particle lengths and thicknesses, $\left(\overline{l_n}/\overline{t_n}\right)$ and $\left(\overline{l_w}/\overline{t_w}\right)$. To ensure statistical validity of the analysis, 200~400 particles were counted to measure the length, thickness, and aspect ratio.

Table 3.1: Results of one population particle analysis of nanocomposites

HDPE-*g*-MA %	Wt % MMT	Mass HDPE-*g*-MA / Mass Organclay	Total number of particles	Number average particle length $\left(\overline{l_n}, nm\right)$	Number average particle thickness $\left(\overline{t_n}, nm\right)$	Weight average particle length $\left(\overline{l_w}, nm\right)$	Weight average particle thickness $\left(\overline{t_w}, nm\right)$	Number average aspect ratio $\left(\overline{l_n}/\overline{t_n}\right)$	Number average aspect ratio $\langle l/t\rangle_n$	Weight average aspect ratio $\left(\overline{l_w}/\overline{t_w}\right)$	Weight average aspect ratio $\langle l/t\rangle_w$
0	5.05	0	206	315.6	23.7	568.1	56.4	13.3	20.3	10.1	30.7
0.5	5.29	0.05	225	289.5	15.1	430.4	33.1	19.2	29.0	13.0	40.5
3	4.87	0.34	221	213.1	9.6	271.1	18.7	22.2	33.1	14.5	46.3
9	4.94	1.01	321	196.2	4.6	256.7	8.5	42.8	58.4	30.2	82.2
18	5.13	1.94	336	99.4	2.3	128.0	7.0	43.7	55.7	18.3	67.5
25	5.20	2.65	340	97.5	1.7	126.5	2.2	57.6	62.1	58.4	76.1
50	5.41	5.08	408	84.9	1.4	109.4	3.3	59.8	64.9	33.6	76.0
65	5.30	6.76	349	73.5	1.2	90.8	1.6	59.2	60.5	55.2	70.2
85	5.31	8.81	355	66.2	1.2	79.9	1.2	56.8	57.8	65.1	68.8
100	5.37	10.25	362	55.5	1.1	70.2	1.2	48.7	48.2	59.1	57.4

Table 3.2: DSC results for neat polymers

Material	**T_m (°C)**	**ΔH_m (J/g)**	**% Crystallinity**
HDPE	136.7	193.2	65.9
HDPE-*g*-MA	133.5	175.0	59.7

RESULTS AND DISCUSSION

Properties of neat blends

Before discussing the morphology and properties of the nanocomposites, it is useful to examine the properties of the neat HDPE/HDPE-*g*-MA blends used as nanocomposite matrices. The melting temperature (peak values), heat of fusion, and percent crystallinity for neat HDPE and HDPE-*g*-MA are shown in Table 3.2, as determined by DSC. HDPE-*g*-MA has lower melting temperature, heat of fusion and degree of crystallinity than HDPE, due to the maleic anhydride groups that disrupt the ordered crystalline structure of polyethylene.

The tensile modulus and the yield strength of neat HDPE/HDPE-*g*-MA blends are shown plotted versus HDPE-*g*-MA content in Figure 3.1(a) and (b) respectively. Both modulus and yield strength decrease at high HDPE-*g*-MA levels, likely due to the lower crystallinity of HDPE-*g*-MA compared with HDPE. Neat blends of HDPE/HDPE-*g*-MA are too ductile to determine the breaking point on the available equipment, therefore, all elongations at break are >400%.

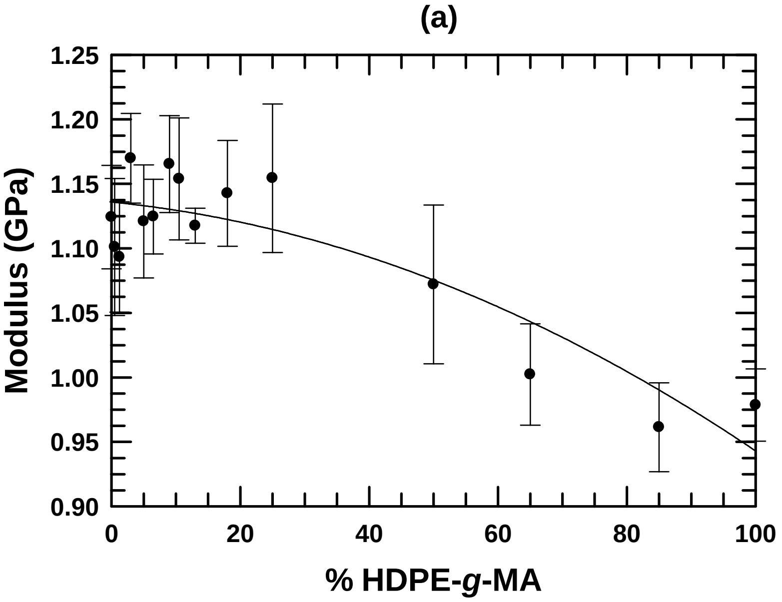

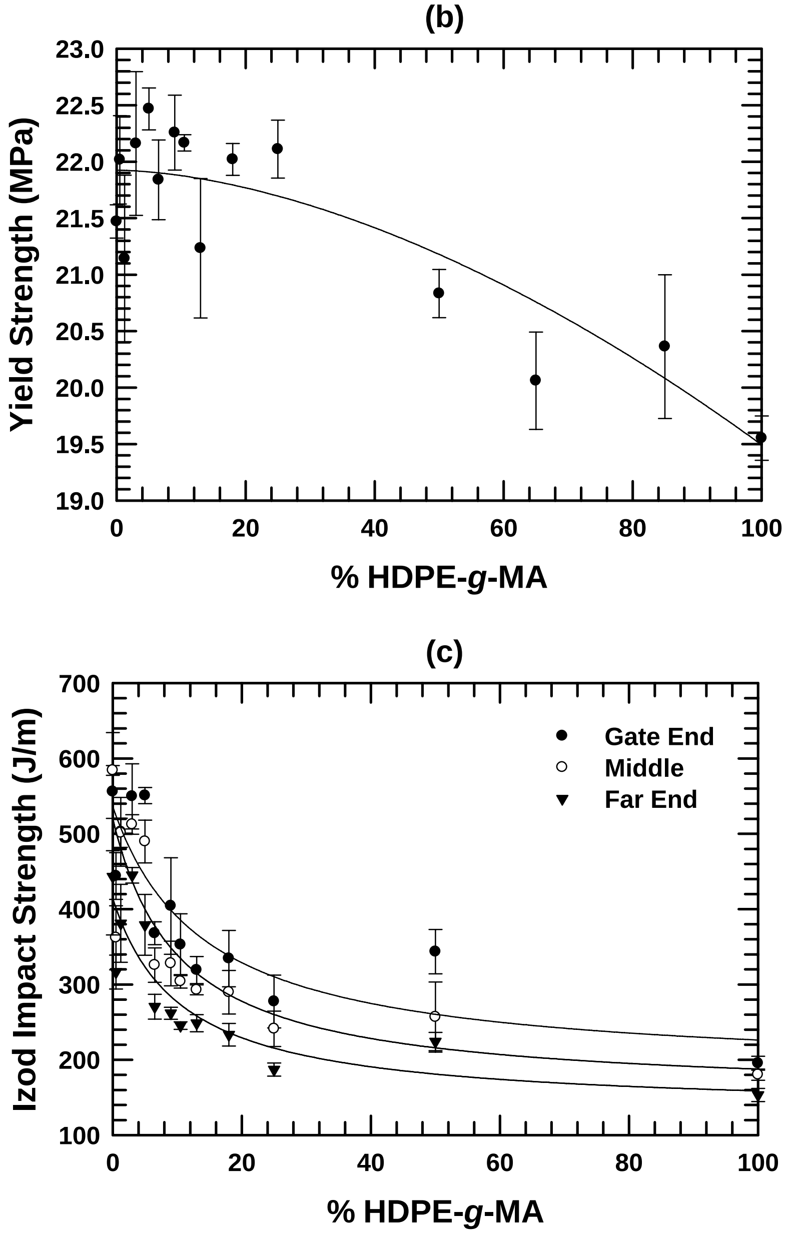

Figure 3.1. Effect of HDPE-*g*-MA content on mechanical properties of HDPE/HDPE-*g*-MA blends without clay: (a) tensile modulus, (b) yield strength, and (c) Izod impact strength.

Neat HDPE has been reported to have different impact values for the gate end and far end of injection-molded Izod bars [47]. Because of large differences measured between the ends in this work, impact strengths were averaged separately for the gate and far ends. In addition, impact strengths were measured at the middle of the Izod bars by cutting off the quarters of the bar near the gate and far end. Izod impact strength data for neat HDPE/HDPE-*g*-MA blends are presented in Figure 3.1(c). Generally, the fracture energy decreases from the gate end to the middle and from the middle to the far end. This could be the result of differences in the molecular orientation, crystal orientation, and percent crystallinity along the length of the bar. Pantani et al. found significant changes in molecular orientation along the flow direction, but no significant change in crystallinity, for injection molded isotactic polypropylene (iPP). They also noted substantial morphological differences by varying the molding conditions [48, 49]. In our study, the molding conditions were held relatively constant. The molding conditions may be optimized to minimize the difference in impact strength along the flow direction of the bar, but this was beyond the scope of this work.

Izod impact strength generally decreases as HDPE-*g*-MA content increases regardless of the portion of the bar tested. At ~6% HDPE-*g*-MA the fracture energy decreases dramatically. Higher levels of HDPE-*g*-MA reduce the impact strength more gradually. Bars with HDPE-*g*-MA levels of < 5% have a large variance in impact strength. The change in impact strength with increased HDPE-*g*-MA content was not expected and the reasons are not well understood. Molding conditions such as injection speed were varied for both neat HDPE and neat HDPE-*g*-MA, but the Izod impact strength for HDPE was always significantly higher than for HDPE-*g*-MA. Differences in crystallinity, interactions between maleic anhydride groups, and differences in the molecular weight distributions may affect the fracture energy; however, sorting out these and possibly other reasons for the differences shown was considered to be beyond the scope of this work.

Morphology

Transmission electron microscopy

TEM observations allow for a visual, qualitative assessment of the degree of organoclay exfoliation in polymer nanocomposites. Figure 3.2 shows representative TEM micrographs for nanocomposites with different HDPE-*g*-MA concentrations having a nominal MMT content of 5 wt%. For the HDPE nanocomposites (Figure 3.2(a)), large tactoids are seen, indicating poor clay dispersion. Particles with thicknesses of 1 μm or greater can be found.

The addition of merely 0.5 wt% HDPE-*g*-MA (Figure 3.2(b)) to the polymer matrix significantly improves the exfoliation of the organoclay. Taking note of the different scale bars, the size of tactoids is decreased dramatically. Though large tactoids are still present, many smaller particles are seen. Clearly, even small amounts of HDPE-*g*-MA dramatically influence the ability of the polymer matrix to exfoliate the organoclay.

As more HDPE-*g*-MA is added to the polymer matrix, exfoliation continues to improve. As seen in Figure 3.2(c), (d), and (e), for nanocomposites with 3 wt%, 9 wt%, and 18 wt% of HDPE-*g*-MA respectively, the size of the clay tactoids continue to decrease and the ratio of smaller particles to larger tactoids increases with increased polar content.

Nanocomposites based on 25 wt%, 50 wt%, 65 wt%, 85 wt%, and 100 wt% HDPE-*g*-MA are shown in Figure 3.2(f), (g), (h), (i), and (j), respectively, and have a well-exfoliated morphology consisting primarily of single platelets. Little difference in the extent of exfoliation can be seen qualitatively.

The noted enhancements in exfoliation with increased amounts of polar MA groups in the polymer matrix indicate improved interactions between the polymer and the organoclay. The exfoliation improves rapidly with the addition of initial amounts of HDPE-*g*-MA, but after a certain threshold value is reached (~25 wt% HDPE-*g*-MA), little change in the extent of exfoliation is seen.

Particle analysis

Particle analysis is used to quantify the extent of exfoliation shown in the TEM images. The statistical results and the MMT concentration of each nanocomposite as determined by incineration are shown in Table 3.1. The aspect ratios obtained by averaging the values of each particle, $\langle l/t \rangle_n$ and $\langle l/t \rangle_w$, are generally larger than those calculated from the ratio of the corresponding average values of length and thickness, $\left(\overline{l_n}/\overline{t_n}\right)$ and $\left(\overline{l_w}/\overline{t_w}\right)$. The ratio of number average particle length and thickness, $\left(\overline{l_n}/\overline{t_n}\right)$, is generally larger than the ratio of weight average particle length and thickness, $\left(\overline{l_w}/\overline{t_w}\right)$ while the weight average aspect ratio obtained by averaging values of each particle, $\langle l/t \rangle_w$, is always larger than the corresponding number average ratio, $\langle l/t \rangle_n$. These trends are in a good agreement with previous reports [21, 50, 51].

Figure 3.3 shows a series of representative histograms of particle length, thickness and aspect ratio for HDPE/HDPE-*g*-MA 25% based nanocomposites containing ~5 wt% MMT. All of these features showed broad distributions based on the analysis of a total of 340 particles. To better understand the relationship between the polarity of the polymer matrix and the organoclay exfoliation, plots of particle lengths and thicknesses (Figure 3.4(a) and (b)) and particle aspect ratios (Figure 3.4(c)) as a function of HDPE-*g*-MA content in the polymer matrix are presented for nanocomposites containing ~5 wt% MMT.

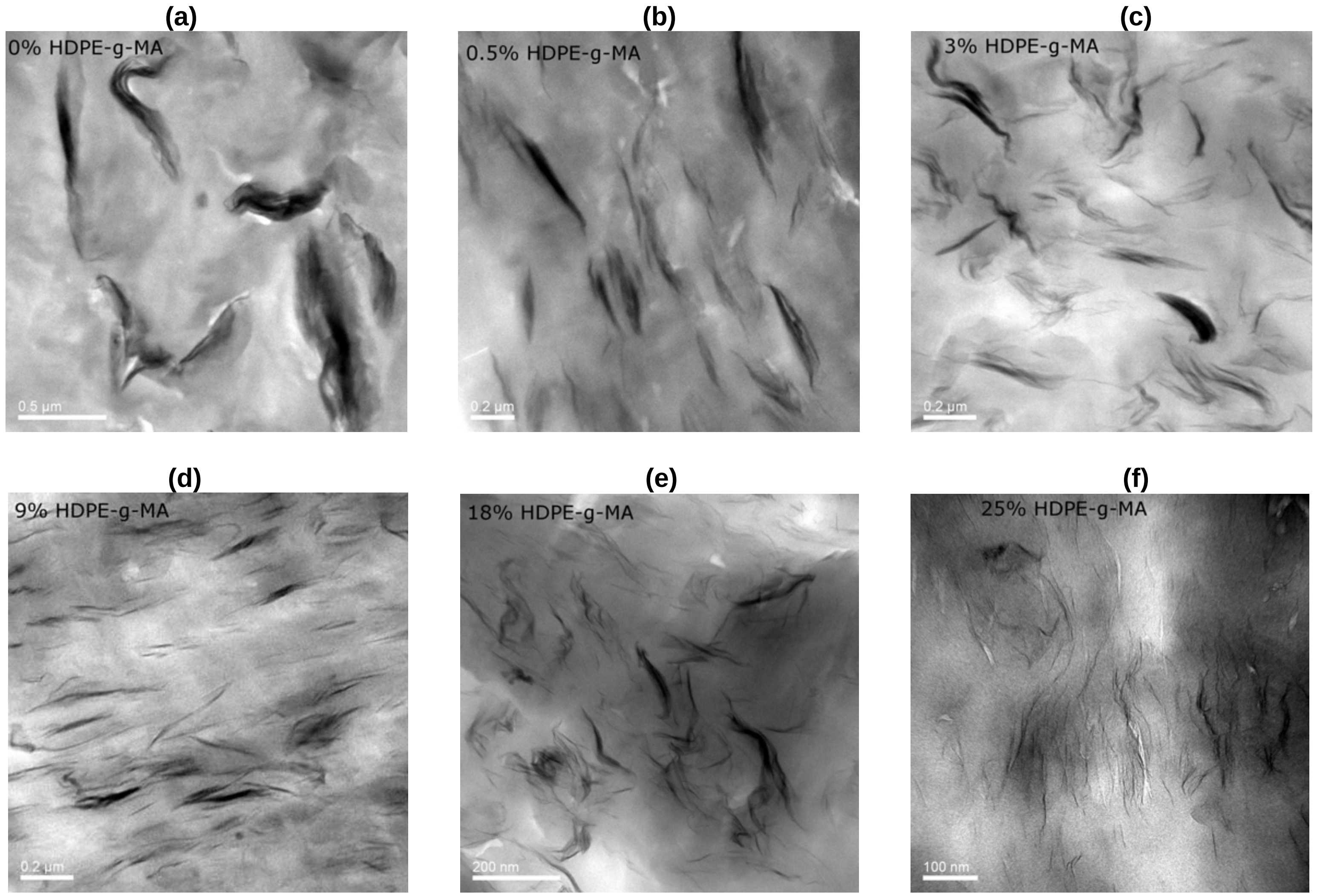
(a)
0% HDPE-g-MA
0.5 µm
(b)
0.5% HDPE-g-MA
0.2 µm
(c)
3% HDPE-g-MA
0.2 µm
(d)
9% HDPE-g-MA
0.2 µm
(e)
18% HDPE-g-MA
200 nm
(f)
25% HDPE-g-MA
100 nm

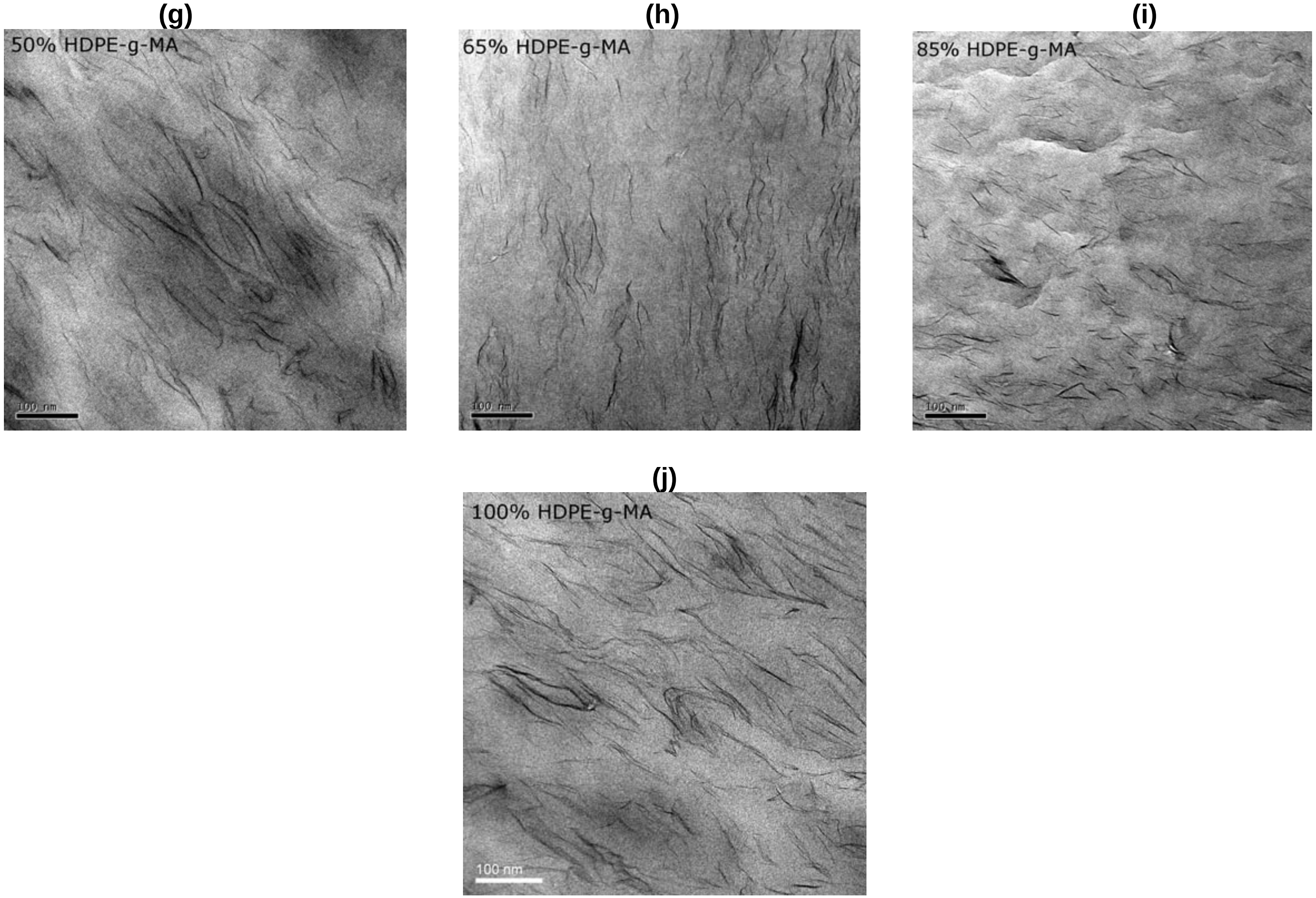

Figure 3.2: TEM photomicrographs of HDPE/HDPE-*g*-MA/$M_2(HT)_2$ nanocomposites with nominally 5 wt% MMT: (a) HDPE, (b) HDPE/HDPE-*g*-MA 0.5%, (c) HDPE/HDPE-*g*-MA 3%, (d) HDPE/HDPE-*g*-MA 9%, (e) HDPE/HDPE-*g*-MA 18%, (f) HDPE/HDPE-*g*-MA 25%, (g) HDPE/HDPE-*g*-MA 50%, (h) HDPE/HDPE-*g*-MA 65%, (i) HDPE/HDPE-*g*-MA 85%, and (j) HDPE-*g*-MA.

The quantitative trends mirror the qualitative TEM results discussed above. Average particle thickness and length decrease rapidly upon the addition of even small amounts of HDPE-*g*-MA. When the particle thickness decreases at a higher rate than the particle length, the aspect ratio increases. At HDPE-*g*-MA contents of 9% and 18% the length and thickness continue to decrease, but not as rapidly, indicating smaller improvements in exfoliation. For nanocomposites based on blends with HDPE-*g*-MA contents of ≥25%, the average particle thickness deceases gradually, due to the particle thickness limit of a single platelet (0.94 nm). Because the average particle length decreases at a greater rate than the particle thickness, the aspect ratio gradually decreases for matrices at >50% HDPE-*g*-MA content.

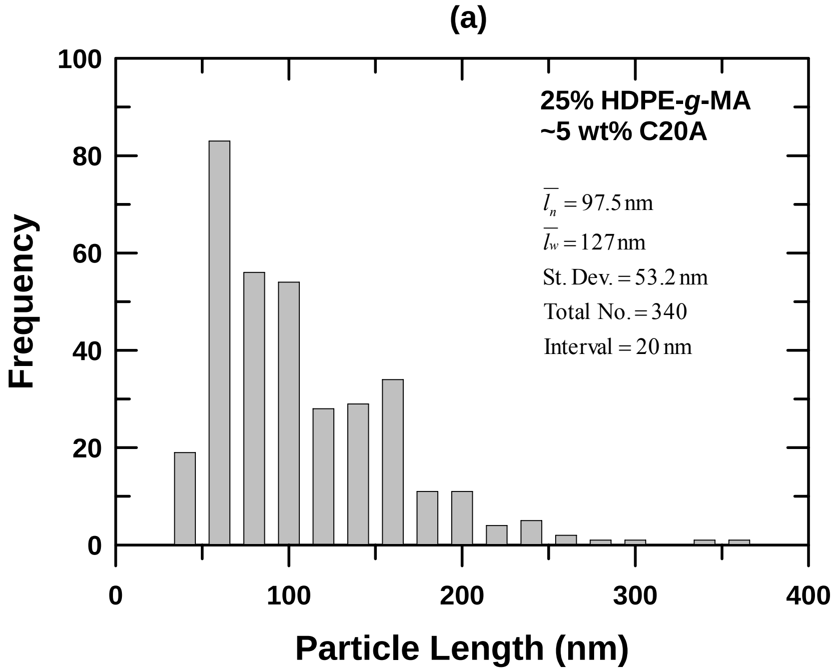

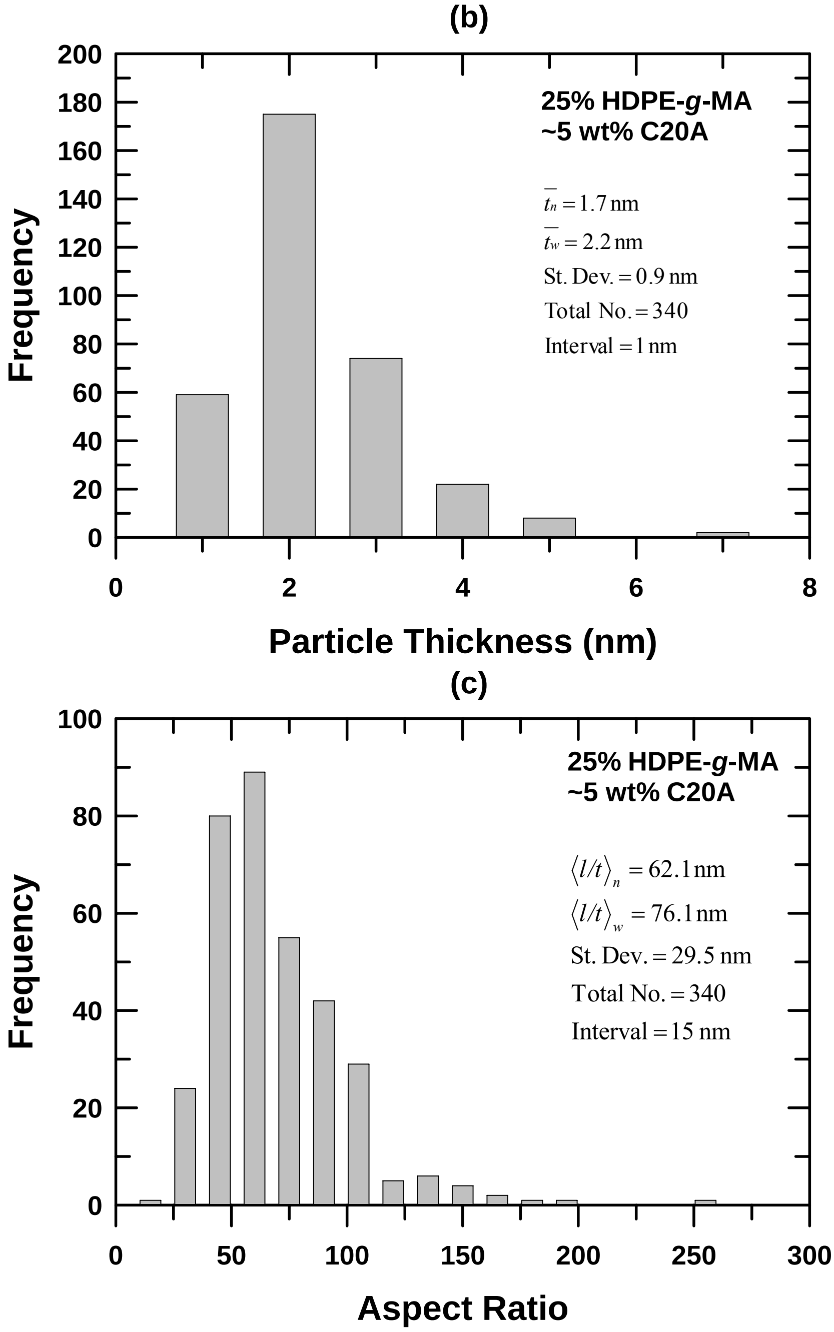

Figure 3.3: Histograms of (a) particle length, (b) particle thickness, and (c) aspect ratio of HDPE/HDPE-*g*-MA 25%/$M_2(HT)_2$ nanocomposites for one population with nominally 5 wt% MMT (total number of particles = 340).

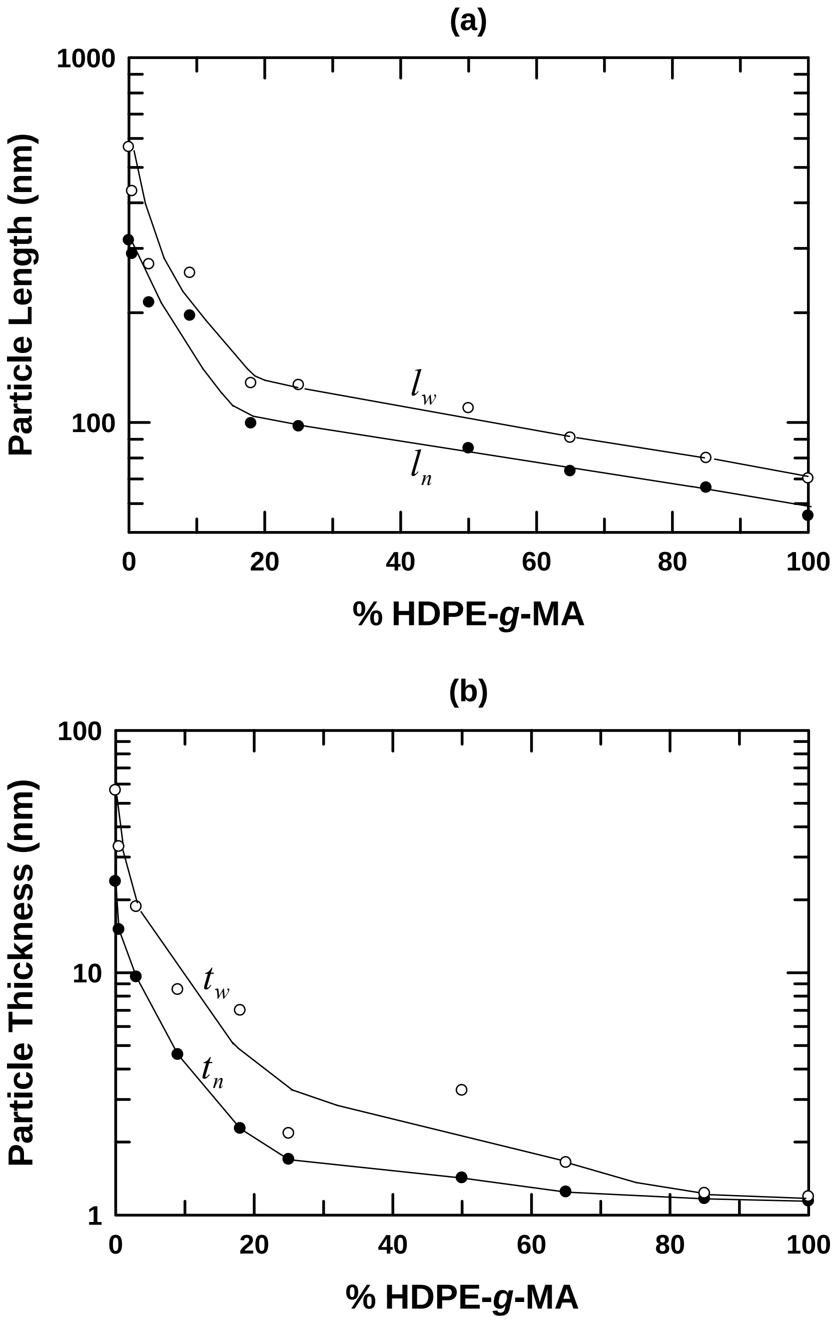
(a)
1000
100
Particle Length (nm)
l_w
l_n
0
20
40
60
80
100
% HDPE-*g*-MA
(b)
100
10
1
Particle Thickness (nm)
t_w
t_n
0
20
40
60
80
100
% HDPE-*g*-MA

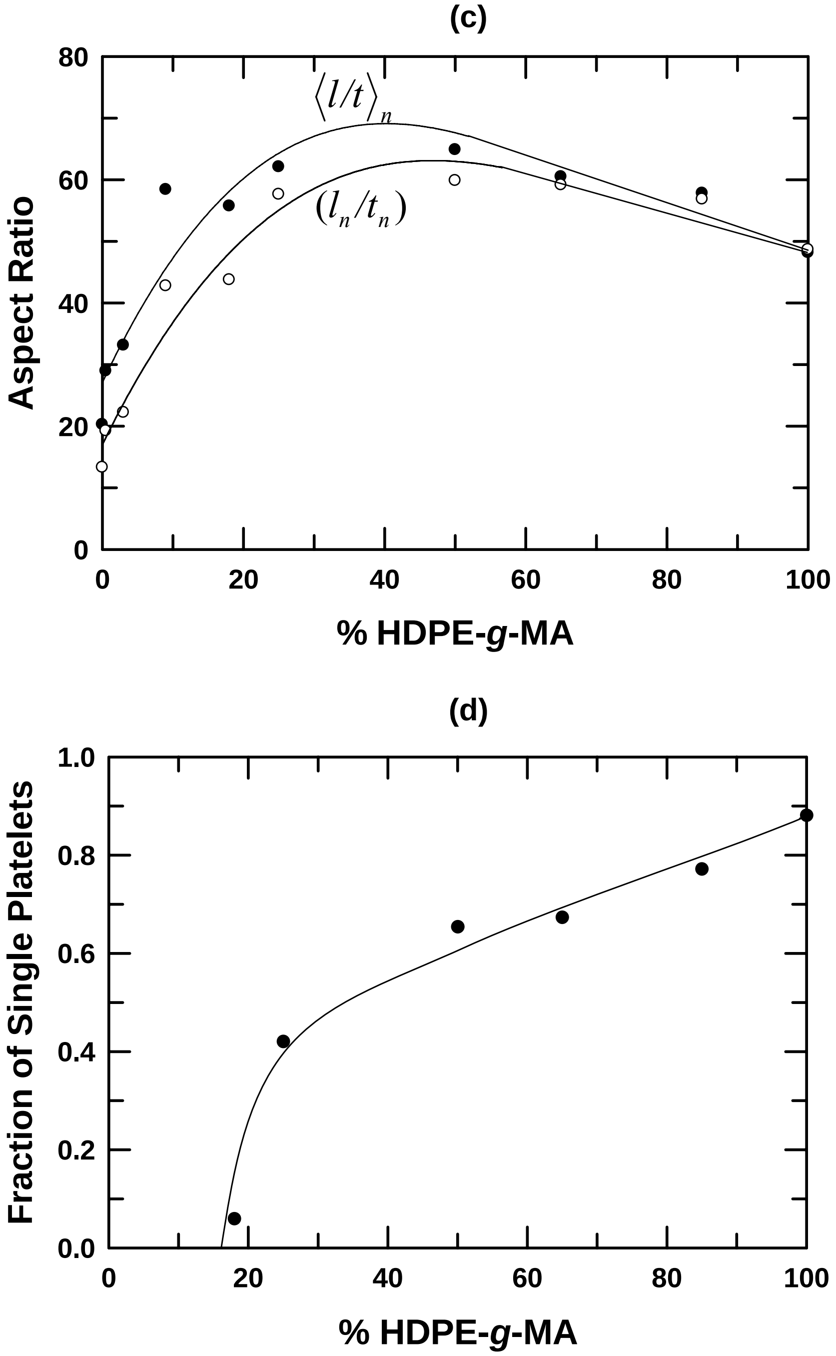

Figure 3.4: The effect of HDPE-*g*-MA content on (a) particle length, (b) particle thickness, (c) number average aspect ratio and ratio of number average particle length and number average particle thickness, and (d) fraction of single platelets of HDPE/HDPE-*g*-MA/$M_2(HT)_2$ nanocomposites based on one filler population at a fixed MMT content of ~5 wt%.

For further insight, the fraction of single platelets (Figure 3.4(d)) was calculated by dividing the number of particles with a thickness of nearly 1 nm by the total number of particles. The fraction of single platelets increases with increasing HDPE-*g*-MA content for nanocomposites with >20% HDPE-*g*-MA. As the amount of single platelets increases, the average particle thickness decreases at a slower rate due to the thickness limit of a single platelet. Increased particle breakup and lower numbers of overlapping particles, however, continues to decrease the average particle length, resulting in a decreased aspect ratio.

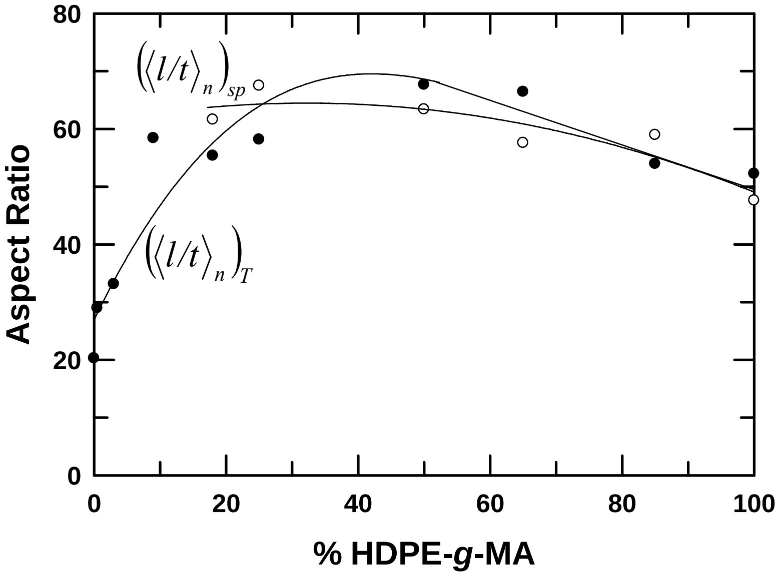

Figure 3.5: The effect of HDPE-*g*-MA content on the two population number average aspect ratios accounting for tactoids and single platelets separately for HDPE/HDPE-*g*-MA/$M_2(HT)_2$ nanocomposites at a fixed MMT content of ~5 wt%.

Because partially exfoliated organoclay tactoids and fully exfoliated single platelets have differing reinforcement effects on the nanocomposites, these two populations of particles were also analyzed separately. The number average aspect ratio, $\langle l/t \rangle_n$, is shown for both single platelets with measured thicknesses of about 1 nm and for the remaining tactoids in Figure 3.5 and Table 3.3. Surprisingly there is not a significant difference in the trends of these two populations. The decrease in single platelet aspect ratio may be attributed to lower amounts of slightly overlapping particles that are measured as single platelets and to increased particle breakup.

A schematic illustration of the change in particle dimensions for increased levels of HDPE-*g*-MA is shown in Figure 3.6. Initially, particle thickness decreases faster than particle length, increasing the aspect ratio. As the average particle thickness approaches the limit of the platelet thickness, the particle length decreases faster than the particle thickness, decreasing the aspect ratio.

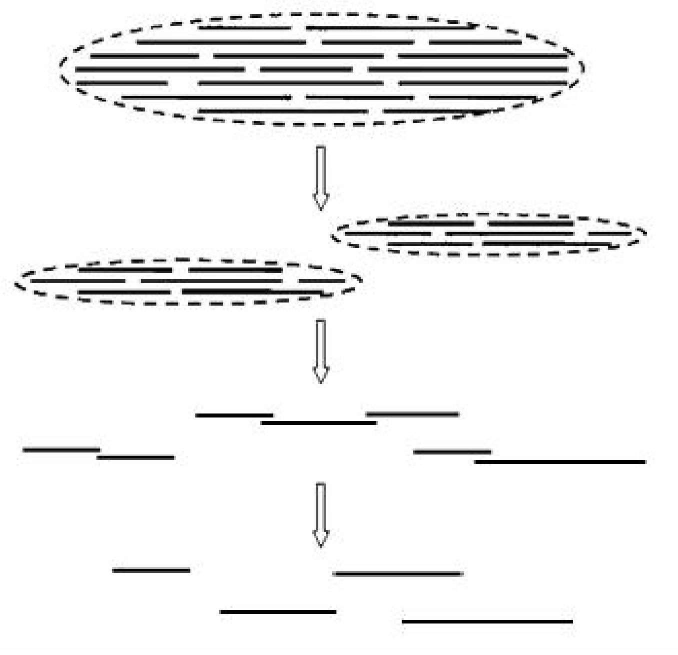

Figure 3.6: Schematic illustration of the change of effective particle length and thickness with increasing HDPE-*g*-MA content.

The average particle lengths for all these nanocomposites are larger than those observed for nylon 6 nanocomposites, where exfoliation is near ideal, i.e., most of the particles are individual platelets [52, 53]. The larger particles seen here are likely due to ‘‘skewing’’ of the platelets in the thicker clay bundles. However, the average particle lengths do approach the values seen in nylon 6 nanocomposites when HDPE-*g*-MA is used as the matrix, indicating near maximum exfoliation.

Ploehn and Liu accurately characterized a commonly used montmorillonite by depositing platelets on a mica surface from a very dilute suspension and then measuring the lateral dimensions by atomic force microscopy [54]. Because the lateral size or shape of the platelets is not uniform, the platelet area, A, was measured and its square-root was normalized by platelet thickness, t, to calculate an “aspect ratio”. If each platelet were circular with diameter D, then

$$\sqrt{A}\big/t = \sqrt{\pi/4}(D/t) = 0.89(D/t) \tag{1}$$

Because t is approximately 1 nm, the most probable lateral dimension is in the range of 100–200 nm [54, 55]. The average particle lengths found in this study fall below this range. However, the observed lengths reflect a random cut through irregular platelets and particles and only rarely will the maximum dimension be seen [56, 57].

Wide angle X-ray scattering

WAXS is commonly used to characterize the exfoliation structure of nanocomposites. WAXS scans of the neat organoclay ($M_2(HT)_2$) and of the skin portion of nanocomposites with ~5% MMT prepared from various polymer matrices are shown in Figure 3.7. The d_{001} peak intensity decreases with increasing HDPE-*g*-MA content and disappears for nanocomposites with >50% HDPE-*g*-MA in the polymer matrix, suggesting a highly exfoliated structure. The d_{001} peak for HDPE-based nanocomposites is shifted slightly to the right of the peak for the neat organoclay. For nanocomposites with HDPE-*g*-MA compatibilizer, the peak shifts slightly to the left of the HDPE-based nanocomposite, but remains to the right of the peak for the neat organoclay. This shift to higher angle and lower *d*-spacing could indicate degradation of the surfactant, causing the clay galleries to collapse as surfactant mass is lost from within the galleries [28]. These differences are so small, however, that it is difficult to attach much physical meaning to them [50, 51]. These results are in good agreement with the TEM analysis discussed above. The WAXS results give only limited information about morphology and TEM, though providing a clearer understanding of exfoliation levels, examines only a small volume and may not be representative of the nanocomposite as a whole. Therefore, bulk mechanical properties were measured to complement TEM and WAXS analyses [50, 51].

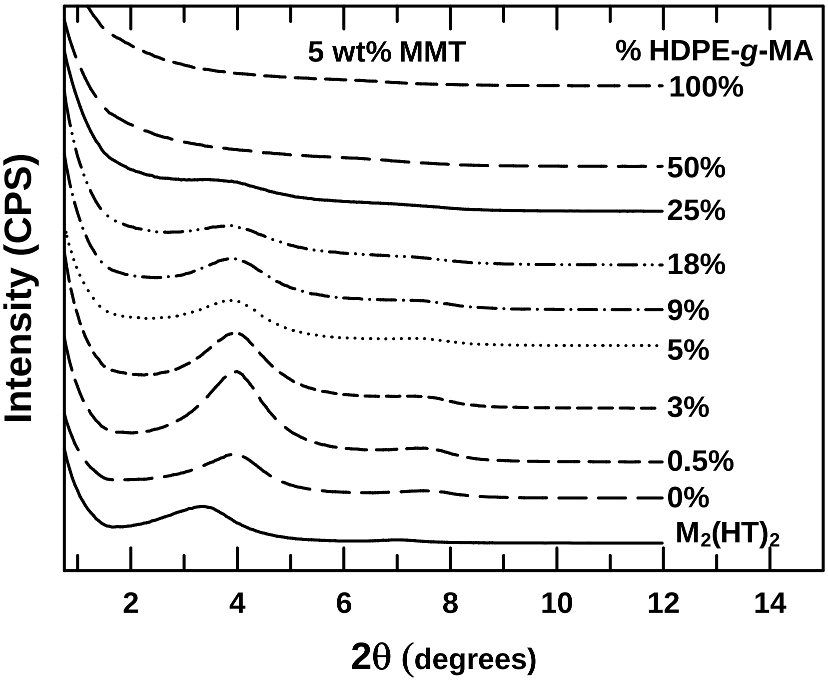

Figure 3.7: WAXS scans of pristine organoclay, $M_2(HT)_2$, and nanocomposites containing ~5 wt% MMT formed from HDPE/HDPE-*g*-MA copolymers with various HDPE-*g*-MA contents. The curves are vertically offset for clarity.

Mechanical properties

Of the various mechanical properties, modulus provides the best indicator of organoclay exfoliation [38]. Modulus data are shown in Table 3.4 for nanocomposites with MMT contents of ~5 wt%. Figure 3.8(a) shows the effect of MMT concentration on the tensile modulus of HDPE nanocomposites with various amounts of HDPE-*g*-MA. As expected, increasing MMT content results in significant improvements in modulus. Because the moduli of the neat HDPE based polymers (E_m) vary with HDPE-*g*-MA content, examining the relative moduli (E/E_m) allows more useful comparisons. Relative modulus as a function of MMT concentration in nanocomposites with various amounts of HDPE-*g*-MA is shown in Figure 3.8(b). At high MMT contents, the improvement in modulus increases rapidly with the addition of small amounts of HDPE-*g*-MA. At higher HDPE-*g*-MA levels, i.e., ≥5%, the increase caused by the HDPE-*g*-MA seems to be independent of the amount of HDPE-*g*-MA added.

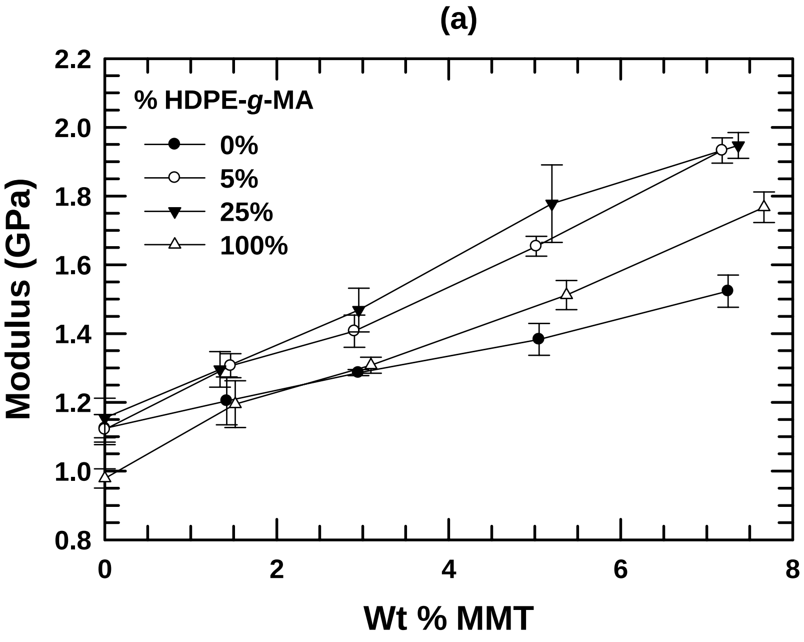

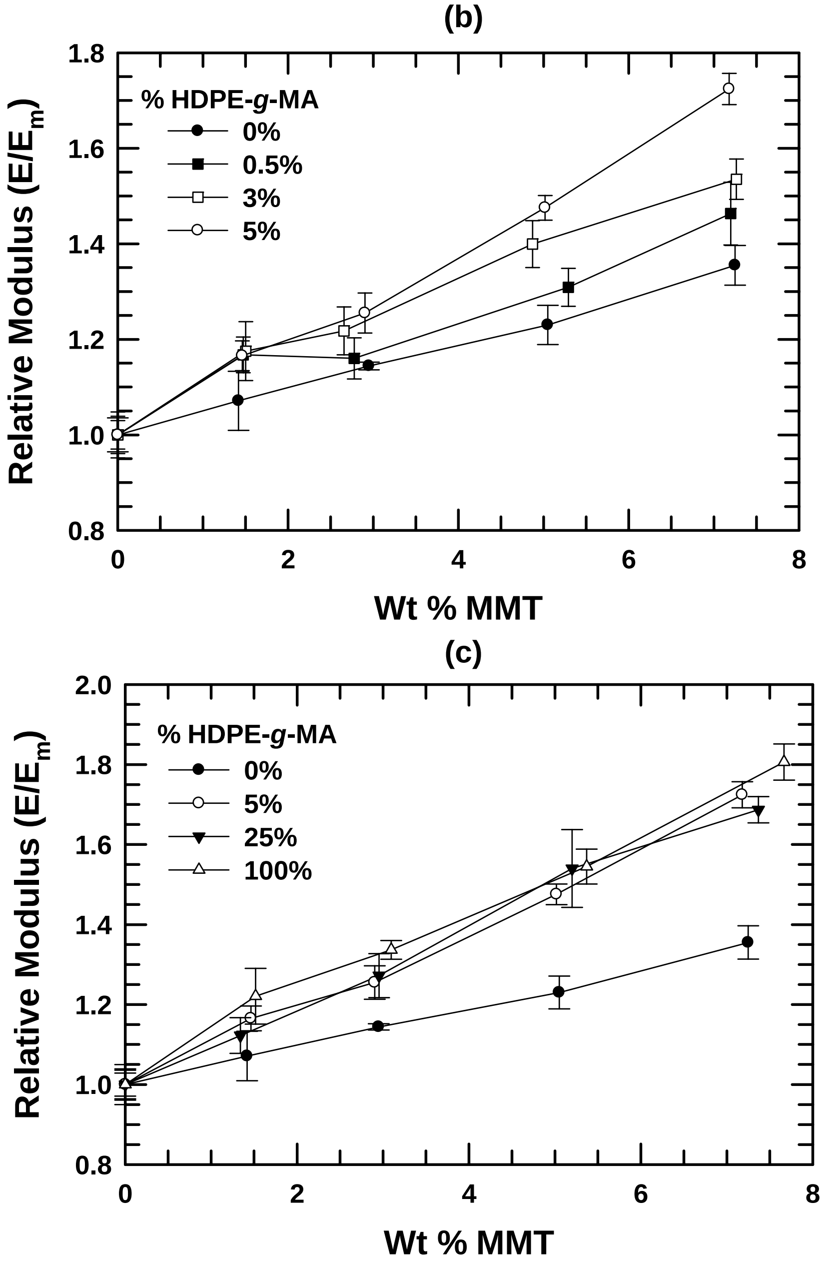

Figure 3.8: Modulus (a) and relative modulus ((b) and (c)) as a function of MMT content for HDPE based nanocomposites with varying levels of HDPE-*g*-MA.

To better understand this, the relative modulus is plotted versus the ratio of the mass of HDPE-*g*-MA to the mass of the organoclay for various MMT loadings in Figure 3.9(a). The relative modulus is increased significantly for nanocomposites with a HDPE-

g-MA/organoclay ratio of about 0.5. Increasing the ratio to 2, however, results in little further change. Kim et al. found a similar trend for PP/PP-*g*-MA/organoclay nanocomposites [51]. Further increasing the amount of HDPE-*g*-MA in the nanocomposites increases the modulus, but at a much lower rate, as shown in Figure 3.9(b). Figure 3.10 shows the relative moduli for nanocomposites with ~5 wt% MMT plotted against the aspect ratios, $\left(\overline{l_n}/\overline{t_n}\right)$, obtained from TEM images. In general, the relative modulus increases as the aspect ratio increases. The nanocomposites with >50% HDPE-*g*-MA in the matrix, however, show a slight increase in relative modulus and a small decrease in aspect ratio. This result might be explained by the decreased modulus of the matrix, allowing for higher improvements in relative modulus [21, 24, 45, 53, 58].

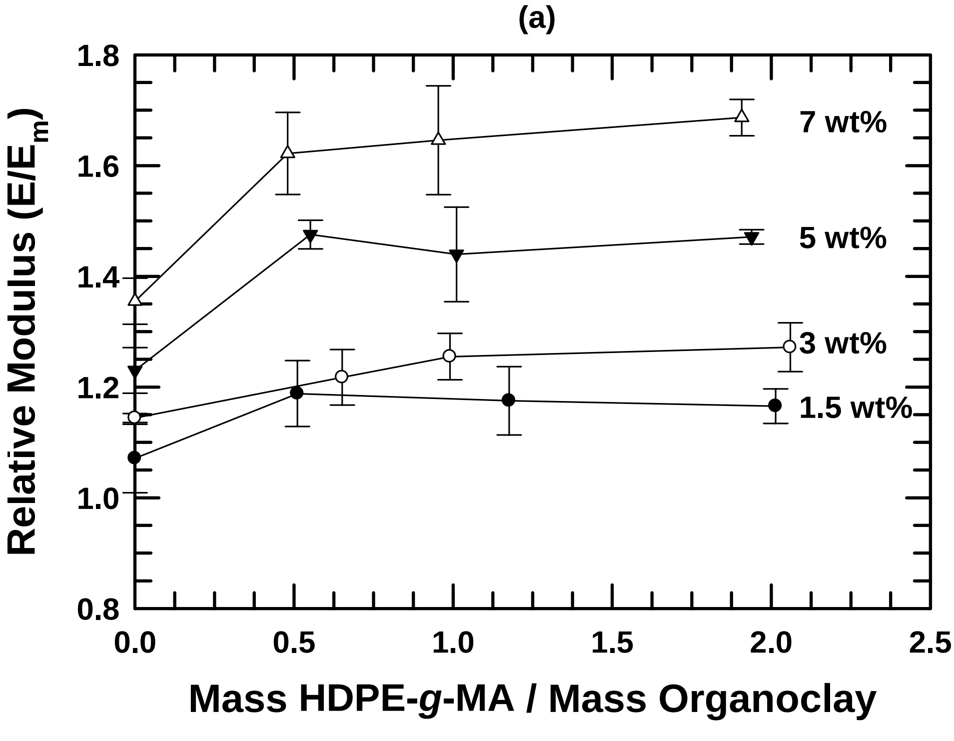

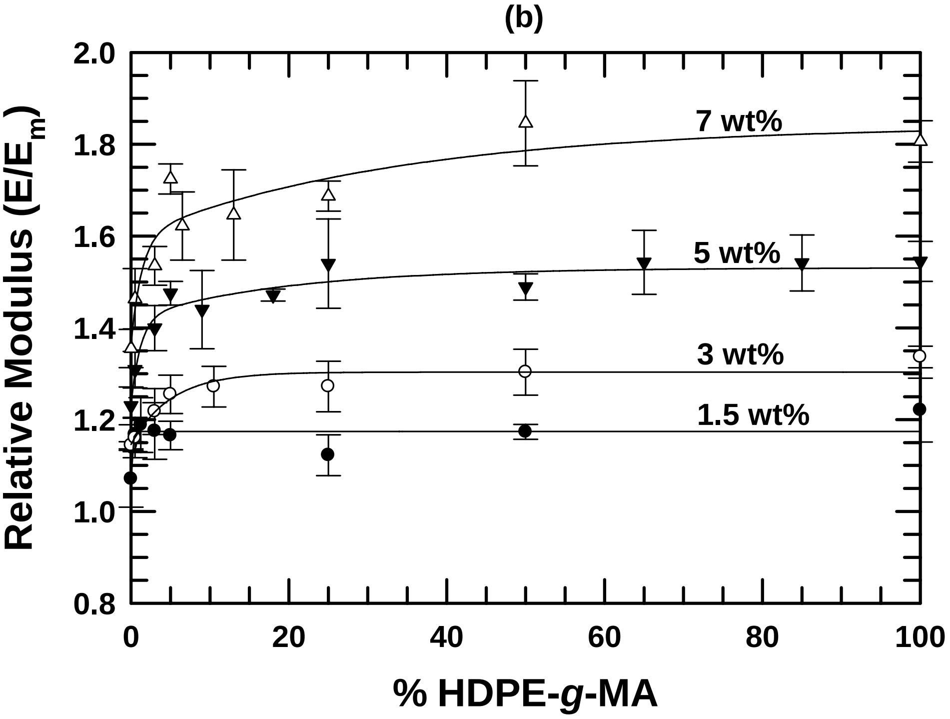

Figure 3.9: Relative modulus for HDPE based nanocomposites with various MMT loadings versus the ratio of HDPE-*g*-MA to organoclay (a) and the percent of HDPE-*g*-MA in the polymer matrix (b).

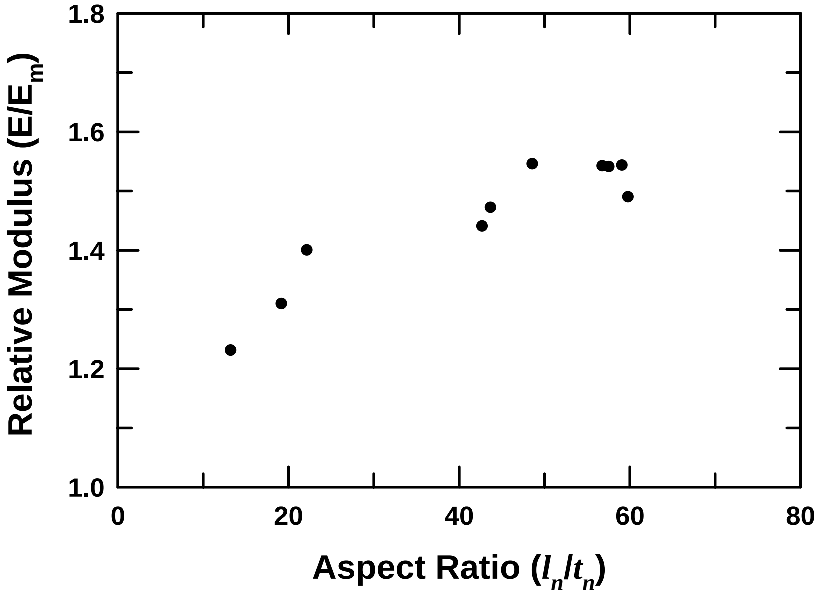

Figure 3.10: Relative modulus versus the ratio of the single population number average particle length and number average particle thickness of HDPE/HDPE-*g*-MA/$M_2(HT)_2$ nanocomposites at a fixed MMT content of ~5 wt%.

The yield strength increases upon addition of MMT, as shown in Figure 3.11(a). Also, the addition of small amounts of HDPE-*g*-MA to the polymer matrix results in relatively large increases in yield strength. With HDPE-*g*-MA levels over ~15-25%, the yield strength levels off and then declines. Thus, the decreased yield strength of the matrix offsets, in part, the benefits associated with improved organoclay exfoliation.

Elongation at break data are presented in Figure 3.11(b). Nanocomposites with low MMT levels (<3 wt%) were too ductile to determine the breaking point using the available equipment. The elongation at break decreases with the addition of MMT and increasing the amount of HDPE-*g*-MA accelerates this decrease. Thus, enhanced exfoliation leads to less ductile nanocomposites.

Fracture toughness measured by the Izod impact strength is an important property for some applications. Polymer nanocomposites based on polyolefins have been reported to have different impact values for the gate end and far end of injection-molded Izod bars [13, 30, 59]. As with the bars of neat polymer, the fracture energy decreases for the nanocomposites from the gate end to the middle and from the middle to the far end (Figure 3.12). This could be the result of differences in the molecular orientation, crystal orientation, and percent crystallinity as discussed above. Similarly, differences in organoclay platelet orientation may contribute. As shown in Figure 3.12, impact strength generally decreases as MMT content increases regardless of the portion of the bar tested. Addition of small amounts of MMT (1.5%) results in a large decrease in impact strength relative to that of the matrix polymer. As the MMT content is increased from 1.5 wt% to 7 wt%, the impact strength decreases gradually for nanocomposites with low HDPE-*g*-MA content (<~25%). Nanocomposites with higher HDPE-*g*-MA content (Figure 3.12(c) and (d)), show a slight minimum in impact strength (~3 wt%) measured at the middle and the gate end.

The Izod impact strength of nanocomposites with various clay loadings is plotted in Figure 3.13(a) versus the ratio of HDPE-*g*-MA to organoclay. The maximum fracture energy occurs for a HDPE-*g*-MA/organoclay ratio between 0.5 and 1. The fracture energy recorded in an impact test reflects the integration of the resisting force of the sample over the range of the sample deflection. Raising the HDPE-*g*-MA/organoclay ratio improves the exfoliation, increasing the forces due to the high modulus and yield strength but decreasing the ductility. Although high levels of exfoliation tend to decrease the impact energy [34, 39, 60-62], in some cases the increase of force outweighs the decrease in ductility [28, 63-65]. In this work, it appears that the initial addition of HDPE-*g*-MA improves the clay exfoliation and, hence, the modulus, to a greater extent than it decreases the ductility. Further increasing the HDPE-*g*-MA/organoclay ratio, however, lowers the impact strength below the pure HDPE level. As shown in Figure 3.13(b), there is not much change at higher levels of HDPE-*g*-MA.

(a)

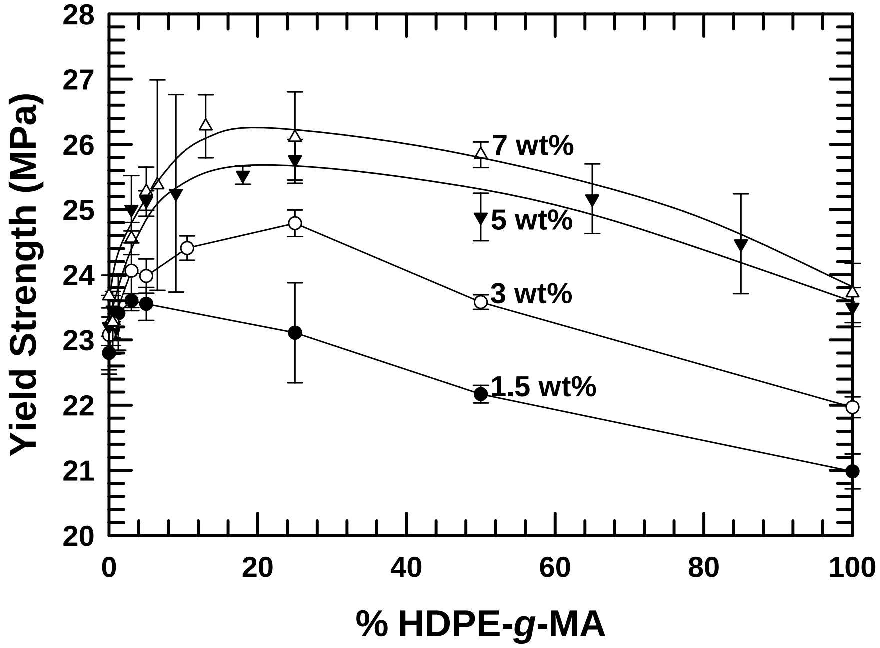

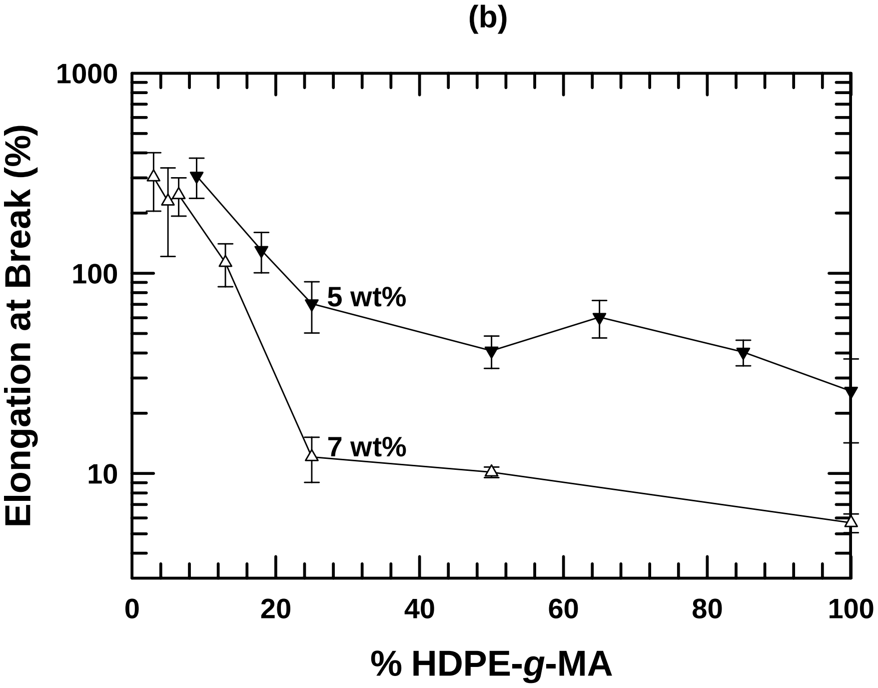

Figure 3.11: Yield strength (a) and elongation at break (b) for nanocomposites based on HDPE/HDPE-*g*-MA with various MMT loadings versus the percent of HDPE-*g*-MA in the polymer matrix.

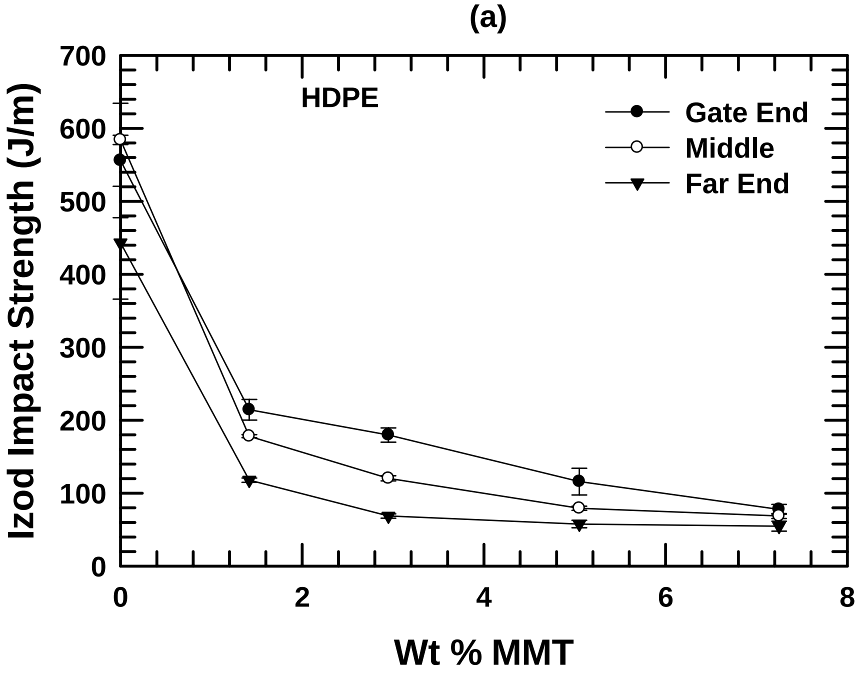

(b)

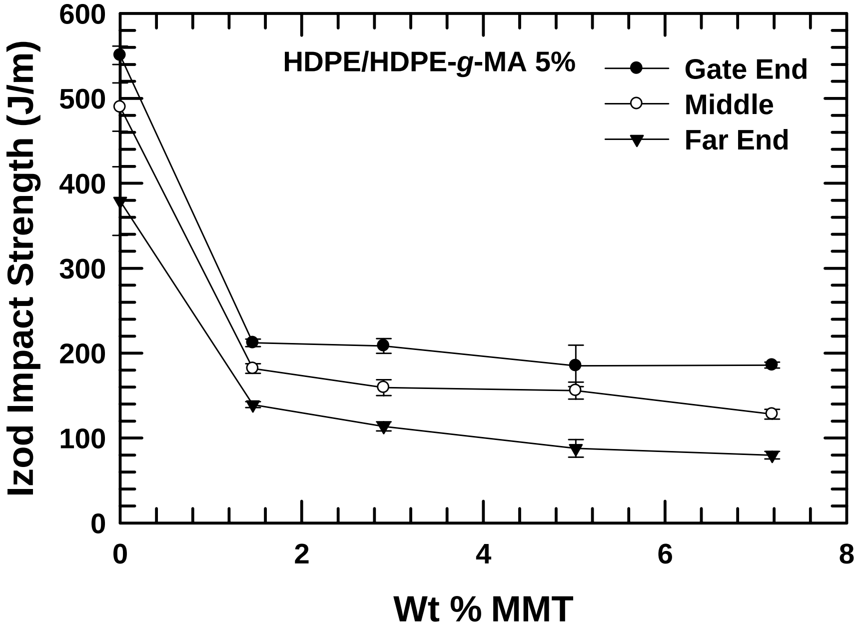
HDPE/HDPE-*g*-MA 5%
Gate End
Middle
Far End
Izod Impact Strength (J/m)
0
100
200
300
400
500
600
0
2
4
6
8
Wt % MMT

(c)

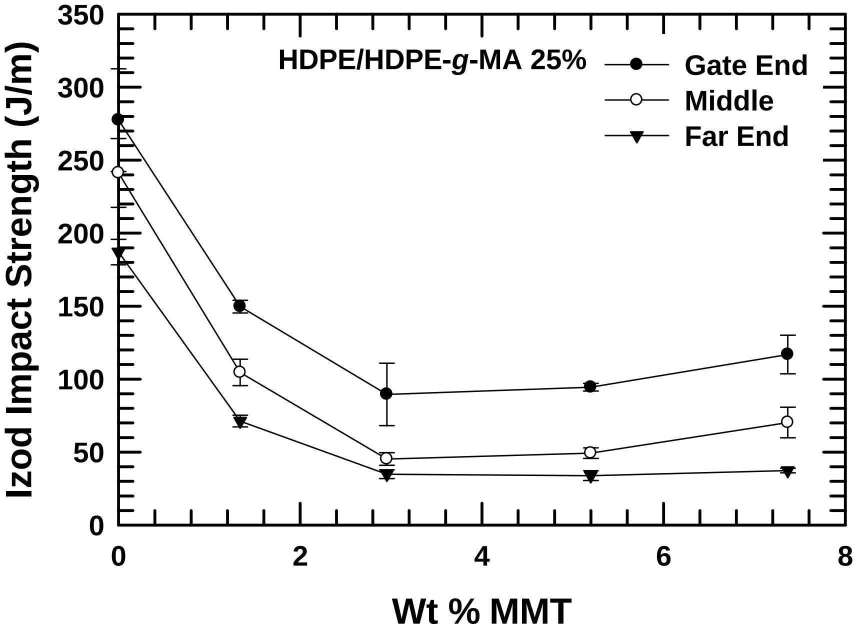
HDPE/HDPE-*g*-MA 25%
Gate End
Middle
Far End
Izod Impact Strength (J/m)
0
50
100
150
200
250
300
350
0
2
4
6
8
Wt % MMT

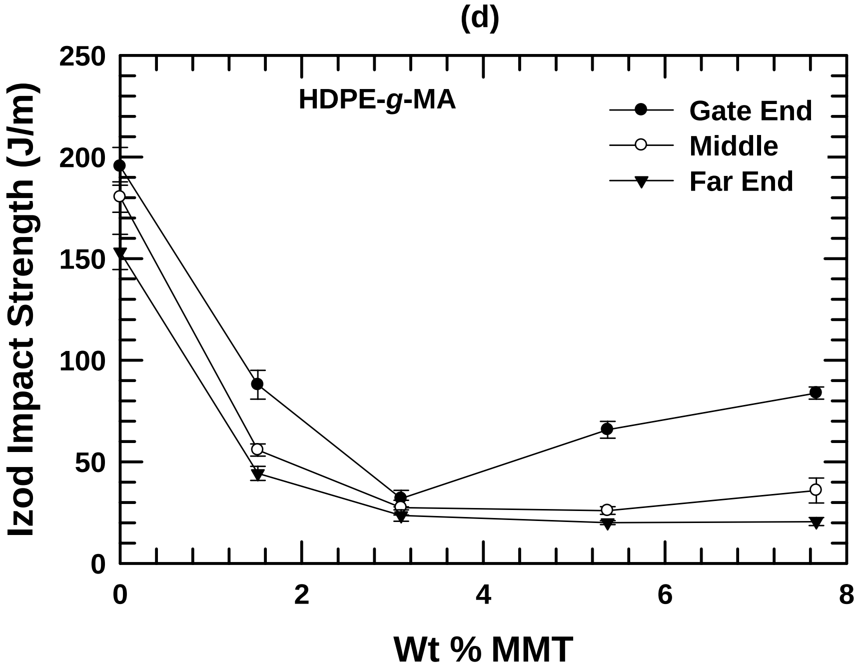

Figure 3.12: Izod impact strength as tested at the gate end, middle, and far end for nanocomposites based on HDPE/HDPE-*g*-MA with 0% (a), 5% (b), 25% (c), and 100% (d) HDPE-*g*-MA in the polymer matrix versus MMT content.

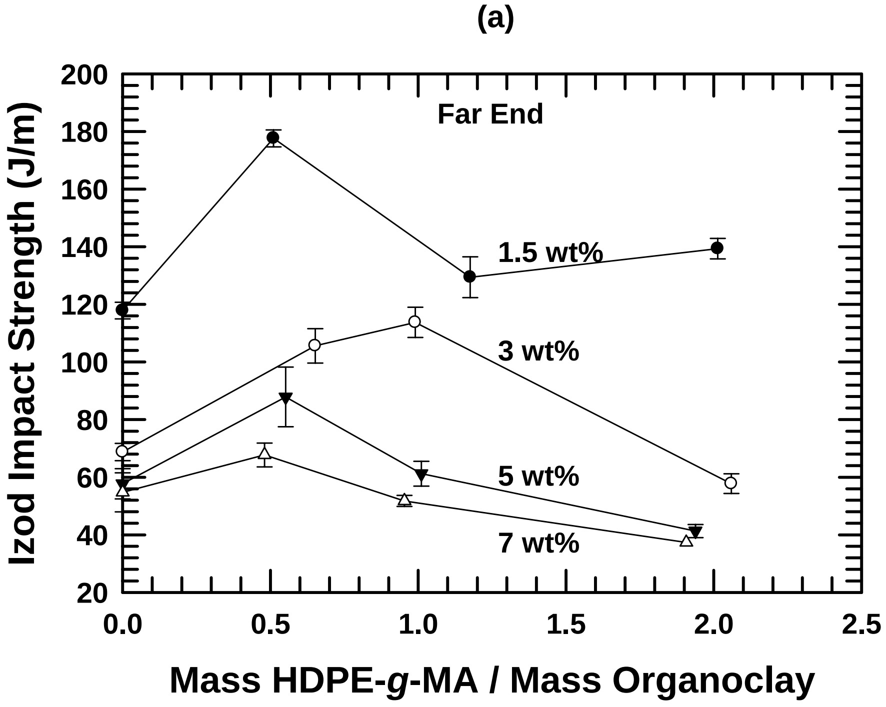

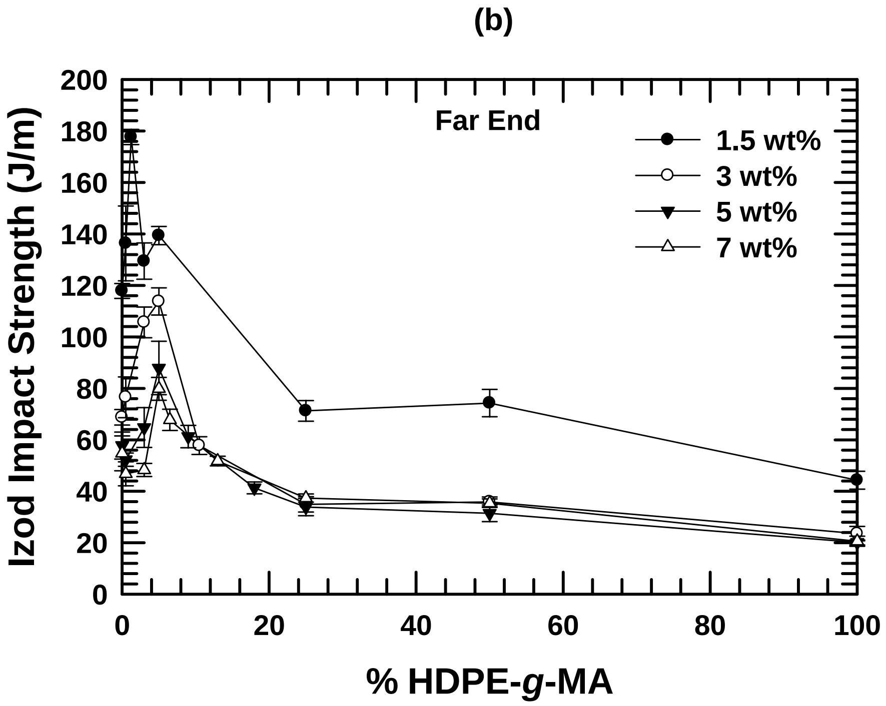

Figure 3.13: Izod impact strength measured at the far end for nanocomposites based on HDPE/HDPE-*g*-MA with various MMT loadings versus the ratio of HDPE-*g*-MA to organoclay (a) and the percent of HDPE-*g*-MA in the polymer matrix (b).

COMPOSITE MODEL PREDICTIONS OF MODULUS

Theoretical modeling is an attractive approach for the design of polymer composite systems, and numerous models [58, 66-68] have been proposed for predicting the properties of composites and for correlating experimental data with such predictions. Previous papers [21, 24, 30, 42, 52, 53] have demonstrated such models can be useful for composites with nanosized fillers. However, numerous assumptions are made when using such models. For example, it is assumed that the polymer matrix is not affected by the presence of the filler, that the filler is of uniform dimensions and is perfectly aligned, that the matrix and filler are isotropic, that the matrix and filler are well bonded, and that there are no particle—particle interactions or agglomerations [53]. Both the Halpin–Tsai equations and the Mori–Tanaka theory are used in this paper to explore the relationship between particle aspect ratio and experimental modulus.

The Halpin-Tsai equations can be used to predict the tensile modulus of nanocomposites from the neat component properties and the particle aspect ratios as determined by quantitative particle analysis of TEM images. The expression for the longitudinal tensile modulus [24, 53, 69] is

$$\frac{E^{(\mathrm{H-T})}}{E_{\mathrm{m}}} = \frac{1 + 2(l/t)\phi\eta}{1 - \phi\eta} \tag{2}$$

where E_{p} and E_{m} are the modulus values of the filler particle and matrix polymer, respectively, ϕ is the volume fraction of the filler particles, (l/t) represents the filler aspect ratio, and η is given by

$$\eta = \frac{(E_{\mathrm{p}}/E_{\mathrm{m}}) - 1}{(E_{\mathrm{p}}/E_{\mathrm{m}}) + 2(l/t)} \tag{3}$$

The Mori-Tanaka average stress theory [70] is based on the principles of Eshelby's inclusion model for predicting an elastic stress field in and around an ellipsoidal particle in an infinite matrix [71]. To account for finite filler concentrations, however, Mori and Tanaka [70], considered a non-dilute composite of many identical ellipsoidal particles that cause the matrix to experience an average stress different from the applied stress. The volume average stress over the entire composite was forced to equal the applied stress to satisfy equilibrium conditions. Tandon and Weng [72] used this assumption together with Eshelby's solution to derive complete analytical solutions for the elastic moduli of an isotropic matrix filled with aligned ellipsoidal inclusions. For a composite with disk-shaped inclusions, the relative modulus parallel to either major axis of the disk-like ellipsoids is

$$\frac{E^{(\mathrm{M-T})}}{E_{\mathrm{m}}} = \frac{2A}{2A + \phi[-2\nu_{\mathrm{m}} A_3 + (1 - \nu_{\mathrm{m}})A_4 + (1 + \nu_{\mathrm{m}})A_5 A]} \tag{4}$$

where ϕ is the volume fraction of filler, ν_m is Poisson's ratio of the matrix, and A, A_3, A_4, A_5, are functions of Eshelby's tensor and the properties of the filler and the matrix, specifically Young's modulus, Poisson's ratio, filler concentration, and filler aspect ratio; complete details of these equations are given elsewhere [72]. The Poisson's ratios of the matrix, ν_m, and of the organoclay, ν_p, are assumed to be 0.35 and 0.20 respectively [53, 73, 74].

In comparing the results of the Halpin-Tsai equations and the Mori-Tanaka theory, there are important differences between the two theories to bear in mind. The Mori–Tanaka theory treats disks as ellipsoidal particles, while the Halpin–Tsai equations treat disks as rectangular platelets. Because the length and, therefore, the aspect ratio are not constant across a particle, the Halpin–Tsai equations assume a larger particle size than the Mori-Tanaka theory. Additionally, the Halpin–Tsai equations are independent of Poisson's ratio of the filler and the matrix [53].

In the model calculations, there are generally two ways of treating the filler particles. One is to assume good exfoliation (method 1) and treat the MMT platelets themselves as the reinforcing filler particles. In this case, Ep = EMMT = 178 GPa [53] and $\phi_p = \phi_{MMT} = 0.0175$ at 5 wt % MMT.

Another way is to consider the partially exfoliated clay particles as parallel arrangements of MMT platelets and gallery material as described in previous reports [21, 24, 51, 53, 69, 75] (method 2). The tensile modulus of such an effective particle is often assumed to be given by the following rule of mixtures

$$E_p = v_{MMT} E_{MMT} + v_{gallery} E_{gallery} \tag{5}$$

where v_{MMT} and $v_{gallery}$ are the volume fraction of montmorillonite and of the gallery space in the effective particle, while E_{MMT} and $E_{gallery}$ are their corresponding moduli. The volume fraction of MMT platelets in the particle, v_{MMT}, is calculated as the ratio of the thickness of an individual platelet and the *d*-spacing of the nanocomposite as determined by the WAXS analysis

$$\mathrm{v}_{\mathrm{MMT}} = \frac{t_{\mathrm{platelet}}}{d_{001}} \tag{6}$$

Considering that the modulus of the organic material in the gallery is significantly smaller than the modulus of the MMT platelets, Eq. (3) reduces to

$$E_{\mathrm{p}} = \mathrm{v}_{\mathrm{MMT}} E_{\mathrm{MMT}} \tag{7}$$

The volume fraction of the filler particles in the composites can be estimated as

$$\phi_{\mathrm{p}} = \frac{\text{volume of MMT}}{\text{volume of nanocomposite}} \frac{\text{volume of filler particle}}{\text{volume of MMT}} = \frac{\phi_{\mathrm{MMT}}}{\mathrm{v}_{\mathrm{MMT}}} \tag{8}$$

Thus, the d_{001} values determined by WAXS are needed for predictions using method 2. It is easy to determine the *d*-spacing from WAXS scans of nanocomposites based on matrices with ≤ 25% HDPE-*g*-MA; however, at higher levels of HDPE-*g*-MA, no distinctive peaks are found in the WAXS scans. Thus, in order to apply the partially exfoliated particle assumption to nanocomposites with ≥ 50% HDPE-*g*-MA, the *d*-spacing is assumed to be equal to that of the 25% HDPE-*g*-MA nanocomposite.

The aspect ratios calculated from ~5 wt% samples are applied in the models for all clay loadings. For simplicity, the $\langle l/t \rangle_n$ aspect ratio is used in all predictions shown. Different aspect ratios give similar, though different, results.

Because TEM and subsequent image analysis reveal that nanocomposites with HDPE-*g*-MA matrices are almost completely exfoliated, method 1 can be used for the model predictions. Figure 3.14(a) compares the predictions for relative modulus as a function of MMT loading obtained from both the Halpin-Tsai and Mori-Tanaka methods with experimental data. The Mori-Tanaka method describes the data well while the Halpin-Tsai method gives significantly higher results. It appears that the Mori-Tanaka method is more applicable in this system.

Method 2 is used for nanocomposites with HDPE matrices because they are not well exfoliated. Figure 3.14(b) shows Halpin-Tsai and Mori-Tanaka predictions with experimental data for nanocomposites with a HDPE matrix. Both methods substantially overestimate the experimental relative modulus. One explanation could be that the particle modulus (Ep) is overestimated by Eq. 7. Because the Mori-Tanaka theory predicts both the exfoliated and the non-exfoliated cases better, it was selected to be the base method for the remaining predictions. If the value of Ep used in method 2 is arbitrarily reduced from 74.7 GPa, as estimated from Eq. 7, to 13.5 GPa, a much better fit of the experimental points is attained, as shown in Figure 3.14(b). The lower apparent modulus for the tactoids suggests that Eq. 7 grossly overestimates the stress transfer between platelets in the tactoids.

(a)

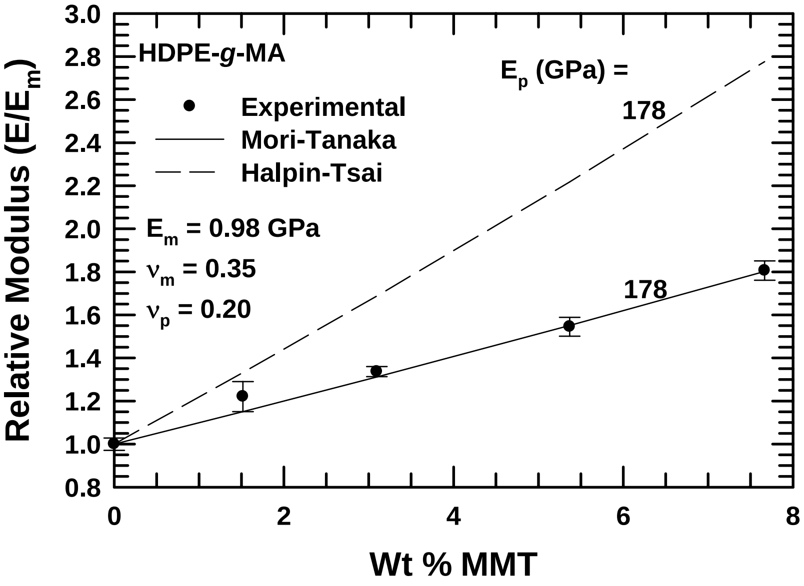

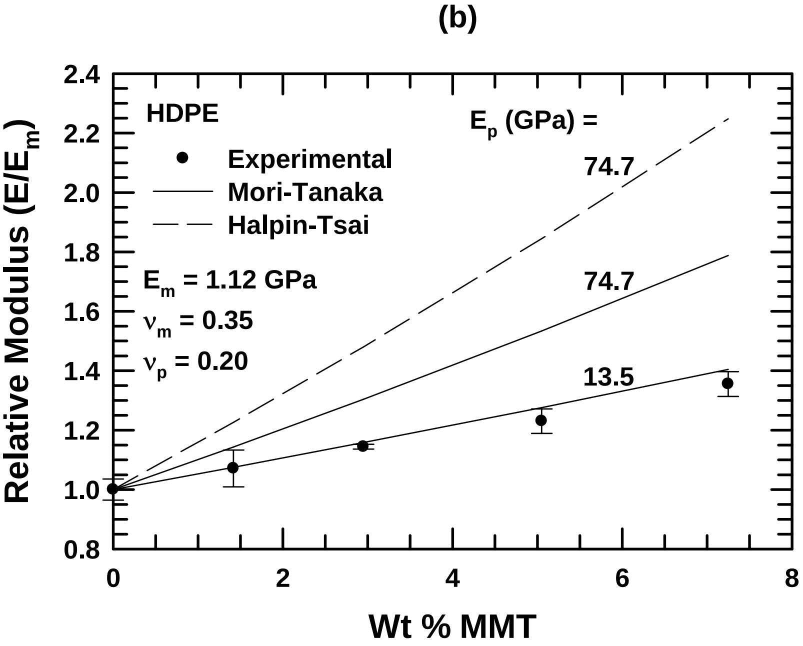

Figure 3.14: Comparison of experimental relative modulus with predictions by the one population model using Halpin-Tsai equations and Mori-Tanaka theory for HDPE-*g*-MA based (a) and HDPE based (b) nanocomposites versus MMT content.

Nanocomposites with ≥25% HDPE-*g*-MA consist of both organoclay tactoids and dispersed single platelets. As shown, these distinct particles have different effects on the mechanical properties of the nanocomposite and separate methods are needed to predict their properties. When both particle types exist in a single nanocomposite, they should be considered separately in a two population model to more accurately predict the experimental modulus. Thus, the aspect ratios for single platelets and the aspect ratios of the remaining tactoids are both employed in the model. The volume fractions of filler in tactoids (ϕ_{T}) and in single platelets (ϕ_{sp}) can be estimated by multiplying the fraction of the particle areas by the volume fraction of MMT as shown in

$$\phi_{\mathrm{T}} = \phi_{\mathrm{MMT}} \frac{\sum_i (l_i t_i)_T}{\sum_i (l_i t_i)_{sp} + \mathrm{v}_{\mathrm{MMT}} \sum_i (l_i t_i)_T} \tag{9}$$

and

$$\phi_{\mathrm{sp}} = \phi_{\mathrm{MMT}} \frac{\sum_i (l_i t_i)_{sp}}{\sum_i (l_i t_i)_{sp} + \mathrm{v}_{\mathrm{MMT}} \sum_i (l_i t_i)_T} \tag{10}$$

where the subscripts T and sp indicate the parameters for the tactoids and the single platelets respectively and $\mathrm{v}_{\mathrm{MMT}}$ is the volume fraction of MMT in the effective particle, as calculated in Eq. 6. Figure 3.15 shows the filler volume fractions versus the HDPE-*g*-MA content of the matrix. Clearly, the volume fraction of tactoids, ϕ_{T}, decreases while the volume fraction of single platelets, ϕ_{sp}, increases with increased levels of HDPE-*g*-MA, reflecting improved exfoliation.

The contributions to the relative modulus of the tactoids and the single platelets are calculated by substituting the appropriate particle parameters into Eq. (4) as shown in

$$\frac{E_T^{\mathrm{(M-T)}}}{E_{\mathrm{m}}} = \frac{2A_T}{2A_T + \phi_{\mathrm{T}}[-2\mathrm{v}_{\mathrm{m}} A_{3,T} + (1-\mathrm{v}_{\mathrm{m}})A_{4,T} + (1+\mathrm{v}_{\mathrm{m}})A_{5,T} A_T]} \tag{11}$$

and

$$\frac{E_{sp}^{\mathrm{(M-T)}}}{E_{\mathrm{m}}} = \frac{2A_{sp}}{2A_{sp} + \phi_{\mathrm{sp}}[-2\mathrm{v}_{\mathrm{m}} A_{3,sp} + (1-\mathrm{v}_{\mathrm{m}})A_{4,sp} + (1+\mathrm{v}_{\mathrm{m}})A_{5,sp} A_{sp}]} \tag{12}$$

The particle moduli used for the tactoids and single platelets are 13.5 GPa and 178 GPa respectively, as suggested above. The Poisson's ratio for both tactoids and single platelets is assumed to be 0.20. Although the Poisson's ratio of the tactoids is likely somewhat higher than that of the single platelets, the model is insensitive to Poisson's ratio of both the matrix and the filler within the range of 0.20 and 0.40. The total relative modulus of the nanocomposite is calculated by adding the tactoid and single platelet contributions and subtracting one to avoid double counting the matrix contribution as follows

$$\frac{E^{\mathrm{(M-T)}}}{E_{\mathrm{m}}} = \frac{E_T^{\mathrm{(M-T)}}}{E_{\mathrm{m}}} + \frac{E_{sp}^{\mathrm{(M-T)}}}{E_{\mathrm{m}}} - 1 \tag{13}$$

The parameters used in the two population Mori-Tanaka model for nanocomposites containing ~5 wt% MMT are listed in Table 3.3.

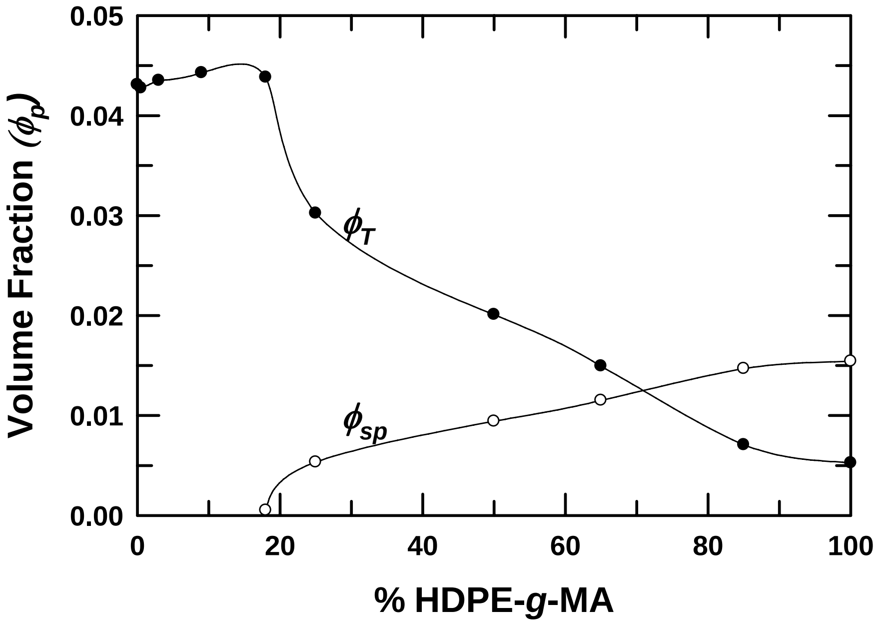

Figure 3.15: Filler volume fractions for tactoids and single platelets used in the two population Mori-Tanaka model for HDPE/HDPE-*g*-MA/$M_2(HT)_2$ nanocomposites at a fixed MMT content of ~5 wt% versus the percent of HDPE-*g*-MA in the polymer matrix.

Figure 3.16(a) and (b) show the resulting predictions by the two population Mori-Tanaka model and the experimental points for nanocomposites with 25% and 50% HDPE-*g*-MA respectively. The predictions fit the data well in both cases, indicating that such a two particle population model appears to be most appropriate for this system. That is, treating tactoids and single platelets separately rather than averaging them together proves to be a more accurate way to model these nanocomposite properties.

To see how well this model works over the entire range of composition of HDPE/HDPE-*g*-MA blends, the two population Mori-Tanaka predictions and experimental data for nanocomposites of 5 wt% MMT are shown in Figure 3.17. The model predictions reasonably fit the experimental data over the entire range of composition. The discrepancies are possibly due to the incomplete orientation of the clay platelets and inadequate parameter estimations for the volume fraction and modulus of the effective particles [30, 51].

Table 3.3: Parameters used in the Mori-Tanaka two population model [a]

HDPE-*g*-MA %	*d*-spacing (d_{001}, nm)	Vol fraction of MMT in particle (ν_{MMT})	Weight fraction of MMT in nanocomposites (%)	Number average aspect ratio for tactoids $\left(\langle l/t \rangle_n\right)_T$	Number average aspect ratio for single platelets $\left(\langle l/t \rangle_n\right)_{sp}$	Vol fraction of the tactoids in nanocomposites (ϕ_T)	Vol fraction of the single platelets in nanocomposites (ϕ_{sp})
0	2.24	0.420	5.2	20.3		0.0431	
0.5	2.21	0.425	5.2	29.0		0.0428	
3	2.24	0.420	5.2	33.1		0.0435	
9	2.27	0.414	5.2	58.4		0.0442	
18	2.30	0.409	5.2	55.3	61.6	0.0438	0.0005
25	2.33	0.404	5.2	58.1	67.5	0.0302	0.0053
50	2.33 [b]	0.404	5.4	67.6	63.4	0.0201	0.0094
65	2.33 [b]	0.404	5.3	66.4	57.6	0.0149	0.0115
85	2.33 [b]	0.404	5.3	53.9	58.9	0.0071	0.0147
100	2.33 [b]	0.404	5.4	52.2	47.6	0.0053	0.0154

[a] For 5 wt% MMT.

[b] Assumed to be assumed to be equal to that of the 25% HDPE-*g*-MA nanocomposite.

Table 3.4: Modulus results for nanocomposites with ~5 wt% MMT

HDPE-*g*-MA %	E (GPa)	E_m (GPa)	E/E_m
0	1.38	1.12	1.23
0.5	1.44	1.10	1.31
3	1.64	1.17	1.40
5	1.65	1.12	1.48
9	1.68	1.17	1.44
18	1.68	1.14	1.47
25	1.78	1.15	1.54
50	1.60	1.07	1.49
65	1.52	1.00	1.54
85	1.48	0.96	1.54
100	1.51	0.98	1.55

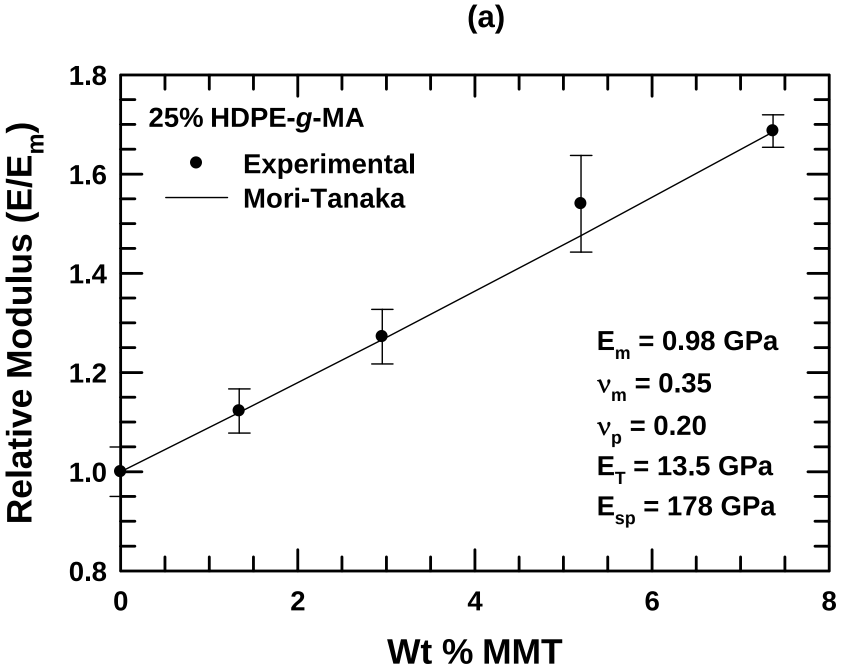

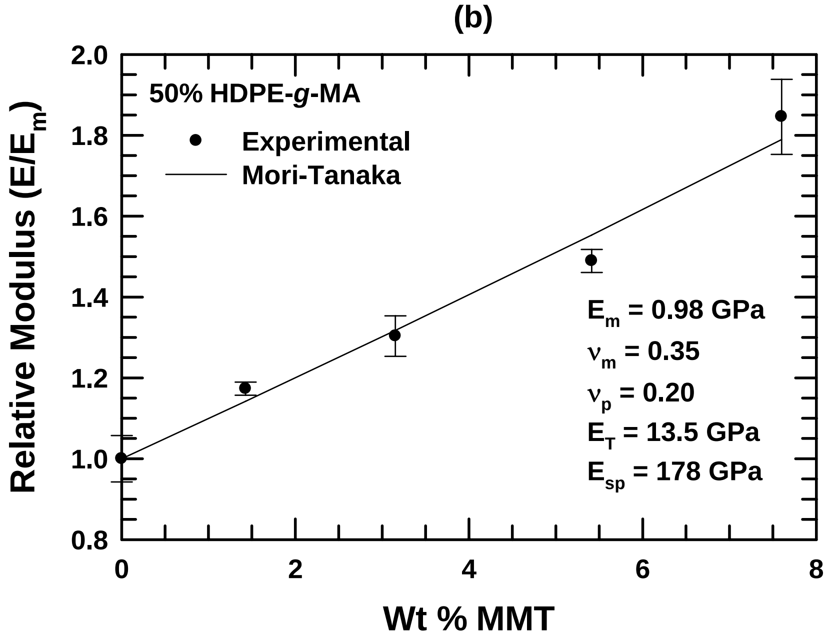

Figure 3.16: Comparison of experimental relative modulus with the predictions by the two population Mori-Tanaka model accounting for tactoids and single platelets separately for HDPE based nanocomposites with 25% (a) and 50% (b) HDPE-*g*-MA in the polymer matrix versus MMT content.

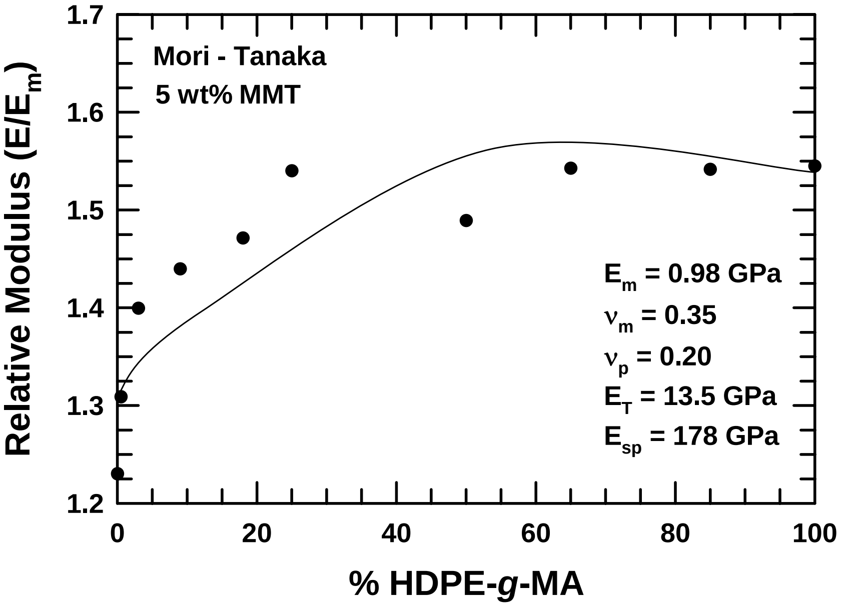

Figure 3.17: Comparison of experimental relative modulus with the predictions by the two population Mori-Tanaka model accounting for tactoids and single platelets separately for HDPE/HDPE-*g*-MA/$M_2(HT)_2$ nanocomposites at a fixed MMT content of ~5 wt% versus the percent of HDPE-*g*-MA in the polymer matrix.

CONCLUSIONS

Nanocomposites formed from blends of HDPE and HDPE-*g*-MA and $M_2(HT)_2$ organoclay were melt processed to explore the extent of exfoliation and the mechanical properties over the entire range of matrix composition. WAXS and TEM coupled with detailed particle analysis were used to determine the effect of HDPE-*g*-MA content on exfoliation. TEM images show drastic improvements in exfoliation with initial amounts of HDPE-*g*-MA while further addition of HDPE-*g*-MA gives little visible change. Particle analysis, however, shows that the fraction of single platelets increases at a steady rate for nanocomposites with HDPE-*g*-MA contents ≥25%. As the HDPE-*g*-MA content increases, particle aspect ratio initially increases drastically, reaches a maximum, and slightly decreases, due to the particle thickness limit of a single platelet (0.94 nm).

Similarly, the relative modulus initially improves significantly with increased levels of HDPE-*g*-MA, while greater HDPE-*g*-MA content only gives a slight increase. The slight increase in relative modulus in spite of a slight decrease in aspect ratio might be due to the decreased modulus of the matrix, facilitating improvements in relative modulus. Modulus increases and Izod impact strength decreases as MMT levels increase, for all HDPE-*g*-MA levels. Fracture energy reaches a maximum at low HDPE-*g*-MA levels, decreases below the value for the pure HDPE nanocomposite, and levels off at higher HDPE-*g*-MA content. Initially, adding HDPE-*g*-MA to the matrix results in significantly improved exfoliation and properties. Further addition of HDPE-*g*-MA, however, lowers the matrix properties enough to offset the benefits of enhanced matrix/organoclay interactions.

Because of the different reinforcement effects of partially exfoliated organoclay tactoids and single platelets, particle analysis was also performed on these two populations separately. A composite model based on the Mori-Tanaka theory was developed to treat organoclay tactoids and single platelets as two separate types of fillers. This two population Mori-Tanaka model gives rather good quantitative agreement between the predicted values of modulus calculated from the TEM results and that measured experimentally.

REFERENCES

1. Hasegawa N, Kawasumi M, Kato M, Usuki A, and Okada A. Journal of Applied Polymer Science 1998;67(1):87-92.
2. Lee H-s, Fasulo PD, Rodgers WR, and Paul DR. Polymer 2005;46(25):11673-11689.
3. Kawasumi M, Hasegawa N, Kato M, Usuki A, and Okada A. Macromolecules 1997;30:6333–6338.

4. Varela C, Rosales C, Perera R, Matos M, Poirier T, Blunda J, and Rojas H. Polymer Composites 2006;27(4):451-460.

5. López-Quintanilla ML, Sánchez-Valdés S, Ramos de Valle LF, and Guedea Miranda R. Polymer Bulletin 2006;57(3):385-393.

6. Galgali G, Ramesh C, and Lele A. Macromolecules 2001;34(4):852-858.

7. Reichert P, Nitz H, Klinke S, Brandsch R, Thomann R, and Mülhaupt R. Macromolecular Materials and Engineering 2000;275(1):8-17.

8. Cui L and Paul DR. Polymer 2007;48(6):1632-1640.

9. Lertwimolnun W and Vergnes B. Polymer 2005;46(10):3462-3471.

10. Hotta S and Paul DR. Polymer 2004;45(22):7639-7654.

11. Hasegawa N, Okamoto H, Kawasumi M, Kato M, Tsukigase A, and Usuki A. Macromolecular Materials and Engineering 2000;280-281(1):76-79.

12. Li X, Wang C-y, Fang L, and Liu L-z. Harbin Ligong Daxue Xuebao 2003;8(2):90-93.

13. Shah RK, Cui L, Williams KL, Bauman B, and Paul DR. Journal of Applied Polymer Science 2006;102(3):2980-2989.

14. Filippi S, Marazzato C, Magagnini P, Famulari A, Arosio P, and Meille SV. European Polymer Journal 2008;44(4):987-1002.

15. Wang KH, Choi MH, Koo CM, Choi YS, and Chung IJ. Polymer 2001;42(24):9819-9826.

16. Gopakumar TG, Lee JA, Kontopoulou M, and Parent JS. Polymer 2002;43(20):5483-5491.

17. Liang G, Xu J, Bao S, and Xu W. Journal of Applied Polymer Science 2004;91(6):3974-3980.

18. Morawiec J, Pawlak A, Slouf M, Galeski A, Piorkowska E, and Krasnikowa N. European Polymer Journal 2005;41(5):1115-1122.

19. Zhang M and Sundararaj U. Macromolecular Materials and Engineering 2006;291(6):697-706.

20. Mainil M, Alexandre M, Monteverde F, and Dubois P. Journal of Nanoscience and Nanotechnology 2006;6:337-344.

21. Cui L, Ma X, and Paul DR. Polymer 2007;48(21):6325-6339.

22. Zanetti M, Camino G, Thomann R, and Mülhaupt R. Polymer 2001;42(10):4501-4507.

23. Cerezo FT, Preston CML, and Shanks RA. Composites Science and Technology 2007;67(1):79-91.

24. Shah RK, Kim DH, and Paul DR. Polymer 2007;48(4):1047-1057.

25. Filippi S, Marazzato C, Magagnini P, Minkova L, Tzankova N, Francesco D, and Mantia PL. Macromolecular Materials and Engineering 2006;291(10):1208-1225.

26. Huang Y, Ma X, Liang G, Wang S, and Zhang Q. Polymer 2008;49(8):2085-2094.

27. Shah RK, Krishnaswamy RK, Takahashi S, and Paul DR. Polymer 2006;47(17):6187-6201.

28. Shah RK, Hunter DL, and Paul DR. Polymer 2005;46(8):2646-2662.

29. Shah RK and Paul DR. Macromolecules 2006;39(9):3327-3336.

30. Cui L, Troeltzsch C, Yoon PJ, and Paul DR. Macromolecules 2009;42(7):2599-2608.

31. Ho RM, Su AC, Wu CH, and Chen SI. Polymer 1993;34(15):3264-3269.

32. Roover BD, Sclavons M, Carlier V, Devaux J, Legras R, and Momtaz A. Journal of Polymer Science Part A: Polymer Chemistry 1995;33(5):829-842.

33. Zhang R, Zhu Y, Zhang J, Jiang W, and Yin J. Journal of Polymer Science Part A: Polymer Chemistry 2005;43(22):5529-5534.

34. Fornes TD, Yoon PJ, Keskkula H, and Paul DR. Polymer 2001;42(25):9929-9940.

35. Borse NK and Kamal MR. Polymer Engineering & Science 2009;49(4):641-650.

36. González-Montiel A, Keskkula H, and Paul DR. Journal of Polymer Science Part B: Polymer Physics 1995;33(12):1751-1767.

37. Huang JJ, Keskkula H, and Paul DR. Polymer 2006;47(2):624-638.

38. Fornes TD, Yoon PJ, Hunter DL, Keskkula H, and Paul DR. Polymer 2002;43(22):5915-5933.

39. Yoon PJ, Hunter DL, and Paul DR. Polymer 2003;44(18):5323-5339.

40. Fornes TD, Yoon PJ, Keskkula H, and Paul DR. Polymer 2002;43(7):2121-2122.

41. Stretz HA and Paul DR. Polymer 2006;47(26):8527-8535.

42. Stretz HA, Paul DR, Li R, Keskkula H, and Cassidy PE. Polymer 2005;46(8):2621-2637.

43. Wunderlich B and Czornyj G. Macromolecules 1977;10(5):906-913.

44. Yoon PJ, Fornes TD, and Paul DR. Polymer 2002;43(25):6727-6741.

45. Fornes TD and Paul DR. Macromolecules 2004;37(20):7698-7709.

46. Paul DR, Zeng QH, Yu AB, and Lu GQ. Journal of Colloid and Interface Science 2005;292(2):462-468.

47. Li B, Gong G, Xie B-H, Yang W, and Yang M-B. Journal of Applied Polymer Science 2008;109(2):1161-1167.

48. Pantani R, Coccorullo I, Speranza V, and Titomanlio G. Progress in Polymer Science 2005;30(12):1185-1222.

49. Pantani R, Coccorullo I, Speranza V, and Titomanlio G. Polymer 2007;48(9):2778-2790.

50. Kim DH, Fasulo PD, Rodgers WR, and Paul DR. Polymer 2007;48(20):5960-5978.

51. Kim DH, Fasulo PD, Rodgers WR, and Paul DR. Polymer 2007;48(18):5308-5323.

52. Chavarria F and Paul DR. Polymer 2004;45(25):8501-8515.

53. Fornes TD and Paul DR. Polymer 2003;44(17):4993-5013.

54. Ploehn HJ and Liu C. Industrial & Engineering Chemistry Research 2006;45(21):7025-7034.

55. Paul DR and Robeson LM. Polymer 2008;49(15):3187-3204.

56. Oshinski AJ, Keskkula H, and Paul DR. Polymer 1996;37(22):4891-4907.

57. Corté L and Leibler L. Polymer 2005;46(17):6360-6368.

58. Halpin JC and Kardos JL. Polymer Engineering & Science 1976;16(5):344-352.

59. Cui L, Hunter DL, Yoon PJ, and Paul DR. Polymer 2008;49(17):3762-3769.

60. Cho JW and Paul DR. Polymer 2001;42(3):1083-1094.

61. Fornes TD and Paul DR. Macromolecules 2004;37(20):7698-7709.

62. Stretz HA, Paul DR, and Cassidy PE. Polymer 2005;46(11):3818-3830.

63. Chen L, Wong S-C, Liu T, Lu X, and He C. J Polym Sci, Part B: Polym Phys 2004;42(14):2759-2768.

64. Wheeler PA, Wang J, Baker J, and Mathias LJ. Chemistry of Materials 2005;17(11):3012-3018.

65. Yoo Y, Shah RK, and Paul DR. Polymer 2007;48(16):4867-4873.

66. Hill R. Journal of the Mechanics and Physics of Solids 1965;13(4):213-222.

67. Halpin J. J. Compos. Mater. 1969;3:732.

68. Hill R. Proc. Phys. Soc., London 1952;65A:349-354.

69. Sheng N, Boyce MC, Parks DM, Rutledge GC, Abes JI, and Cohen RE. Polymer 2004;45(2):487-506.

70. Mori T and Tanaka K. Acta Metallurgica 1973;21(5):571-574.

71. Eshelby JD. Proceedings of the Royal Society of London. Series A. Mathematical and Physical Sciences 1957;241(1226):376-396.

72. Tandon GP and Weng GJ. Polymer Composites 1984;5(4):327-333.

73. Hui CY and David S. Polymer Engineering & Science 1998;38(5):774-782.

74. van Es M, Xiqiao F, van Turnhout J, and van der Giessen E. Comparing polymer–clay nanocomposites with conventional composites using composite modeling. In: Al-Malaika S, Golovoy A, and Wilkie C, editors. Specialty polymer additives: principles and applications. London: Blackwell Science, 2001. pp. Chapter 21.

75. Brune DA and Bicerano J. Polymer 2002;43(2):369-387.

Chapter 4: Morphology and properties of polypropylene nanocomposites based on a silanized organoclay

Polymer nanocomposites based on organoclays can potentially lead to substantial enhancement in mechanical [1-3], barrier [4-6], thermal [7, 8], and flammability [9-11] properties at very low filler concentrations while maintaining similar density and optical properties, making them attractive replacements for conventional composites. Melt mixing or compounding of polymer nanocomposites offers efficient exfoliation without the higher costs, complications, and environmental effects associated with in situ polymerization or solution blending. To obtain a well-exfoliated nanocomposite, with greatest property improvements, the individual organoclay platelets must interact favorably with the polymer matrix.

The structure of the ammonium surfactants used to modify montmorillonite (MMT) clay can be chosen to increase the affinity between the hydrophilic aluminosilicate clay and the organophilic polymer matrix. In our previous studies, nylon 6-based nanocomposites showed the best exfoliation with organoclays formed from a surfactant with only one long alkyl tail, allowing the polar polyamide more access to the silicate surface of the clay [1, 12, 13]. Non-polar polyolefin-based nanocomposites, such as polypropylene or polyethylene, have better clay dispersion when organoclays modified by a surfactant with two or more long alkyl tails are used, providing increased alkyl-polyolefin interactions and decreased silicate-polyolefin interaction [3, 14-16]. However, these organoclays are still poorly exfoliated in polyolefin nanocomposites.

Nanocomposites formed from polyolefin matrices are often modified with a polar compatibilizer to improve exfoliation and enhance properties. The grafting of maleic anhydride to the polyolefin backbone significantly increases the polarity, and the addition of such materials to polypropylene [3, 17-24] or polyethylene [14, 25-34] can significantly improve organoclay exfoliation. Other approaches include the incorporation of polar comonomers like vinyl acetate [26, 35, 36], methacrylic acid [37-40], or methacrylic acid ionomers [16, 41-43].

Maleated polypropylene, PP-*g*-MA, is typically used in relatively low quantities, comparable to the mass of organoclay, to form polypropylene-based nanocomposites and is thought of as a "compatibilizer" [19-24]. The addition of PP-*g*-MA lowers the neat matrix properties such as the tensile modulus due to its decreased molecular weight and its maleated groups that disrupt the crystallinity of the matrix [44-46]. Higher performance nanocomposites could be achieved if exfoliated nanocomposites could be made without the addition of PP-*g*-MA. In addition, eliminating the use of PP-*g*-MA would be advantageous commercially due to the substantially higher cost of PP-*g*-MA compared to unmodified PP. More extensive utilization of PP-based nanocomposites would be possible if an organoclay with improved intrinsic thermodynamic affinity with unmodified polyolefins were available.

Although the exfoliation of the organoclay in the polymer matrix is desired when melt-processing a nanocomposite, organoclay agglomerates often form during the process. Agglomeration leads to inefficient use of the organoclay and negatively affects downstream applications of the nanocomposite: surface pitting in injection molded parts, resin build up around the agglomerates giving the appearance of gels or unmelts in films, and plugging of the filter pot and breaking of the fiber strand in fibers. Thus, it is also of interest to find an organoclay that minimizes organoclay agglomeration.

Silane coupling agents are commonly used in glass fiber composites to improve the binding of polymer matrix to the glass fibers. The coupling agent, an organofunctional alkoxysilane, is hydrolyzed to form reactive silanol groups which can condense with the silanol groups on the glass surface. The organic portion of the coupling agent bonds with the polymer.

Montmorillonite (MMT) platelets consist of one Al-octahedral sheet sandwiched between two Si-tetrahedral sheets. Si-OH groups are accessible on the edges of the MMT platelets [47-49] and at the structural defects on the platelet faces [50, 51]. The purpose of this chapter is to explore the possibility of using a silanized organoclay that might better exfoliate into PP than currently available organoclays without using a compatibilizer such as PP-*g*-MA.

This chapter explores the extent of organoclay exfoliation and the mechanical properties of melt compounded nanocomposites using a silanized organoclay (s-$M_2(HT)_2$) and the non-silanized precursor ($M_2(HT)_2$) with matrices of PP and PP/PP-*g*-MA blends. The extent of agglomeration of s-$M_2(HT)_2$ and $M_2(HT)_2$ is also examined in this chapter using different extruders and screw configurations.

EXPERIMENTAL

Materials

The matrix materials used were polypropylene, PP, (Pro-Fax® PH020, LyondellBasell) and the maleic anhydride-grafted polypropylene, PP-*g*-MA, (Polybond® 3200, Chemtura). It is expected that the PP and the PP-*g*-MA used are miscible with each other based on prior work with related polyolefins [52, 53]. The organoclay designated as $M_2(HT)_2$, donated by Southern Clay Products, was prepared by a cation exchange reaction between sodium montmorillonite (Na^+ MMT) and a two-tailed quaternary ammonium surfactant, dimethyl bis(hydrogenated-tallow) ammonium chloride (Arquad 2HT-75). Some frequently used abbreviations are employed here to represent the substituents on the ammonium cation, e.g., M for methyl and HT represents long alkyl chains from hydrogenated tallow [1, 16, 54]. This organoclay was selected based upon recent studies showing improved organoclay exfoliation in polyethylene using surfactants with two tails on the ammonium ion instead of one tail [14, 16, 35, 38]. The polymers employed have better affinity for the largely aliphatic organic modifier than for the unmodified clay surface. The larger area of the clay surface covered by two tails increases the favorable surfactant-polymer interaction and decreases the unfavorable polymer-clay interaction.

An experimental silanized organoclay designated as s-$M_2(HT)_2$, donated by Southern Clay Products, was prepared by silanizing $M_2(HT)_2$ with 6% trimethoxyphenyl silane based on the weight of the MMT. Calculations indicate that this amount of silane is more than sufficient to react with all the Si-OH groups that might be exposed on the platelet edge surfaces. Tables 2.1 and 2.2 in Chapter 2 provide further details on the materials used in this study.

Melt processing

The organoclay and the PP-*g*-MA were dried for a minimum of 24 h in a vacuum oven at 80 °C, prior to melt processing. Nanocomposites were melt compounded in a Haake co-rotating, intermeshing twin screw extruder (diameter = 30 mm, L/D = 10) using a barrel temperature of 170 - 190 °C, a screw speed of 280 rpm , and a feed rate of 1 kg/h. The PP, the PP-*g*-MA, and the organoclay were hand-mixed prior to extrusion and introduced into the extruder by a single hopper. The ratio of the mass of PP-*g*-MA to the mass of the organoclay was fixed at 1 because Kim et al. previously reported this ratio to be an optimum for PP/PP-*g*-MA/organoclay nanocomposites [15]. Additional nanocomposite samples were melt compounded in a Coperion ZSK 25 (diameter = 25 mm, L/D = 48) extruder for comparative agglomeration testing described below.

Tensile specimens (ASTM D638, Type I) and Izod bars (ASTM D256) were prepared by an Arburg Allrounder 305-210-700 injection-molding machine using a barrel temperature of 185 °C (feed) to 220 °C (die), an injection pressure of 35 bar, and a holding pressure of 35 bar. After molding, the samples were immediately sealed in a polyethylene bag and placed in a vacuum desiccator for a minimum of 24 h prior to testing.

The montmorillonite content of the nanocomposite was determined by placing pre-dried nanocomposite pellets in a furnace at 900 °C for 45 min and weighing the remaining MMT ash, correcting for loss of structural water [13, 55-57].

Characterization

Morphology was examined via a FEI TECNAI G2 F20 X-TWIN TEM operating under an accelerating voltage of 200 kV. Ultra-thin sections (~50 nm) for morphological analysis were taken from the core portion of an injection molded bar in the plane defined by the flow direction (FD) and the normal direction (ND) using an RMC PowerTome XL microtome [58]. The nanocomposite samples and the diamond knife were cooled to between -65 °C and -58 °C, respectively, using liquid nitrogen. Cut sections were collected onto 400 mesh grids and dried with filter paper.

Wide angle X-ray scattering (WAXS) scans were performed using a Bruker-AXS D8 Advance diffractometer in the reflection mode, using an incident X-ray wavelength of 0.1541 nm at a scan rate of 3.0°/min over the range of $2\theta = 1°$ to 12°. The major face of the rectangular nanocomposite bars and the organoclay powder were scanned [59].

The extent of agglomeration was examined by performing light microscopy on an Olympus BX51 Cross Polarized Optical Microscope with a 10X lens in the transmission, brightfield mode with a polarizing filter between the light source and the sample and another polarizing filter set at 90º to the first filter located between the sample and the camera. Images were collected on an Olympus DP72 Microscope Digital Camera. Samples were prepared by compression molding thin films (~40µm) at 180 °C between two sheets of Mylar for a total of 4.5 minutes (including a 2.5 minute preheat/melting time) in a manual Carver press and quenching the hot films in an ice bath. The films were mounted between a 25 by 75 mm slide and a 22 mm cover slide with low viscosity mineral oil on both sides of the specimen. The number and size of the particles were determined using D. E Details, Build 1275, Version 5.1 by Olympus. The micrograph pictures were optimized as needed to a black background appearance. The sensitivity was adjusted to measure a minimum particle diameter of 3.68 µm.

Melt rheological characteristics of the PP-based nanocomposites were determined using an AR 2000ex Rheometer using a parallel plate fixture. All the rheological measurements were carried out at a fixed temperature of 180 °C under a nitrogen gas flow. Strain sweep tests were carried out for each sample to ensure that the strain used is within the linear viscoelastic range. Frequency sweep tests were made over a range of 0.1–200 rad/s at strains of 0.5–2%, which was within the linear region for each sample. Specimens for rheological testing were taken from the far end of injection molded samples and trimmed after heating on the rheometer plate to a disk with a diameter of 25 mm and a thickness of 1 mm.

Tensile tests were performed according to ASTM D638 using an Instron model 1137 machine upgraded for computerized data acquisition. Tensile modulus values were determined using an extensometer at a crosshead rate of 0.51 cm/min and averaged from at least five specimens. Elongation at break and yield strength data were taken at 0.51 cm/min and averaged from at least four specimens. Elongations greater than 400% could not be measured due to the limitations of crosshead travel.

Notched Izod impact tests were conducted at room temperature with a 6.8 J hammer at an impact velocity of 3.5 m/s using a TMI Impact tester (model 43-02). Standard notches were made according to ASTM D256. As-molded rectangular bars were cut in half (to generate more samples), and the Izod impact strength data from the gate end (the end at which the molten polymer enters the mold during injection molding) and the far end were averaged together because the difference between the two is relatively small. The reported values were averaged from at least ten specimens.

Thermal expansion tests were conducted according to ASTM D696 using a Perkin–Elmer thermomechanical analyzer (TMA 7). Rectangular specimens were prepared from the central region of Izod bars. The dimensions of the specimens were approximately as follows: thickness = 3.2 mm, width = 6.4 mm, and height = 12.7 mm. Thermal expansion measurements were made in the flow direction (FD). Each specimen was held at −40 °C for 5 min, heated at a rate of 5 °C/min to 125 °C and subsequently held for 30 min, and then quenched to room temperature. In order to assess both reversible and non-reversible effects, each specimen was stored at room temperature for at least 24 h after the first heating and then rescanned from −40 °C to 125 °C at a rate of 5 °C/min. All measurements were done in a nitrogen atmosphere.

Particle analysis

Particle analyses were performed on TEM micrographs at magnifications of 3.6K to 13.5K, depending on the extent of exfoliation in the sample. Because of low contrast, TEM images were converted into .jpg format and opened in GIMP (GNU Image Manipulation Program). Two tracings in separate, transparent layers were made of particle length and thickness. For nanocomposites with single platelets, the thickness of these platelets could not be accurately measured and was set to 0.94 nm corresponding to the known result for MMT platelets [35, 60]. Each tracing was saved separately in .tif format and imported into the image analysis program, SigmaScan Pro, where each particle tracing was assigned a number and their characteristic dimensions were measured. Because the numbers assigned in the tracing of the length and the tracing of the thickness of the particles do not correspond, the particle dimensions must be matched manually. In this work, four different kinds of aspect ratios are calculated, i.e., the number and weight averages of the aspect ratios calculated for individual particles, $\langle l/t \rangle_n$ and $\langle l/t \rangle_w$, and ratios of the number and weight averages of particle lengths and thicknesses, $\left(\overline{l_n}/\overline{t_n}\right)$ and $\left(\overline{l_w}/\overline{t_w}\right)$. To ensure statistical validity of the analysis, 200~400 particles were counted to measure the length, thickness, and aspect ratio. The results are summarized in Table 4.1.

RESULTS AND DISCUSSION

Morphology

Transmission electron microscopy

TEM observations allow for a visual, qualitative assessment of the degree of organoclay exfoliation in polymer nanocomposites. Figure 4.1 shows representative TEM micrographs for nanocomposites with s-$M_2(HT)_2$ and $M_2(HT)_2$ in PP and PP/PP-*g*-MA (mass PP-*g*-MA/mass organoclay = 1) matrices having a nominal MMT content of 3 wt%. For the PP/$M_2(HT)_2$ nanocomposites (Figure 4.1(a)), large tactoids are seen, indicating poor clay dispersion. The PP/s-$M_2(HT)_2$ nanocomposites (Figure 4.1(b)) have a decreased tactoid size and an increased density of tactoids per unit area of the 2-D image. Nanocomposites with either organoclay in a PP/PP-*g*-MA matrix (Figure 4.1(c) and (d)) have improved exfoliation as demonstrated by the significant decrease in the size of the clay tactoids and the appearance of single platelets.

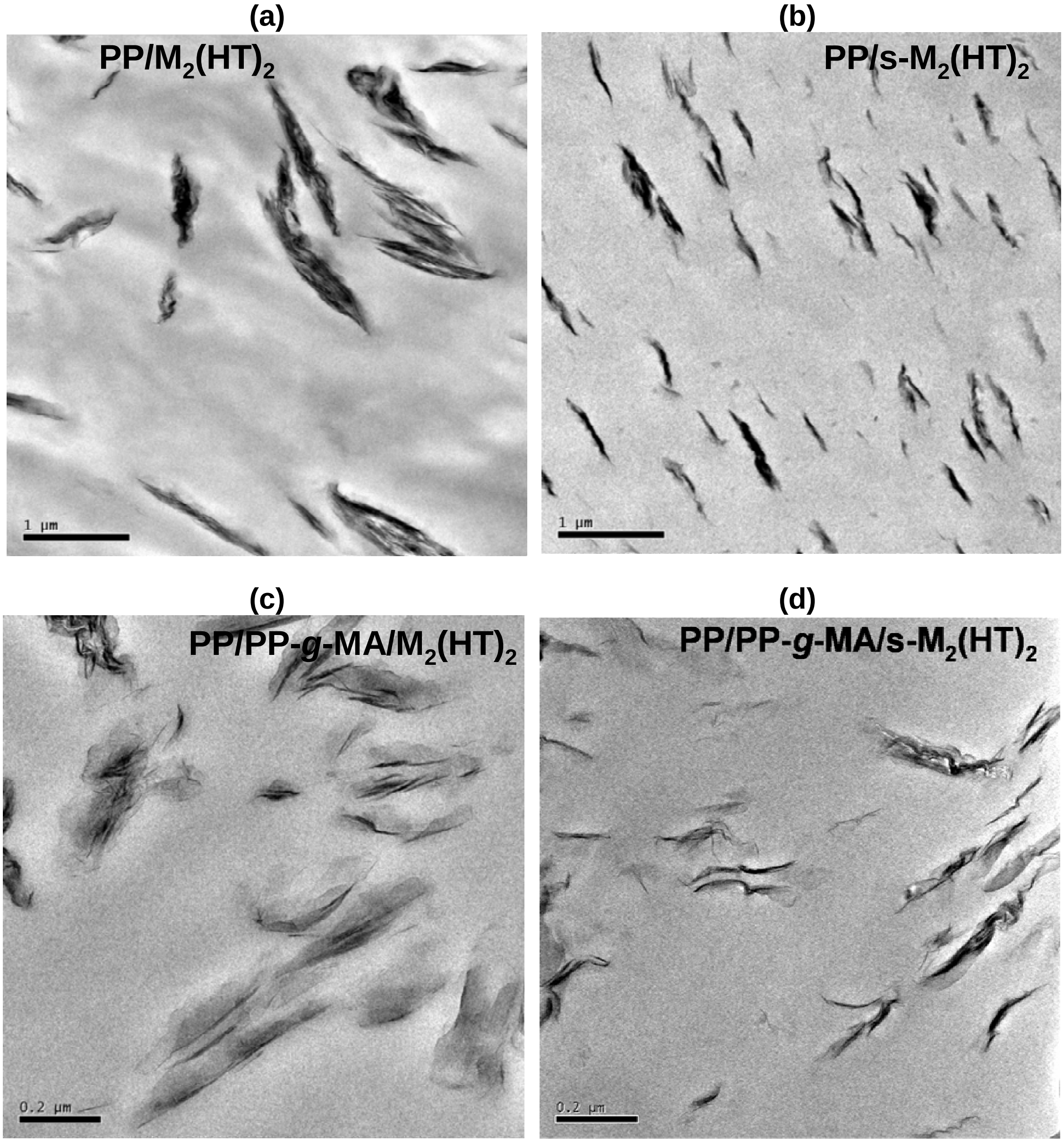

Figure 4.1: TEM photomicrographs of nanocomposites with ~3 wt% MMT: (a) PP/M_2(HT)$_2$, (b) PP/s-M_2(HT)$_2$, (c) PP/PP-*g*-MA/M_2(HT)$_2$, (d) PP/PP-*g*-MA/s-M_2(HT)$_2$.

The enhanced exfoliation of the s-M_2(HT)$_2$ in PP indicates improved interactions between the polymer and the silanized organoclay. There is little difference, however, between the level of exfoliation for the two organoclays when PP-*g*-MA is used as a compatibilizer.

Particle analysis

Particle analysis is used to quantify the extent of exfoliation shown in the TEM images. The statistical results and the MMT concentration of each nanocomposite as determined by incineration are shown in Table 2 for nanocomposites containing ~3 wt% MMT based on PP and PP/PP-*g*-MA (ratio of PP-*g*-MA to organoclay = 1) and $M_2(HT)_2$ and s-$M_2(HT)_2$. The aspect ratios obtained by averaging the values of each particle, $\langle l/t \rangle_n$ and $\langle l/t \rangle_w$, are always larger than those calculated from the ratio of the corresponding average values of length and thickness, $\left(\overline{l_n}/\overline{t_n}\right)$ and $\left(\overline{l_w}/\overline{t_w}\right)$. The ratio of number average particle length and thickness, $\left(\overline{l_n}/\overline{t_n}\right)$, is always larger than the ratio of weight average particle length and thickness, $\left(\overline{l_w}/\overline{t_w}\right)$ while the weight average aspect ratio obtained by averaging values of each particle, $\langle l/t \rangle_w$, is always larger than the corresponding number average ratio, $\langle l/t \rangle_n$. These trends are in a good agreement with previous reports [15, 35, 61, 62].

The quantitative trends mirror the qualitative TEM results discussed above. Average particle thickness and length decrease with the addition of PP-*g*-MA, and the aspect ratio increases because the particle thickness decreases at a higher rate than the particle length. The PP/s-$M_2(HT)_2$ nanocomposites have lower particle thicknesses and lengths than the PP/$M_2(HT)_2$ nanocomposites, but the aspect ratio remains the same. The particle density, another measure of exfoliation, is higher for the PP/s-$M_2(HT)_2$ nanocomposites than for the PP/$M_2(HT)_2$ nanocomposites. The particle densities of the PP-*g*-MA compatibilized nanocomposites are significantly higher than the particle densities of the PP-based nanocomposites.

Table 4.1: Results of nanocomposite particle analysis

Components	Wt % MMT	Total number of particles	Particle Density (particles/μm^2)	Number average particle length $\left(\overline{l_n}, nm\right)$	Number average particle thickness $\left(\overline{t_n}, nm\right)$	Weight average particle length $\left(\overline{l_w}, nm\right)$	Weight average particle thickness $\left(\overline{t_w}, nm\right)$	Number average aspect ratio $\left(\overline{l_n} / \overline{t_n}\right)$	Number average aspect ratio $\langle l / t \rangle_n$	Weight average aspect ratio $\left(\overline{l_w} / \overline{t_w}\right)$	Weight average aspect ratio $\langle l / t \rangle_w$
PP/$M_2(HT)_2$	2.7	209	1.7	578.5	32.0	757.8	71.3	18.1	29.4	10.6	41.7
PP/PP-g-MA/ $M_2(HT)_2$	2.8	275	83.0	105.1	2.6	135.8	3.8	40.1	48.2	35.6	60.9
PP/s-$M_2(HT)_2$	2.7	300	3.1	426.7	20.8	542.0	38.0	20.5	28.9	14.3	36.6
PP/PP-g-MA/ s-$M_2(HT)_2$	2.7	374	70.0	99.9	3.0	130.0	5.3	33.5	41.6	25.8	50.9

Wide angle X-ray scattering

WAXS is commonly used to characterize the structure of nanocomposites. WAXS scans of the neat $M_2(HT)_2$ and s-$M_2(HT)_2$ organoclays and of the skin portion of nanocomposites with ~5% MMT prepared from PP and PP/PP-*g*-MA (mass PP-*g*-MA/mass organoclay = 1) matrices are shown in Figure 4.2. The d_{001} peaks of the organoclays are not significantly different, indicating that most of the silanization occurred on the platelet edges [47-49] or on the external surface of the clay [50] rather than on the interlayer surfaces [51], as might be expected.

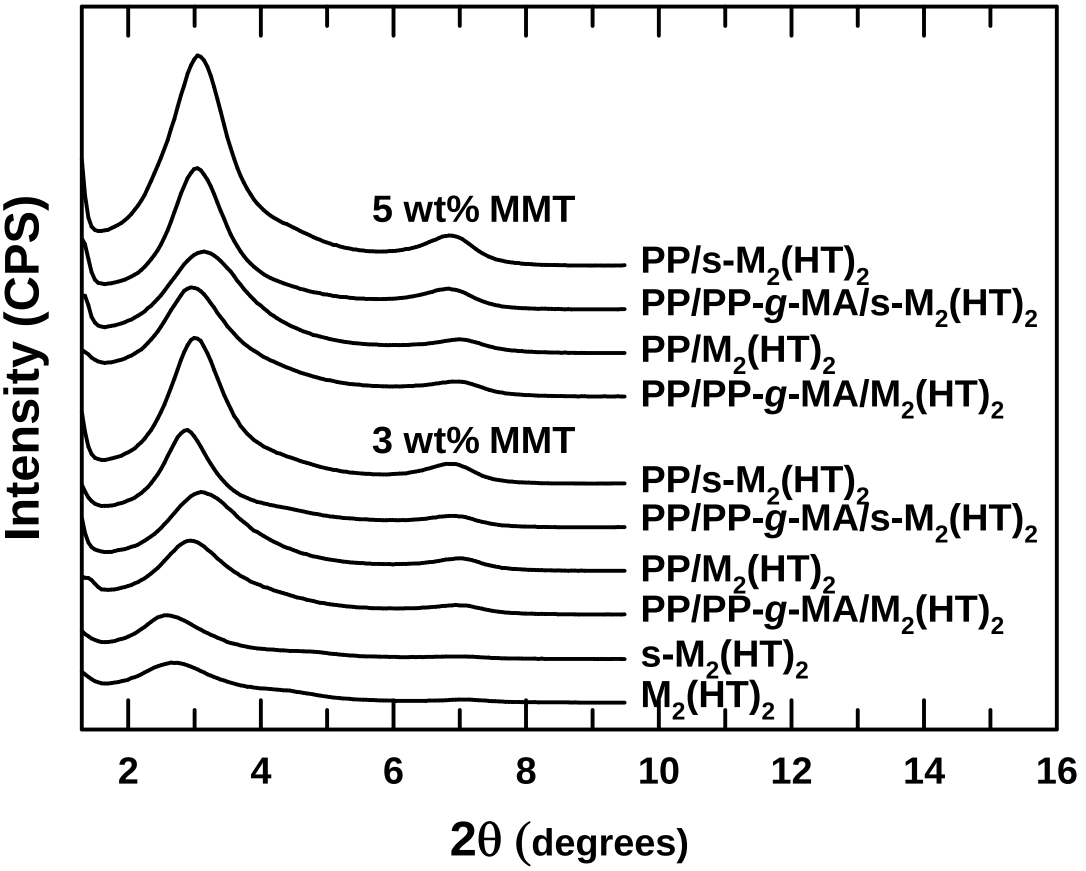

Figure 4.2: WAXS scans of pristine $M_2(HT)_2$ and s-$M_2(HT)_2$ organoclays and nanocomposites containing ~3 and ~5 wt% MMT formed from PP and PP/PP-*g*-MA. The curves are vertically offset for clarity.

The scans for the neat organoclays show a single basal reflection due to the random orientation of the organoclay platelets in the powder, while scans of the nanocomposites show higher order reflections, indicating a high degree of platelet orientation [43, 63]. The intensity of the s-$M_2(HT)_2$ organoclay nanocomposites is higher than that of the $M_2(HT)_2$ organoclay nanocomposites, likely due to the higher alignment of the tactoids in the flow direction or to the higher alignment of the particles within the tactoids.

The d_{001} peaks of the nanocomposites are shifted slightly to the right of the neat organoclay peaks. This shift to higher angle and lower *d*-spacing could indicate degradation of the surfactant, causing the clay galleries to collapse as surfactant mass is lost from within the galleries [16]. These differences are so small, however, that it is difficult to attach much physical meaning to them [15, 61]. The WAXS results give only limited information about the morphology and TEM, though providing a clearer understanding of exfoliation levels, examines only a small volume and may not be representative of the nanocomposite as a whole. Therefore, rheological, mechanical, and thermal expansion properties were measured to complement TEM and WAXS analyses [15, 61].

Agglomeration

Although TEM and WAXS assess the submicron morphology, larger agglomerates often exist to varying extents in nanocomposites. Clay agglomerates have greatly reduced surface areas and aspect ratios, decreasing the potential benefits of clay addition. In addition, Fasulo et al. [64] reported surface imperfections in injection molded parts caused by agglomeration.

The degree of clay agglomeration can be examined by optical microscopy of thin films. Although some agglomerates are crushed by compression molding the ~40 μm-thick films, agglomerate fragments are still distinguishable. Films were made from nanocomposites melt compounded in the Haake extruder and the ZSK extruder. Differences in the extruders are explained in more detail previously by Yoon et al. [65]. Various screw configurations were tested to gain a better understanding of how they affect the agglomeration level. Diagrams of the screw configurations tested and the particle count results are contained in Appendix D.

Optical micrographs of films of PP nanocomposites with ~3 wt% MMT of both s-$M_2(HT)_2$ and $M_2(HT)_2$ made using the Haake extruder (Figure 4.3) and using the ZSK extruder using a low shear configuration (Figure 4.4) are shown. Additional micrographs are contained in Appendix D. Nanocomposites with s-$M_2(HT)_2$ have less agglomeration than $M_2(HT)_2$ nanocomposites regardless of the extruder used.

Experiments were performed on the ZSK extruder, primarily with PP/$M_2(HT)_2$, with different screw configurations to determine which factors influence the amount of agglomeration. Runs were conducted with and without turbine mixing elements (TME) in the screw configuration. Samples processed on the ZSK extruder with TME had higher average particle counts (228) than those with out TME (43), demonstrating that TME in the screw configuration increase the agglomeration. The average particle counts without TME for upstream runs (54) and downstream runs (33) indicate that downstream clay feeding generally leads to less agglomeration than upstream clay feeding. The effect of shear can be assessed by comparing the particle counts of PP/ $M_2(HT)_2$ composites at low shear (89), medium shear (28), and high shear (11) fed to the extruder downstream, indicating that increasing the shear leads to less agglomeration when no TME are used.

The nanocomposites produced by the Haake extruder generally have fewer agglomerates than those formed on the ZSK extruder; an unexpected result because the only feed port is at the throat of the extruder. Although the Haake extruder has upstream clay feeding, its high shear, higher residence time, self-wiping elements, and lack of distributive elements result in less agglomerated nanocomposites than the ZSK extruder.

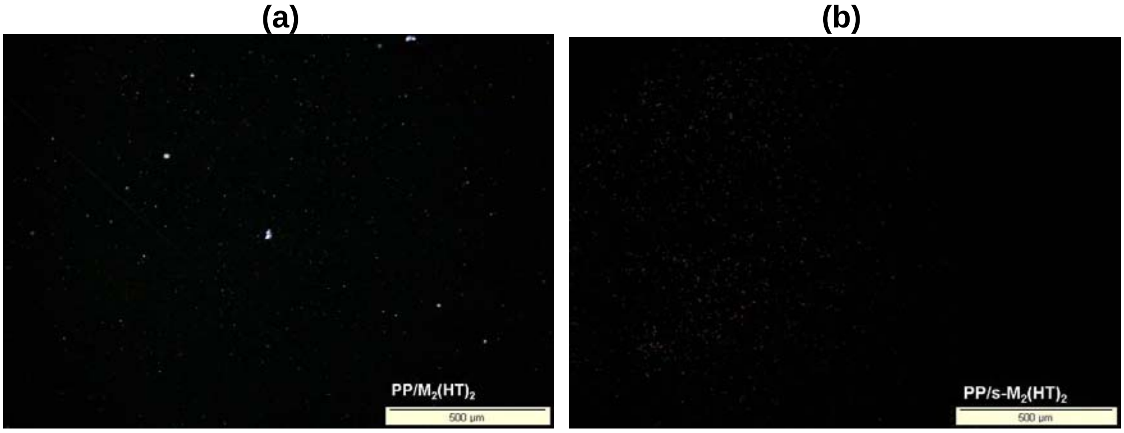

Figure 4.3: Optical photomicrographs of nanocomposite films made by the Haake extruder with ~3 wt% MMT: (a) PP/$M_2(HT)_2$, (b) PP/s-$M_2(HT)_2$.

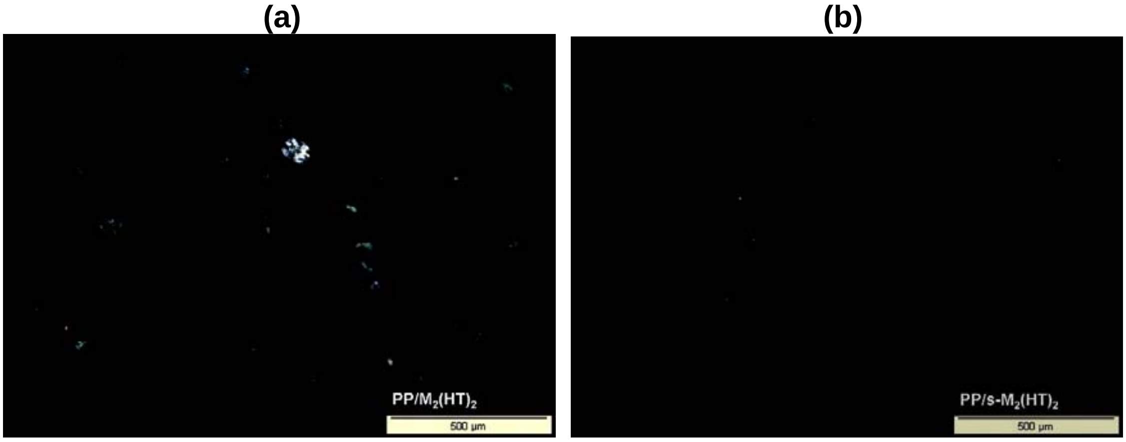

Figure 4.4: Optical photomicrographs of nanocomposite films made by the Haake extruder with ~3 wt% MMT: (a) PP/$M_2(HT)_2$, (b) PP/s-$M_2(HT)_2$.

Rheological properties

The melt rheological properties of nanocomposites provide fundamental insights into the processability and morphology for these materials. Viscoelastic measurements are highly sensitive to the nanoscale and mesoscale structure of the nanocomposites and appear to be a powerful method to probe the state of dispersion in such materials [15, 66-68]. The addition of organoclay to the polymer matrix increases the storage modulus by several orders of magnitude and alters the shear-thinning behavior at low frequencies to indicate a transition from liquid-like ($G' \propto \omega^2$, $G'' \propto \omega^1$) to solid-like (G', $G'' \propto \omega^0$) rheological behavior. It is generally believed that the extent of these changes reflects the state of dispersion of the clay and has been attributed to the formation, in the quiescent state, of a percolated network superstructure of the exfoliated layers or stacks of intercalated layers called tactoids [15, 66-68]. Figure 4.5 shows the rheological properties for PP nanocomposites with ~5 wt% MMT. The nanocomposites tested show increased complex viscosity and storage modulus compared to the neat polymer, especially at low frequencies. PP/s-$M_2(HT)_2$ nanocomposites have slightly higher increases than PP/$M_2(HT)_2$ nanocomposites. Nanocomposites with PP-*g*-MA compatibilizer have much higher increases in complex viscosity and storage modulus at low frequencies, and the storage modulus for these nanocomposites begins to plateau at low frequencies. The complex viscosity and storage modulus of the PP/PP-*g*-MA/s-$M_2(HT)_2$ nanocomposites is less than for the PP/PP-*g*-MA/$M_2(HT)_2$ nanocomposites. The maleic anhydride groups may react [69] or interact with the hydroxyl groups on the clay platelet edges, increasing the rheological response. The effect of the silane partially blocking the interaction between the maleic anhydride groups and the platelet edges is likely responsible, at least in part, for the lower rheological response of the PP/PP-*g*-MA/s-$M_2(HT)_2$ nanocomposites.

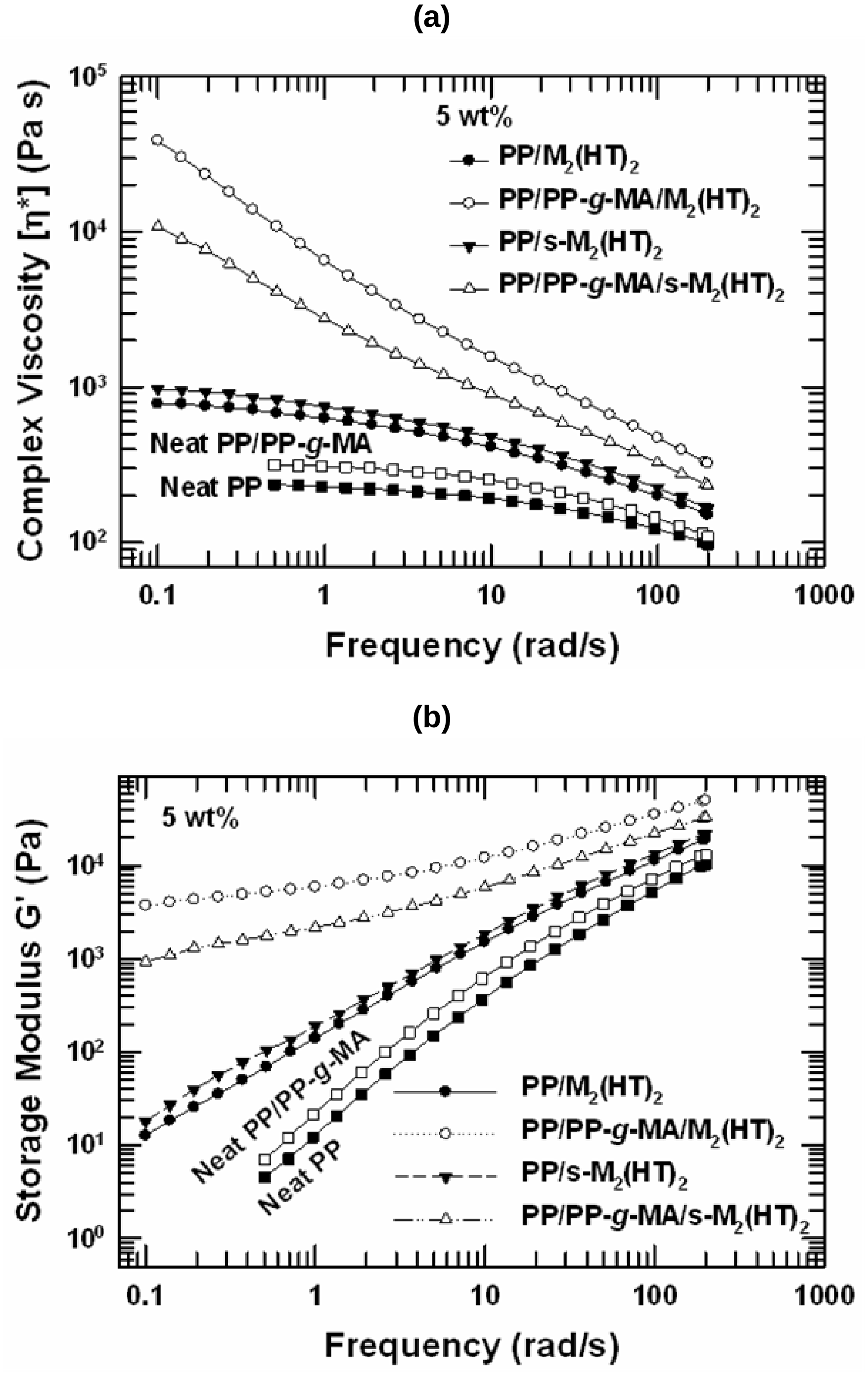

Figure 4.5: Frequency sweep results for PP and PP/PP-*g*-MA nanocomposites at 180 °C: complex viscosity (a) and storage modulus (b) with $M_2(HT)_2$ and s-$M_2(HT)_2$ organoclays at a fixed MMT content of ~5 wt%.

Mechanical properties

Of the various mechanical properties, modulus provides the best indicator of organoclay exfoliation [1]. Figure 4.6(a) shows the effect of MMT concentration on the tensile modulus of the nanocomposites. As expected, increasing MMT content results in significant improvements in modulus. Because the moduli of the neat PP-based polymers (E_m) vary with PP-*g*-MA content, examining the relative moduli (E/E_m) allows more useful comparisons. Relative modulus as a function of MMT concentration is shown in Figure 4.6(b). Although s-$M_2(HT)_2$ gives better modulus improvements than $M_2(HT)_2$ for PP-based nanocomposites, PP-*g*-MA compatibilized nanocomposites using either organoclay have even higher modulus enhancements with increasing MMT content.

(a)

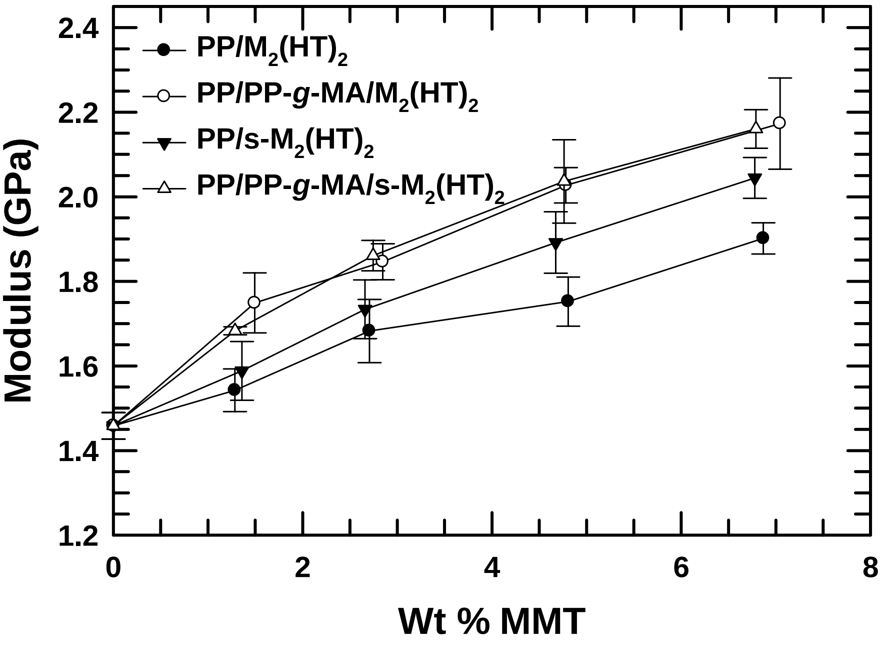

(b)

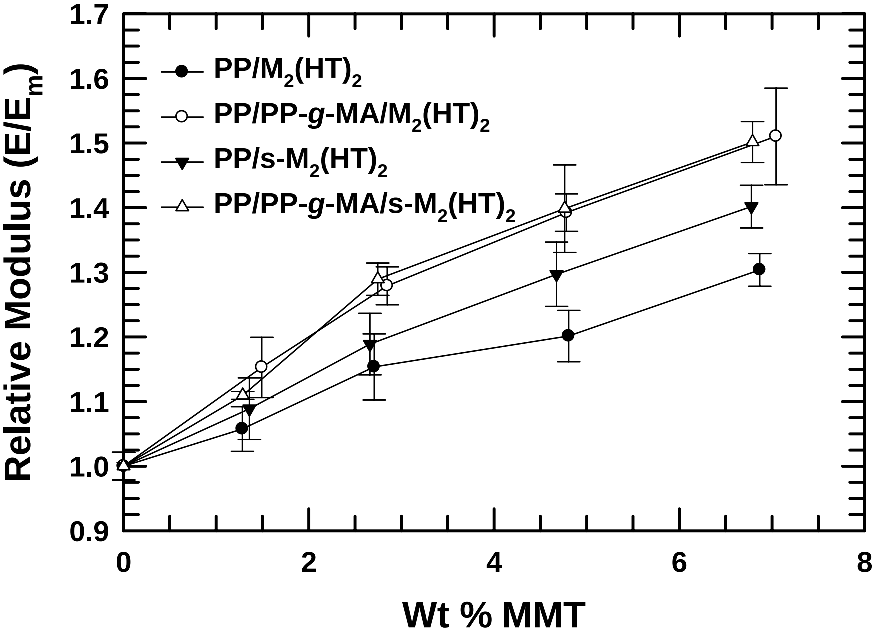

Figure 4.6: Modulus (a) and relative modulus (b) as a function of montmorillonite content for PP and PP/PP-g-MA nanocomposites with M2(HT)2 and s-M2(HT)2 organoclays.

Elongation at break data are presented in Figure 4.7. Neat polymer specimens and s-$M_2(HT)_2$ nanocomposites with low MMT levels (≤1.5 wt%) were too ductile to determine the breaking point using the available equipment. The elongation at break decreases with the addition of MMT and the addition of PP-*g*-MA accelerates this decrease for both organoclays. There does not appear to be a significant difference between the two organoclays.

Fracture toughness measured by the Izod impact strength is an important property for some applications. Izod impact strength values (Table 4.2) were averaged from both gate end and far end samples because the difference between the two is relatively small. PP itself is very brittle by this test; thus, it is not surprising that all these materials exhibit complete breakage of specimens during the impact tests, irrespective of the amount of PP-*g*-MA and MMT.

The fracture energy recorded in an impact test reflects the integration of the resisting force of the sample over the range of the sample deflection. Although the addition of organoclay and improved exfoliation tend to decrease the impact energy [13, 54, 70-72], in some cases the increase of force outweighs the decrease in ductility [16, 73-75]. In this work, large standard deviations were observed and no meaningful trends could be found.

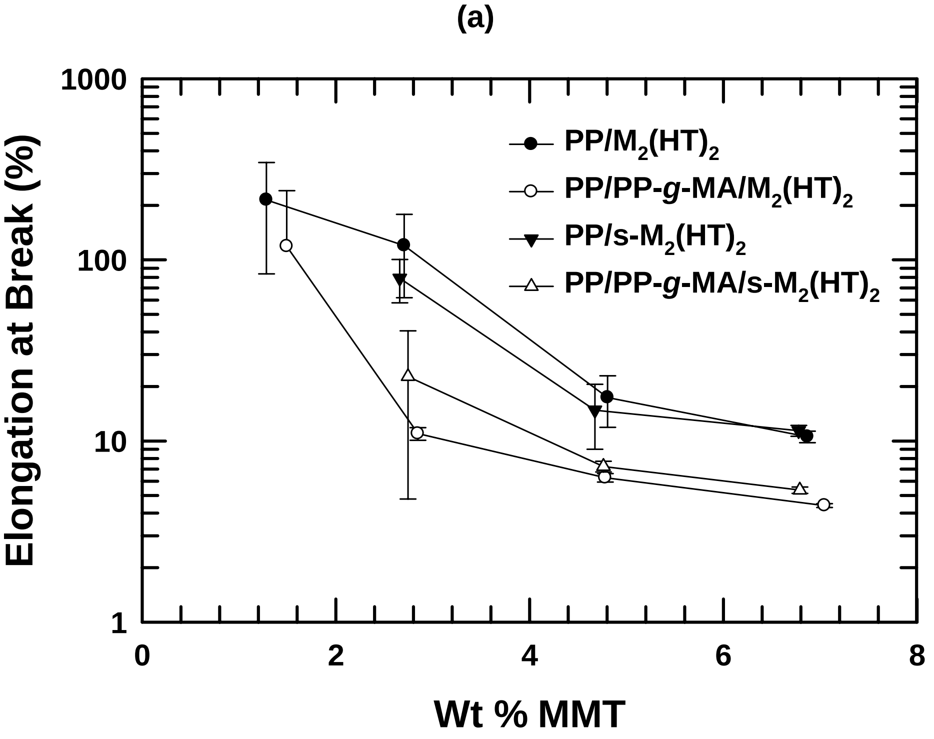

Figure 4.7: Elongation at break as a function of montmorillonite content for PP and PP/PP-*g*-MA nanocomposites with $M_2(HT)_2$ and s-$M_2(HT)_2$ organoclays.

Table 4.2: Izod impact strength results (J/m) for nanocomposites with various MMT contents

Components	0 wt%	1.5 wt%	3.0 wt%	5.0 wt%	7.0 wt%
PP/PP-*g*-MA[a]	21.2	21.4	23.3	17.2	24.8
PP/$M_2(HT)_2$		26.9	21.5	21.5	24.5
PP/PP-*g*-MA/$M_2(HT)_2$		34.0	20.0	21.5	17.1
PP/s-$M_2(HT)_2$		24.1	19.8	17.2	22.9
PP/PP-*g*-MA/s-$M_2(HT)_2$		29.6	17.4	17.4	20.6

[a] Neat blends with the ratio of the mass of PP-*g*-MA to the mass of organoclays fixed at 1.

Thermal expansion properties

PP and PP-based nanocomposites show significant non-linearity in thermal expansion as the temperature increases as reported by Lee et al. [7]. Thus, all the thermal expansion coefficients (CTE) presented in this paper were obtained over a 0–30 °C temperature range during the second heating scan because these values should be related to the mechanical property data measured at room temperature. Figure 4.8(a) shows the CTE in the flow direction of the PP and PP/PP-*g*-MA (mass PP-*g*-MA/mass organoclay = 1) nanocomposites with $M_2(HT)_2$ and s-$M_2(HT)_2$ organoclays as a function of the MMT content. While the CTE decreases slightly for PP-based composites with the addition of MMT, the CTE for PP/PP-*g*-MA-based nanocomposites decreases much more as the MMT content increases. This reflects the increased degree of exfoliation and better orientation of the clay platelets in the flow direction when PP-*g*-MA is added.

Because PP-*g*-MA has a higher thermal expansion coefficient than PP, the CTE of neat PP/PP-*g*-MA blends increases as the amount of PP-*g*-MA increases as shown in Figure 4.8(a). Just as PP-*g*-MA lowers the modulus of the neat polymer blend and increases the modulus of the nanocomposite by increasing the filler aspect ratio, adding PP-*g*-MA results in higher expansion of the neat polymers and reduced CTE of the nanocomposites. For better understanding of the thermal expansion behavior of these nanocomposites, the CTE of the nanocomposites is normalized by the corresponding PP or PP/PP-*g*-MA blend without MMT as shown in Figure 4.8(b). Contrary to expectations, the s-$M_2(HT)_2$ nanocomposites appear to decrease the CTE to a lesser extent than the $M_2(HT)_2$ nanocomposites. Further work is needed to understand this phenomenon.

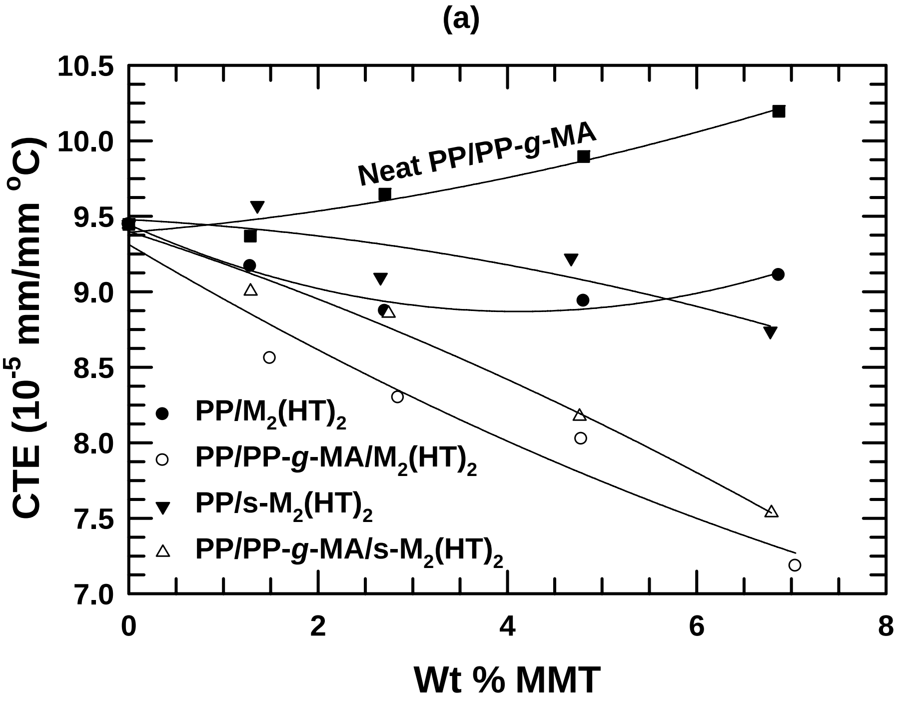

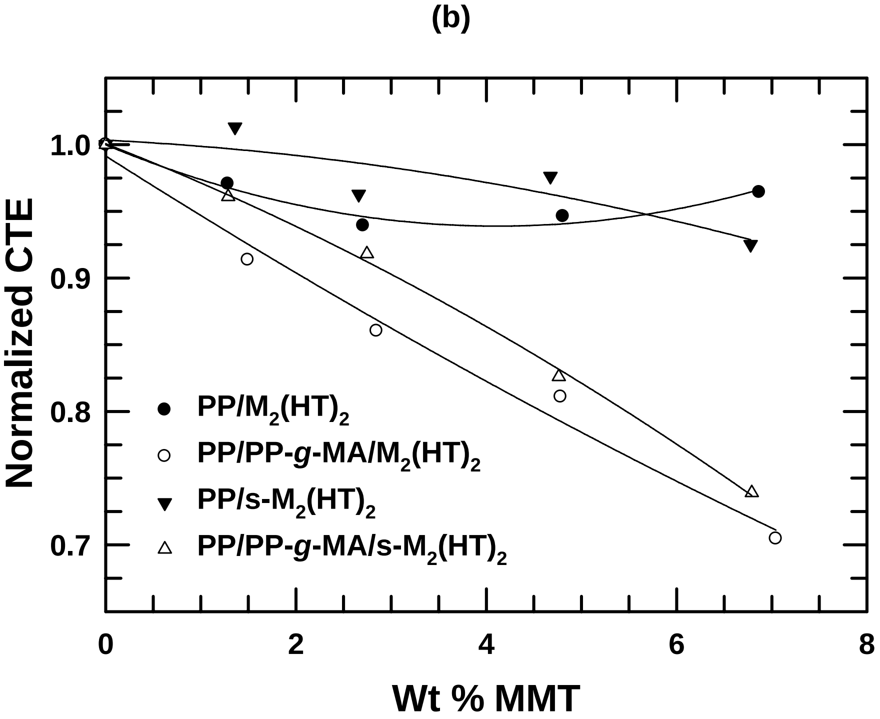

Figure 4.8: Thermal expansion coefficient for PP and PP/PP-*g*-MA nanocomposites with $M_2(HT)_2$ and s-$M_2(HT)_2$ organoclays (a) and the relative thermal expansion coefficient (b) where the data are normalized by the CTE of neat PP and PP/PP-*g*-MA blends.

CONCLUSION

Nanocomposites formed from PP and PP/PP-*g*-MA (mass PP-*g*-MA/mass organoclay = 1) and $M_2(HT)_2$ and s-$M_2(HT)_2$ organoclays were melt processed to explore the extent of exfoliation and the mechanical, rheological, and thermal expansion properties. WAXS and TEM coupled with detailed particle analysis were used to determine the effect of the organoclay used and the PP-*g*-MA compatibilizer on exfoliation. The PP/s-$M_2(HT)_2$ nanocomposites have higher particle densities than the PP/$M_2(HT)_2$ nanocomposites though the aspect ratio remains the same. The platelet dispersion is significantly improved by using PP-*g*-MA compatibilizer for both organoclays. Nanocomposites with s-$M_2(HT)_2$ have less agglomeration than $M_2(HT)_2$

nanocomposites. In general, nanocomposite produced with downstream organoclay feeding, with no TME in the screw design, and at high shear rates have lower agglomeration. The rheological properties and the relative modulus improve for the PP/s-$M_2(HT)_2$ nanocomposites but not to the same degree as either organoclay in a PP-*g*-MA compatibilized matrix. The elongation at break decreases with the addition of MMT and the addition of PP-*g*-MA accelerates this decrease for both organoclays. No meaningful trends were found for the Izod impact strength due to the brittle nature of the PP and the large standard deviations observed. The thermal expansion properties, however, are not improved by using the s-$M_2(HT)_2$ organoclay.

The silanized organoclay nanocomposites show mostly improved properties compared to the non-silanized precursor nanocomposites, though the improvements were less than those observed for PP-*g*-MA compatibilized nanocomposites. Organoclay silanization leads to some improvement in the mechanical properties of nanocomposites; other silane coupling agents might produce more significant improvements in exfoliation and, thus, reinforcement [48].

REFERENCES

1. Fornes TD, Yoon PJ, Hunter DL, Keskkula H, and Paul DR. Polymer 2002;43(22):5915-5933.
2. Giannelis EP. Applied Organometallic Chemistry 1998;12(10-11):675-680.
3. Lee H-s, Fasulo PD, Rodgers WR, and Paul DR. Polymer 2005;46(25):11673-11689.
4. Bharadwaj RK. Macromolecules 2001;34(26):9189-9192.
5. Messersmith PB and Giannelis EP. Journal of Polymer Science Part A: Polymer Chemistry 1995;33(7):1047-1057.
6. Yano K, Usuki A, Okada A, Kurauchi T, and Kamigaito O. Journal of Polymer Science Part A: Polymer Chemistry 1993;31(10):2493-2498.

7. Lee H-s, Fasulo PD, Rodgers WR, and Paul DR. Polymer 2006;47(10):3528-3539.

8. Kim DH, Fasulo PD, Rodgers WR, and Paul DR. Polymer 2008;49(10):2492-2506.

9. Gilman JW. Applied Clay Science 1999;15(1-2):31-49.

10. Gilman JW, Kashiwagi T, Brown JET, Lomakin S, Giannelis EP, and Manias E. Int. SAMPE Symp. Exhibit. 1998;43:1053.

11. Bourbigot S, Le Bras M, Dabrowski F, Gilman JW, and Kashiwagi T. Fire and Materials 2000;24(4):201-208.

12. Fornes TD, Hunter DL, and Paul DR. Macromolecules 2004;37(5):1793-1798.

13. Fornes TD, Yoon PJ, Keskkula H, and Paul DR. Polymer 2001;42(25):9929-9940.

14. Hotta S and Paul DR. Polymer 2004;45(22):7639-7654.

15. Kim DH, Fasulo PD, Rodgers WR, and Paul DR. Polymer 2007;48(18):5308-5323.

16. Shah RK, Hunter DL, and Paul DR. Polymer 2005;46(8):2646-2662.

17. Hasegawa N, Kawasumi M, Kato M, Usuki A, and Okada A. Journal of Applied Polymer Science 1998;67(1):87-92.

18. Kawasumi M, Hasegawa N, Kato M, Usuki A, and Okada A. Macromolecules 1997;30:6333–6338.

19. Varela C, Rosales C, Perera R, Matos M, Poirier T, Blunda J, and Rojas H. Polymer Composites 2006;27(4):451-460.

20. López-Quintanilla ML, Sánchez-Valdés S, Ramos de Valle LF, and Guedea Miranda R. Polymer Bulletin 2006;57(3):385-393.

21. Galgali G, Ramesh C, and Lele A. Macromolecules 2001;34(4):852-858.

22. Reichert P, Nitz H, Klinke S, Brandsch R, Thomann R, and Mülhaupt R. Macromolecular Materials and Engineering 2000;275(1):8-17.

23. Cui L and Paul DR. Polymer 2007;48(6):1632-1640.

24. Lertwimolnun W and Vergnes B. Polymer 2005;46(10):3462-3471.

25. Hasegawa N, Okamoto H, Kawasumi M, Kato M, Tsukigase A, and Usuki A. Macromolecular Materials and Engineering 2000;280-281(1):76-79.

26. Li X, Wang C-y, Fang L, and Liu L-z. Harbin Ligong Daxue Xuebao 2003;8(2):90-93.

27. Shah RK, Cui L, Williams KL, Bauman B, and Paul DR. Journal of Applied Polymer Science 2006;102(3):2980-2989.

28. Filippi S, Marazzato C, Magagnini P, Famulari A, Arosio P, and Meille SV. European Polymer Journal 2008;44(4):987-1002.

29. Wang KH, Choi MH, Koo CM, Choi YS, and Chung IJ. Polymer 2001;42(24):9819-9826.

30. Gopakumar TG, Lee JA, Kontopoulou M, and Parent JS. Polymer 2002;43(20):5483-5491.

31. Liang G, Xu J, Bao S, and Xu W. Journal of Applied Polymer Science 2004;91(6):3974-3980.

32. Morawiec J, Pawlak A, Slouf M, Galeski A, Piorkowska E, and Krasnikowa N. European Polymer Journal 2005;41(5):1115-1122.

33. Zhang M and Sundararaj U. Macromolecular Materials and Engineering 2006;291(6):697-706.

34. Mainil M, Alexandre M, Monteverde F, and Dubois P. Journal of Nanoscience and Nanotechnology 2006;6:337-344.

35. Cui L, Ma X, and Paul DR. Polymer 2007;48(21):6325-6339.

36. Zanetti M, Camino G, Thomann R, and Mülhaupt R. Polymer 2001;42(10):4501-4507.

37. Cerezo FT, Preston CML, and Shanks RA. Composites Science and Technology 2007;67(1):79-91.

38. Shah RK, Kim DH, and Paul DR. Polymer 2007;48(4):1047-1057.

39. Filippi S, Marazzato C, Magagnini P, Minkova L, Tzankova N, Francesco D, and Mantia PL. Macromolecular Materials and Engineering 2006;291(10):1208-1225.

40. Huang Y, Ma X, Liang G, Wang S, and Zhang Q. Polymer 2008;49(8):2085-2094.

41. Shah RK, Krishnaswamy RK, Takahashi S, and Paul DR. Polymer 2006;47(17):6187-6201.

42. Shah RK and Paul DR. Macromolecules 2006;39(9):3327-3336.

43. Cui L, Troeltzsch C, Yoon PJ, and Paul DR. Macromolecules 2009;42(7):2599-2608.

44. Ho RM, Su AC, Wu CH, and Chen SI. Polymer 1993;34(15):3264-3269.

45. Roover BD, Sclavons M, Carlier V, Devaux J, Legras R, and Momtaz A. Journal of Polymer Science Part A: Polymer Chemistry 1995;33(5):829-842.

46. Zhang R, Zhu Y, Zhang J, Jiang W, and Yin J. Journal of Polymer Science Part A: Polymer Chemistry 2005;43(22):5529-5534.

47. Chen G-X, Choi JB, and Yoon JS. Macromolecular Rapid Communications 2005;26(3):183-187.

48. Joo JH, Shim JH, Choi JH, Choi C-H, Kim D-S, and Yoon J-S. Journal of Applied Polymer Science 2008;109(6):3645-3650.

49. Herrera NN, Letoffe J-M, Putaux J-L, David L, and Bourgeat-Lami E. Langmuir 2004;20(5):1564-1571.

50. Park M, Shim I-K, Jung E-Y, and Choy J-H. Journal of Physics and Chemistry of Solids 2004;65(2-3):499-501.

51. He H, Duchet J, Galy J, and Gerard J-F. Journal of Colloid and Interface Science 2005;288(1):171-176.

52. González-Montiel A, Keskkula H, and Paul DR. Journal of Polymer Science Part B: Polymer Physics 1995;33(12):1751-1767.

53. Huang JJ, Keskkula H, and Paul DR. Polymer 2006;47(2):624-638.

54. Yoon PJ, Hunter DL, and Paul DR. Polymer 2003;44(18):5323-5339.

55. Fornes TD, Yoon PJ, Keskkula H, and Paul DR. Polymer 2002;43(7):2121-2122.

56. Stretz HA and Paul DR. Polymer 2006;47(26):8527-8535.

57. Stretz HA, Paul DR, Li R, Keskkula H, and Cassidy PE. Polymer 2005;46(8):2621-2637.

58. Yoon PJ, Fornes TD, and Paul DR. Polymer 2002;43(25):6727-6741.

59. Fornes TD and Paul DR. Macromolecules 2004;37(20):7698-7709.

60. Paul DR, Zeng QH, Yu AB, and Lu GQ. Journal of Colloid and Interface Science 2005;292(2):462-468.

61. Kim DH, Fasulo PD, Rodgers WR, and Paul DR. Polymer 2007;48(20):5960-5978.

62. Spencer MW, Cui L, Yoo Y, and Paul DR. Polymer 2010;51(5):1056-1070.

63. Chavarria F and Paul DR. Polymer 2006;47(22):7760-7773.

64. Fasulo PD, Rodgers WR, Ottaviani RA, and Hunter DL. Polymer Engineering & Science 2004;44(6):1036-1045.

65. Yoon PJ, Hunter DL, and Paul DR. Polymer 2003;44(18):5341-5354.

66. Ren J, Silva AS, and Krishnamoorti R. Macromolecules 2000;33(10):3739-3746.

67. Krishnamoorti R and Yurekli K. Current Opinion in Colloid & Interface Science 2001;6(5-6):464-470.

68. Okamoto M, Nam PH, Maiti P, Kotaka T, Hasegawa N, and Usuki A. Nano Letters 2001;1(6):295-298.

69. Fordiani F, Aubry T, and Grohens Y. Journal of Applied Polymer Science 2009;114(6):4011-4019.

70. Cho JW and Paul DR. Polymer 2001;42(3):1083-1094.

71. Fornes TD and Paul DR. Macromolecules 2004;37(20):7698-7709.

72. Stretz HA, Paul DR, and Cassidy PE. Polymer 2005;46(11):3818-3830.

73. Chen L, Wong S-C, Liu T, Lu X, and He C. J Polym Sci, Part B: Polym Phys 2004;42(14):2759-2768.

74. Wheeler PA, Wang J, Baker J, and Mathias LJ. Chemistry of Materials 2005;17(11):3012-3018.

75. Yoo Y, Shah RK, and Paul DR. Polymer 2007;48(16):4867-4873.

Chapter 5: Modeling the mechanical and thermal expansion behavior of TPO-based nanocomposites

Polymer nanocomposites based on organoclays can potentially lead to substantial enhancement in mechanical [1-4], barrier [5-7], thermal [8-10], and flammability [11-13] properties at very low filler concentrations while maintaining similar density and optical properties, making them attractive replacements for conventional composites. Melt mixing or compounding of polymer nanocomposites offers efficient exfoliation with good property improvements, provided the organoclay interacts favorably with the polymer matrix.

Non-polar polyolefin matrices, such as polypropylene or polyethylene, result in better exfoliation with organoclays modified by a surfactant with two or more long alkyl tails, providing increased alkyl-polyolefin interactions and decreased silicate-polyolefin interaction [3, 10, 14, 15]. In addition, nanocomposites formed from polyolefin matrices are often modified with a polar compatibilizer to improve exfoliation and enhance properties. The grafting of maleic anhydride to the polyolefin backbone significantly increases the polarity and, thus, improves the organoclay exfoliation in polypropylene (PP) [3, 16-23].

Although organoclay exfoliation in PP improves stiffness, the toughness of the material is sacrificed. Thus, there has been great interest in talc composites [24-27] and montmorillonite (MMT) nanocomposites [3, 4, 8, 9, 28] based on thermoplastic polyolefin (TPO) materials, i.e., blends of PP with ethylene-based elastomers made by compounding or formed *in situ* during polymerization, rather than on PP in order to achieve the optimum balance of stiffness and toughness required for many applications. It would be useful to model the PP/elastomer/organoclay nanocomposite system using theoretical composite models to better understand the morphology/property relationships.

Composite models, such as those by Mori-Tanaka, Lee, and Chow, have generally been used for a single-filler population in a matrix. However, the composites of interest here consist of both organoclay and elastomer particles. Recently, models have been reported for treating exfoliated single MMT platelets and intercalated tactoids [29] and for treating organoclay particles and glass fibers [30] as separate populations. A similar two-population approach is applied here to model the combined effects of the organoclay particles and the elastomer particles in these composites.

The models developed in this chapter are compared to experimental mechanical and thermal expansion results reported previously [3, 4, 8-10]. The purpose of this chapter is to demonstrate the prediction of the moduli and thermal expansion coefficients of TPO nanocomposites by applying ternary-phase approaches employing binary theoretical models such as the Mori-Tanaka, Lee, and Chow models.

EXPERIMENTAL RESULTS

Materials and composite preparation

Two series of nanocomposites are modeled in this chapter. The first is a series by Lee et al. [3, 8] that were produced by melt compounding mixtures of PP (melt index = 37 g/10 min), an ethylene–octene based elastomer (EOR, melt index = 0.5 g/10 min), and a masterbatch material containing equal parts of maleic anhydride-grafted polypropylene (PP-*g*-MA, MA content = 1.0 wt%) and an organically modified montmorillonite (dimethyl bis(hydrogenated-tallow) ammonium montmorillonite). The second is a series by Kim et al. [4, 9] of nanocomposites formed by melt compounding mixtures of a commercial TPO (CA 387 from Basell Polyolefins, melt index = 17 g/10 min), maleic anhydride-grafted polypropylene (PP-*g*-MA, MA content = 1.0 wt%) and an organoclay (dimethyl bis(hydrogenated-tallow) ammonium montmorillonite). Kim et al. also reported the morphology and properties of PP/PP-*g*-MA/MMT nanocomposites [10]. Further details of the melt processing steps used to form and shape these materials are given in the first papers in these series [3, 4, 10]. The ratio of the mass of PP-*g*-MA to the mass of organoclay is equal to one for all the composites modeled in this chapter.

Morphology characterization and particle analysis

Particle analyses of TEM and AFM images of TPO nanocomposites provide a quantitative assessment of the degree of organoclay exfoliation and of the elastomer morphology, respectively. Although various ways of averaging the particle aspect ratio exist, Hine et al. showed that using the number average fiber length in the Halpin-Tsai equations for glass fiber composites with a distribution of fiber lengths best matches more rigorous modeling that fully accounts for the length distribution [31]. Previous modeling efforts have shown good agreement with experimental data when using the number average aspect ratio, $\langle l/t \rangle_n$, or the ratio of number average particle length and thickness, $\left(\overline{l_n}/\overline{t_n}\right)$ [29, 32]. The series by Lee et al. reported the latter but not $\langle l/t \rangle_n$, while Kim et al. also reported $\langle l/t \rangle_n$. For these reasons, the experimental $\left(\overline{l_n}/\overline{t_n}\right)$ and $\langle l/t \rangle_n$ aspect ratios are used to model the nanocomposites in the series by Lee et al. and the series by Kim et al., respectively. Tables 5.1, 5.2, and 5.3 show the aspect ratios of the clay and elastomer particles used in the modeling in this work. Different aspect ratio measurements give similar, though different, results. The elastomer particles are generally aligned in the flow direction (FD) and the clay particles are generally aligned in the plane defined by the FD and the transverse direction (TD). Further details of the morphology and particle analysis procedures are reported elsewhere [3, 4, 10].

Table 5.1: MMT and EOR aspect ratios for composites by Lee et al. [3]

MMT (wt%)	MMT	EOR (30 wt%)
	$\left(\overline{l}_n / \overline{t}_n\right)$	$\left(\overline{l}_n / \overline{t}_n\right)$
0		1.5
1	63	1.8
2.8	37	2.1
6.8	31	2.8

Table 5.2: MMT aspect ratios for PP/PP-*g*-MA/MMT composites by Kim et al. [10]

MMT (wt%)	$\langle l/t \rangle_n$
0.97	56
3.00	45
5.38	44
7.36	43

Table 5.3: MMT and EOR aspect ratios for composites by Kim et al. [4]

MMT (wt%)	MMT	EOR (25 wt%)
	$\langle l/t \rangle_n$	$\langle l/t \rangle_n$
0		2.12
0.84	46	2.07
2.63	40	2.94
4.71	38	3.98
6.75	32	4.75

Mechanical and thermal expansion properties

The experimental modulus and thermal expansion properties compared with the modeling done in this work were reported previously [3, 4, 8-10]. The experimental error for the modulus is < 10%.

Modulus and thermal expansion measurements were performed on a neat EOR (used by Lee et al.) sample compression molded at 220 °C. The tensile modulus (7.6 MPa) was determined according to ASTM D638 with an Instron model 1137 machine upgraded for computerized data acquisition using an extensometer at a crosshead rate of

0.51 cm/min. Thermal expansion tests were conducted according to ASTM D696 using a Perkin–Elmer thermomechanical analyzer (TMA 7). Due to the softness and low melting temperature of the EOR, thermal expansion tests were performed on a stack of three specimens with the following approximate dimensions: thickness = width = 6.4 mm and height = 12.7 mm. Each specimen was held at −40 °C for 5 min, heated at a rate of 5 °C/min to 60 °C. The thermal expansion coefficient (CTE) determined over the 0-30 °C temperature range was 25.2 x 10^{-5} mm/mm $°C^{-1}$. The elastomer was assumed to be isotropic with a bulk CTE of 75.6 x 10^{-5} mm^3/mm^3 $°C^{-1}$.

COMPOSITE MODELS

Theoretical modeling is an attractive approach for the design of polymer composite systems, and numerous models [33-36] have been proposed for predicting the properties of composites and for correlating experimental data with such predictions. Previous papers [32, 37-41] have demonstrated such models can be useful for composites with nano- and micro-sized fillers. However, numerous assumptions are made when using these models. For example, it is assumed that the polymer matrix is not affected by the presence of the filler, that the filler is of uniform dimensions and is perfectly aligned, that the matrix and filler are isotropic, that the matrix and filler are well bonded, and that there are no particle—particle interactions or agglomerations [37]. Both the Mori–Tanaka and the Chow models are used in this paper to explore the relationship between the particle aspect ratio and the experimental modulus, while the Lee and Chow models are used to examine the relationship between the aspect ratio and the CTE.

These models all treat the fillers as aligned ellipsoidal particles characterized by the ratio of the major to the minor axes, i.e., $a = l/t$ for prolate ellipsoids (fiber-shaped inclusions) and $a = t/l$ for oblate ellipsoids (disk-shaped particles), with the major axis defined as being in the **1** direction (Figure 5.1). Because in an idealized injection-molded composite the major axes of fiber-shaped inclusions are parallel to the flow direction (FD) while the major axes of disk-shaped inclusions are perpendicular to the plane defined by the FD and the transverse direction (TD), the coordinate system depicted in Figure 5.2 is used to describe the composite properties. Tables 5.4 and 5.5 show which equations to use to calculate the modulus for fibers and disks for each direction of applied load and which equations to use to calculate the CTE for fibers and disks for each testing direction, respectively.

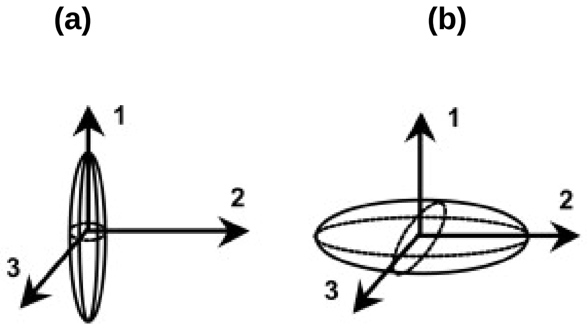

Figure 5.1: Physical representations and coordinate systems for fiber- (a) and disk-shaped (b) particles.

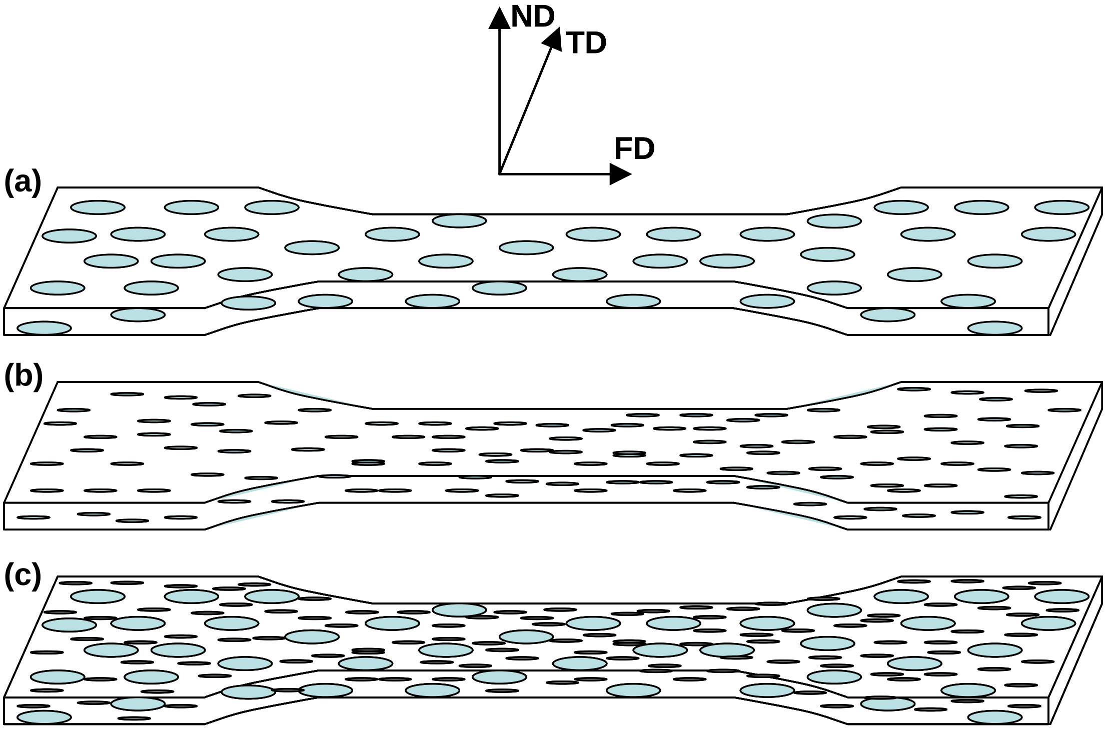

Figure 5.2: Physical representations and coordinate system for elastomer (a) organoclay (b) and elastomer/organoclay (c) composites.

Table 5.4: The Mori-Tanaka and Chow equations used to calculate the composite modulus for fiber- and disk-shaped particles

Direction of Applied Load	Mori-Tanaka		Chow	
	Fibers	Disks	Fibers	Disks
FD	$E_{FD} = E_{\parallel}$ (Eq. 1)	$E_{FD} = E_{\perp}$ (Eq.2)	$E_{FD} = E_{\parallel}$ (Eq. 7)	$E_{FD} = E_{\perp}$ (Eq.8)
TD	$E_{TD} = E_{\perp}$ (Eq. 2)	$E_{TD} = E_{\perp}$ (Eq. 2)	$E_{TD} = E_{\perp}$ (Eq. 8)	$E_{TD} = E_{\perp}$ (Eq. 8)
ND	$E_{ND} = E_{\perp}$ (Eq. 2)	$E_{ND} = E_{\parallel}$ (Eq. 1)	$E_{ND} = E_{\perp}$ (Eq. 8)	$E_{ND} = E_{\parallel}$ (Eq. 7)

Table 5.5: The Lee and Chow equations used to calculate the composite CTE for fiber- and disk-shaped particles

Direction of Testing	Lee		Chow	
	Fibers	Disks	Disks	Fibers
FD	$\alpha_{FD} = \alpha_{\parallel}$ (Eq. 3)	$\alpha_{FD} = \alpha_{\perp}$ (Eq. 4)	$\alpha_{FD} = \alpha_{\parallel}$ (Eq. 9)	$\alpha_{FD} = \alpha_{\perp}$ (Eq. 10)
TD	$\alpha_{TD} = \alpha_{\perp}$ (Eq. 4)	$\alpha_{TD} = \alpha_{\perp}$ (Eq. 4)	$\alpha_{TD} = \alpha_{\perp}$ (Eq. 10)	$\alpha_{TD} = \alpha_{\perp}$ (Eq. 10)
ND	$\alpha_{ND} = \alpha_{\perp}$ (Eq. 4)	$\alpha_{ND} = \alpha_{\parallel}$ (Eq. 3)	$\alpha_{ND} = \alpha_{\perp}$ (Eq. 10)	$\alpha_{ND} = \alpha_{\parallel}$ (Eq. 9)

Mori-Tanaka model

The Mori-Tanaka average stress theory [42] is based on the principles of Eshelby's inclusion model for predicting an elastic stress field in and around an ellipsoidal particle in an infinite matrix [43]. To account for finite filler concentrations, however, Mori and Tanaka [42], considered a non-dilute composite of many identical ellipsoidal particles that cause the matrix to experience an average stress different from the applied stress. The volume average stress over the entire composite was forced to equal the applied stress to satisfy equilibrium conditions. Tandon and Weng [44] used this assumption together with Eshelby's solution to derive complete analytical solutions for the elastic moduli of an isotropic matrix filled with aligned ellipsoidal inclusions. The relative tensile modulus when the direction of the applied load is parallel to the major axes of the inclusions is

$$\frac{E_{\parallel}^{M-T}}{E_m} = \frac{A}{A + \phi[A_1 + 2\nu_m A_2]} \tag{1}$$

and the relative modulus when the direction of the applied load is perpendicular to the major axes of the inclusions is

$$\frac{E_{\perp}^{M-T}}{E_m} = \frac{2A}{2A + \phi[-2\nu_m A_3 + (1-\nu_m)A_4 + (1+\nu_m)A_5 A]} \tag{2}$$

where ϕ is the volume fraction of filler, ν_m is Poisson's ratio of the matrix, and A, A_1, A_2, A_3, A_4, A_5, are functions of Eshelby's tensor and the properties of the filler and the matrix, specifically Young's modulus, Poisson's ratio, filler concentration, and filler aspect ratio (a) (see Appendices A and B) [44].

For composites based on fiber-shaped inclusions, the tensile modulus in the FD is calculated using Eq. (1), $E_{FD} = E_{\|}$, and the modulus in the normal direction (ND) and the TD is calculated using Eq. (2), $E_{ND} = E_{TD} = E_{\perp}$. For composites based on disk-shaped inclusions, the tensile modulus in the FD and the TD is calculated using Eq. (2), $E_{FD} = E_{TD} = E_{\perp}$, and the modulus in the ND is calculated using Eq. (1), $E_{ND} = E_{\|}$.

Lee model

The Lee model employs the same assumptions and procedures used in the Mori-Tanaka average stress theory to derive the coefficients of thermal expansion (CTE). The linear CTE parallel to the major axis direction is

$$\frac{\alpha_{\|}^{L}}{\alpha_{\mathrm{m}}} = 1 + \phi \frac{D_4(2B_2 - B_4 - B_5)}{(2B_2B_3 - B_1B_4 - B_1B_5)} \tag{3}$$

and the CTE perpendicular to the major axes of the inclusions is

$$\frac{\alpha_{\perp}^{L}}{\alpha_{\mathrm{m}}} = 1 + \phi \frac{D_4(B_3 - B_1)}{(2B_2B_3 - B_1B_4 - B_1B_5)} \tag{4}$$

where ϕ is the volume fraction of filler, and B_1, B_2, B_3, B_4, B_5, and D_4 are functions of Eshelby's tensor and the properties of the filler and the matrix, specifically Young's modulus, Poisson's ratio, filler concentration, and filler aspect ratio (a) (see Appendices A and B) [45].

For composites based on fiber-shaped inclusions, the CTE in the FD is calculated using Eq. (3), $\alpha_{FD} = \alpha_{\|}$, and the CTE in the ND and the TD is calculated using Eq. (4), $\alpha_{ND} = \alpha_{TD} = \alpha_{\perp}$. The bulk CTE is

$$\gamma = \alpha_{FD} + 2\alpha_{ND} \tag{5}$$

For composites based on disk-shaped inclusions, the CTE in the FD and the TD is calculated using Eq. (4), $\alpha_{FD} = \alpha_{TD} = \alpha_{\perp}$, and the CTE in the ND is calculated using Eq. (3), $\alpha_{ND} = \alpha_{\|}$. The bulk CTE is

$$\gamma = 2\alpha_{FD} + \alpha_{ND} \tag{6}$$

Chow model

The Chow model treats the fillers as aligned ellipsoidal particles characterized by the ratio of the major to the minor axes [46, 47]. The relative tensile modulus when the direction of the applied load is parallel to the major axes of the inclusions is

$$\frac{E_{\|}^{Ch}}{E_{\mathrm{m}}} = 1 + \frac{(k_f/k_m - 1)G_1 + 2(\mu_f/\mu_m - 1)K_1}{2K_1G_3 + G_1K_3}\phi \tag{7}$$

and the relative modulus when the direction of the applied load is perpendicular to the major axes of the inclusions is

$$\frac{E_{\perp}^{Ch}}{E_{\mathrm{m}}} = 1 + \frac{(k_f/k_m - 1)G_3 + (\mu_f/\mu_m - 1)(G_3\xi + K_1\zeta)}{2K_1G_3 + G_1K_3}\phi \tag{8}$$

where ϕ is the volume fraction of filler, and k_f and k_m are the bulk modulus and μ_f and μ_m are the shear modulus of the filler and matrix, respectively. Other parameters used are defined in Appendix C.

For composites based on fiber-shaped inclusions, the modulus in the FD is calculated using Eq. (7), $E_{\mathrm{FD}} = E_{\|}$, and the modulus in the ND and the TD is calculated using Eq. (8), $E_{\mathrm{ND}} = E_{\mathrm{TD}} = E_{\perp}$. For composites based on disk-shaped inclusions, the modulus in the FD and the TD is calculated using Eq. (8), $E_{\mathrm{FD}} = E_{\mathrm{TD}} = E_{\perp}$, and the modulus in the ND is calculated using Eq. (7), $E_{\mathrm{ND}} = E_{\|}$.

The CTE parallel to the major axes of the inclusions is

$$\frac{\alpha_{\parallel}^{Ch}}{\alpha_{\mathrm{m}}} = 1 + \frac{k_f}{k_m} \frac{(\gamma_f - \gamma_m)\tilde{G}_1}{2\tilde{K}_1\tilde{G}_3 + \tilde{G}_1\tilde{K}_3} \frac{\phi}{\alpha_{\mathrm{m}}} \tag{9}$$

and the CTE perpendicular to the major axes of the inclusions is

$$\frac{\alpha_{\perp}^{Ch}}{\alpha_{\mathrm{m}}} = 1 + \frac{k_f}{k_m} \frac{(\gamma_f - \gamma_m)\tilde{G}_3}{2\tilde{K}_1\tilde{G}_3 + \tilde{G}_1\tilde{K}_3} \frac{\phi}{\alpha_{\mathrm{m}}} \tag{10}$$

where the parameters used are defined in Appendix C.

For composites based on fiber-shaped inclusions, the CTE in the FD is calculated using Eq. (9), $\alpha_{FD} = \alpha_{\parallel}$, and the CTE in the ND and the TD is calculated using Eq. (10), $\alpha_{ND} = \alpha_{TD} = \alpha_{\perp}$. The bulk CTE is

$$\gamma = \alpha_{FD} + 2\alpha_{ND} \tag{11}$$

For composites based on disk-shaped inclusions, the CTE in the FD and the TD is calculated using Eq. (10), $\alpha_{FD} = \alpha_{TD} = \alpha_{\perp}$, and the CTE in the ND is calculated using Eq. (9), $\alpha_{ND} = \alpha_{\parallel}$. The bulk CTE is

$$\gamma = 2\alpha_{FD} + \alpha_{ND} \tag{12}$$

Filler parameters

In the model calculations, there are generally two ways of treating the organoclay particles. One is to assume good exfoliation (method 1) and treat the MMT platelets themselves as the reinforcing filler particles. In this case, $E_{\mathrm{p}} = E_{\mathrm{MMT}}$ = 178 GPa [37], ν = 0.20, and $\phi_{\mathrm{p}} = \phi_{\mathrm{MMT}} = 0.0163$ at 5 wt% MMT.

Because TEM analysis indicates good exfoliation is not achieved, the partially exfoliated clay particles, or tactoids, are considered to be parallel arrangements of MMT platelets and gallery material as described in previous reports [10, 32, 37, 41, 48, 49] (method 2). The tensile modulus of such an effective particle is often assumed to be given by the following rule of mixtures

$$E_{\mathrm{p}} = \mathrm{v}_{\mathrm{MMT}} E_{\mathrm{MMT}} + \mathrm{v}_{\mathrm{gallery}} E_{\mathrm{gallery}} \tag{13}$$

where v_{MMT} and v_{gallery} are the volume fraction of montmorillonite and of the gallery space in the effective particle, while E_{MMT} and E_{gallery} are their corresponding moduli. The volume fraction of MMT platelets in the particle, v_{MMT}, is calculated as the ratio of the thickness of an individual platelet and the *d*-spacing (2.42 nm) of the nanocomposite as determined by the WAXS analysis

$$v_{\mathrm{MMT}} = \frac{t_{\mathrm{platelet}}}{d_{001}} \tag{14}$$

Considering that the modulus of the organic material in the gallery is significantly smaller than the modulus of the MMT platelets, Eq. (13) reduces to

$$E_{\mathrm{p}} = v_{\mathrm{MMT}} E_{\mathrm{MMT}} \tag{15}$$

The volume fraction of the filler particles in the composites can be estimated as

$$\phi_{\mathrm{p}} = \frac{\text{volume of MMT}}{\text{volume of nanocomposite}} \frac{\text{volume of filler particle}}{\text{volume of MMT}} = \frac{\phi_{\mathrm{MMT}}}{v_{\mathrm{MMT}}} \tag{16}$$

In this case, $E_{\mathrm{p}} = E_{\mathrm{Tact}} = 70.6$ GPa and $\phi_{\mathrm{p}} = 0.0411$ at 5 wt% MMT. The Poisson's ratios of the matrix, ν_{m}, and of the organoclay, ν_{p}, are assumed to be 0.35 and 0.20 respectively [37, 50, 51]. The Poisson's ratio of the tactoids is estimated to be 0.29 by using a simple rule of mixtures similar to Eq. (13). The models are insensitive to the Poisson's ratio of the matrix within the range of 0.35 – 0.42 and to the Poisson's ratio of the organoclay within the range of 0.20 and 0.30.

It should be noted that all the composite models discussed here assume that the filler particles are isotropic, which is clearly not the case for organoclay tactoids where, in all likelihood, the modulus is lower in the direction perpendicular to the MMT platelets than the above estimate that considers forces acting parallel to the platelets. The CTE of the tactoids are, on the other hand, likely to be higher in the direction perpendicular to the platelets than parallel to them. Such effects are possibly important in making predictions of composite properties and their directional dependence.

Two-population models

The above models are generally used for a single-filler population in a matrix. However, the composites of interest here consist of both organoclay and elastomer particles. These particles have different effects on the mechanical properties of the composites, and separate methods are needed to predict their contributions to the properties of the composite. When both components exist in a single nanocomposite, they must be considered separately to accurately predict the experimental modulus. Recently, similar approaches based on these concepts for treating exfoliated single MMT platelets and intercalated tactoids [29] and for treating organoclay particles and glass fibers [30] as separate populations have been reported. A similar two-population approach was used here to model the combined effects of the organoclay particles and the elastomer particles in these composites.

A two-population model can be thought of in terms of an *additive* approach or a *multiplicative* approach. To keep the nomenclature consistent in describing these models, E_m and α_m are the modulus and CTE of the PP/PP-*g*-MA matrix, E_{nano} and α_{nano} are the modulus and CTE calculated for the PP/PP-*g*-MA/MMT nanocomposites, E_{TPO} and α_{TPO} are the modulus and CTE calculated for the PP/EOR blends, and E_C and α_C are the modulus and CTE calculated for the PP/PP-*g*-MA/EOR/MMT nanocomposites. In the *additive* approach, the contributions of each component are calculated separately and summed together without double counting the matrix contribution as follows

$$\frac{(E_C)_{add}}{E_m} = \frac{E_{nano}}{E_m} + \frac{E_{TPO}}{E_m} - 1 \tag{17}$$

$$\frac{(\alpha_C)_{add}}{\alpha_m} = \frac{\alpha_{nano}}{\alpha_m} + \frac{\alpha_{TPO}}{\alpha_m} - 1 \tag{18}$$

Specific details of this approach and its application for predicting the stiffness behavior of nanocomposites containing a mixture of single platelets and tactoids are given in a prior publication [29].

There are two different ways to apply the *multiplicative* approach. In one, the contribution of the clay is calculated first and the nanocomposite is then considered to be the matrix for the elastomer particles. The effect of the elastomer is calculated using the calculated modulus (E_{nano}) and CTE (α_{nano}) of the clay nanocomposite as the matrix properties rather than those of the neat polymer matrix. The contributions of the components are multiplied as follows

$$\frac{(E_C)_{mult}}{E_m} = \frac{E_{nano}}{E_m} \cdot \frac{E_C}{E_{nano}} \tag{19}$$

$$\frac{(\alpha_C)_{mult}}{\alpha_m} = \frac{\alpha_{nano}}{\alpha_m} \cdot \frac{\alpha_C}{\alpha_{nano}} \tag{20}$$

In the other approach, the contribution of the elastomer is calculated first and the TPO is then considered to be the matrix to which the organoclay is added. The effect of the organoclay is calculated using the calculated modulus (E_{TPO}) and CTE (α_{TPO}) of the TPO as the matrix properties rather than those of the neat polymer matrix. The contributions of the components are multiplied as follows

$$\frac{(E_C)_{mult}}{E_m} = \frac{E_C}{E_{TPO}} \cdot \frac{E_{TPO}}{E_m} \tag{21}$$

$$\frac{(\alpha_C)_{mult}}{\alpha_m} = \frac{\alpha_C}{\alpha_{TPO}} \cdot \frac{\alpha_{TPO}}{\alpha_m} \tag{22}$$

For simplicity, the first *multiplicative* approach is used in all the modeling presented in this work. The second *multiplicative* approach gives similar results.

The contributions to the relative modulus of the organoclay and the elastomer are calculated by substituting the appropriate particle parameters into the proper equations for each model as described above. Table 5.6 lists pertinent physical property data for the composite materials investigated in this work [3, 4, 8-10, 37, 50, 51].

Table 5.6: Materials properties used in models [3, 4, 8-10, 37, 50, 51]

Components	Modulus (GPa)	Bulk CTE x 10^5 (K^{-1})	Density (g/cm^3)	Poisson's ratio
PP / PP-*g*-MA	1.51	30.5	0.90	0.35
TPO (Lee)	0.81	52.0	0.89	0.395^a
TPO (Kim)	0.78	43.3	0.89	0.387^a
EOR	0.0076	75.6	0.854	0.499
MMT: Platelet	178	0.5	2.83	0.20
Tactoid	70.6^a	0.5	1.67^a	0.29^a

^{a} Calculated using rule of mixtures.

Another alternative is to calculate the effect of the organoclay on the TPO blend matrix by using the experimental parameters for the organoclay and the TPO in the single population models. Likewise the effect of elastomer addition on the PP/PP-*g*-MA nanocomposites can be calculated using the experimental parameters for the elastomer and the PP/PP-*g*-MA nanocomposites in the single population models.

COMPARISON OF EXPERIMENTAL DATA AND MODELING RESULTS

Single-population model comparisons

Before attempting to model composites containing both MMT and EOR, it is important to examine PP/PP-*g*-MA/MMT and PP/EOR systems. Figures 5.3 and 5.4 compare the relative modulus predictions from the Mori-Tanaka and Chow models and the normalized CTE predictions from the Lee and Chow models with experimental data [3, 8] for PP/PP-*g*-/MMT composites and PP/EOR blends, respectively. Figure 5.3(a) indicates there is little difference between the relative modulus predictions from the

Mori-Tanaka and Chow models for MMT nanocomposites. Figure 5.4(a), however, shows that the relative modulus predictions for PP/EOR blends by the Mori-Tanaka model are significantly lower than the Chow predictions and better match the experimental trend with increasing EOR content. Thus, the Mori-Tanaka model was selected for all subsequent modulus predictions.

Similarly, Figure 5.3(b) reveals little difference between the normalized CTE predictions from the Lee and Chow models for MMT nanocomposites, while Figure 5.4(b) indicates that the normalized CTE predictions for PP/EOR blends by the Chow model are significantly higher than the Lee predictions and better fit the experimental trend with increasing EOR content. Thus, the Chow model was selected for all subsequent CTE predictions.

(a)

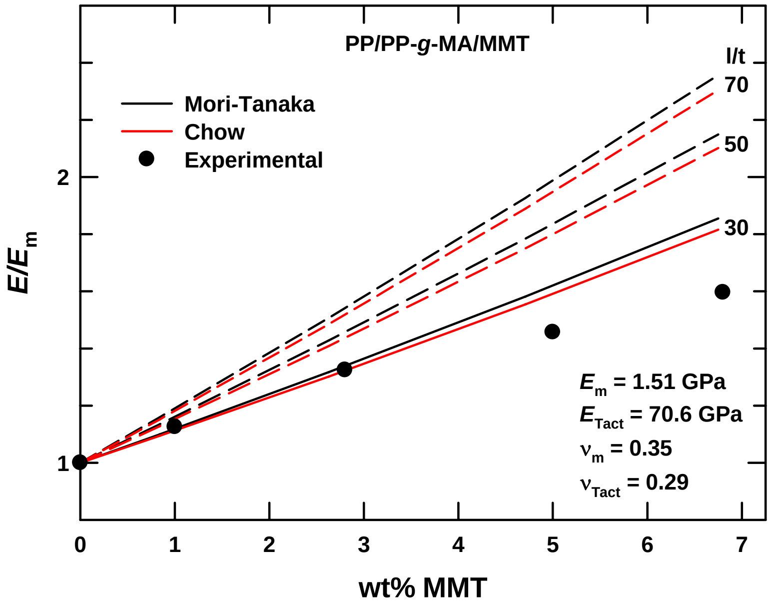

(b)

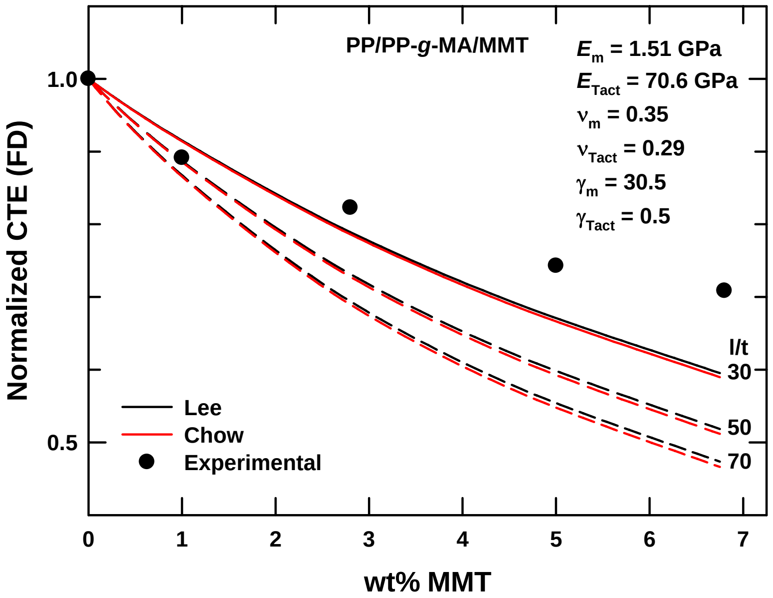

Figure 5.3: Comparison of relative modulus predictions from the Mori-Tanaka and Chow models (a) and comparison of normalized CTE predictions from the Lee and Chow models (b) for PP/PP-*g*-MA/MMT nanocomposites versus wt% MMT using MMT aspect ratios of 30, 50, and 70. The experimental data are from Lee et al. [3, 8]; Table 1 shows the experimentally determined aspect ratios of the MMT tactoids.

(a)

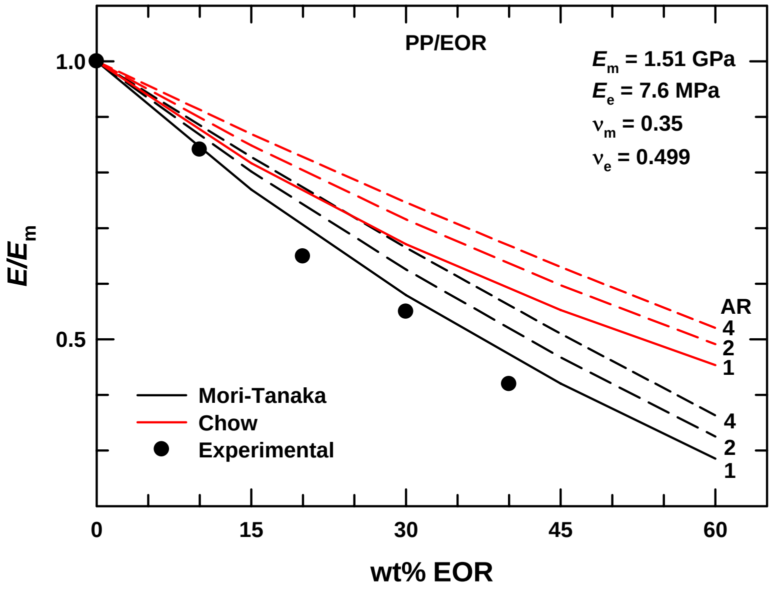

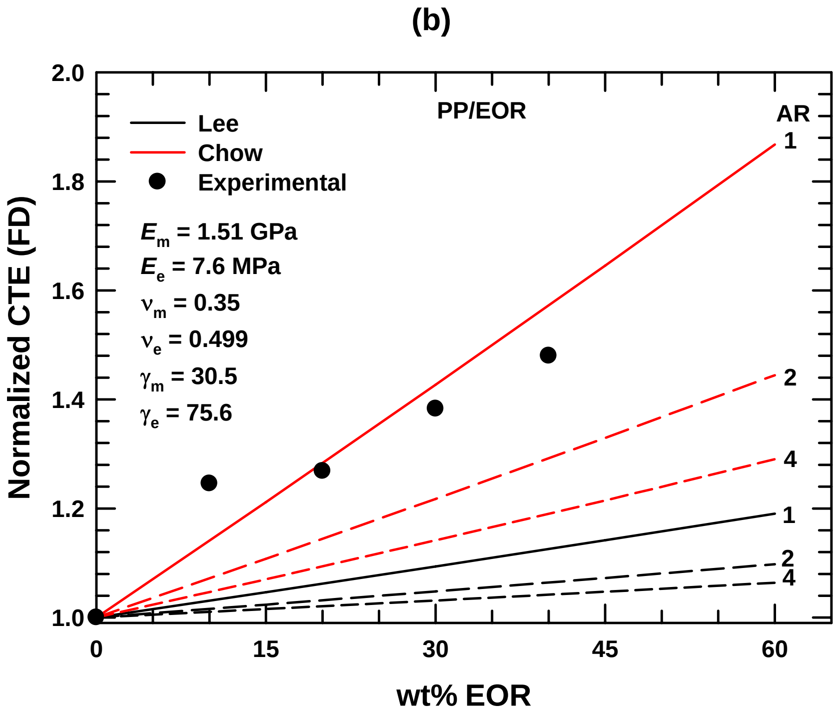

Figure 5.4: Comparison of relative modulus predictions from the Mori-Tanaka and Chow models (a) and comparison of normalized CTE predictions from the Lee and Chow models (b) for PP/ EOR blends versus wt% EOR using EOR aspect ratios of 1, 2, and 4. The experimental data are from Lee et al. [3, 8] ; Table 1 shows the experimentally determined aspect ratios of the EOR particles.

Although the relative modulus predictions shown in Figure 5.3(a) for PP/PP-*g*-MA/MMT composites over the range of experimental aspect ratios (31-63) match the general experimental trends, they overestimate the composite modulus. Similarly, the normalized CTE predictions shown in Figure 5.3(b) for PP/PP-*g*-/MMT composites match the general experimental trends, but they underestimate the thermal expansion coefficient. These discrepancies may result from incomplete particle alignment or overestimation of the tactoid modulus by Eq. 15.

Figure 5.5 shows comparisons between the experimental results of Lee et al. [3, 8] and Mori-Tanaka predictions using experimental aspect ratios and tactoid moduli (E_{Tact}) of 70.6, 32, and 13.5 GPa for PP/PP-*g*-MA/MMT composites. The predictions using a tactoid modulus of 70.6 GPa determined using the rule of mixtures (Eq. 15) overestimate the relative modulus and underestimate the normalized CTE in the FD. Although in a previous work an adjusted E_{Tact} of 13.5 GPa enabled better modulus predictions for HDPE-based nanocomposites [29], the predictions using this E_{Tact} underestimate the relative modulus and overestimate the normalized CTE in the FD . An adjusted E_{Tact} of 32 GPa gives a much better fit of the experimental relative modulus and normalized CTE in the FD. Figure 5.6 also indicates that an adjusted E_{Tact} of 32 GPa results in the best fit of the experimental relative modulus and normalized CTE trends reported by Kim et al. [10]. The lower apparent modulus for the tactoids suggests that Eq. (15) overestimates the stress transfer between platelets in the tactoids. Figure 5.5(c), however, indicates that the E_{Tact} of 70.6 GPa best matches the experimental normalized CTE in the ND. The model assumes that the tactoids are isotropic, when, in reality, they are not as mentioned in Section 2.4. This fact may play some role in these comparisons.

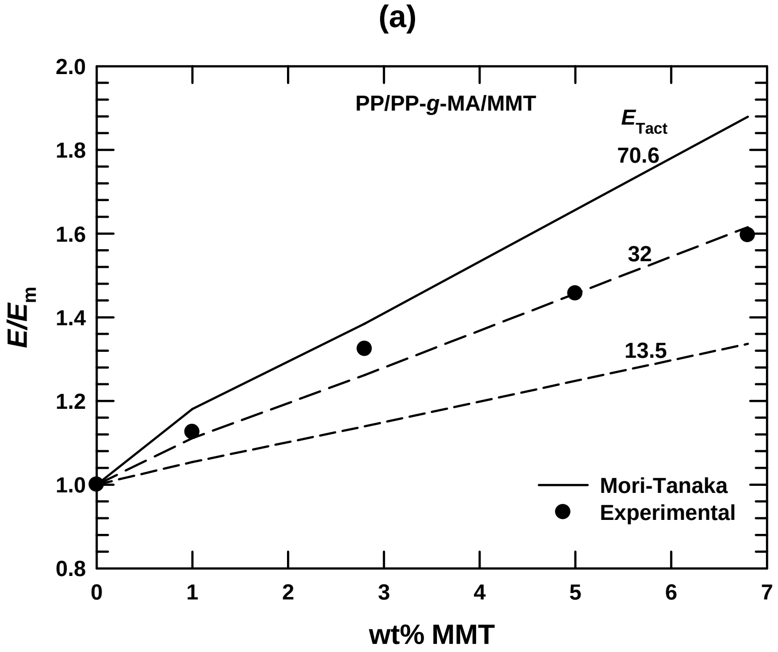

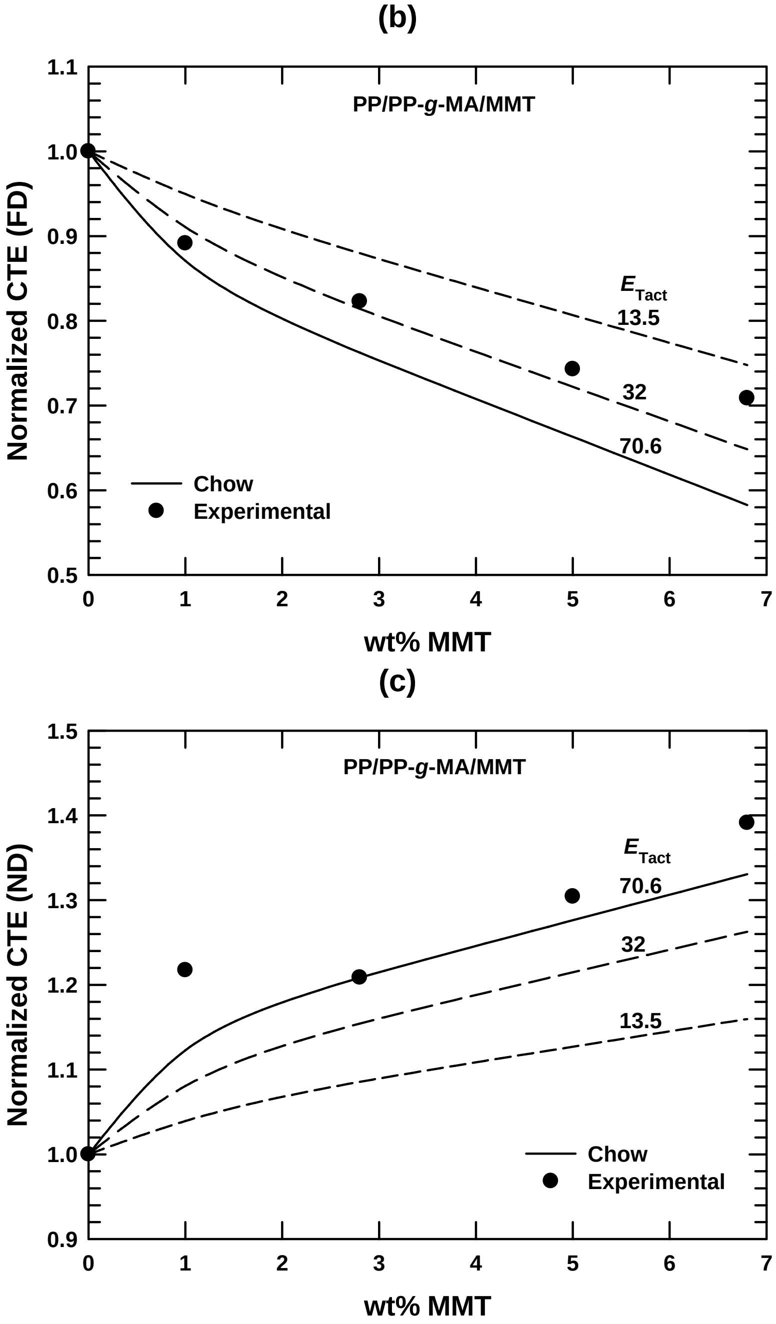

Figure 5.5: Comparison of the relative modulus predictions from the Mori-Tanaka model (a) and comparisons of the normalized CTE predictions from the Chow model in the FD (b) and the ND (c) for PP/PP-g-MA/MMT nanocomposites versus wt% MMT using tactoid moduli of 70.6, 32, and 13.5 GPa. The experimental data are from Lee et al. [3, 8] ; Table 1 shows the experimentally determined aspect ratios of the MMT tactoids.

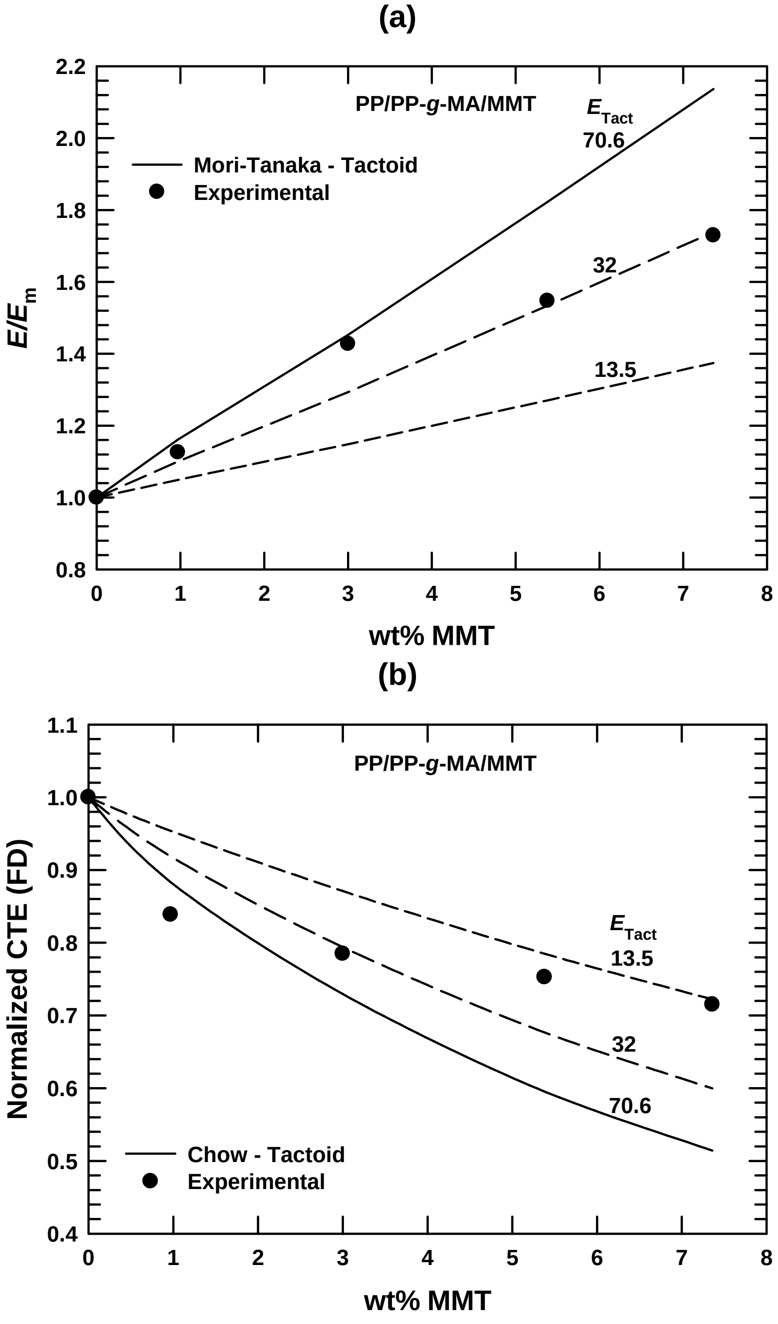

Figure 5.6: Comparison of the relative modulus predictions from the Mori-Tanaka model (a) and comparison of the normalized CTE in the FD predictions from the Chow model (b) for PP/PP-*g*-MA/MMT nanocomposites versus wt% MMT using tactoid moduli of 70.6, 32, and 13.5 GPa. The experimental data are from Kim et al. [10]; Table 2 shows the experimentally determined aspect ratios of the MMT tactoids.

For PP/EOR blends, the Mori-Tanaka predictions using an aspect ratio of 1.5 experimentally determined for a blend with 30 wt% EOR match the general experimental trends for relative modulus and normalized CTE in the FD with increasing elastomer content, as shown in Figure 5.7. However, the experimental relative modulus and normalized CTE in the FD are lower and higher than predicted, respectively. A much larger discrepancy is seen for the normalized CTE in the ND in Figure 5.7(c), where the predicted rate of increase in the CTE in the ND with increasing EOR content is much lower than the experimental trend. This result, coupled with the underestimation of the CTE in the ND in the PP/PP-*g*-MA/MMT composites, suggests that the Chow model is not adequately capturing the constraining effects of the MMT on the matrix and of the PP matrix on the EOR.

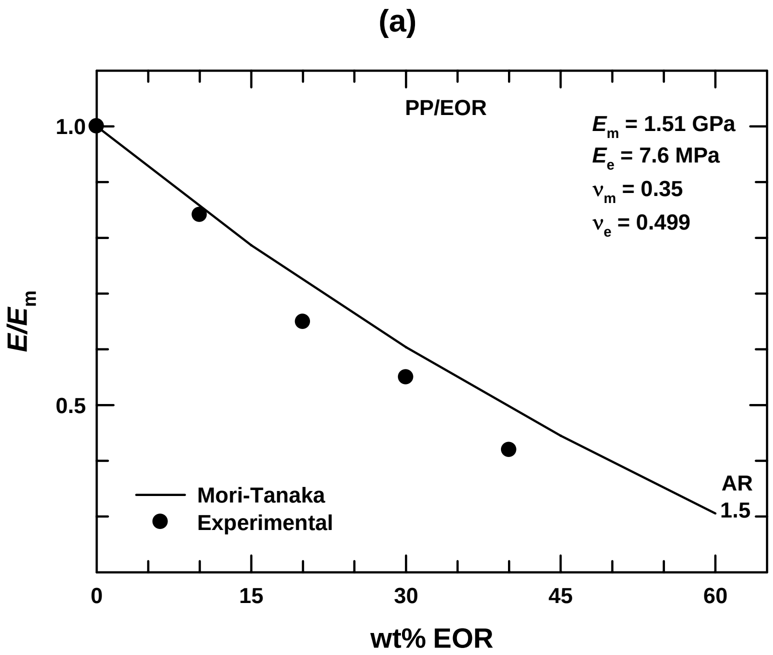

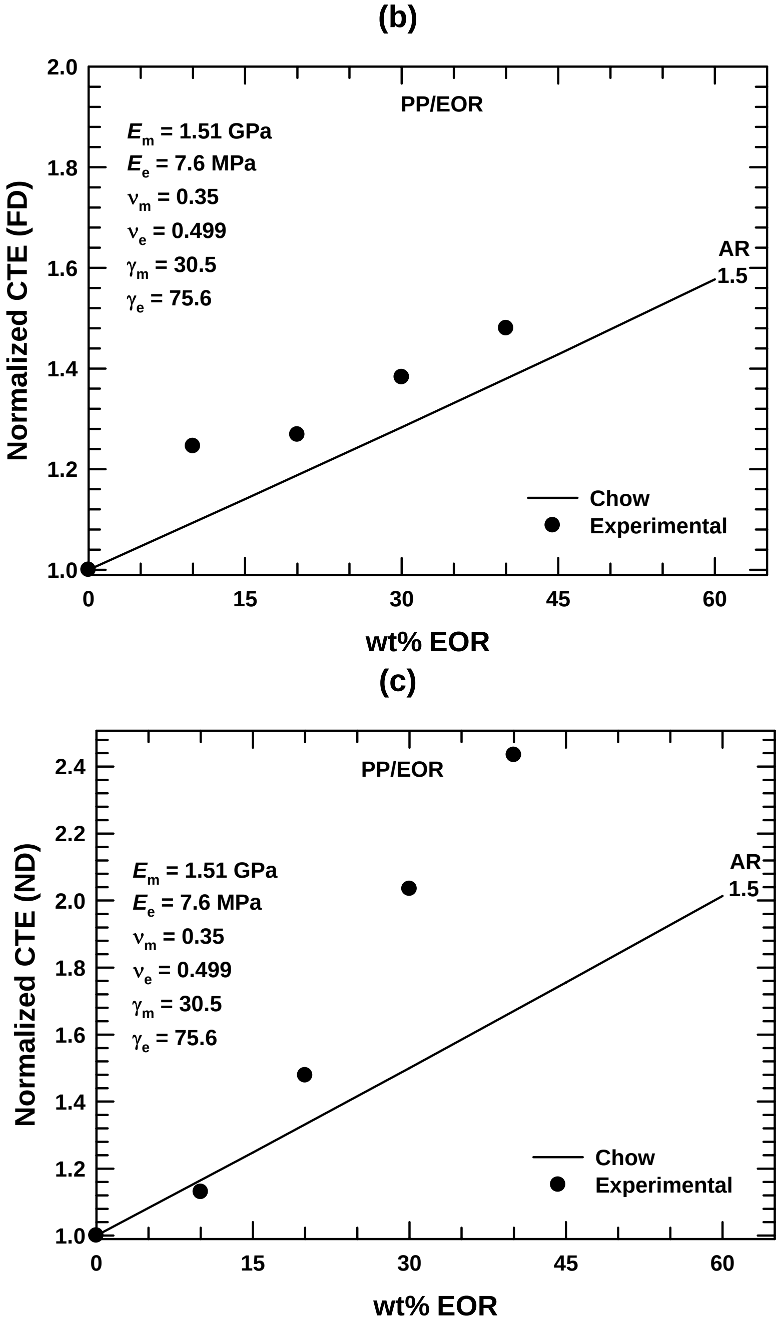

Figure 5.7: Comparison of relative modulus predictions from the Mori-Tanaka model (a) and comparisons of the normalized CTE predictions from the Chow model in the FD (b) and the ND (c) for PP/ EOR blends versus wt% EOR using an EOR aspect ratio of 1.5 with experimental data by Lee et al. [3, 8]; Table 1 shows the experimentally determined aspect ratios of the EOR particles.

Two-population model comparisons

When both EOR and MMT are added to a PP matrix, a two-population approach must be applied to predict the experimental properties. Figure 5.8 compares the *additive* and *multiplicative* approaches for predicting the modulus and the CTE in the FD of PP/PP-*g*-MA/EOR/MMT composites by the Mori-Tanaka and Chow models, respectively, using tactoid moduli of 70.6 and 32 GPa with experimental data by Lee et al. [3, 8]. The *multiplicative* approach, wherein the contribution of the clay is calculated first and the nanocomposite is then considered to be the matrix for the elastomer blend, appears to better match the experimental trend for modulus with increasing MMT, particularly for an E_{Tact} of 32 GPa. The slightly higher modulus predictions can be attributed to the tendency of the model to underestimate the modulus reduction upon addition of EOR, as shown in Figure 5.5(a).

(a)

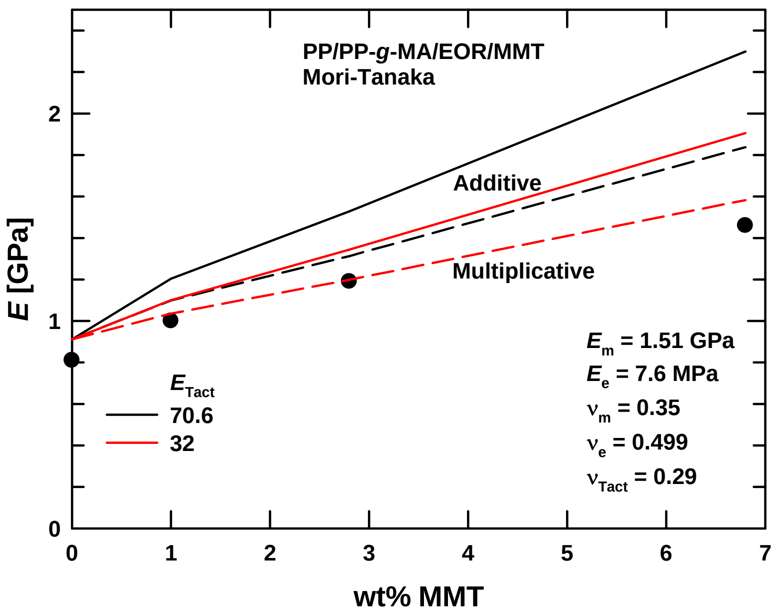

(b)

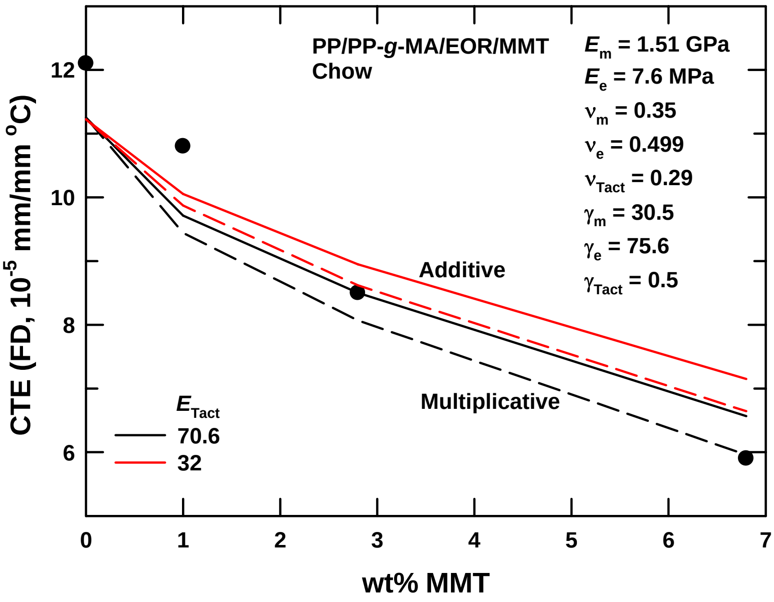

Figure 5.8: Comparisons of the *additive* and *multiplicative* two-population approaches for predicting the modulus (a) and the CTE in the FD (b) by the Mori-Tanaka and Chow models, respectively, for PP/PP-*g*-MA/EOR/MMT nanocomposites versus wt% MMT using tactoid moduli of 70.6 and 32 GPa. The experimental data are from Lee et al. [3, 8]; Table 1 shows the experimentally determined aspect ratios used in the calculations.

Similarly, the discrepancy in Figure 5.8(b) between the predicted and experimental CTE in the FD at 0 wt% MMT is due to the model's underestimation of the CTE increase upon EOR addition, as shown in Figure 5.5(b). As with the modulus predictions, the *multiplicative* approach gives better agreement with the experimental trend for CTE with increasing MMT. However, for the CTE, an E_{Tact} of 70.6 GPa gives a better match with the experimental trend. The models seem to better capture the effects of the addition of MMT than those of the addition of EOR.

Figure 5.9 compares the models for predicting either the effect of the MMT tactoids on the experimental TPO using Eq. 21 and 22 (TPO/tactoid approach) or the effect of the EOR particles on the experimental nanocomposites using Eq. 19 and 20 (nanocomposite/EOR approach) with experimental data from Lee et al. [3, 8]. Both approaches match the experimental trends fairly well. The nanocomposite/EOR approach consistently overestimates the composite modulus, but agrees well with the rate of increase upon MMT addition. For the CTE in the FD, the nanocomposite/EOR approach underestimates the increase in CTE due to the EOR and underestimates the rate of decrease with increasing MMT. The TPO/tactoid approach best matches the experimental trends. For relative modulus, an E_{Tact} of 70.6 GPa fits best at low MMT levels, while an E_{Tact} of 32 GPa matches the experimental data best at high MMT loadings. Setting E_{Tact} = 70.6 GPa fits the experimental CTE in the FD trend best, while E_{Tact} = 32 GPa better matches the experimental CTE in the ND trend.

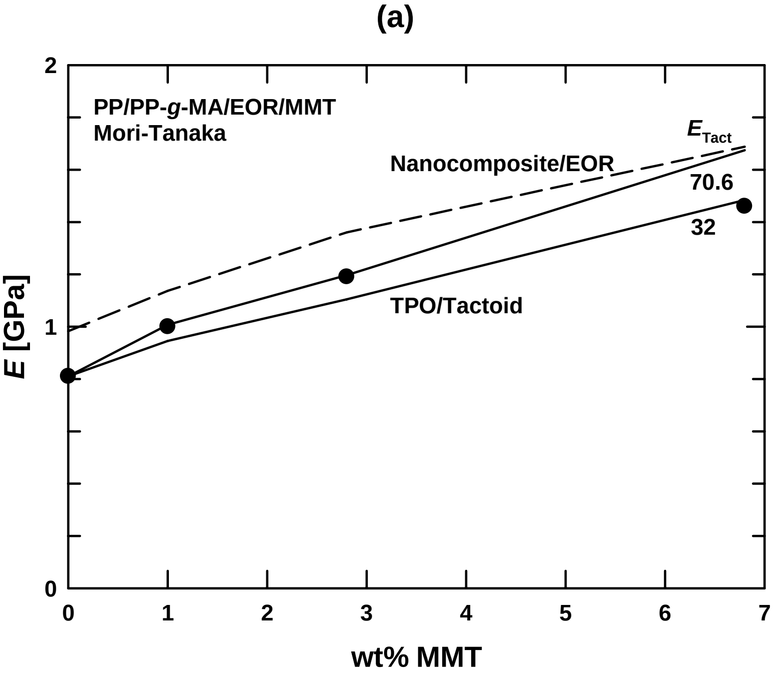

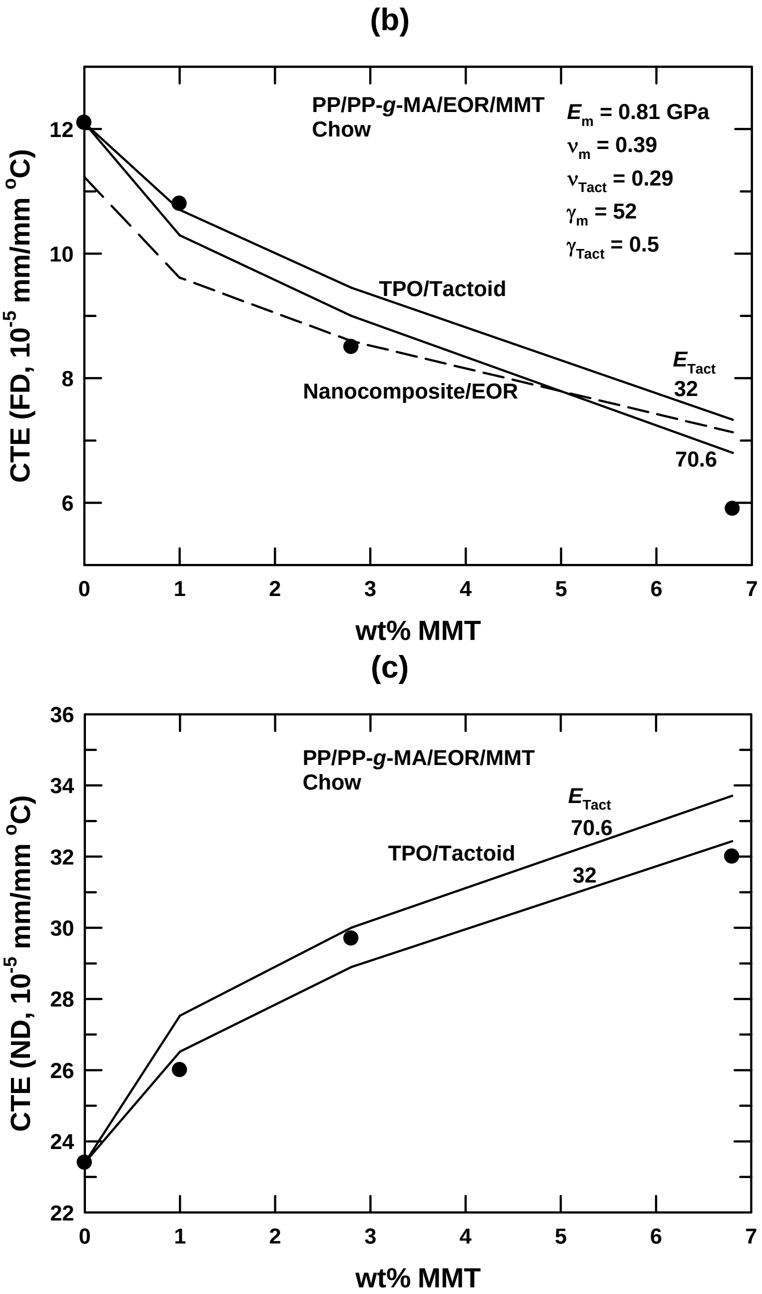

Figure 5.9: Comparison of the modulus predictions from the Mori-Tanaka model (a) and comparisons of the CTE predictions from the Chow model in the FD (b) and the ND (c) for PP/PP-*g*-MA/EOR/MMT nanocomposites versus wt% MMT using tactoid moduli of 70.6 and 32 GPa with experimental data by Lee et al. [3, 8]; Table 1 shows the experimentally determined aspect ratios used in the calculations. The composites are modeled as either nanocomposites filled with EOR or as a TPO filled with MMT tactoids.

Because Kim et al. used a commercial TPO with unspecified elastomer content and properties, a TPO/tactoid model is needed to describe these composites. Figure 5.10 compares the predictions treating the composite as a TPO filled with MMT tactoids (using Eq. 21 and 22) with experimental data from Kim et al. [4, 9]. An E_{Tact} of 70.6 GPa best fits the experimental modulus and CTE in the FD trends with increasing MMT.

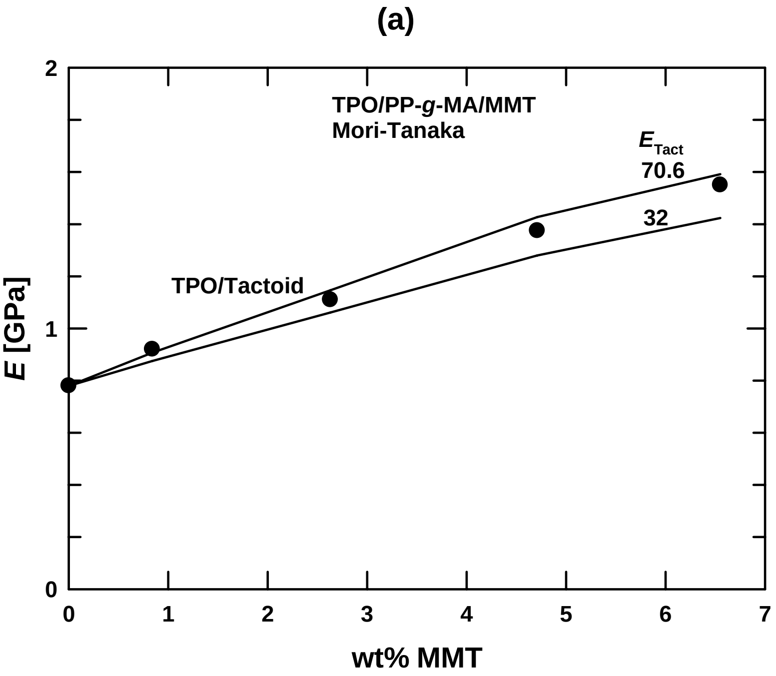

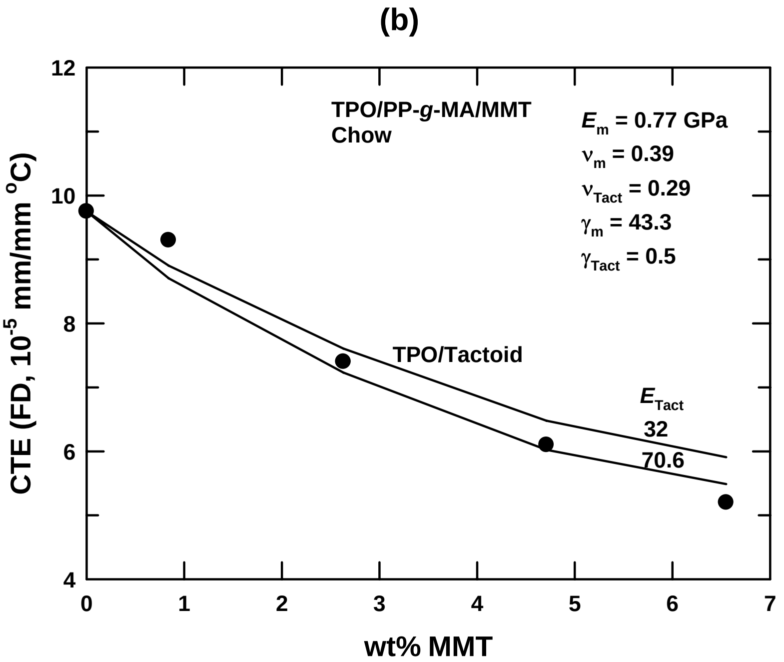

Figure 5.10: Comparisons of the modulus predictions from the Mori-Tanaka model (a) and of the CTE predictions from the Chow model in the FD (b) for PP/PP-*g*-MA/EOR/MMT nanocomposites versus wt% MMT treating the composites as a TPO filled with MMT tactoids with moduli of 70.6 or 32 GPa with experimental data by Kim et al. [4, 9] ; Table 3 shows the experimentally determined aspect ratios used in the calculations.

CONCLUSIONS

The Mori-Tanaka, Lee, and Chow composite models were used to predict the modulus and CTE of PP/PP-*g*-MA/MMT nanocomposites and PP/EOR blends. The Mori-Tanaka and Chow model predictions best match the experimental trends. Although the predictions for PP/PP-*g*-MA/MMT nanocomposites using a tactoid modulus of 70.6 GPa overestimate the modulus and underestimate the CTE in the FD, an adjusted E_{Tact} of 32 GPa matches the experimental data well. The predictions for PP/EOR blends overestimate the modulus and underestimate the CTE in the FD. In both systems, the predictions underestimate the CTE in the ND, suggesting the Chow model does not adequately capture the constraining effects of the MMT on the matrix and of the PP matrix on the EOR.

Various ternary-phase approaches were used to predict the modulus and CTE of PP/PP-*g*-MA/EOR/MMT nanocomposites. A *multiplicative* approach, wherein the contribution of the clay is calculated first and the nanocomposite is then considered to be the matrix for the elastomer blend, best matches the experimental trends. The models better capture the effects of the MMT than those of the EOR.

Models predicting the effect of the MMT tactoids on the experimental TPO (using Eq. 21 and 22) or the effect of the EOR particles on the experimental nanocomposites (using Eq. 19 and 20) were also used. The TPO/tactoid approach that predicts the effect of the MMT tactoids on the experimental TPO best matches the experimental trends. This TPO/tactoid model gives rather good quantitative agreement between the predicted values of modulus and CTE calculated using the experimentally determined aspect ratios and those measured experimentally for TPO nanocomposites.

REFERENCES

1. Fornes TD, Yoon PJ, Hunter DL, Keskkula H, and Paul DR. Polymer 2002;43(22):5915-5933.
2. Giannelis EP. Applied Organometallic Chemistry 1998;12(10-11):675-680.
3. Lee H-S, Fasulo PD, Rodgers WR, and Paul DR. Polymer 2005;46(25):11673-11689.
4. Kim DH, Fasulo PD, Rodgers WR, and Paul DR. Polymer 2007;48(20):5960-5978.
5. Bharadwaj RK. Macromolecules 2001;34(26):9189-9192.
6. Messersmith PB and Giannelis EP. Journal of Polymer Science Part A: Polymer Chemistry 1995;33(7):1047-1057.
7. Yano K, Usuki A, Okada A, Kurauchi T, and Kamigaito O. Journal of Polymer Science Part A: Polymer Chemistry 1993;31(10):2493-2498.

8. Lee H-s, Fasulo PD, Rodgers WR, and Paul DR. Polymer 2006;47(10):3528-3539.

9. Kim DH, Fasulo PD, Rodgers WR, and Paul DR. Polymer 2008;49(10):2492-2506.

10. Kim DH, Fasulo PD, Rodgers WR, and Paul DR. Polymer 2007;48(18):5308-5323.

11. Gilman JW. Applied Clay Science 1999;15(1-2):31-49.

12. Gilman JW, Kashiwagi T, Brown JET, Lomakin S, Giannelis EP, and Manias E. Int. SAMPE Symp. Exhibit. 1998;43:1053.

13. Bourbigot S, Le Bras M, Dabrowski F, Gilman JW, and Kashiwagi T. Fire and Materials 2000;24(4):201-208.

14. Hotta S and Paul DR. Polymer 2004;45(22):7639-7654.

15. Shah RK, Hunter DL, and Paul DR. Polymer 2005;46(8):2646-2662.

16. Hasegawa N, Kawasumi M, Kato M, Usuki A, and Okada A. Journal of Applied Polymer Science 1998;67(1):87-92.

17. Kawasumi M, Hasegawa N, Kato M, Usuki A, and Okada A. Macromolecules 1997;30:6333–6338.

18. Varela C, Rosales C, Perera R, Matos M, Poirier T, Blunda J, and Rojas H. Polymer Composites 2006;27(4):451-460.

19. López-Quintanilla ML, Sánchez-Valdés S, Ramos de Valle LF, and Guedea Miranda R. Polymer Bulletin 2006;57(3):385-393.

20. Galgali G, Ramesh C, and Lele A. Macromolecules 2001;34(4):852-858.

21. Reichert P, Nitz H, Klinke S, Brandsch R, Thomann R, and Mülhaupt R. Macromolecular Materials and Engineering 2000;275(1):8-17.

22. Cui L and Paul DR. Polymer 2007;48(6):1632-1640.

23. Lertwimolnun W and Vergnes B. Polymer 2005;46(10):3462-3471.

24. Ou Y-C, Guo T-T, Fang X-P, and Yu Z-Z. Journal of Applied Polymer Science 1999;74(10):2397-2403.

25. Premphet-Sirisinha K and Preechachon I. Journal of Applied Polymer Science 2003;89(13):3557-3562.

26. Long Y and Shanks RA. Journal of Applied Polymer Science 1996;62(4):639-646.

27. Jang BZ, Uhlmann DR, and Sande JBV. Journal of Applied Polymer Science 1985;30(6):2485-2504.

28. Mehta S, Mirabella FM, Rufener K, and Bafna A. Journal of Applied Polymer Science 2004;92(2):928-936.

29. Spencer MW, Cui L, Yoo Y, and Paul DR. Polymer 2010;51(5):1056-1070.

30. Yoo Y, Spencer MW, and Paul DR. Polymer 2011;52(1):180-190.

31. Hine PJ, Rudolf Lusti H, and Gusev AA. Composites Science and Technology 2002;62(10-11):1445-1453.

32. Cui L, Ma X, and Paul DR. Polymer 2007;48(21):6325-6339.

33. Halpin JC and Kardos JL. Polymer Engineering & Science 1976;16(5):344-352.

34. Hill R. Journal of the Mechanics and Physics of Solids 1965;13(4):213-222.

35. Halpin J. J. Compos. Mater. 1969;3:732.

36. Hill R. Proc. Phys. Soc., London 1952;65A:349-354.

37. Fornes TD and Paul DR. Polymer 2003;44(17):4993-5013.

38. Stretz HA, Paul DR, Li R, Keskkula H, and Cassidy PE. Polymer 2005;46(8):2621-2637.

39. Chavarria F and Paul DR. Polymer 2004;45(25):8501-8515.

40. Cui L, Troeltzsch C, Yoon PJ, and Paul DR. Macromolecules 2009;42(7):2599-2608.

41. Shah RK, Kim DH, and Paul DR. Polymer 2007;48(4):1047-1057.

42. Mori T and Tanaka K. Acta Metallurgica 1973;21(5):571-574.

43. Eshelby JD. Proceedings of the Royal Society of London. Series A. Mathematical and Physical Sciences 1957;241(1226):376-396.

44. Tandon GP and Weng GJ. Polymer Composites 1984;5(4):327-333.

45. Lee KY, Kim KH, Jeoung SK, Ju SI, Shim JH, Kim NH, Lee SG, Lee SM, Lee JK, and Paul DR. Polymer 2007;48(14):4174-4183.

46. Chow TS. Journal of Polymer Science: Polymer Physics Edition 1978;16(6):967-970.

47. Chow TS. Journal of Polymer Science: Polymer Physics Edition 1978;16(6):959-965.

48. Sheng N, Boyce MC, Parks DM, Rutledge GC, Abes JI, and Cohen RE. Polymer 2004;45(2):487-506.

49. Brune DA and Bicerano J. Polymer 2002;43(2):369-387.

50. Hui CY and David S. Polymer Engineering & Science 1998;38(5):774-782.

51. van Es M, Xiqiao F, van Turnhout J, and van der Giessen E. Comparing polymer–clay nanocomposites with conventional composites using composite modeling. In: Al-Malaika S, Golovoy A, and Wilkie C, editors. Specialty polymer additives: principles and applications. London: Blackwell Science, 2001. pp. Chapter 21.

Chapter 6: Effect of acid neutralization on the properties of K^+ and Na^+ poly(ethylene-*co*-methacrylic acid) ionomers

Polymers with small mole fractions (< 15 mol%) of ionic groups covalently bonded to the polymer backbone are called ionomers [1-3]. Random copolymers of ethylene and methacrylic acid where some of the acid groups (15 – 80%) are neutralized to form metal salts are a commercially important class of ionomers. The morphology of ionomers based on poly(ethylene-co-methacrylic acid) (EMAA) consists of three regions: amorphous phases, crystalline phases, and ionic clusters [4-6]. The ionic clusters act as thermoreversible crosslinks and improve the toughness, melt viscosity, clarity, and adhesion properties of the copolymer.

Various structural aspects of an ionomer matrix affect its properties, including the molecular weight, melt rheology (melt index), acid content, type of acid, type of neutralizing ion, and degree of neutralization. This chapter examines the effects of the type of neutralizing ion, the degree of neutralization, and the precursor melt index on the ionomer properties.

Many ionomers based on sodium cations (Na^+) are available commercially; they can be produced by a relatively simple neutralization process involving a ubiquitous cation and have advantageous properties, including excellent adhesion to glass. There has been recent interest in ionomers based on potassium cations (K^+) because of their higher affinity for water that gives rise to several interesting properties, including favorable antistatic properties.

This chapter explores the effects of the degree of neutralization of the acid groups and, to some extent, the precursor melt index on the properties of two series of EMAA ionomers; one is based on sodium cations, and the other is based on potassium cations.

Chapter 7 explores the extent of organoclay exfoliation and the properties of nanocomposites based on these two series of ionomers. The properties of the neat ionomers described here are used as a reference point when describing the nanocomposite properties.

EXPERIMENTAL

Materials

The experimental ionomers were based on EMAA copolymers containing 15 wt% of methacrylic acid. The series of sodium and potassium ionomers were prepared by extrusion neutralization of various ethylene-methacrylic acid base resins with different molecular weights (melt indices of 25, 60, and 200 g/10 min). These materials compose a wide range of both neutralization levels (from 14% to 60%) and melt indices (0.5 to 48 g/10 min) as shown in Table 2.1 in Chapter 2 and Figure 6.1; the data points for the base resin precursors are shown connected to those of the K^+ ionomers by dashed lines. Because both the melt index of the precursor and the degree of neutralization [7-9] affect the melt index of the ionomer, it is difficult to make ionomers with a constant melt index and varying neutralization levels, or vice versa.

Melt processing

The ionomers were dried in a vacuum oven at 50 °C for a minimum of 48 h prior to injection molding. Tensile specimens (ASTM D638, Type I) and Izod bars (ASTM D256) were prepared by an Arburg Allrounder 305-210-700 injection-molding machine using a barrel temperature of 200 – 225 °C, a mold temperature of 25 °C, an injection speed of 34 mm/s, an injection pressure of 55 – 65 bar, and a holding pressure of 50 – 55 bar. After molding, the samples were immediately sealed in polyethylene bags and placed in a vacuum desiccator for 21 days prior to testing, unless otherwise specified.

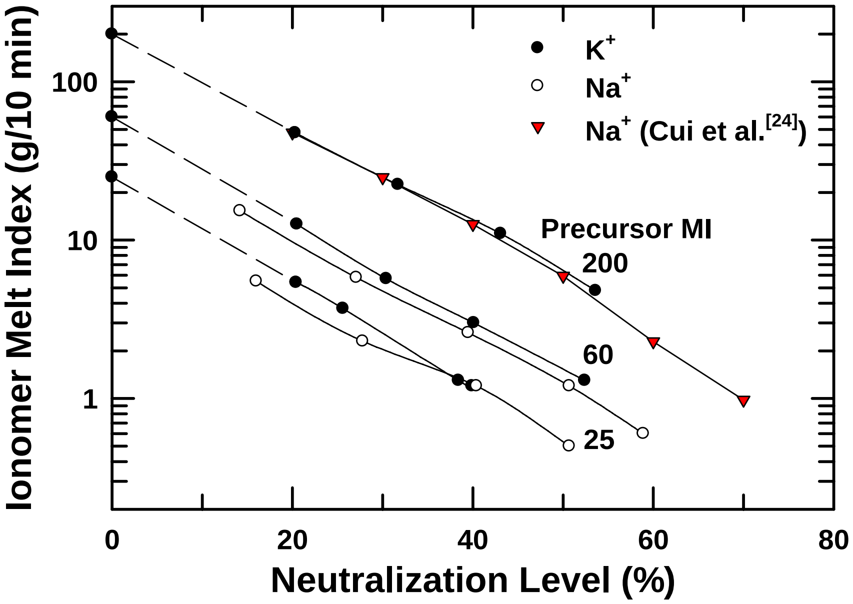

Figure 6.1: Melt indices and neutralization levels of neat K$^+$ and Na$^+$ ionomers used.

Characterization

Differential scanning calorimetric (DSC) thermograms were recorded using a Perkin-Elmer Model DSC-7 at a heating rate of 10 °C/min under an extra dry N_2 atmosphere over a temperature range of 0 °C to 140 °C. The predried virgin ionomer samples of 8 mg to 10 mg were packed in aluminum pans, melted at 205 – 230 °C, and then kept in a desiccator for 21 days before the measurements unless otherwise indicated. These pretreatments were performed to remove previous thermal history and to ensure that each sample experienced the same length of room temperature aging time because a number of factors, such as moisture content and room temperature aging, can affect the details of the DSC thermograms [7, 10, 11].

Melt rheological characteristics were determined using an AR 2000ex Rheometer with a parallel plate fixture. All the rheological measurements were carried out at a fixed temperature of 200 °C under a nitrogen gas flow. Frequency sweep tests were made over a range of 0.5–200 rad/s at a strain of 0.02%, which was within the linear viscoelastic region. Specimens for rheological testing were taken from the far end of injection molded samples and trimmed after heating on the rheometer plate to a disk with a diameter of 25 mm and a thickness of 1 mm.

The dynamic mechanical properties were determined by a Rheometric Scientific Dynamic Mechanical Thermal Analyzer (DMTA) Mk III at a frequency of 1 Hz, a strain level setting of 4 (~0.07% strain), and under a single cantilever mode. Injection-molded (0.318 cm thick) specimens of neat ionomers were heated from 0 to 85 °C at a rate of 2 °C/min and analyzed for storage modulus (E'), loss modulus (E''), and tan δ.

Tensile tests were performed according to ASTM D638 using an Instron model 1137 machine upgraded for computerized data acquisition. Tensile modulus values were determined using an extensometer at a crosshead rate of 0.51 cm/min. Elongation at break and yield strength data were measured at a crosshead speed of 5.1 cm/min. Data reported here are averaged from at least five specimens.

Notched Izod impact tests were conducted at room temperature using a 6.8 J hammer and 3.5 m/s impact velocity using a TMI Impact tester (model 43-02). Standard notches were made according to ASTM D256. Frequently, as-molded rectangular bars are cut in half (to generate more samples) and the Izod impact strength data from the gate end (the end at which the molten polymer enters the mold during injection molding) and the far end are averaged together. Morphological differences arising from the injection molding process can result in significant differences between the Izod impact strength measured at the gate end and the far end of the samples. Although the Izod impact strength measured at the gate end is up to 27% less than that measured at the far end of the neat ionomer samples, values from both ends are averaged together here for simplicity.

RESULTS AND DISCUSSION

Ionomer ageing

EMAA copolymer-based ionomers are known to undergo a physical ageing process during room temperature storage over a period of days to months [12]. This phenomenon has been attributed to secondary crystallization [12-16] and to increased ordering in and around the ionic aggregates [17-20]. Recent X-ray scattering [21] and NMR [15] studies indicate that the ageing effect is primarily due to secondary crystallization. The aggregation of ionic groups results in a high local viscosity [8, 22] that impedes the diffusion of crystallizable segments, as evidenced by the slower rate of primary crystallization of ionomers as compared with unneutralized EMAA copolymers [13]. Thus, high amounts of crystallizable segments are able to crystallize in a secondary crystallization process during room-temperature ageing. The secondary crystals may serve as bridges between the ionic aggregates, or the immobilized zones surrounding the aggregates, to form percolating pathways between the primary crystals [23].

Effect of ageing time on ionomer DSC

Typical DSC thermograms of K^+ and Na^+ ionomers measured 21 days after high temperature annealing (205-230 °C) are shown in Figure 6.2. The DSC scans reveal a low temperature (T_i) peak (45 – 52 °C) and a high temperature (T_m) peak (87 – 94 °C) associated with the melting of the secondary and primary crystallites, respectively. These peaks change with time after molding. Figure 6.3 shows how the enthalpy change for the T_i peak (ΔH_i) of K^+ and Na^+ ionomers changes with time after annealing at 205 – 230 °C. The ΔH_i increases with ageing time, indicating higher crystallization levels, and appears to plateau near an ageing time of 21 days. Due to the proximity of the two peaks, estimating the enthalpy change for the T_m peak (ΔH_m) is more difficult.

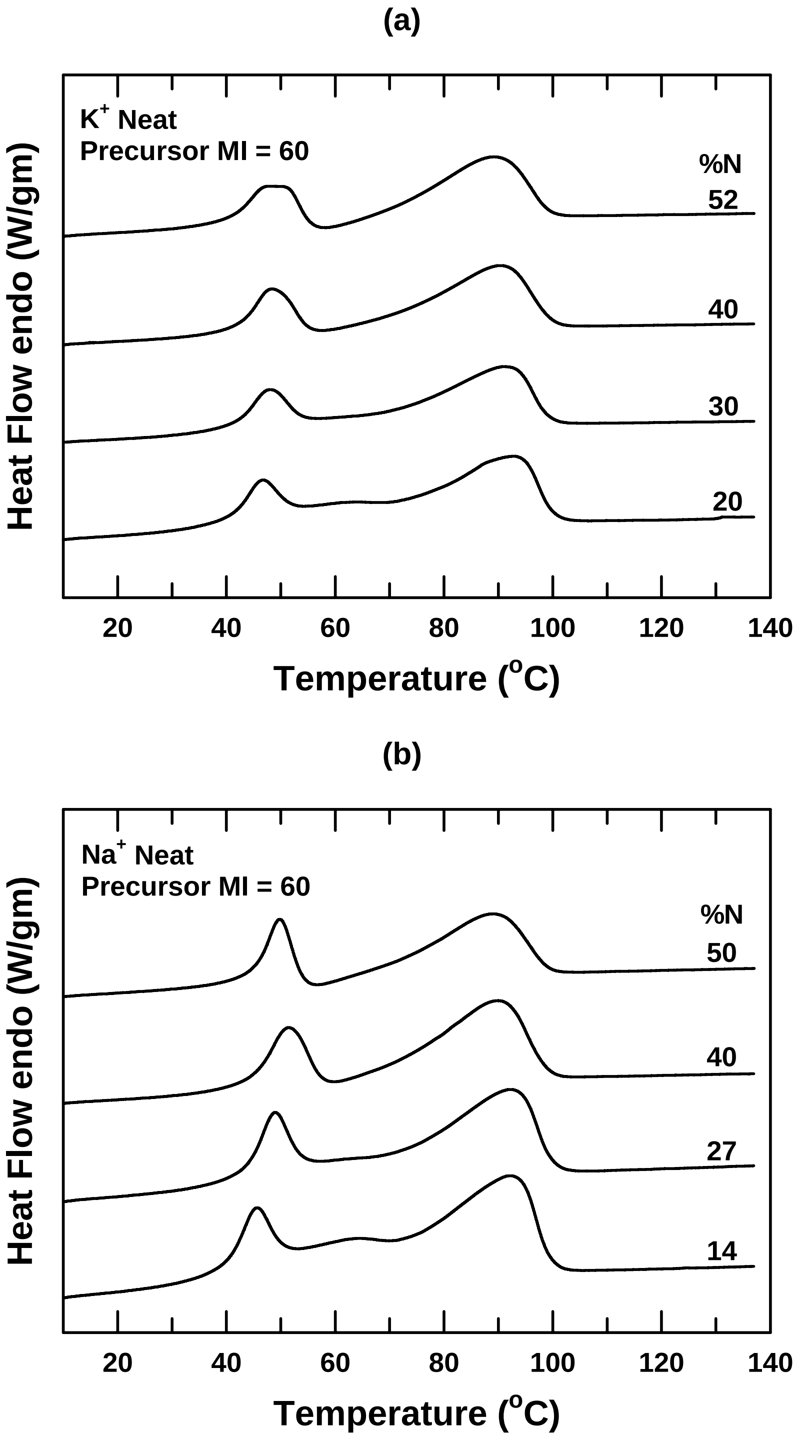

Figure 6.2: DSC thermograms of selected neat K^+ (a) and Na^+ (b) ionomers with a precursor melt index of 60 g/10 min and various levels of neutralization (%N) measured 21 days after high temperature annealing. The curves are vertically shifted for clarity.

(a)

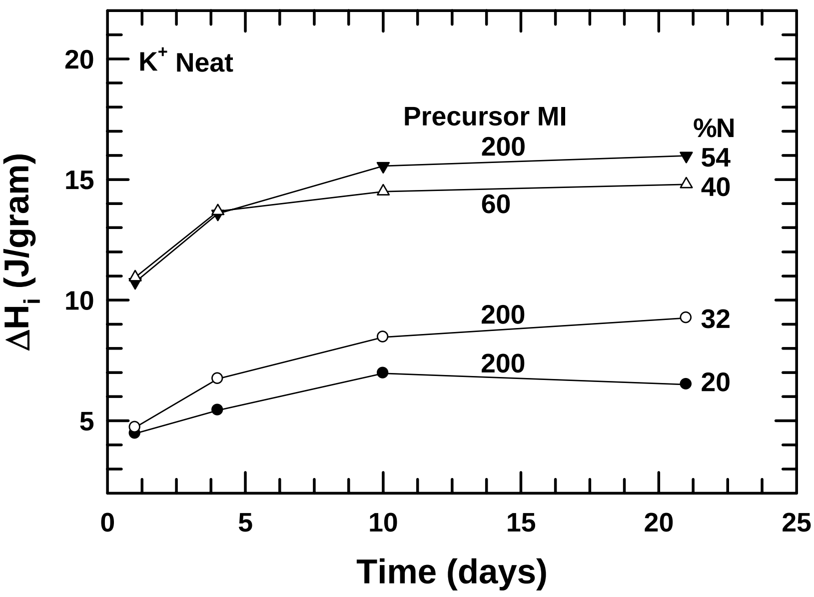

(b)

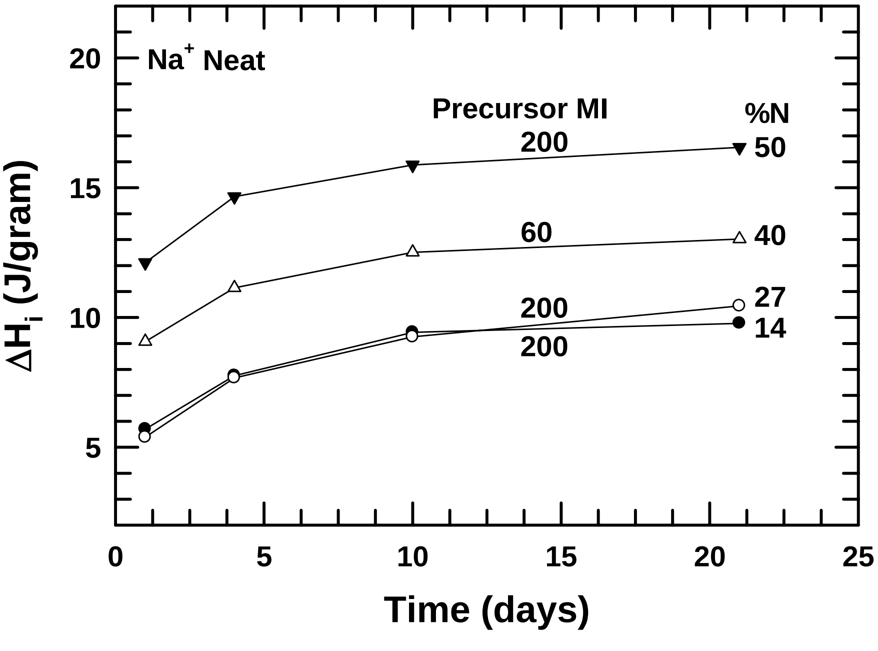

Figure 6.3: The ΔH of the low temperature peak in DSC scans of various neat K^+ (a) and Na^+ (b) ionomers measured after various times after high temperature annealing.

Effect of ageing time on ionomer modulus

The secondary crystallites have been shown to form between primary crystallites and to be arranged parallel to the primary crystallites [21]. The formation of secondary crystals creates more sample-spanning pathways by connecting the immobilized areas near the ionic aggregates, increasing the modulus significantly [23]. As expected, this secondary crystallization results in increased modulus over time, as shown in Figure 6.4. The modulus seems to increase substantially with time up to about two or three weeks after molding. The modulus appears to plateau with further ageing time. Because both the modulus and the crystallinity as measured by DSC seem to have leveled off after 21 days, the remaining mechanical properties were measured 21 days after molding.

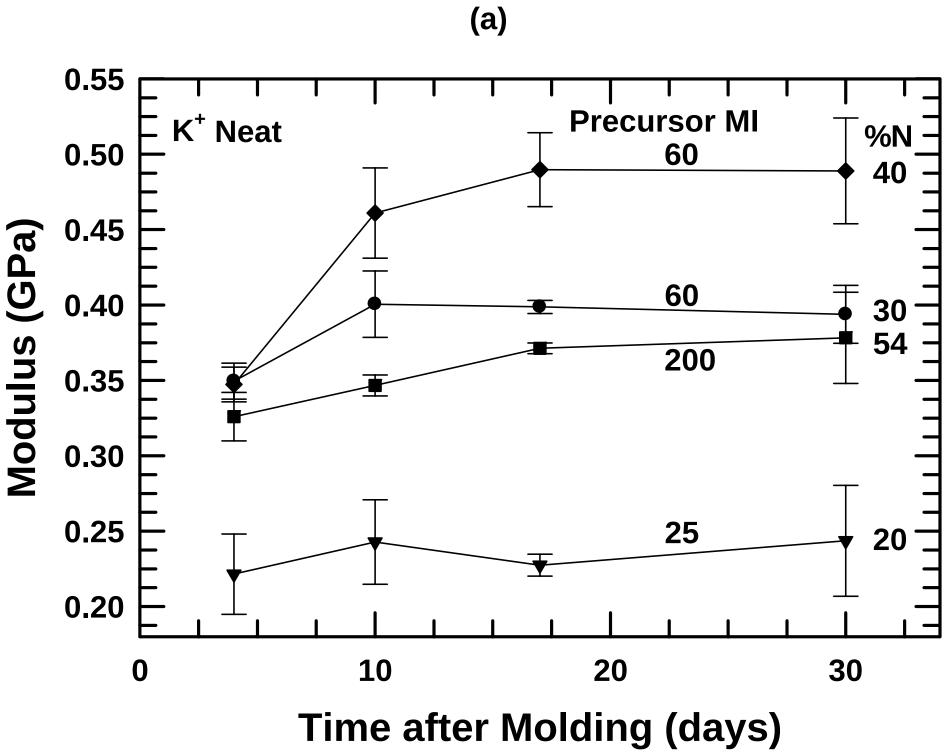

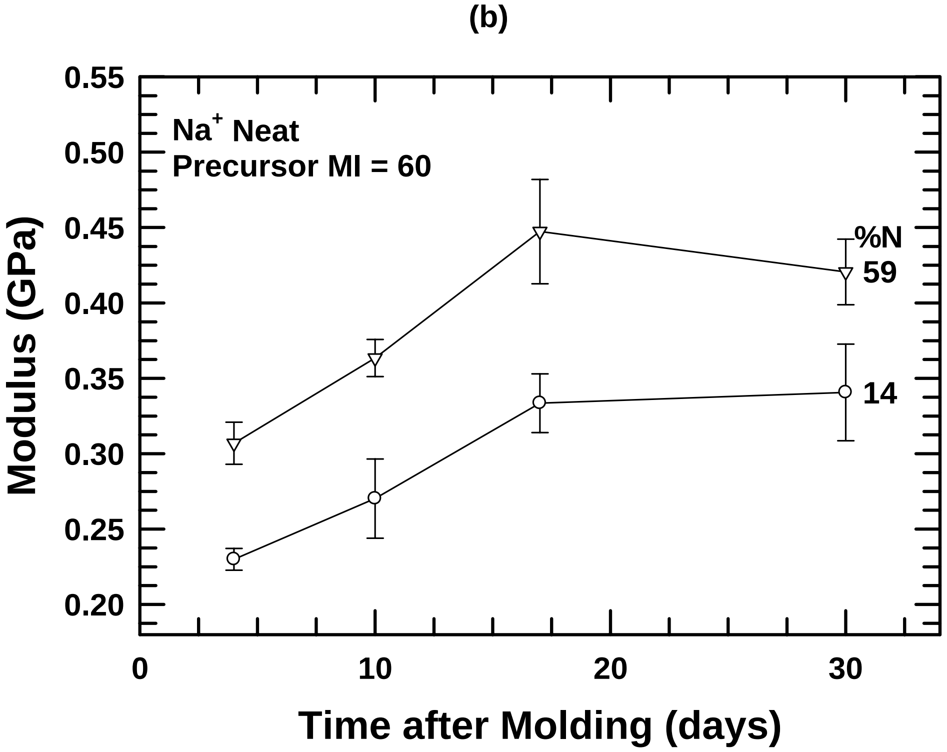

Figure 6.4: Modulus of various neat K^+ (a) and Na^+ (b) ionomers measured after various times after molding.

Effect of water content on ionomer properties

The cations of EMAA ionomers attract and absorb water; K^+ ionomers absorb more water than Na^+ ionomers [10]. Figure 6.5 shows the water content of selected K^+ and Na^+ ionomers and ionomer nanocomposites versus the soaking time in water. The addition of 5 wt% montmorillonite (MMT) to the ionomer results in little further increase in the water content.

Table 6.1 shows the effect of moisture on the neat ionomer properties of selected K^+ and Na^+ ionomers. For both ionomers the modulus decreases and the elongation at break and Izod impact strength increase upon absorption of water, consistent with the expected plasticization effect of water on ionomer materials [10].

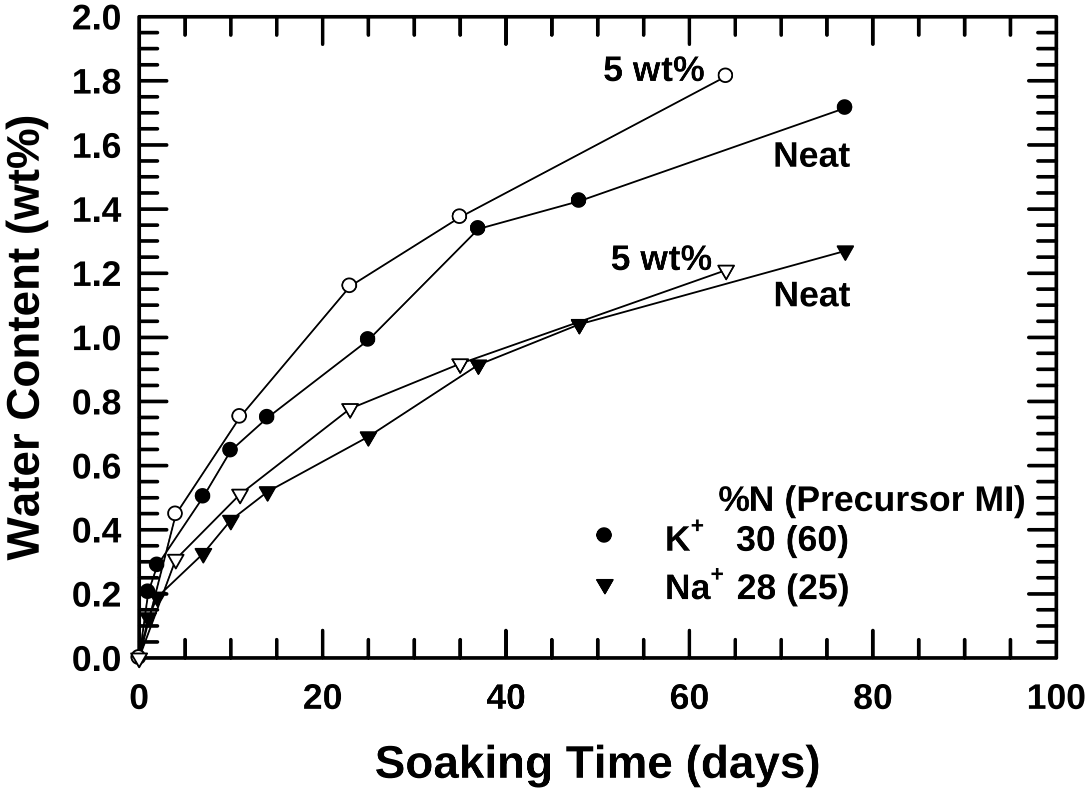

Figure 6.5: Modulus of various neat K^+ (a) and Na^+ (b) ionomers measured after various times after molding.

Table 6.1: Effect of moisture on neat ionomer properties

	K^+ Precursor MI = 60 N = 40%			Na^+ Precursor MI = 60 N = 40%		
	Modulus (GPa)	% Elongation	Izod Impact Strength (J/m)	Modulus (GPa)	% Elongation	Izod Impact Strength (J/m)
Dry as molded	0.37	172	534	0.36	140	457
3 days in H_2O	0.32	188	588	0.32	193	565

Differential scanning calorimetry

Figures 6.6 and 6.7 show the dependence of the T_i and ΔH_i, respectively, measured 21 days after high temperature annealing on the neutralization level for K^+ and Na^+ ionomers. The T_i and ΔH_i increase for both ionomer types with increasing neutralization. At any neutralization level, the ΔH_i of the ionomers with a precursor melt index of 60 g/10 min is typically higher and that of the K^+ ionomers with a precursor melt index of 200 g/10 min is typically lower. The T_m, however, decreases with increasing neutralization level for both ionomer types, as shown in Figure 6.8; the T_m is generally lowest for ionomers with a precursor melt index of 60 g/10 min at any neutralization level. The ΔH_m shown in Figure 6.9 increases with increasing neutralization, except for the Na^+ ionomer with the highest neutralization level (59%). At any neutralization level, the ΔH_m generally decreases as the precursor melt index increases. These results indicate that the crystallization level increases with increasing neutralization level. In general, the T_i is higher and both the ΔH_i and ΔH_m increase at a lower rate for the Na^+ ionomers than for the K^+ ionomers.

Increases in T_i and ΔH_i and decreases in T_m and ΔH_m with increasing neutralization level have been reported previously for various ionomer types [7, 14, 23, 24]. The T_i, T_m, and ΔH_i trends agree with those reported here, but the ΔH_m reported here tends to increase as the neutralization increases. This disparity may be due in part to difficulties in measuring the peak areas due to the proximity of the peaks and to differences in room-temperature ageing time. Neutralization and the resulting aggregation of ionic and acid groups may result in further segregation of the amorphous methacrylic acid chain segments, allowing for higher crystallization levels. Several reports have suggested that an optimal spacing of alkaline ions and carboxyl groups within ionic groups may exist at a neutralization level of 33% (three carboxyl groups per ion) [7, 9, 25, 26].

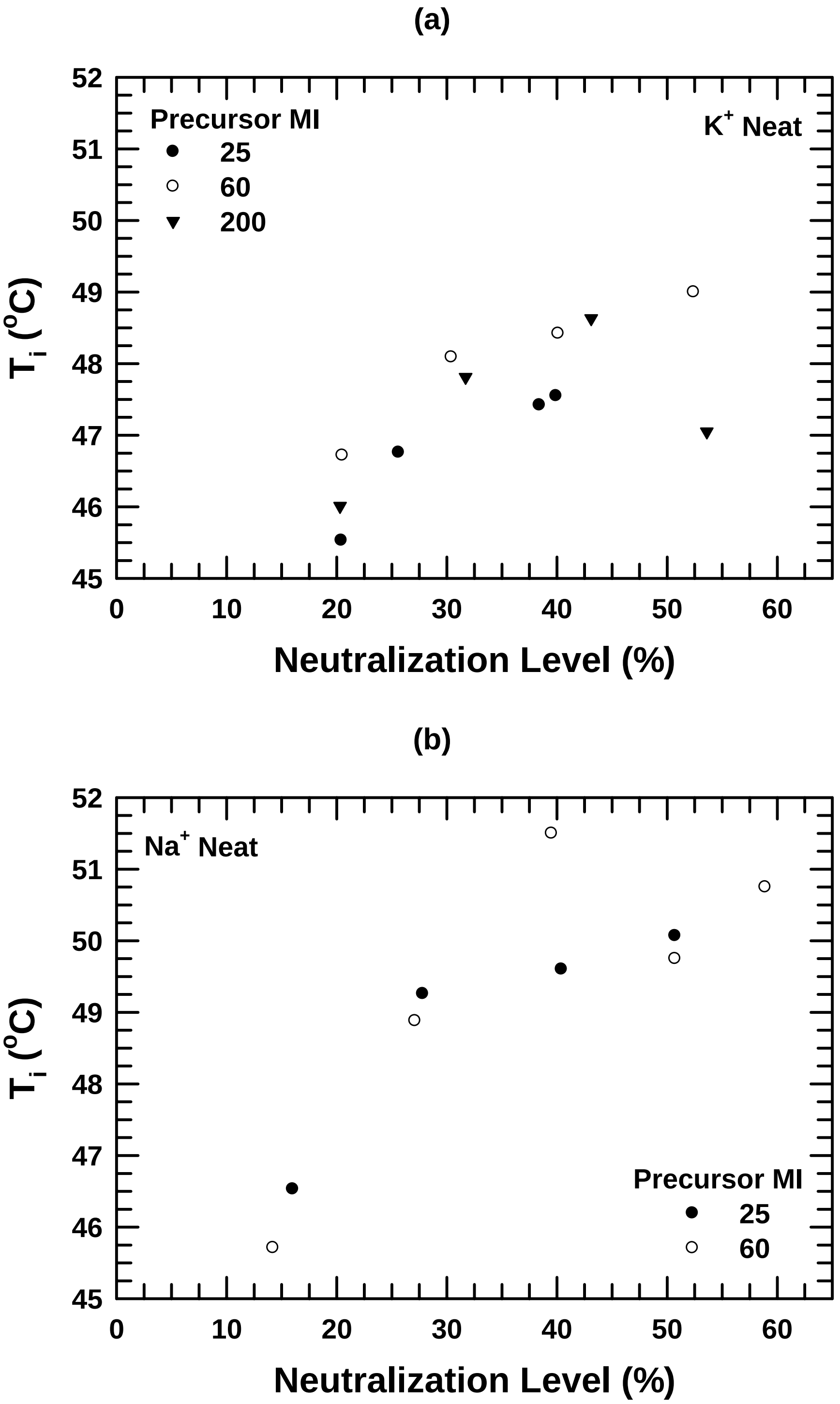

Figure 6.6: The low temperature peak temperatures in DSC scans of neat K^+ (a) and Na^+ (b) ionomers measured 21 days after high temperature annealing.

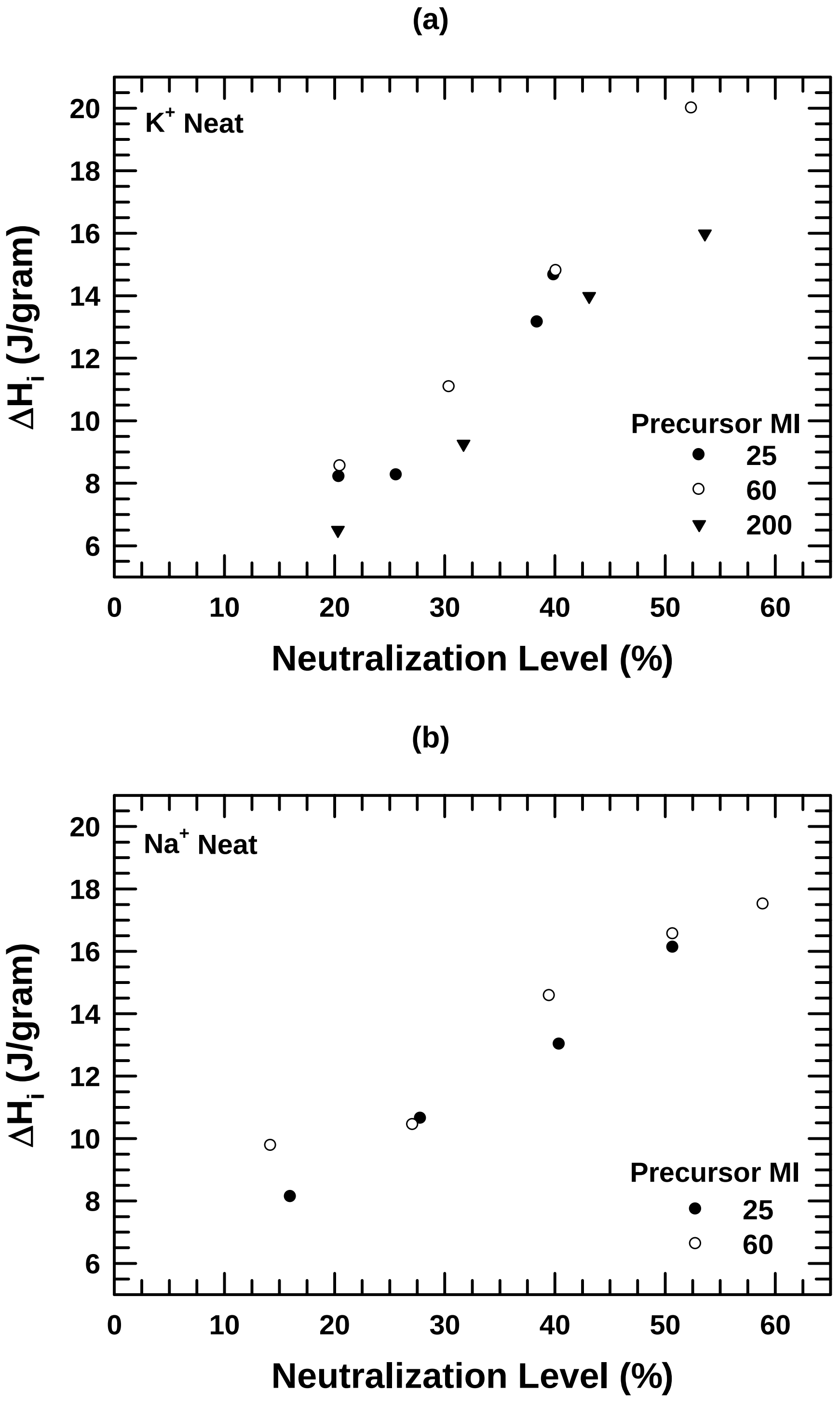

Figure 6.7: The ΔH of the low temperature peak in DSC scans of neat K^+ (a) and Na^+ (b) ionomers measured 21 days after high temperature annealing.

(a)

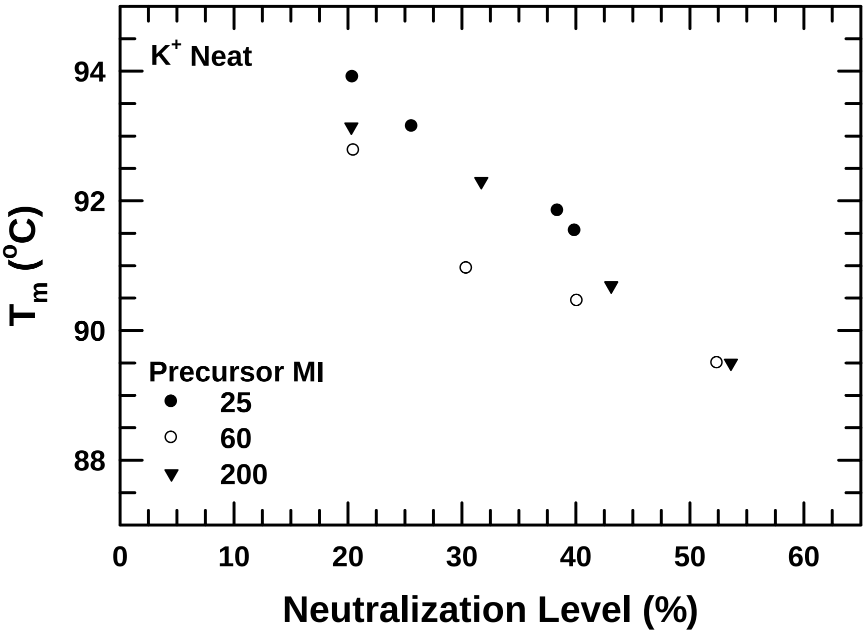

(b)

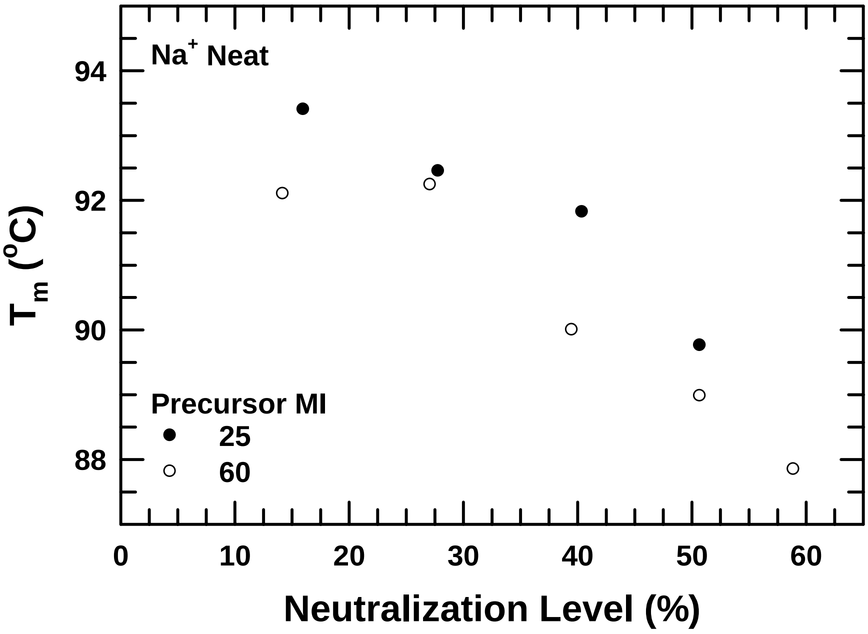

Figure 6.8: The high temperature peak temperatures in DSC scans of neat K^+ (a) and Na^+ (b) ionomers measured 21 days after high temperature annealing.

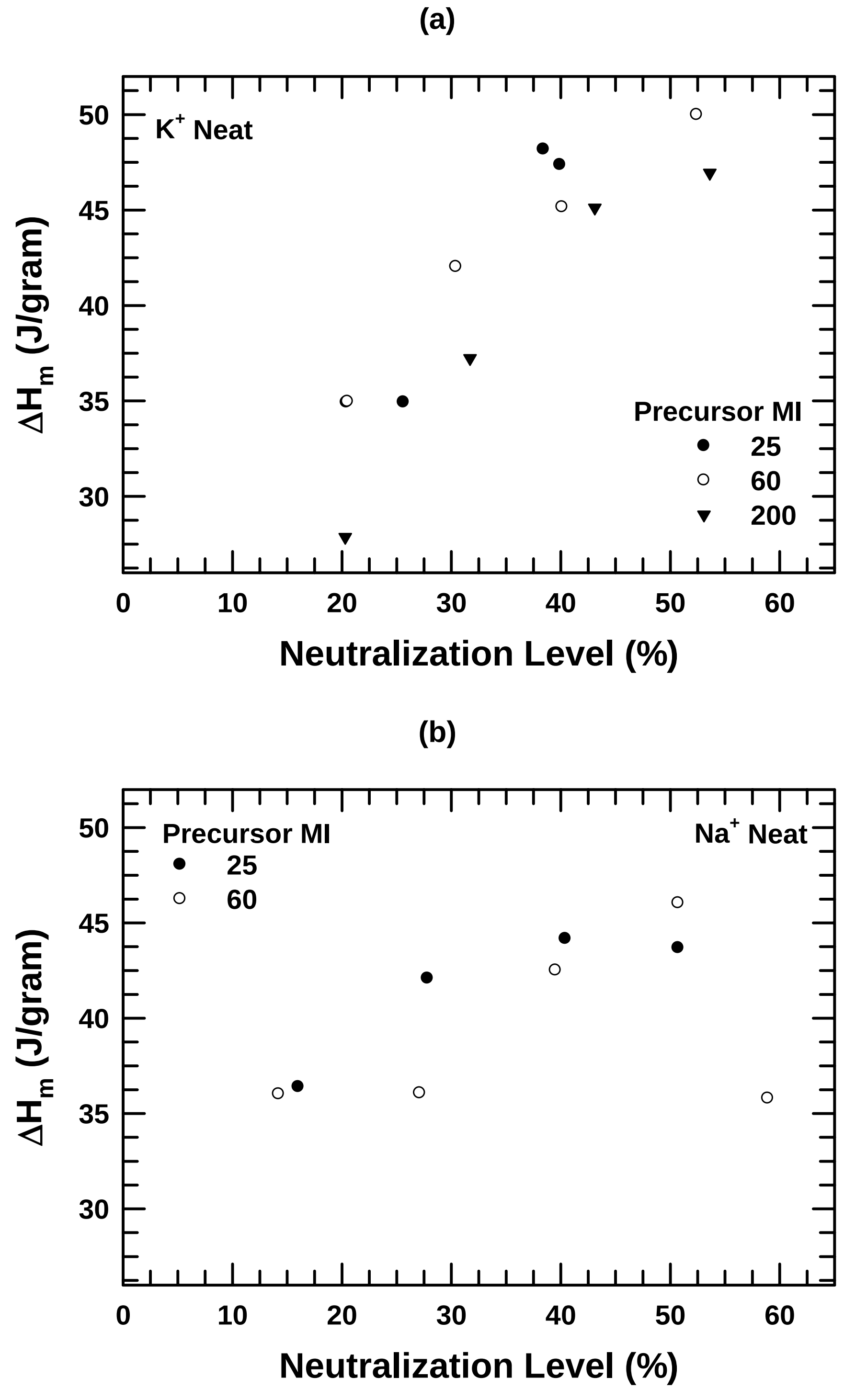

Figure 6.9: The ΔH of the high temperature peak in DSC scans of neat K^+ (a) and Na^+ (b) ionomers measured 21 days after high temperature annealing.

Dynamic mechanical analysis

Several mechanical relaxations have been reported between -40 and 70 °C in previous DMTA studies of EMAA ionomers [7, 23, 27-29]. EMAA copolymers and ionomers with < 20% neutralization exhibit only one clear relaxation between -40 and 70 °C that has been shown to be the glass transition of the amorphous phase in these materials [30]. As the neutralization level increases, this relaxation splits into two: one at a lower temperature and one at a higher temperature. The lower temperature relaxation is generally considered to reflect the glass transition of ion-depleted domains within the amorphous phase [23, 27, 31]. The higher temperature relaxation has been attributed to the melting of secondary crystals and the devitrification of the ion-rich regions [23].

Figure 6.10 shows the dynamic mechanical properties of K^+ ionomers with neutralization levels of ~20%. For this fixed level of neutralization, changes in the precursor melt index appear to have little effect on the storage modulus (E'). As the precursor melt index increases, the loss modulus (E") increases significantly below the T_i and decreases slightly above the T_i.

Dynamic mechanical properties of selected K^+ and Na^+ ionomers with a precursor melt index of 60 g/10 min and various degrees of neutralization are shown in Figures 6.11 and 6.12, respectively. The relaxation denoted by the decrease in E' and the peaks in E" and tan δ that occur in the vicinity of the T_i seen by DSC shifts to higher temperatures as the degree of neutralization is increased, as expected from the DSC results and in agreement with previous reports for Na^+ and Zn^{2+} ionomers [23, 27, 29]. Though the temperature range examined here is not sufficiently low to be certain, it appears that ionomers with neutralization levels < 20% have single relaxation similar to that of EMAA, while ionomers with higher neutralizations likely exhibit a split relaxation behavior with a relaxation somewhat below the temperature range examined.

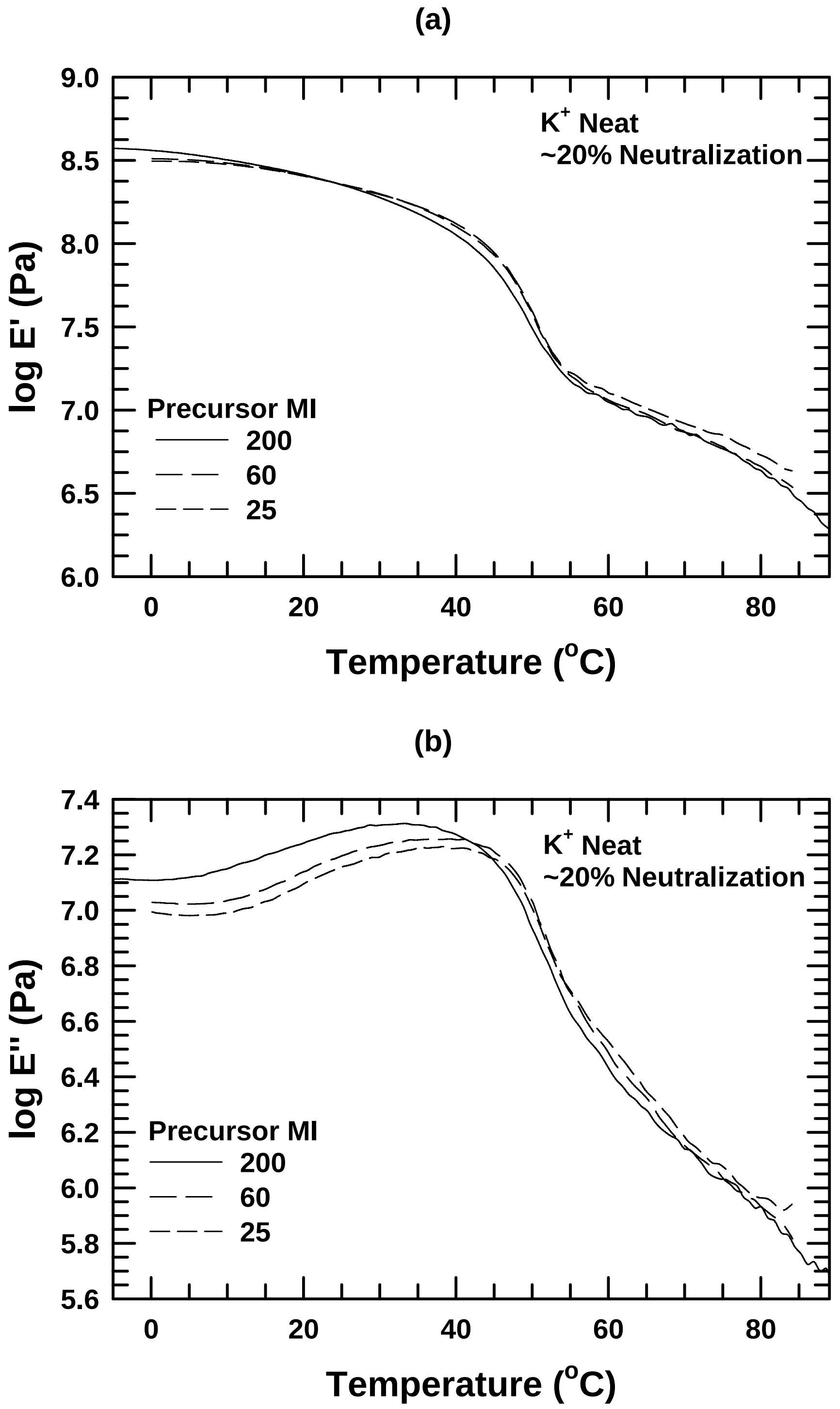

Figure 6.10: Storage modulus, *E*′, (a) and loss modulus, *E*″, (b) for neat K^+ ionomers with neutralization levels of ~20%.

(a)

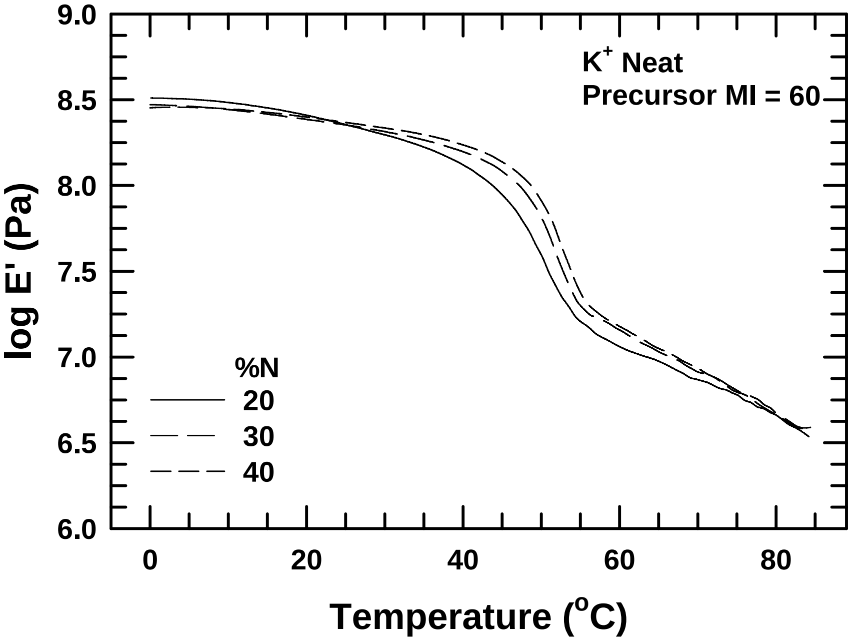
K$^+$ Neat
Precursor MI = 60
%N
20
30
40
log E' (Pa)
9.0
8.5
8.0
7.5
7.0
6.5
6.0
0
20
40
60
80
Temperature (^{o}C)

(b)

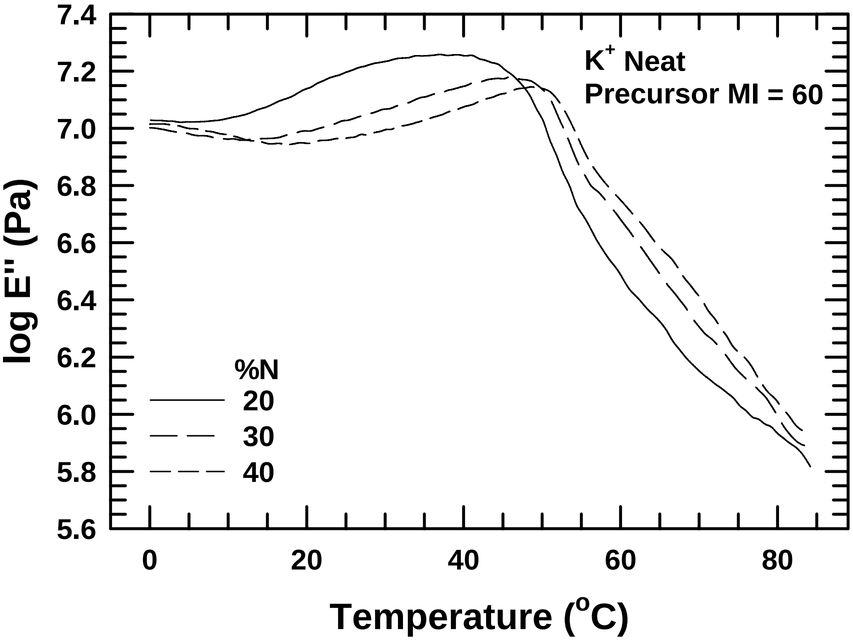
K$^+$ Neat
Precursor MI = 60
%N
20
30
40
log E'' (Pa)
7.4
7.2
7.0
6.8
6.6
6.4
6.2
6.0
5.8
5.6
0
20
40
60
80
Temperature (^{o}C)

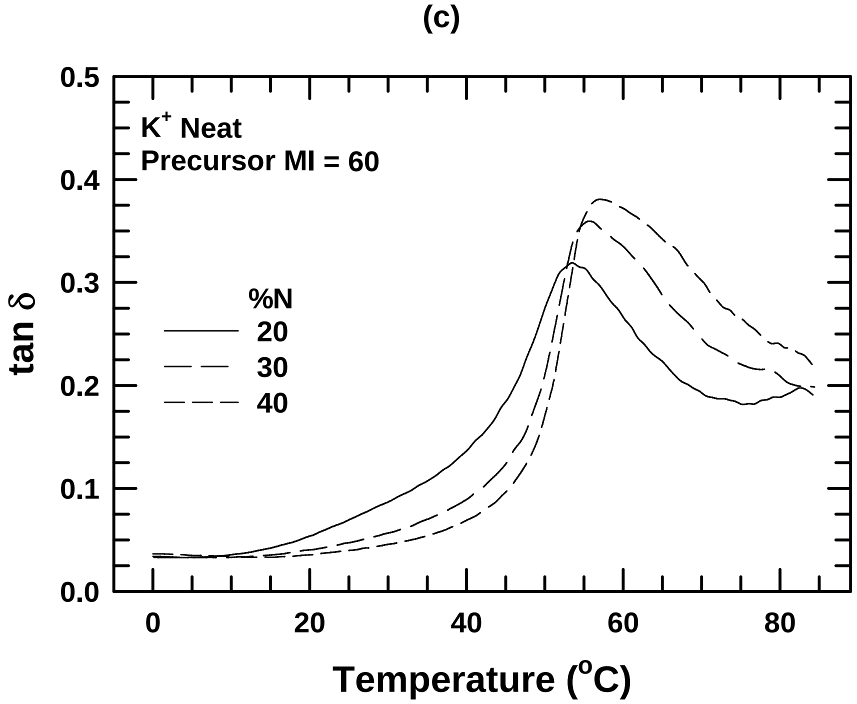

Figure 6.11: Storage modulus, *E*′, (a), loss modulus, *E*″, (b), and tan *δ* (c) for neat K^+ ionomers with a precursor melt index of 60 g/10 min.

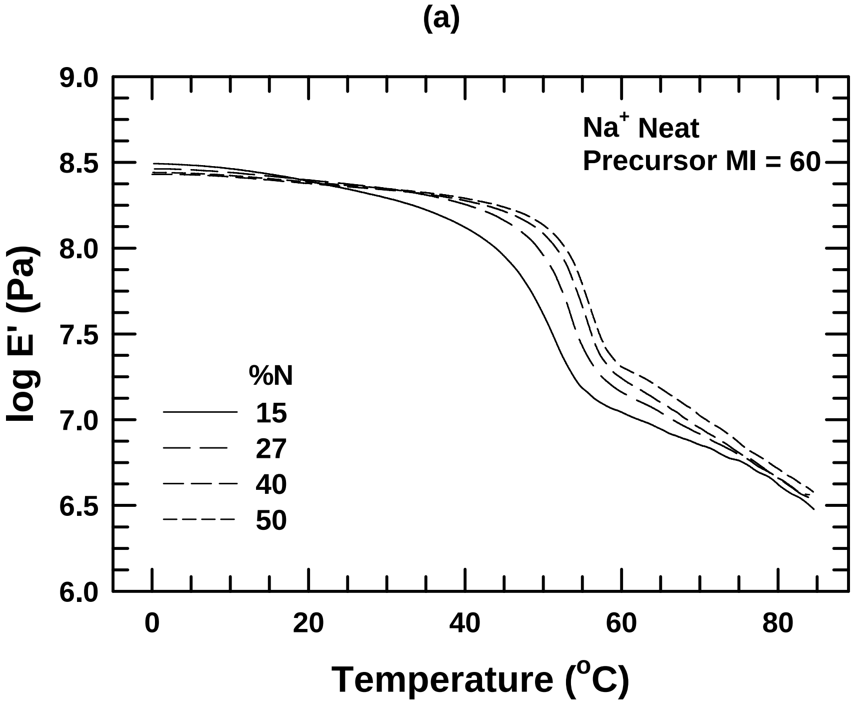

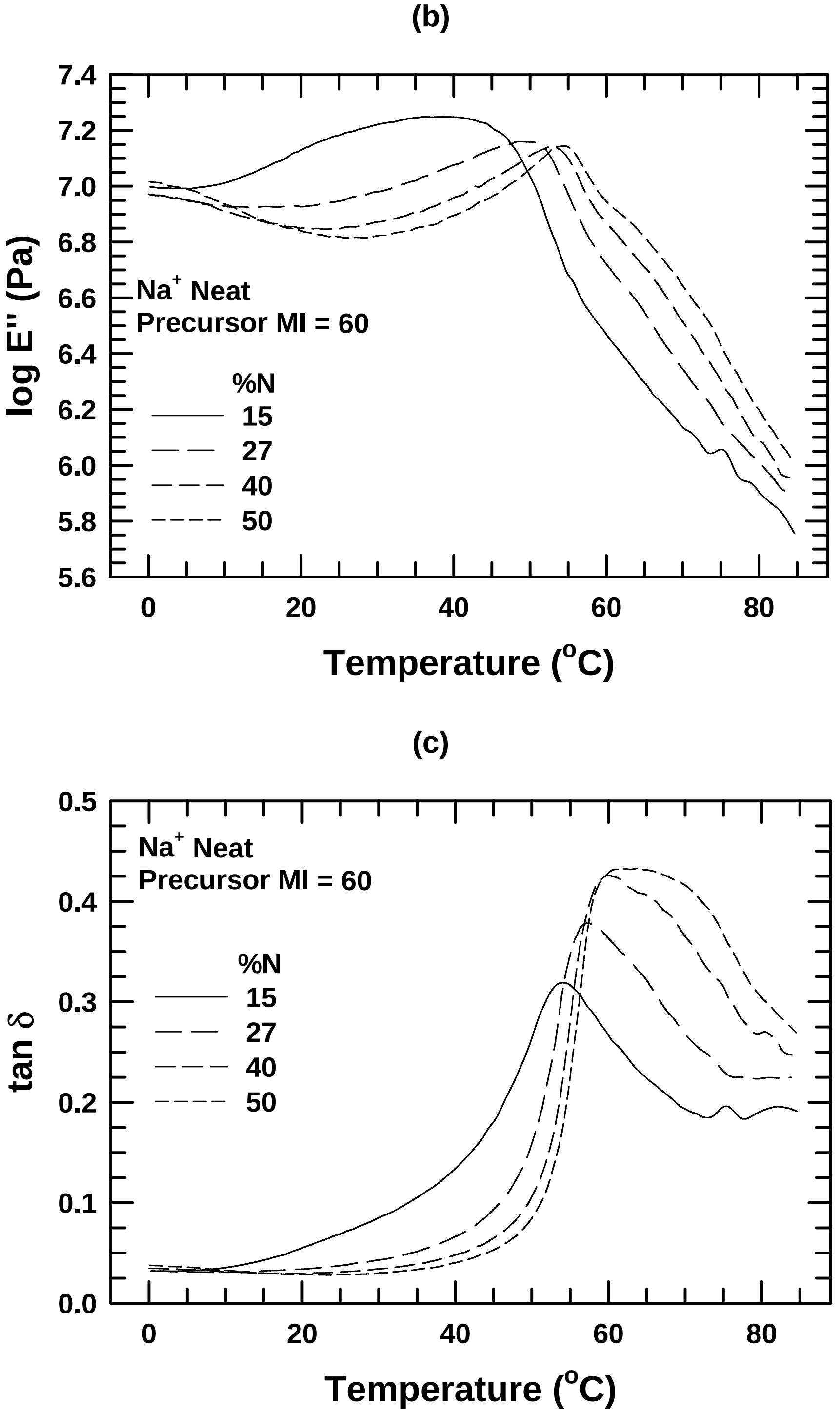

Figure 6.12: Storage modulus, *E*′, (a), loss modulus, *E*″, (b), and tan *δ* (c) for neat Na^+ ionomers with a precursor melt index of 60 g/10 min.

Figure 6.13 shows the dynamic mechanical properties of selected K^+ and Na^+ ionomers with comparable precursor melt indices and neutralization levels. The decrease in E' and the peaks in E" and tan δ that occur in the vicinity of the T_i seen by DSC occur at higher temperatures for the Na^+ ionomers than for the K^+ ionomers, as expected from the DSC results.

(a)

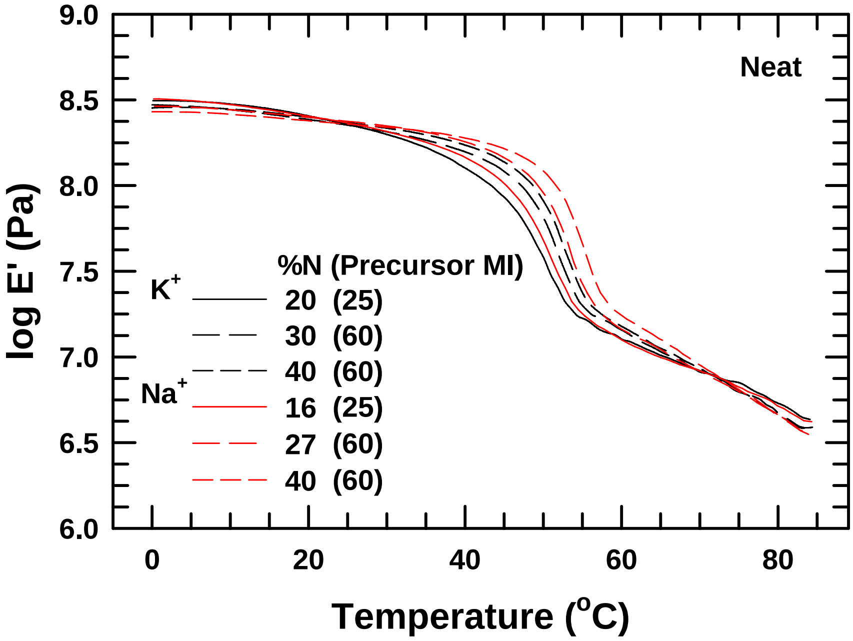

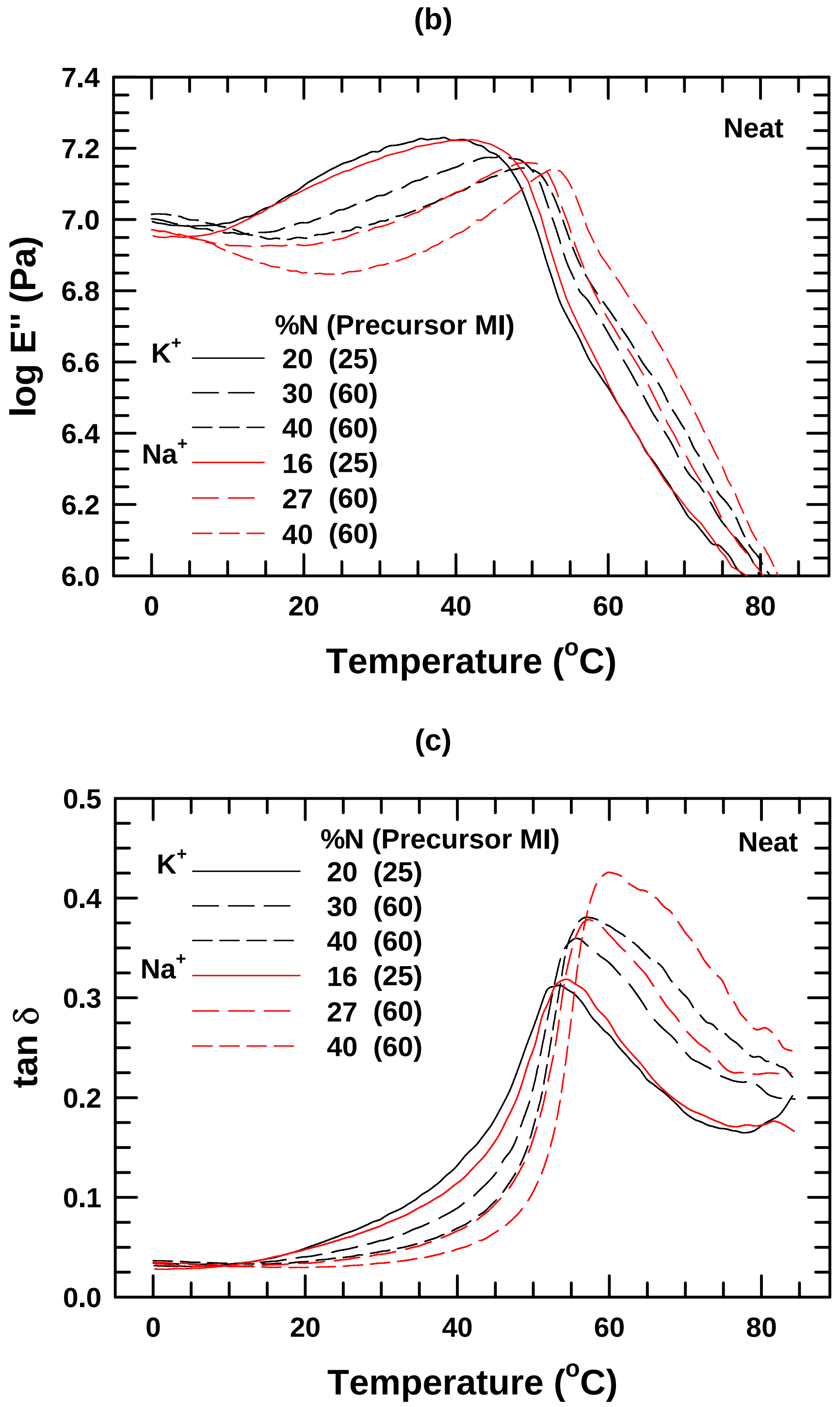

Figure 6.13: Storage modulus, *E*′, (a), loss modulus, *E*″, (b), and tan *δ* (c) for neat K^+ and Na^+ ionomers.

Melt rheology

Melt rheology results for K^+ ionomers with neutralization levels of ~20% are shown in Figure 6.14. As expected, the complex viscosity, storage modulus, and loss modulus decrease dramatically with increasing precursor melt index at all frequencies. The ionomers demonstrate Newtonian behavior at low frequencies and experience shear thinning at higher frequencies. The difference in melt viscosity for ionomers with different melt indices is not as dramatic at the high shear rates used in melt processing, though it is still significant.

(a)

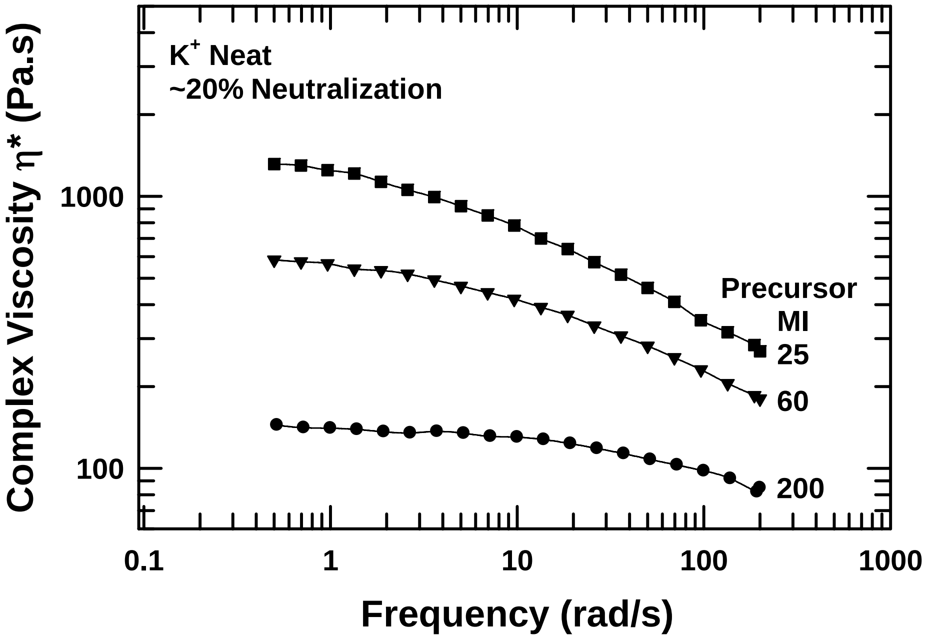

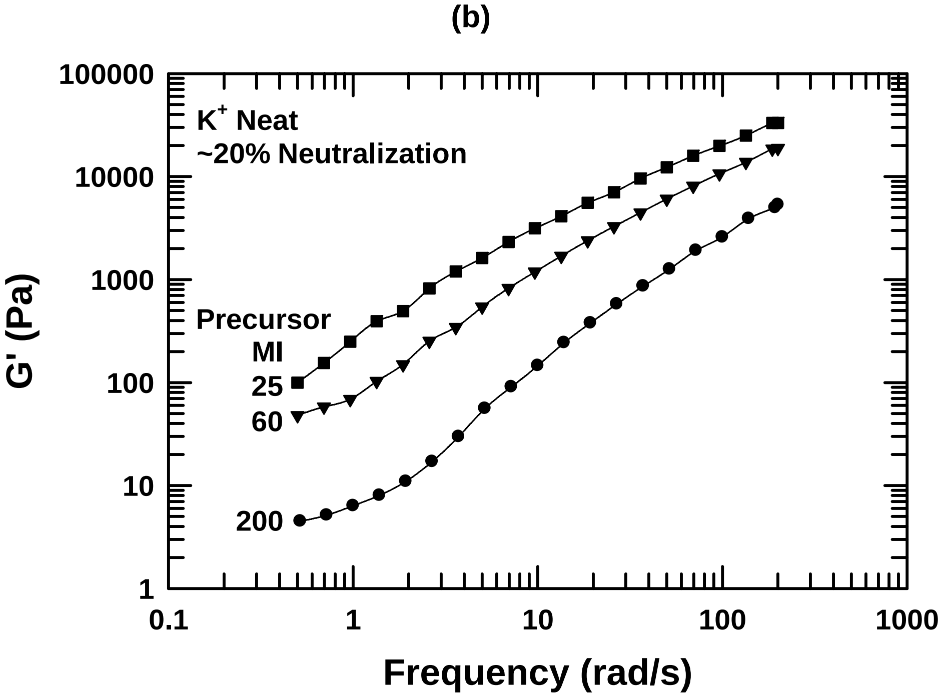

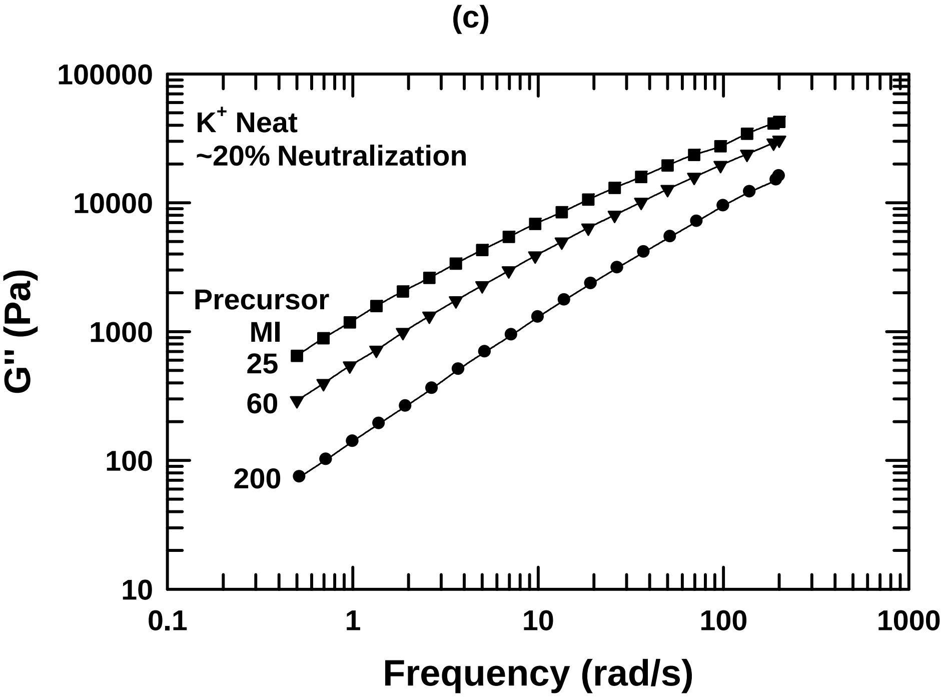

Figure 6.14: Frequency sweep results for neat K^+ ionomers with neutralization levels of ~20% at 200 °C: complex viscosity, η*, (a), storage modulus, *G*′, (b), and loss modulus, *G*″, (c).

Figures 6.15 and 6.16 show the melt rheology properties of selected K^+ and Na^+ ionomers with a precursor melt index of 60 g/10 min, respectively. The melt viscosity, storage modulus, and loss modulus increase as the neutralization level increases. Others have similarly reported that increasing neutralization level dramatically increased the complex viscosity of Na^+ ionomers [22, 24]. The melt viscosity, storage modulus, and loss modulus of the K^+ ionomers are somewhat lower than those of the Na^+ ionomers, possibly due to the higher affinity of K^+ for water; there may be some water retained in the K^+ ionomers after drying that would lower the rheological properties via plasticization.

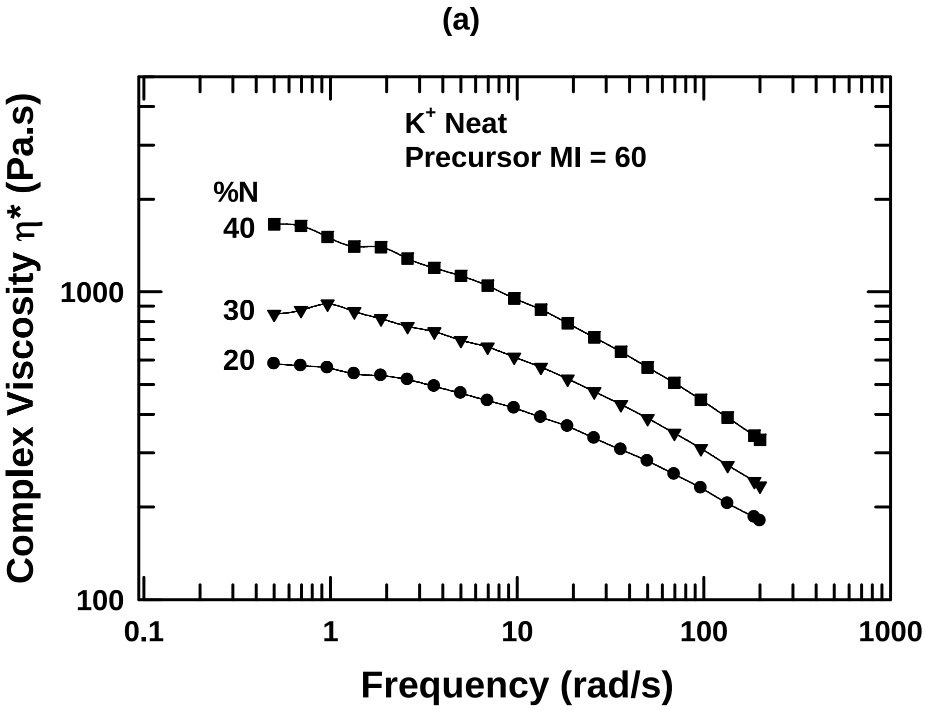

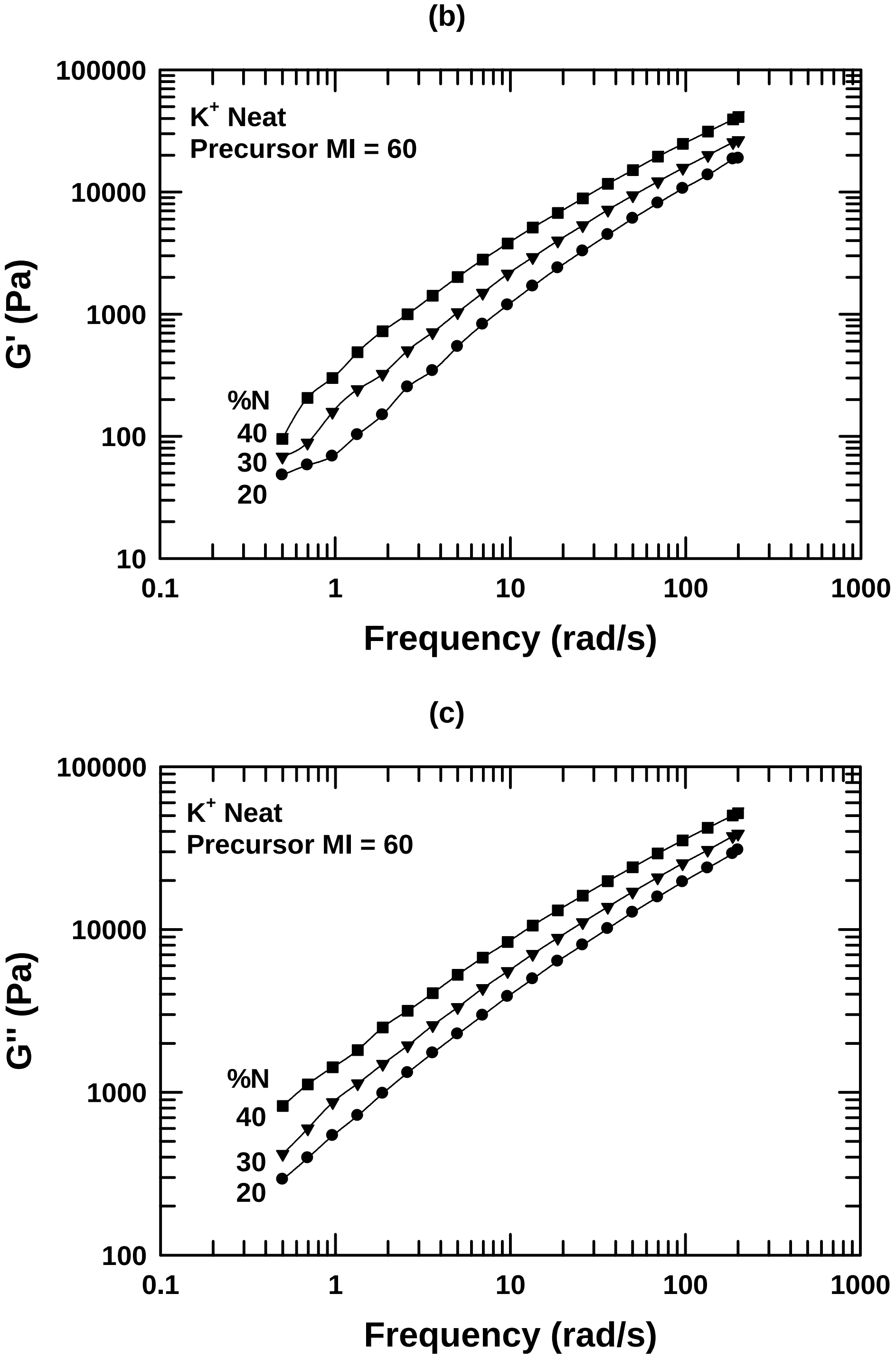

Figure 6.15: Frequency sweep results for selected neat K^+ ionomers with a precursor melt index of 60 g/10 min at 200 °C: complex viscosity, η^*, (a), storage modulus, G', (b), and loss modulus, G'', (c).

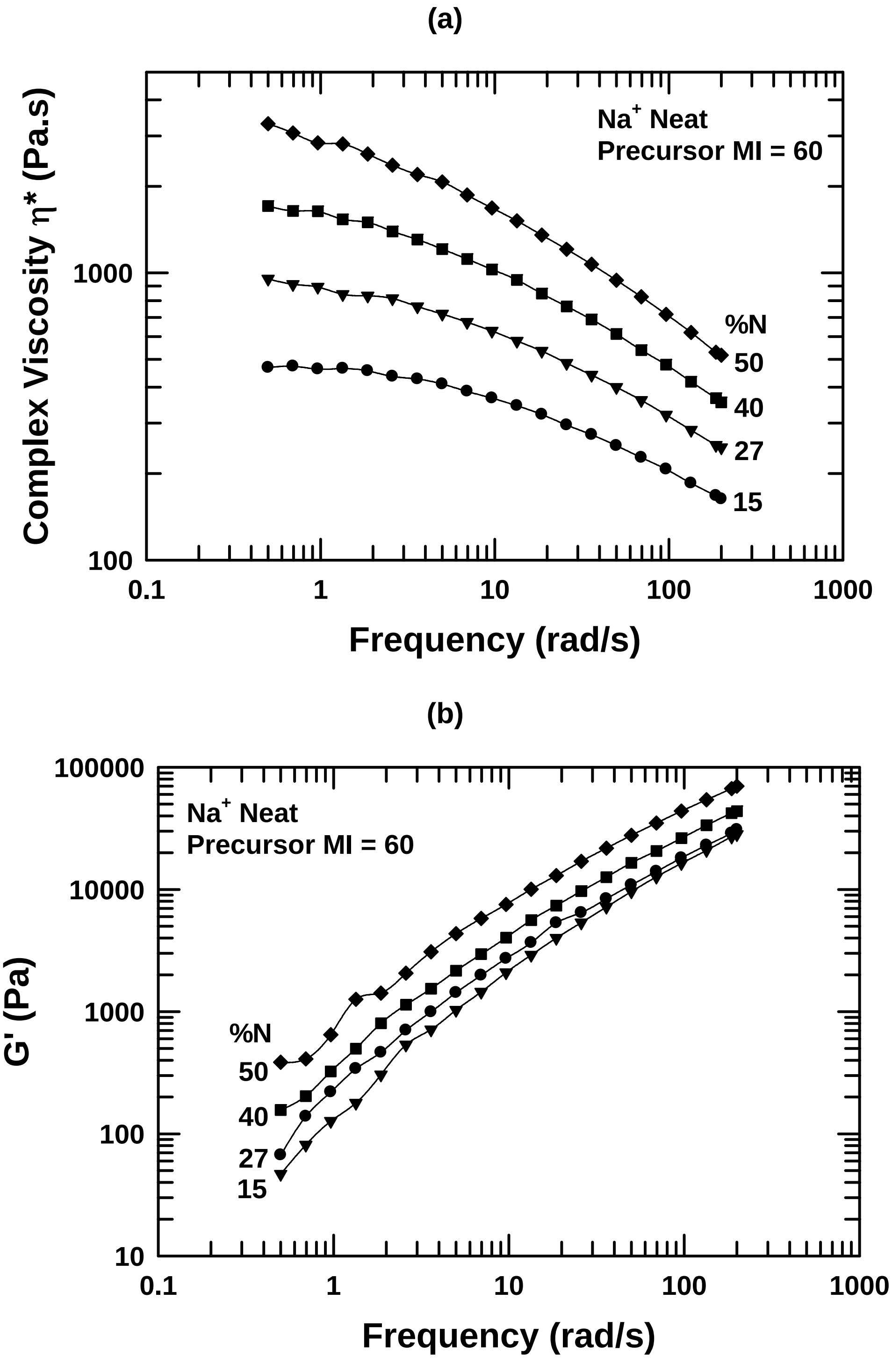
(a)
Na$^+$ Neat
Precursor MI = 60
Complex Viscosity η* (Pa.s)
1000
100
%N
50
40
27
15
0.1
1
10
100
1000
Frequency (rad/s)
(b)
Na$^+$ Neat
Precursor MI = 60
G' (Pa)
100000
10000
1000
100
10
%N
50
40
27
15
0.1
1
10
100
1000
Frequency (rad/s)

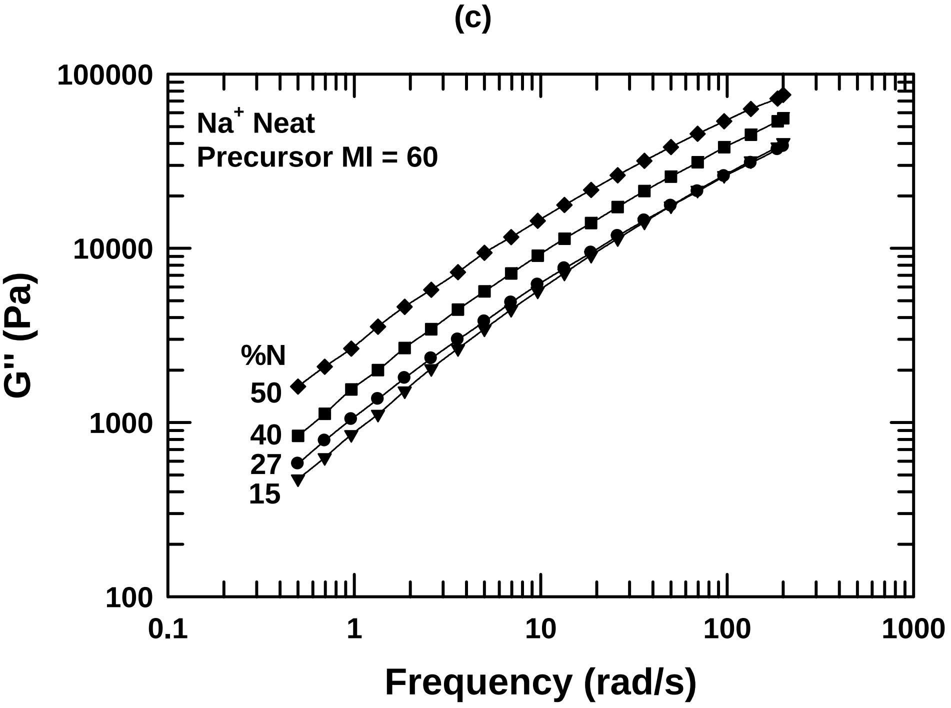

Figure 6.16: Frequency sweep results for selected neat Na$^+$ ionomers with a precursor melt index of 60 g/10 min at 200 °C: complex viscosity, η^*, (a), storage modulus, G', (b), and loss modulus, G'', (c).

Mechanical properties

Representative stress-strain curves of selected K$^+$ and Na$^+$ ionomers are shown in Figure 6.17. The curves of both ionomer types show distinct yield points, strain hardening after yield, and high post-yield elongations.

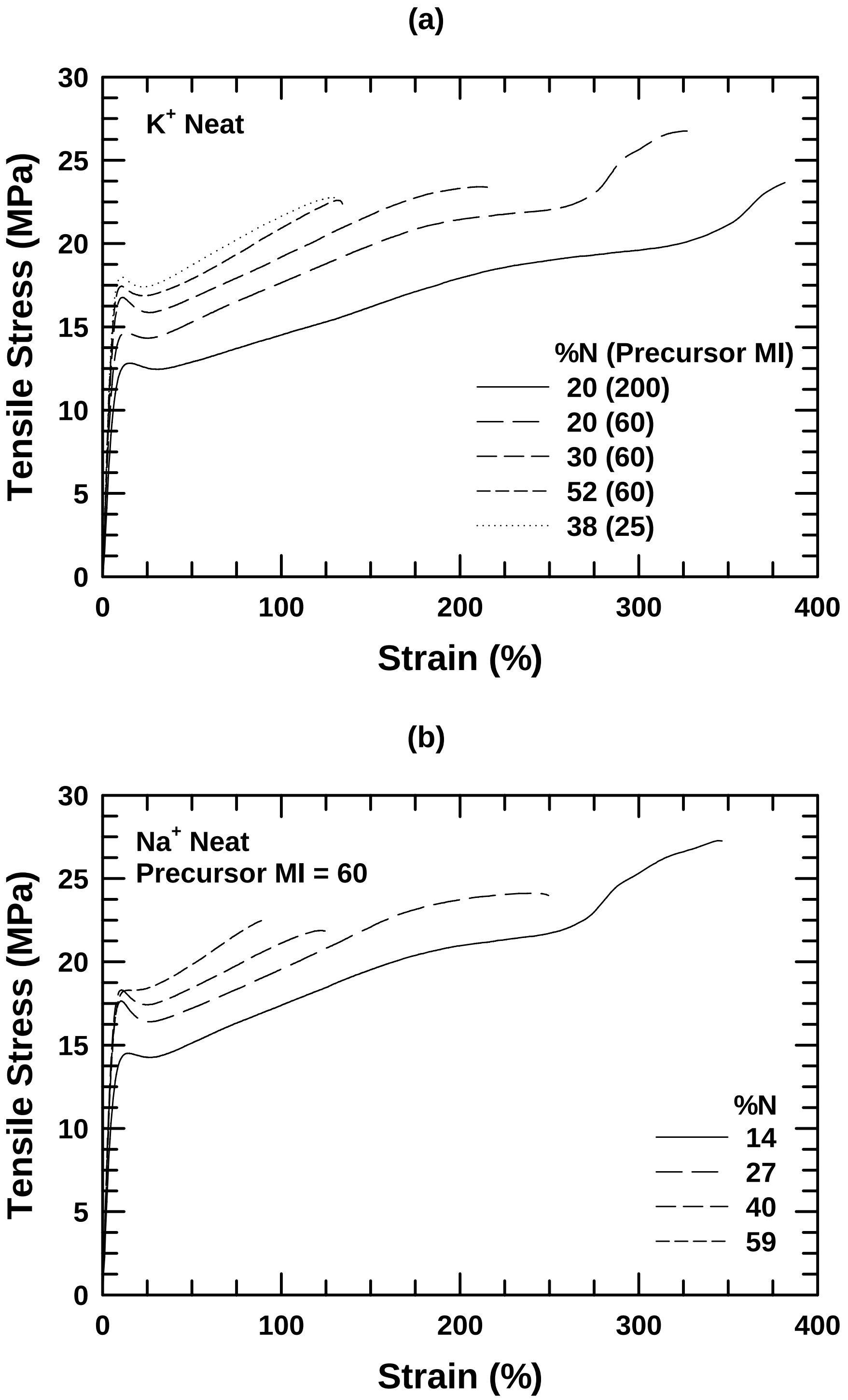

Figure 6.17: Stress-strain diagrams for selected neat K$^+$ (a) and Na$^+$ (b) ionomers at a crosshead speed of 5.1 cm/min.

The tensile moduli of the K^+ ionomers are plotted versus the neutralization level in Figure 6.18(a). The modulus increases with increasing neutralization level, except for neutralization levels above 50%. Generally, the modulus also increases as the precursor melt index decreases at any given neutralization level. Figure 6.18(b) plots the effect of the neutralization level on the modulus of the Na^+ ionomers from this work and those reported by Cui et al. [24]. The modulus increases up to a neutralization level of 40% and plateaus with further neutralization increases; the precursor melt index does not significantly affect the modulus. The lower values reported by Cui et al. can be attributed to the higher precursor melt index (200 g/10 min) and the shorter time between molding and testing (minimum of 24 h versus 21 days) of the samples.

It is interesting that there is an apparent maximum in the modulus of the K^+ ionomers between 40 and 50% neutralization, while the modulus of the Na^+ ionomers plateaus at high neutralization levels. Several groups have reported a maximum or a plateau in modulus or stiffness with increasing neutralization level [7, 9, 23-25]. This phenomenon may be due to an optimal packing within the ionic groups near 33% neutralization. Higher neutralization levels may disrupt the ionic group structure and possibly reduce the amount of material immobilized by the ionic groups, lowering the effectiveness of the percolating pathways formed by secondary crystals and immobilized ionic aggregates.

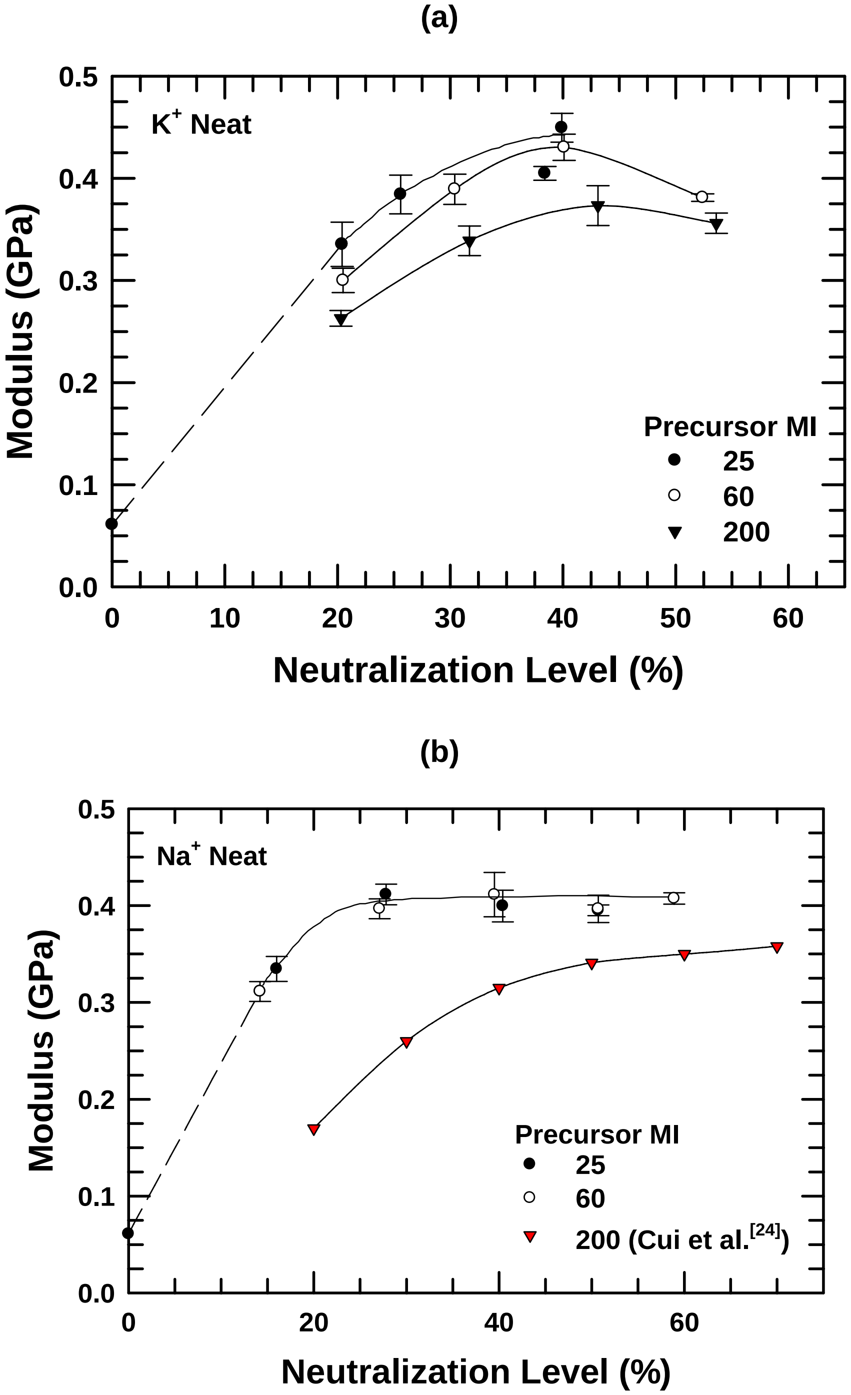
(a)

(b)

Figure 6.18: Effect of neutralization level on the tensile modulus of neat K$^+$ (a) and Na$^+$ (b) ionomers used in this study and those reported by Cui et al. [24]. The modulus for the EMAA with a MI of 25 g/10 min [24] is connected with a dashed line.

The yield stress of K^+ and Na^+ ionomers versus the neutralization level is shown in Figure 6.19. The trends are similar to those seen for modulus and agree with previous reports [7, 25, 28]. The yield stress increases with increasing neutralization up to a neutralization level of 40% and plateaus at higher neutralization levels. The yield stress of the Na^+ ionomers is generally somewhat higher than that of the K^+ ionomers. Generally, the yield stress also increases as the precursor melt index decreases at any given neutralization level.

(a)

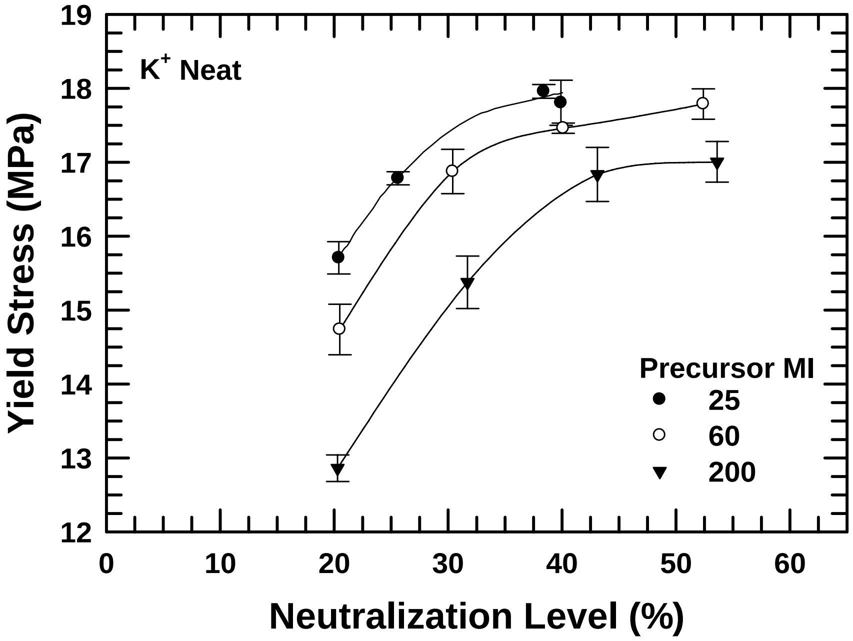

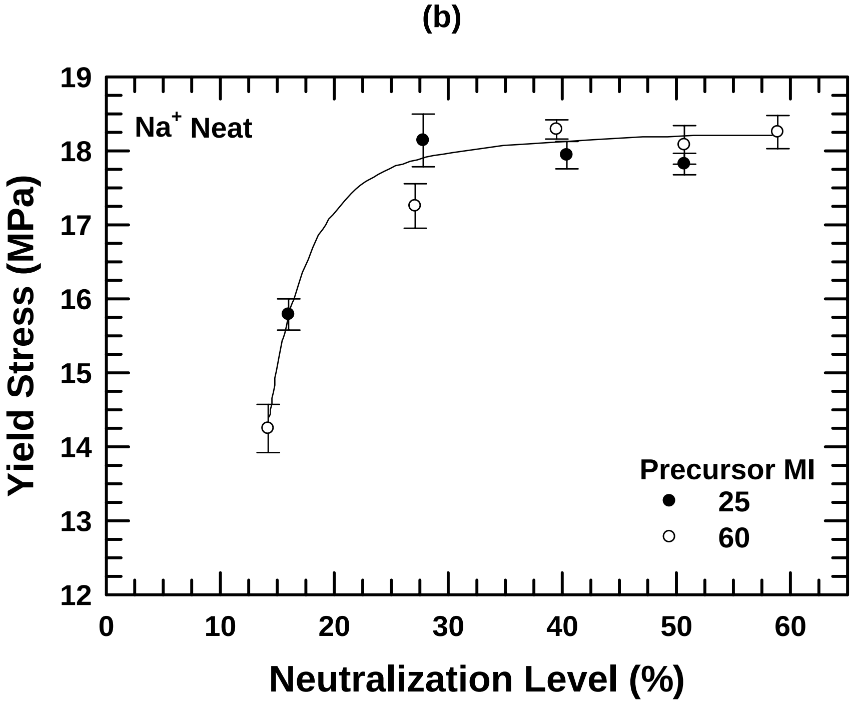

Figure 6.19: Effect of neutralization level on the yield stress of neat K^+ (a) and Na^+ (b) ionomers used in this study.

Figure 6.20 shows the elongation at break of K^+ and Na^+ ionomers versus the neutralization level. The elongation at break decreases as the neutralization level increases for both ionomer types, reflecting the increasing volumetric concentration of the ionic aggregates and the stronger interactions between the ionic groups. The results reported by Cui et al. [24] show a similar trend, though they are somewhat higher due to the difference in the time between molding and testing and the higher precursor melt index. The unneutralized EMAA was too ductile to determine the breaking point on the available equipment (> 400%). The elongation at break decreases significantly with decreasing precursor melt index at any given neutralization level. In fact, there is a much better correlation between the elongation at break and the ionomer melt index, as shown in Figure 6.21. It appears that the precursor melt index and the neutralization level have a similar effect on both the ionomer rheology as measured by the melt index and on the elongation at break. The elongation at break of the Na$^+$ ionomers is generally somewhat lower than that of the K$^+$ ionomers, in agreement with a previous report [7].

(a)

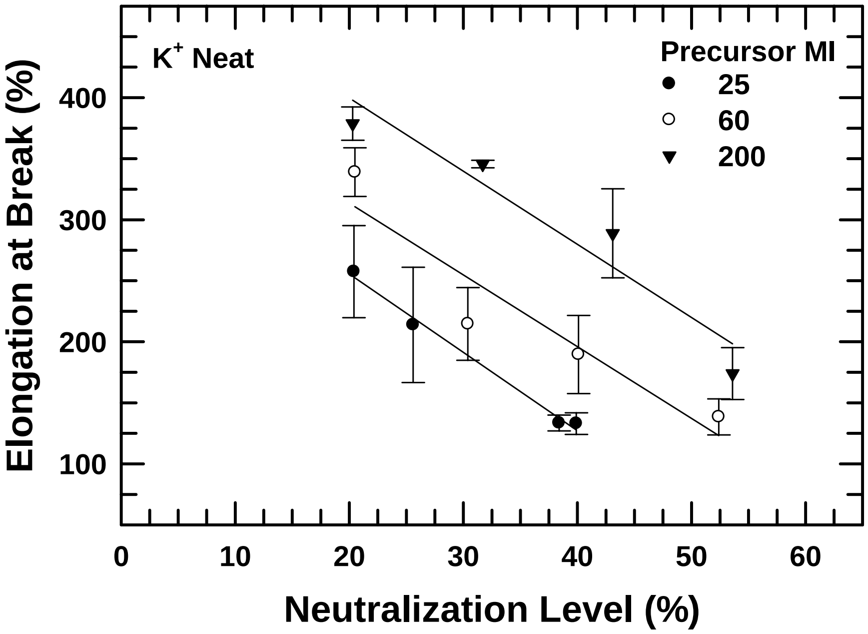

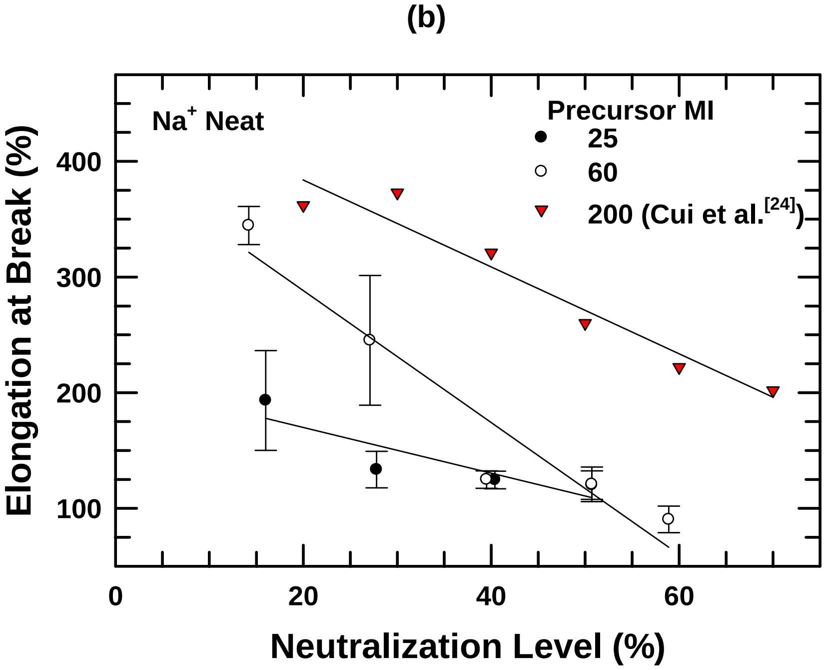

Figure 6.20: Effect of neutralization level on the elongation at break of neat K^+ (a) and Na^+ (b) ionomers used in this study and a comparison with the neat Na^+ ionomers reported by Cui et al. [24] (c).

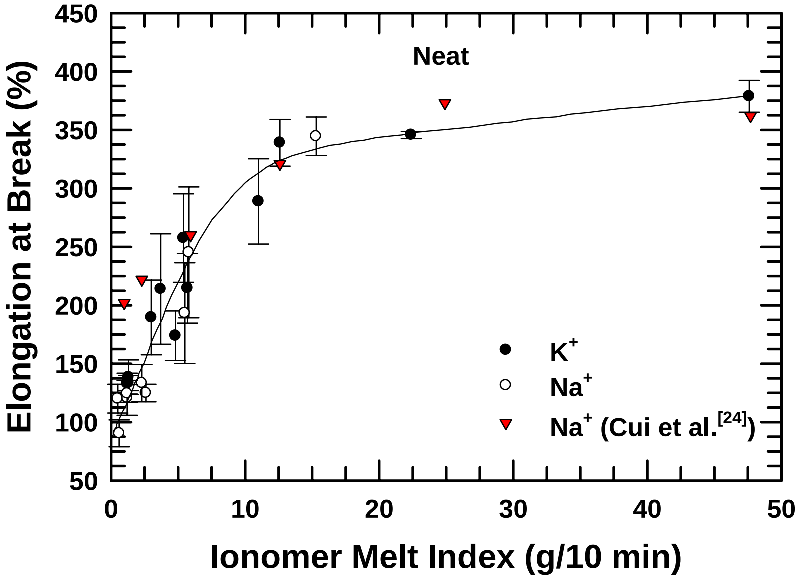

Figure 6.21: Effect of melt index on the elongation at break of neat K^+ and Na^+ ionomers used in this study and of the neat Na^+ ionomers reported by Cui et al. [24].

The Izod impact strength of K^+ and Na^+ ionomers versus the neutralization level is shown in Figure 22. Although the Izod impact strength measured at the far end is generally higher than that measured at the gate end of the neat ionomer samples, values from both ends averaged together are plotted here for simplicity. The impact strength initially increases with increasing neutralization levels, reaches a maximum between 15 and 40% neutralization, and decreases as the neutralization level further increases; the rate of this decrease is higher for the Na^+ ionomers. The fracture energy measured in an impact test reflects the integration of the resisting force of the sample over the range of sample deflection. Increasing the neutralization level increases the resisting force and decreases the ductility. At lower neutralization levels the increase in the resisting force outweighs the decrease in ductility. At higher neutralization levels, however, ductility decreases to the point where the impact strength decreases below that of the EMAA. The impact strengths of the ionomers with a precursor melt index of 200 g/10 min are generally somewhat lower than those of the ionomers with lower precursor melt indices. As shown in Figure 22(b), a similar trend was reported by Cui et al. [24], though the results reported here are higher partly due to the difference in the time between molding and testing and the higher precursor melt index. The higher crystallinity arising from the longer time between molding and testing of the ionomers examined in this work results in increased resistance to fracture that outweighs any possible decrease in ductility.

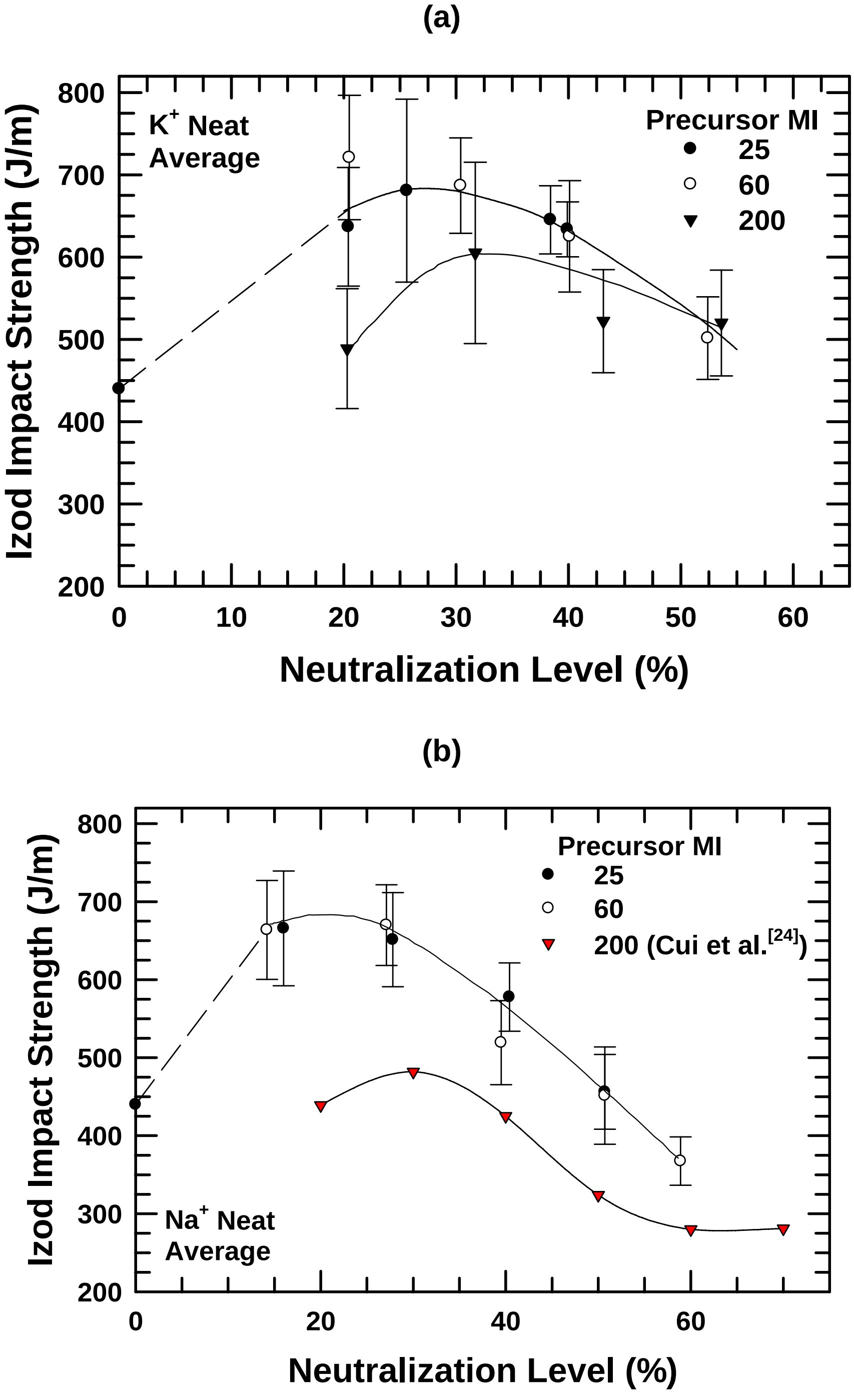

Figure 6.22: Effect of neutralization level on the Izod impact strength of neat K^+ (a) and Na^+ (b) ionomers used in this study and those reported by Cui et al. [24]. The impact strength for the EMAA with a MI of 25 g/10 min [24] is connected with a dashed line.

CONCLUSION

The effects of the degree of neutralization of the acid groups and, to some extent, the precursor melt index on the properties of Na^+ and K^+ EMAA ionomers are examined. DSC and modulus results indicate that the physical ageing effect due to secondary crystallization generally plateaus after 21 days after melt processing. K^+ ionomers absorb more water than Na^+ ionomers, and water absorption has a plasticization effect on the ionomers. DSC results indicate that the T_i, ΔH_i, and ΔH_m increase, while the T_m decreases with increasing neutralization level. These results indicate that crystallization increases with increased neutralization. The mechanical relaxation seen by DMA in the vicinity of the T_i shifts to higher temperatures as the neutralization level increases. The effects of precursor melt index are not as significant.

The complex viscosity, storage modulus, and loss modulus increase dramatically with decreasing precursor melt index. The rheological properties also increase as the neutralization level increases to a lesser extent. The Na^+ ionomers have somewhat higher rheological properties than the K^+ ionomers.

The ionomer modulus and yield strength increase with increasing neutralization level up to 40% neutralization and then plateau or slightly decrease with further neutralization. The plateaus/maxima may be the result of an optimal spacing of alkaline ions and carboxyl groups within ionic groups at neutralization levels near 33%. The elongation at break decreases with increasing neutralization. The precursor melt index and the neutralization level appear to affect both the elongation at break and the melt index of the ionomers similarly, resulting in a good correlation between the ionomer melt index and the elongation at break. The elongation at break of the K^+ ionomers is generally higher that that of the Na^+ ionomers. The impact strength decreases with increasing neutralization level. The modulus, yield stress, and impact strength are generally lowest for the ionomers with the highest precursor melt index.

REFERENCES

1. Eisenberg A and Kim J-S. Introduction to Ionomers. New York: Wiley, 1998.
2. Schlick S. Ionomers: Characterization, Theory, and Applications. Boca Raton, FL: CRC Press, 1996.
3. Tant MR, Mauritz KA, and Wilkes GL. Ionomers: Synthesis, Structure, Properties and Applications. London: Blackie Academic & Professional, 1997.
4. Grady BP. Polymer Engineering & Science 2008;48(6):1029-1051.
5. Longworth R and Vaughan DJ. Nature 1968;218(5136):85-87.
6. Register RA and Cooper SL. Macromolecules 1990;23(1):318-323.
7. Hirasawa E, Yamamoto Y, Tadano K, and Yano S. Journal of Applied Polymer Science 1991;42(2):351-362.
8. Tierney NK and Register RA. Macromolecules 2002;35(6):2358-2364.
9. Bonotto S and Bonner EF. Macromolecules 1968;1(6):510-515.
10. Tachino H, Hara H, Hirasawa E, Kutsumizu S, and Yano S. Journal of Applied Polymer Science 1995;55(1):131-138.
11. Kutsumizu S, Tadano K, Matsuda Y, Goto M, Tachino H, Hara H, Hirasawa E, Tagawa H, Muroga Y, and Yano S. Macromolecules 2000;33(24):9044-9053.
12. Marx CL and Cooper SL. Journal of Macromolecular Science, Part B 1974;9(1):19 - 33.
13. Tsujita Y, Shibayama K, Takizawa A, Kinoshita T, and Uematsu I. Journal of Applied Polymer Science 1987;33(4):1307-1314.
14. Kohzaki M, Tsujita Y, Takizawa A, and Kinoshita T. Journal of Applied Polymer Science 1987;33(7):2393-2402.
15. Kuwabara K and Horii F. Journal of Polymer Science Part B: Polymer Physics 2002;40(11):1142-1153.
16. Kulkarni HP, Mogilevsky G, Mullins WM, and Wu Y. Journal of Materials Research 2009;24:1087-1092.
17. Tadano K, Hirasawa E, Yamamoto H, and Yano S. Macromolecules 1989;22(1):226-233.

18. Ray AK. Journal of Thermal Analysis and Calorimetry 1996;46(6):1527-1539.
19. Akimoto H, Kanazawa T, Yamada M, Matsuda S, Shonaike GO, and Murakami A. Journal of Applied Polymer Science 2001;81(7):1712-1720.
20. Kutsumizu S, Goto M, and Yano S. Macromolecules 2004;37(13):4821-4829.
21. Loo Y-L, Wakabayashi K, Huang YE, Register RA, and Hsiao BS. Polymer 2005;46(14):5118-5124.
22. Vanhoorne P and Register RA. Macromolecules 1996;29(2):598-604.
23. Wakabayashi K and Register RA. Macromolecules 2006;39(3):1079-1086.
24. Cui L, Troeltzsch C, Yoon PJ, and Paul DR. Macromolecules 2009;42(7):2599-2608.
25. Rees RW and Vaughan D. J. Polym. Prepr. (Am. Chem. Soc., Div. Polym. Chem.) 1965;6:296.
26. Wilson FC, Longworth R, and Vaughan DJ. ACS Polym Prepr 1968;9(1):505–514.
27. Tachino H, Hara H, Hirasawa E, Kutsumizu S, Tadano K, and Yano S. Macromolecules 1993;26(4):752-757.
28. Rees RW and Vaughan D. J. Polym. Prepr. (Am. Chem. Soc., Div. Polym. Chem.) 1965;6:287.
29. MacKnight WJ, McKenna LW, and Read BE. Journal of Applied Physics 1967;38(11):4208-4212.
30. Wakabayashi K and Register RA. Polymer 2005;46(20):8838-8845.
31. MacKnight WJ and Earnest TR, Jr. J. Polym. Sci., Macromol. Rev. 1981;16:41.

Chapter 7: Effect of acid neutralization on the morphology and properties of K^+ and Na^+ poly(ethylene-*co*-methacrylic acid) ionomer nanocomposites

Polymer-organoclay nanocomposites can possess substantial enhancements in mechanical [1-3], barrier [4-6], thermal [7, 8], and flammability [9-11] properties at very low filler concentrations while maintaining a similar density, making them attractive replacements for conventional composites. Only high levels of exfoliation will produce nanocomposites that maximize the benefits of the high aspect ratio fillers. Although process optimization can improve organoclay exfoliation, the individual organoclay platelets must interact favorably with the polymer matrix to achieve high levels of exfoliation.

Nonpolar polyolefin matrices interact poorly with the hydrophilic silicate platelets, making uniform dispersion and effective exfoliation particularly difficult to achieve. These materials are often modified with a polar compatibilizer such as maleated polypropylene [3, 12-19] or a maleated polyethylene [20-31] to improve exfoliation and enhance properties. Another approach is the incorporation of polar comonomers like vinyl acetate [22, 32, 33] or methacrylic acid [34-37]. An extension of this approach is to neutralize some of the acid groups with metal cations to form ionomers, such as those based on poly(ethylene-co-methacrylic acid) (EMAA) [38-41]. The ionic groups enable favorable interactions between the polymer and the organoclay, resulting in a more exfoliated morphology.

Various structural aspects of an ionomer matrix affect its ability to exfoliate the organoclay, including the molecular weight, melt rheology (melt index), the acid content, the type of acid, the type of neutralizing ion, and the degree of neutralization. Previous studies have focused on finding the best organoclay structure for a given sodium ionomer

[39], the effect of different cations [40], and the effect of the degree of neutralization of the acid groups [41].

Chapter 6 explored the effects of the degree of neutralization of the acid groups and, to some extent, the precursor melt index on the properties of two series of EMAA ionomers; one is based on sodium cations, and the other is based on potassium cations [42]. This chapter explores the extent of organoclay exfoliation and the properties of nanocomposites formed from these two series of ionomers.

EXPERIMENTAL

Materials

The experimental ionomers were based on EMAA copolymers containing 15 wt% of methacrylic acid. The series of sodium and potassium ionomers compose a wide range of both neutralization levels (from 14% to 60%) and melt indices (0.5 to 48 g/10 min) as shown in Table 2.1 in Chapter 2, Table 7.1, and Figure 7.1. These materials were prepared at DuPont by extrusion neutralization of various ethylene-methacrylic acid base resins (melt indices of 25, 60, and 200 g/10 min).

The organoclay designated as $M_2(HT)_2$, donated by Southern Clay Products, was prepared by a cation exchange reaction between sodium montmorillonite (Na^+ MMT, CEC = 92 mequiv/100 g clay) and a two-tailed quaternary ammonium surfactant, dimethyl bis(hydrogenated-tallow) ammonium chloride (Arquad 2HT-75). Some frequently used abbreviations are employed here to represent the substituents on the ammonium cation, e.g., M for methyl and HT represents long alkyl chains from hydrogenated tallow [1, 39, 43]. This organoclay was selected based upon recent reports that this organoclay resulted in the best exfoliation in similar ionomer matrices [39, 41].

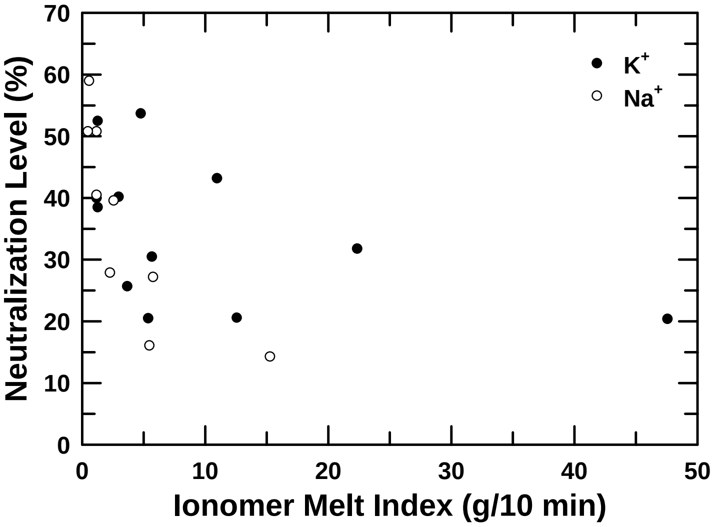

Figure 7.1: Melt indices and neutralization levels of neat K^+ and Na^+ ionomers used.

Melt processing

The ionomers and the organoclay were dried in a vacuum oven at 50 °C for a minimum of 48 h or 24 h, respectively, prior to melt processing. Nanocomposites were melt compounded in a Haake co-rotating, intermeshing twin screw extruder (diameter = 30 mm, L/D = 10) using a screw speed of 280 rpm, a feed rate of 1 kg/h, and a barrel temperature of 200 – 225 °C depending on the degree of neutralization of the ionomer.

The desired amounts of organoclay and ionomer were hand-mixed prior to extrusion and introduced into the extruder by a single hopper. Precautions were taken to minimize the loss of organoclay during extrusion to ensure that the predetermined polymer/MMT ratio was maintained. The ashing method commonly used in prior studies from this laboratory [31, 44, 45] to determine the amount of montmorillonite in the nanocomposite was not employed for these ionomers because the burning of the polymer at 900 °C resulted in a hard, yellowish-green coating on the inside of the crucible, indicating the formation of complex compounds from the inorganic component of the ionomers. The amount of the residue varied from sample to sample, rendering this method useless for quantitative analysis.

Nanocomposite pellets were dried in a vacuum oven at 50 °C for a minimum of 4 days prior to injection molding. Tensile specimens (ASTM D638, Type I) and Izod bars (ASTM D256) were prepared by an Arburg Allrounder 305-210-700 injection-molding machine using a barrel temperature of 200 – 225 °C, a mold temperature of 25 °C, an injection speed of 34 mm/s, an injection pressure of 55 – 65 bar, and a holding pressure of 50 – 55 bar. After molding, the samples were immediately sealed in polyethylene bags and placed in a vacuum desiccator for 21 days prior to testing, unless otherwise specified. The results below are reported in terms of the weight percent montmorillonite (MMT) in the composites rather than the amount of organoclay because the silicate is the reinforcing component.

Characterization

Differential scanning calorimetric (DSC) thermograms recorded using a Perkin-Elmer Model DSC-7, melt rheological characteristics measured using an AR 2000ex Rheometer with a parallel plate fixture, and dynamic mechanical analyses of the nanocomposites determined using a Rheometric Scientific Dynamic Mechanical Thermal Analyzer (DMTA) Mk III were performed on ionomer nanocomposite samples as described in more detail in Chapter 6 [42].

Morphology was examined via a FEI TECNAI G2 F20 X-TWIN TEM operating under an accelerating voltage of 200 kV. Ultra-thin sections (~50 nm) for morphological analysis were taken from the core portion of an injection molded bar in the plane defined by the flow direction (FD) and the normal direction (ND) using an RMC PowerTome XL microtome [46]. The nanocomposite samples and the diamond knife were cooled to -

100 °C and -58 °C, respectively, using liquid nitrogen. Cut sections were collected onto 400-mesh grids and dried with filter paper. Quantitative particle analysis was performed on TEM micrographs to determine the particle length, thickness, and various averages of the aspect ratio using the methods described previously [31].

Wide angle X-ray scattering (WAXS) scans were performed using a Bruker-AXS D8 Advance diffractometer in the reflection mode, using an incident X-ray wavelength of 0.1541 nm at a scan rate of 3.0°/min over the range of $2\theta = 1°$ to $12°$. The skin of the major face of the rectangular nanocomposite bars and the organoclay powder were scanned [47].

Tensile tests and notched Izod impact tests were performed on an Instron model 1137 machine upgraded for computerized data acquisition, and a TMI Impact tester (model 43-02), respectively; a more detailed description is found in Chapter 6 [42]. Data reported here are averaged from at least five specimens. As discussed in Chapter 6 [42], morphological differences arising from the injection molding process can result in significant differences between the Izod impact strength measured at the gate end (the end at which the molten polymer enters the mold during injection molding) and the far end of the samples. Because significant differences are found between the two ends in this work, the Izod impact strength data were averaged from at least five samples each of the gate end and of the far end of the bars. In some cases, values from both ends are averaged together here for simplicity.

Particle analysis

Particle analyses were performed on TEM micrographs at a magnification of 13.5K. Because of low contrast, TEM images were converted into .jpg format and opened in GIMP (GNU Image Manipulation Program). Two tracings in separate, transparent layers were made of particle length and thickness. For nanocomposites with single platelets, the thickness of these platelets could not be measured accurately and was assigned a thickness of 0.94 nm corresponding to the known results for MMT platelets [32, 48]. Each tracing was saved separately in .tif format and imported into the image analysis program, SigmaScan Pro, where each particle tracing was assigned a number and their characteristic dimensions were measured. Because the numbers assigned in the tracing of the length and the tracing of the thickness of the particles do not correspond, the particle dimensions must be matched manually. In this work, four different kinds of aspect ratios are calculated, i.e., the number and weight averages of the aspect ratios calculated for individual particles, $\langle l/t \rangle_n$ and $\langle l/t \rangle_w$, and ratios of the number and weight averages of particle lengths and thicknesses, $\left(\overline{l_n}/\overline{t_n}\right)$ and $\left(\overline{l_w}/\overline{t_w}\right)$. To ensure statistical validity of the analysis, > 400 particles were counted to measure the length, thickness, and aspect ratio. The particle density was estimated by dividing the number of particles in a TEM micrograph by the micrograph area.

RESULTS AND DISCUSSION

Based on previous work [32, 49, 50], the degree of organoclay exfoliation and, hence, the properties of the nanocomposites are affected by the interaction between the organoclay and the polymer and to some extent the melt rheology of the matrix polymer [51]. This interaction may be affected by the type of neutralizing ion (K^+ or Na^+) and the degree of neutralization. The melt rheology of the polymer also plays a role in organoclay exfoliation [51]. Because both the molecular weight of the EMAA precursor and the degree of neutralization affect the melt index, it is difficult to make ionomers with constant melt indices and varying neutralization levels, or vice versa; thus, it can be difficult to determine which variable is responsible for the effects observed The ionomers used in this work allow for some comparisons to be made on ionomers with similar neutralization level and different melt indices, or vice versa, as shown in Figure 7.1.

Morphology

Transmission electron microscopy

TEM observations allow for a visual, qualitative assessment of the degree of organoclay exfoliation in polymer nanocomposites. Figures 7.2 and 7.3 show representative TEM micrographs for K^+ and Na^+ ionomer nanocomposites with a nominal MMT content of 5 wt%. For all the nanocomposites, a mixture of intercalated stacks (tactoids) and individual platelets are observed, indicating good, though incomplete, organoclay exfoliation. Differences in the extent of organoclay exfoliation are difficult to see qualitatively. From the microscopy performed, it appears that the Na^+ ionomer nanocomposites generally have a greater degree of organoclay orientation than the K^+ ionomer nanocomposites.

Particle analysis

Particle analysis is used to quantify the extent of exfoliation shown in the TEM images. The particle analysis results for K^+ and Na^+ ionomer nanocomposites with ~5 wt% MMT are listed in Table 7.1. The aspect ratios obtained by averaging the values of each particle, $\langle l/t \rangle_n$ and $\langle l/t \rangle_w$, are generally larger than those calculated from the ratio of the corresponding average values of length and thickness, $\left(\overline{l_n}/\overline{t_n}\right)$ and $\left(\overline{l_w}/\overline{t_w}\right)$. The ratio of weight average particle length and thickness, $\left(\overline{l_w}/\overline{t_w}\right)$, is generally larger than the ratio of number average particle length and thickness, $\left(\overline{l_n}/\overline{t_n}\right)$, while the weight average aspect ratio obtained by averaging values of each particle, $\langle l/t \rangle_w$, is always larger than the corresponding number average ratio, $\langle l/t \rangle_n$. These trends generally agree with previous reports [32, 49, 52].

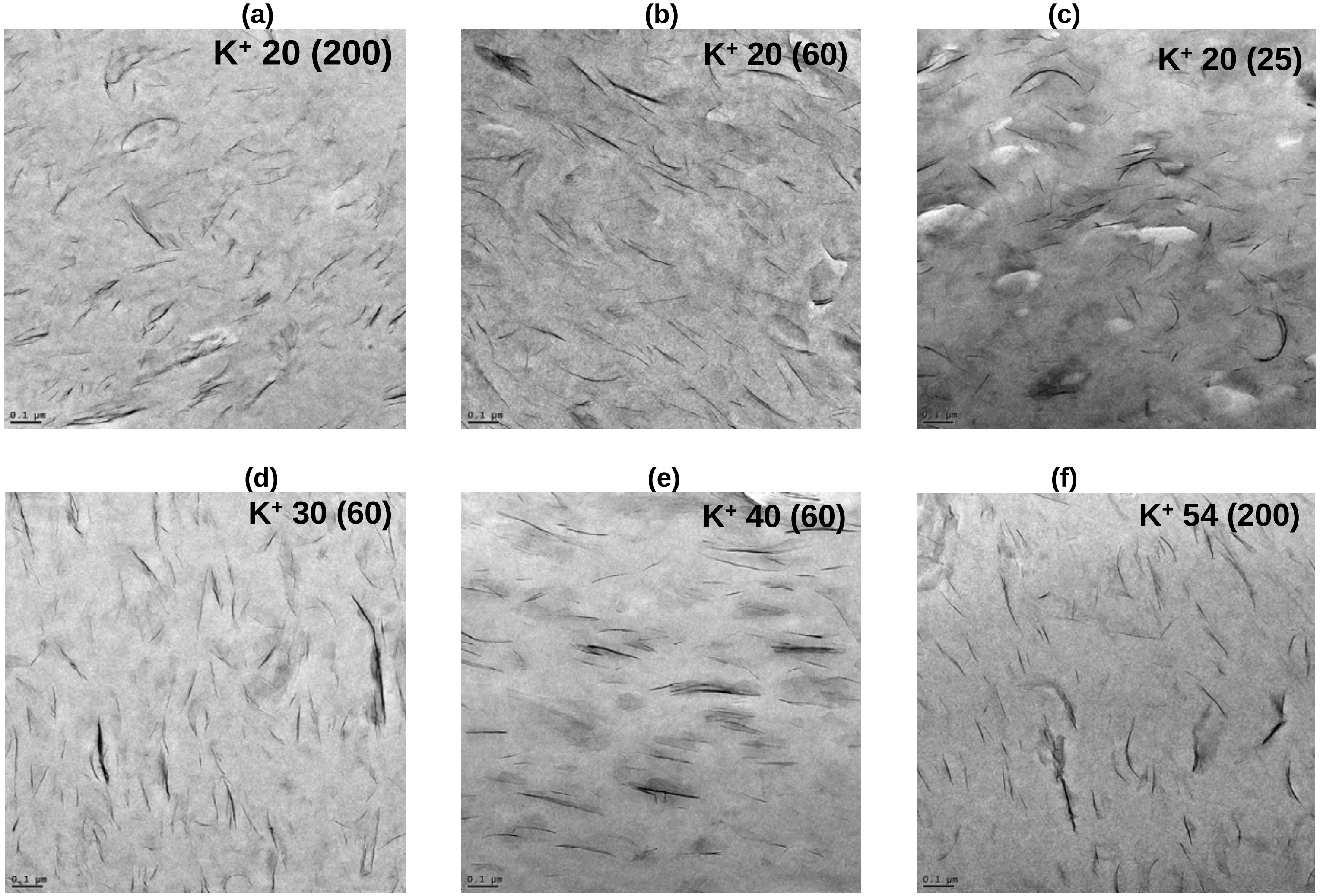

Figure 7.2: TEM photomicrographs of selected K^+ ionomer nanocomposites with ~5 wt% MMT; the neutralization level and precursor melt index (in parentheses) are noted.

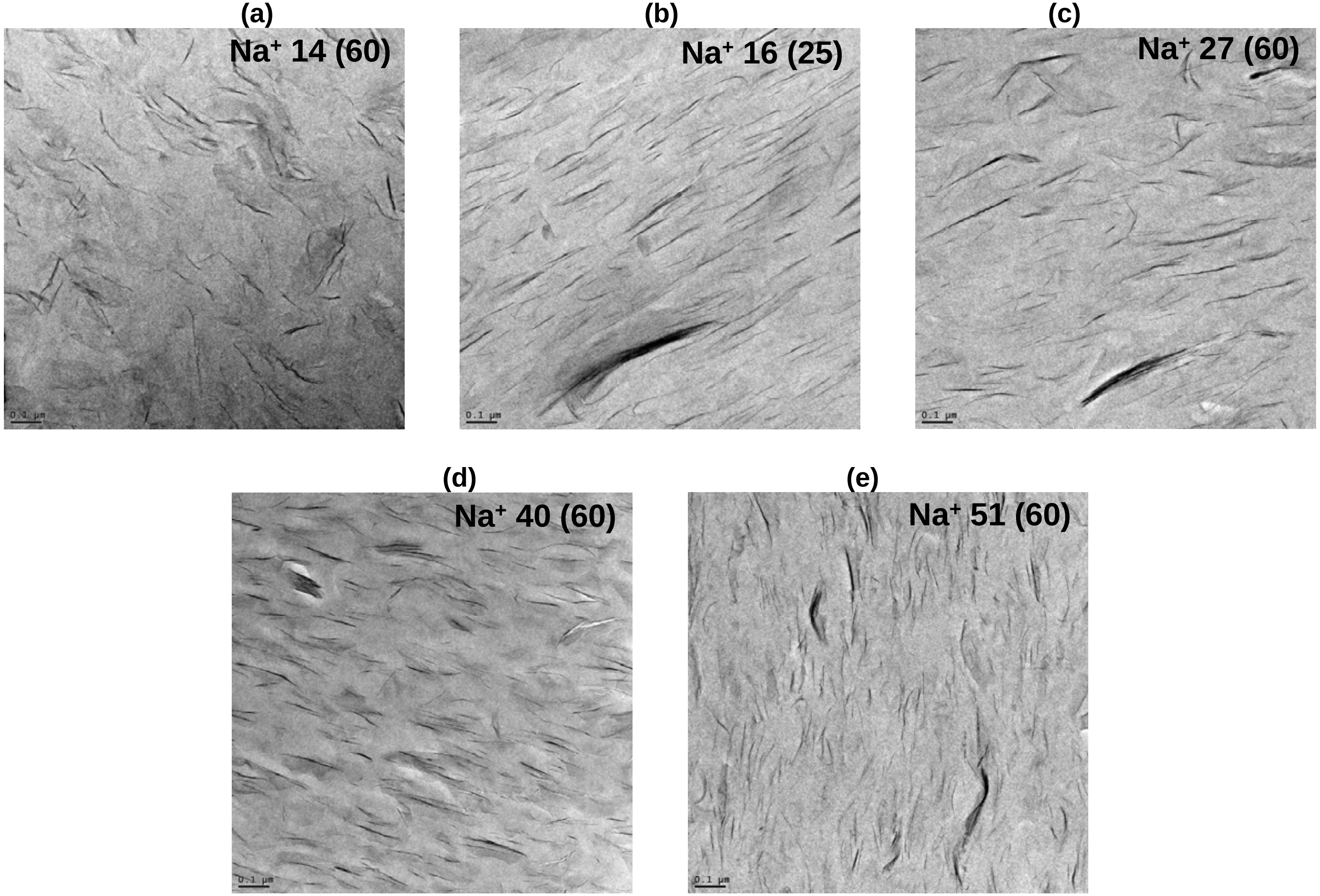

Figure 7.3: TEM photomicrographs of selected Na^+ ionomer nanocomposites with ~5 wt% MMT; the neutralization level and precursor melt index (in parentheses) are noted.

Table 7.1: Particle analysis results for K^+ and Na^+ ionomer nanocomposites

Ionomer	Precursor Melt Index (g/10 min)	Melt Index (g/10 min)	Neutralization (%)	Total number of particles	Number average particle length $\left(\overline{l_n}, nm\right)$	Number average particle thickness $\left(\overline{t_n}, nm\right)$	Weight average particle length $\left(\overline{l_w}, nm\right)$	Weight average particle thickness $\left(\overline{t_w}, nm\right)$	Number average aspect ratio $\left(\overline{l_n} / \overline{t_n}\right)$	Number average aspect ratio $\langle l / t \rangle_n$	Weight average aspect ratio $\left(\overline{l_w} / \overline{t_w}\right)$	Weight average aspect ratio $\langle l / t \rangle_w$
Na 1	60	15.3	14.2	415	90.9	1.61	106.5	1.98	56.4	59.5	53.7	68.1
Na 2	60	5.8	27.1	500	113.3	1.75	146.2	2.29	64.7	67.6	63.7	78.7
Na 3	60	2.6	39.5	503	111.8	1.64	138.9	1.91	68.1	69.9	72.7	81.0
Na 4	60	1.2	50.7	451	79.5	1.62	92.9	1.85	49.0	50.5	50.4	57.1
Na 5	60	0.6	58.9	429	84.5	1.60	100.8	1.74	52.7	53.6	57.8	61.3
Na 6	25	5.5	16	442	103.2	1.65	126.9	1.95	62.4	63.7	65.0	73.1
Na 7	25	2.3	27.8	418	93.9	1.59	113.0	1.77	59.1	60.3	63.8	69.1
Na 8	25	1.2	40.4	470	96	1.54	118.0	1.68	63.2	63.6	70.1	75.2
Na 9	25	0.5	50.7									
K 1	200	47.6	20.3	482	72.5	1.57	93.1	1.71	46.2	46.3	54.5	53.7
K 2	200	22.4	31.7	454	89.9	1.67	105.5	1.94	53.8	55.2	54.4	61.5
K 3	200	11	43.1	454	89.1	1.62	105.3	1.76	54.9	55.8	59.7	63.5
K 4	200	4.8	53.6	468	100.0	1.75	125.1	2.13	56.8	59.8	58.7	71.0
K 5	60	12.6	20.5	521	80.7	1.56	100.6	1.74	51.8	52.0	57.8	60.1
K 6	60	5.7	30.4	468	88.3	1.60	108.7	1.83	55.2	56.3	59.5	65.5
K 7	60	3	40.1	624	105.7	1.69	129.9	1.94	62.7	64.9	67.1	76.9
K 8	60	1.3	52.4	447	109.5	1.64	138.1	1.92	66.7	68.3	71.8	80.6
K 9	25	5.4	20.4	487	82.8	1.58	102.1	1.82	52.3	53.6	56.1	61.5
K 10	25	3.7	25.6	420	90.1	1.52	113.5	1.62	59.4	59.4	69.9	69.2
K 11	25	1.3	38.4									
K 12	25	1.2	39.9	618	98.9	1.65	123.1	1.97	59.8	60.9	62.4	69.0

Plots of number average particle lengths (Figures 7.4(a) and 7.5(a)) and thicknesses (Fig. 7.4(b) and 7.5(b)) and number average particle aspect ratios (Figures 7.4(c) and 7.5(c)) as a function of neutralization level are presented for K^+ and Na^+ ionomer nanocomposites containing ~5 wt% MMT. In general, the particle lengths and thicknesses increase as the neutralization level increases for K^+ ionomer nanocomposites. The particle thickness of Na^+ ionomer nanocomposites slightly decreases as the neutralization level increases and the particle length reaches a maximum at a neutralization level of approximately 40%. The particle length and thickness increase more rapidly with increasing neutralization for K^+ ionomer nanocomposites than for Na^+ ionomer nanocomposites. The aspect ratio generally increases as the neutralization level increases, except for Na^+ ionomer nanocomposites with neutralization levels > 50%. The aspect ratio of K^+ ionomer nanocomposites generally increases as the precursor melt index decreases at any given neutralization level. The aspect ratios of the Na^+ ionomer nanocomposites are generally somewhat higher than those of the K^+ ionomer nanocomposites, except for neutralization levels > 50%.

The particle density estimated from TEM images can also be used to quantify the extent of organoclay exfoliation. Figures 7.4(d) and 7.5(d) show the particle densities of K^+ and Na^+ ionomer nanocomposites containing ~5 wt% MMT. The particle density of K^+ ionomer nanocomposites does not show any definitive trends; if anything, it may decrease with increasing neutralization. However, the particle density of Na^+ ionomer nanocomposites clearly increases with increasing neutralization level. The particle density at any given neutralization level increases as the precursor melt index decreases. In addition, the particle density of Na^+ ionomer nanocomposites is generally higher than that of the K^+ ionomer nanocomposites. Considering both the aspect ratio and the particle density, it seems that the Na^+ ionomer nanocomposites have higher levels of exfoliation than K^+ ionomer nanocomposites. This result may be due to differences in the ionic group morphology and the interactions between the ionic groups and the organoclay between the K^+ and the Na^+ ionomer nanocomposites.

The particle length and aspect ratio for Na^+ ionomer nanocomposites with > 50% neutralization are lower than those of Na^+ ionomer nanocomposites with lower neutralization levels, possibly due to increased particle breakup and lower numbers of overlapping particles. The high particle densities for these nanocomposites indicate that the exfoliation is likely higher than that reflected by the aspect ratio.

(a)

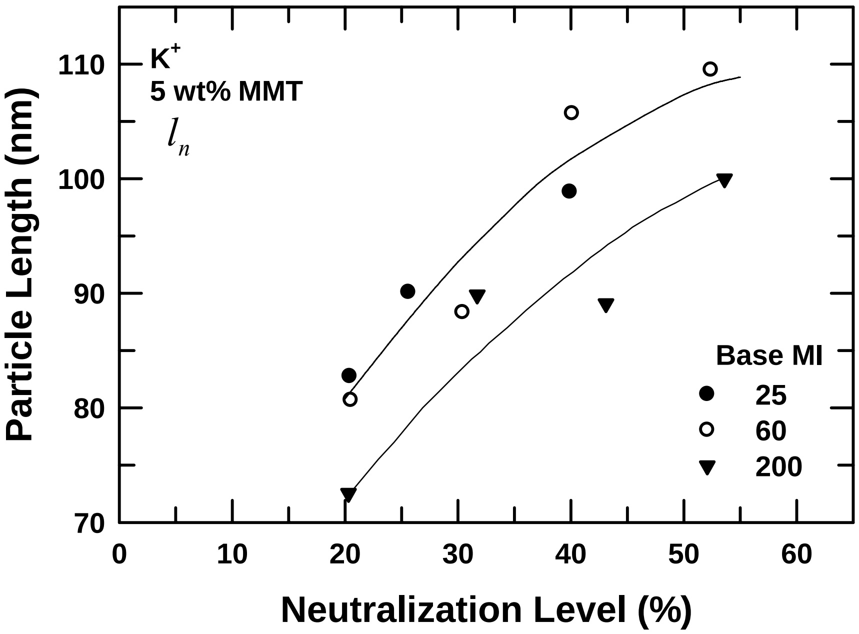

(b)

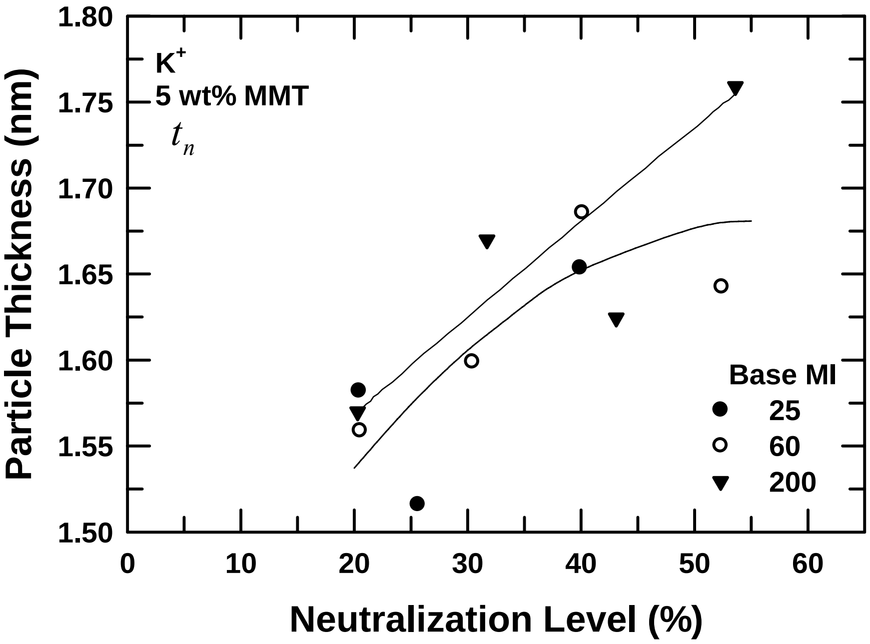
K$^+$
5 wt% MMT
t_n
Particle Thickness (nm)
1.80
1.75
1.70
1.65
1.60
1.55
1.50
0
10
20
30
40
50
60
Neutralization Level (%)
Base MI
● 25
○ 60
▼ 200

(c)

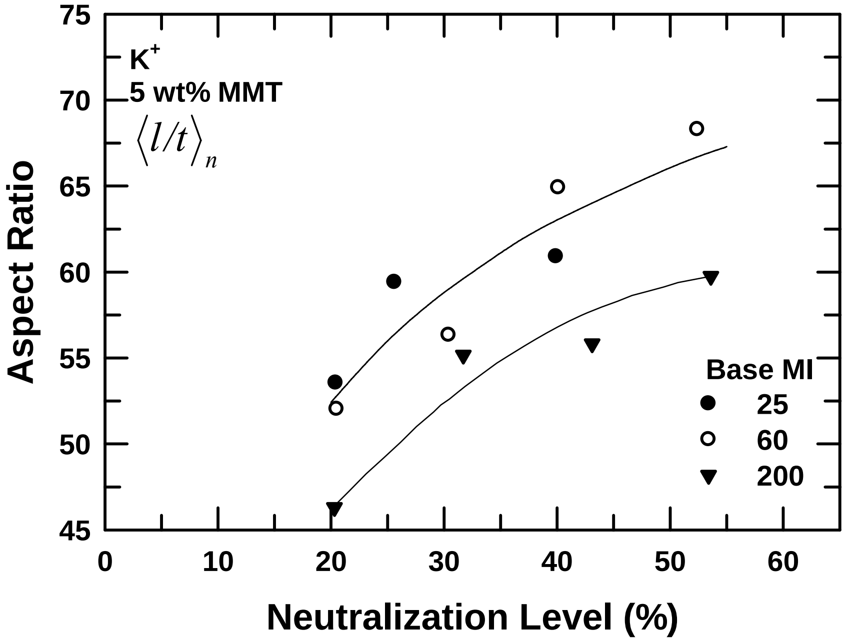
K$^+$
5 wt% MMT
$\langle l/t \rangle_n$
Aspect Ratio
75
70
65
60
55
50
45
0
10
20
30
40
50
60
Neutralization Level (%)
Base MI
● 25
○ 60
▼ 200

(d)

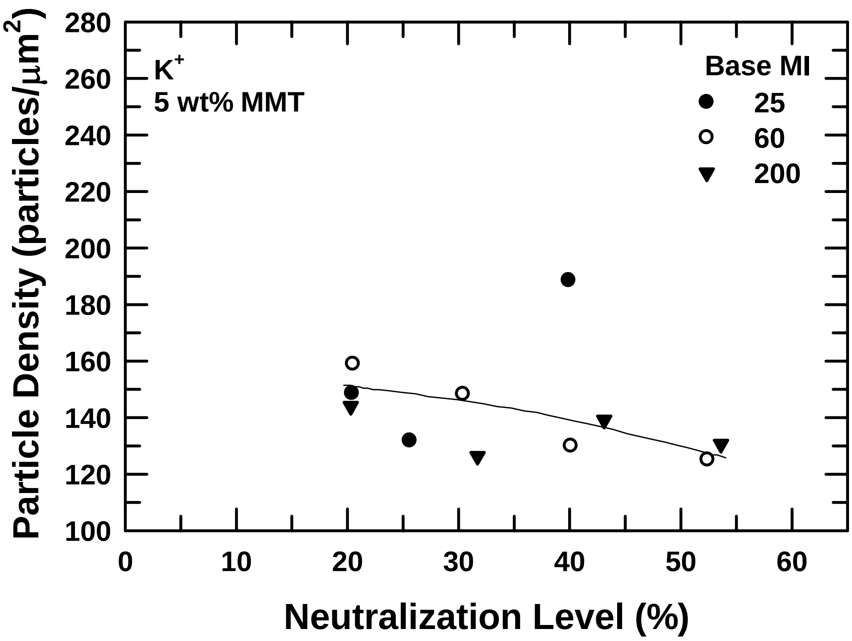

Figure 7.4: The effect of neutralization level on (a) particle length, (b) particle thickness, (c) number average aspect ratio, and (d) particle density for K$^+$ ionomer nanocomposites at a fixed MMT content of ~5 wt%.

(a)

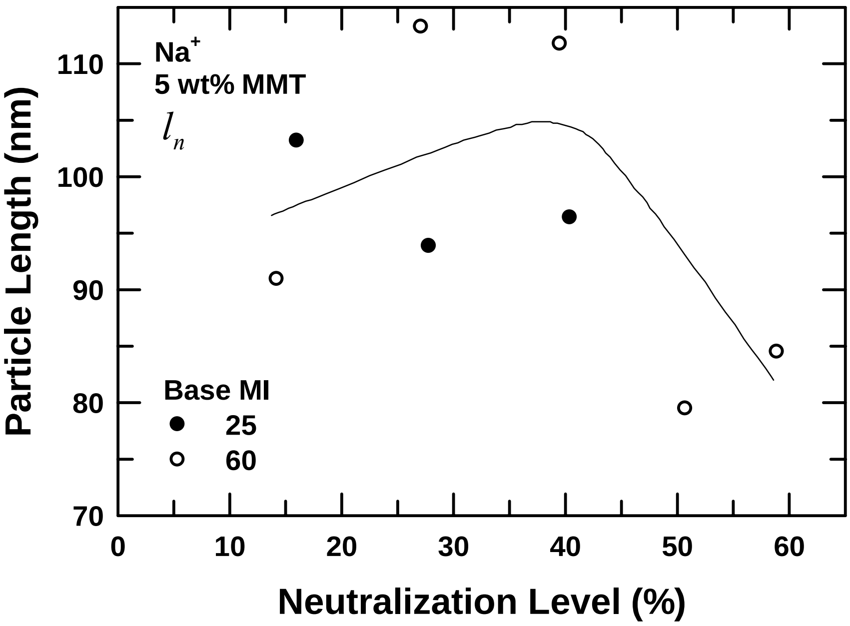

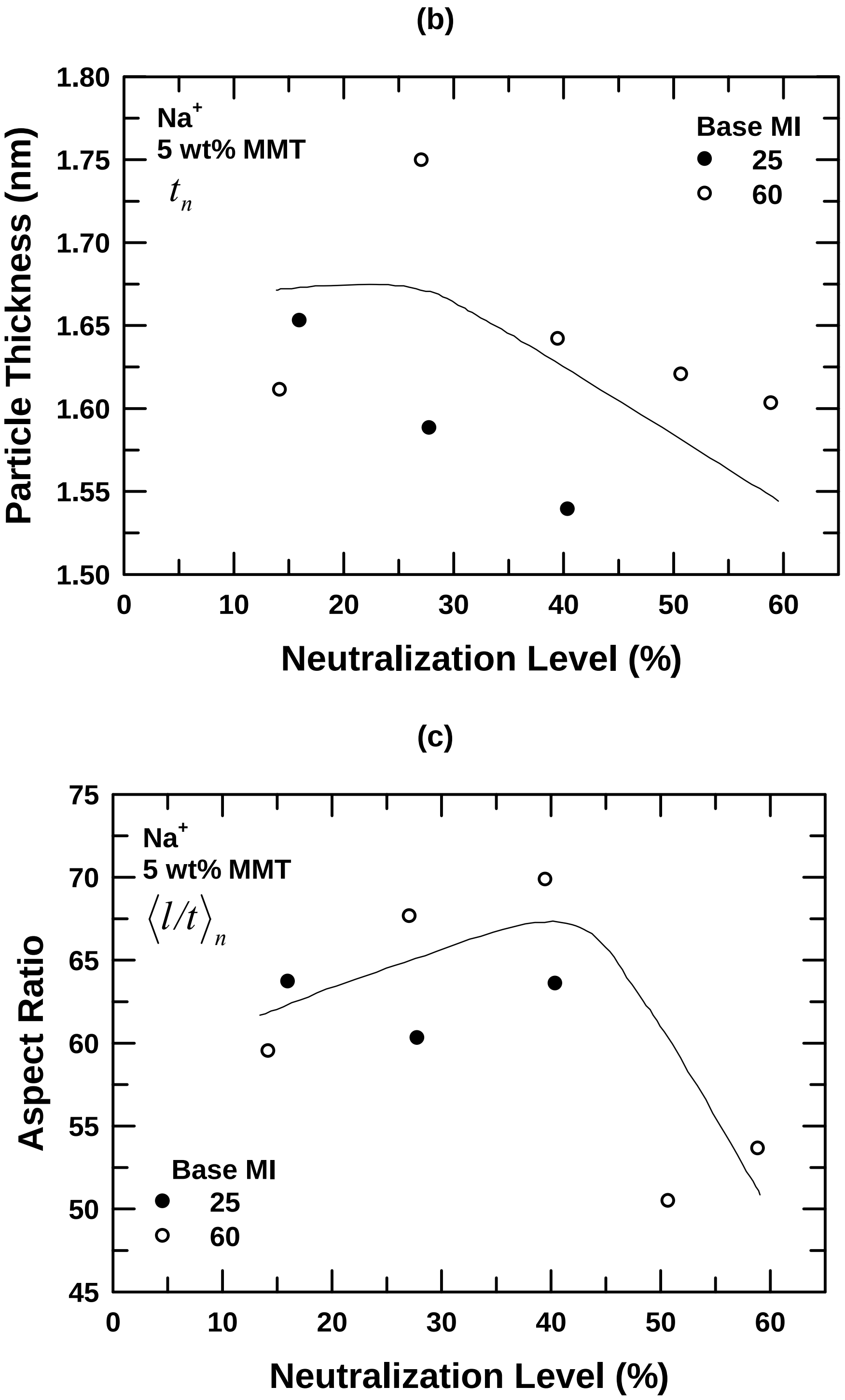
(b)
Na+
5 wt% MMT
t_n
Base MI
25
60
Particle Thickness (nm)
1.50
1.55
1.60
1.65
1.70
1.75
1.80
0
10
20
30
40
50
60
Neutralization Level (%)
(c)
Na+
5 wt% MMT
$\langle l/t \rangle_n$
Base MI
25
60
Aspect Ratio
45
50
55
60
65
70
75
0
10
20
30
40
50
60
Neutralization Level (%)

(d)

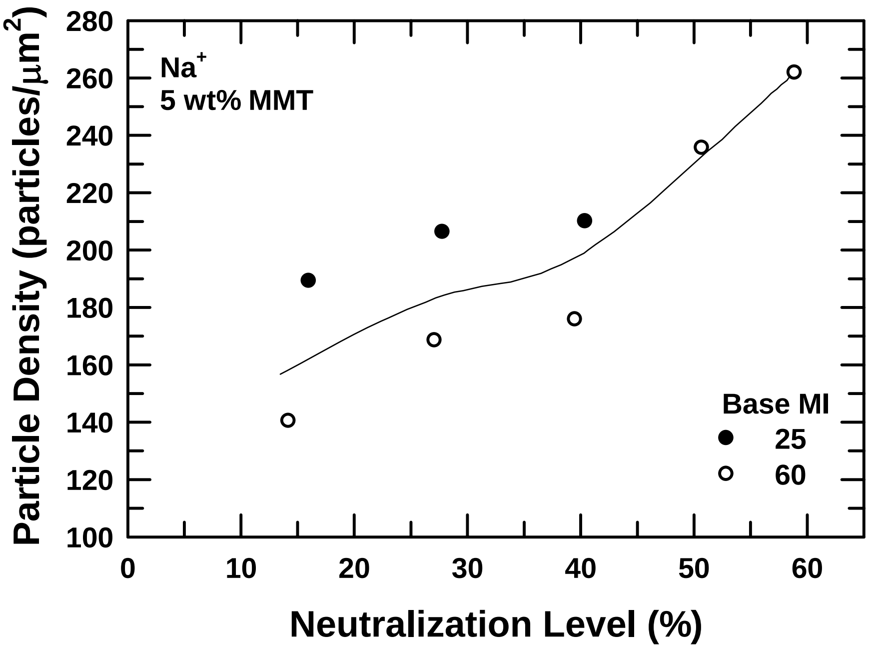

Figure 7.5: The effect of neutralization level on (a) particle length, (b) particle thickness, (c) number average aspect ratio, and (d) particle density for K^+ ionomer nanocomposites at a fixed MMT content of ~5 wt%.

Wide angle X-ray scattering

WAXS is commonly used to characterize the exfoliation of nanocomposites. WAXS scans of the neat organoclay ($M_2(HT)_2$) and of the skin portion of selected K^+ and Na^+ ionomer nanocomposites with ~5% MMT are shown in Figure 7.6. Table 7.2 shows the *d*-spacings calculated from the d_{001} peak positions. The scans of Na^+ ionomer nanocomposites with low neutralization levels (< 30%) have distinctive peaks shifted to lower angles and higher *d*-spacings, indicating polymer intercalation into the clay galleries. Na^+ ionomer nanocomposites with higher neutralization levels show no clear peaks, though there are hints of curvature at lower angles than the neat organoclay peak position. These results suggest that increasing neutralization level leads to improved exfoliation for Na^+ ionomer nanocomposites.

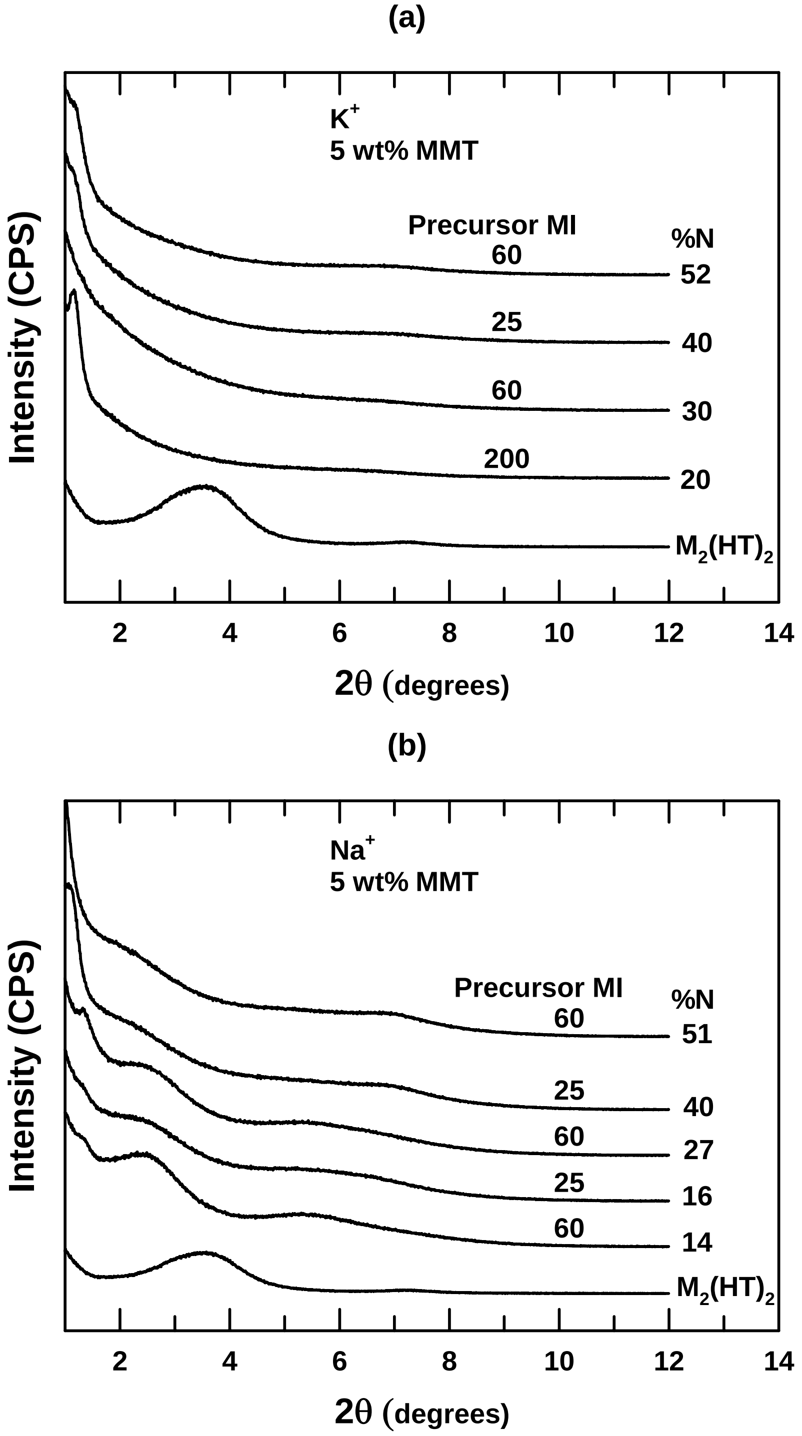

Figure 7.6: WAXS scans for the pristine $M_2(HT)_2$ organoclay and selected nanocomposites containing ~5 wt % MMT formed from K^+ (a) and Na^+ (b) ionomers. The curves are vertically shifted for clarity.

Table 7.2: Comparison of *d*-spacings of various Na^+ ionomer nanocomposites

Polymer Matrix	Organoclay	*d*-spacing (d_{001}, nm)
	$M_2(HT)_2$	2.42
Na^+ N=14% Precursor MI=60		3.49
Na^+ N=16% Precursor MI=25		3.69
Na^+ N=27% Precursor MI=60		3.67

The scans for the neat organoclay show one basal reflection due to the random orientation of the organoclay platelets in the powder, while scans of Na^+ ionomer nanocomposites show higher order reflections, indicating a high degree of orientation of the clay platelets [41, 53]. The K^+ ionomer nanocomposite scans show no basal spacing peaks. Although this result suggests a highly exfoliated structure, it may also result from less alignment of the platelets within the tactoids or from less alignment of the tactoids in the flow direction. It appears both from WAXS and TEM analysis that the Na^+ ionomer nanocomposites have higher levels of particle orientation in the flow direction. The WAXS results give only limited information about morphology and TEM, though providing a clearer understanding of exfoliation levels, examines only a small volume and may not be representative of the nanocomposite as a whole. Therefore, bulk rheological and mechanical properties were measured to complement the TEM and WAXS analyses [49, 52].

Rheological properties

The melt rheological properties of nanocomposites provide fundamental insights into the processability and morphology of these materials. Viscoelastic measurements are highly sensitive to the nanoscale and mesoscale structure of the nanocomposites and appear to be a powerful method to probe the state of dispersion in such materials [49, 54-56]. Figure 7.7 shows the rheological properties for selected K^+ and Na^+ ionomers and the corresponding nanocomposites with ~5 wt% MMT. The nanocomposites show increased complex viscosity compared to the neat polymer, especially at low frequencies, indicating the formation of a percolated network superstructure of the exfoliated platelets and tactoids. The complex viscosity of the Na$^+$ ionomer nanocomposites increases more with MMT addition than the K$^+$ ionomer nanocomposites, indicating that Na$^+$ ionomer nanocomposites have a higher level of exfoliation.

Figure 7.8 shows the ratio of the complex viscosity of the nanocomposites with ~5 wt% MMT to that of the ionomer versus the neutralization level for selected K$^+$ and Na$^+$ ionomers at a frequency of 1 rad/s, clearly demonstrating that MMT addition has a greater effect on the viscosity of Na$^+$ ionomers. The lower rheological properties of the K$^+$ ionomers may also be due in part to a plasticization effect due to residual water not removed by the drying processes. The viscosity improvement with MMT addition decreases with increasing neutralization level, particularly for Na$^+$ ionomers.

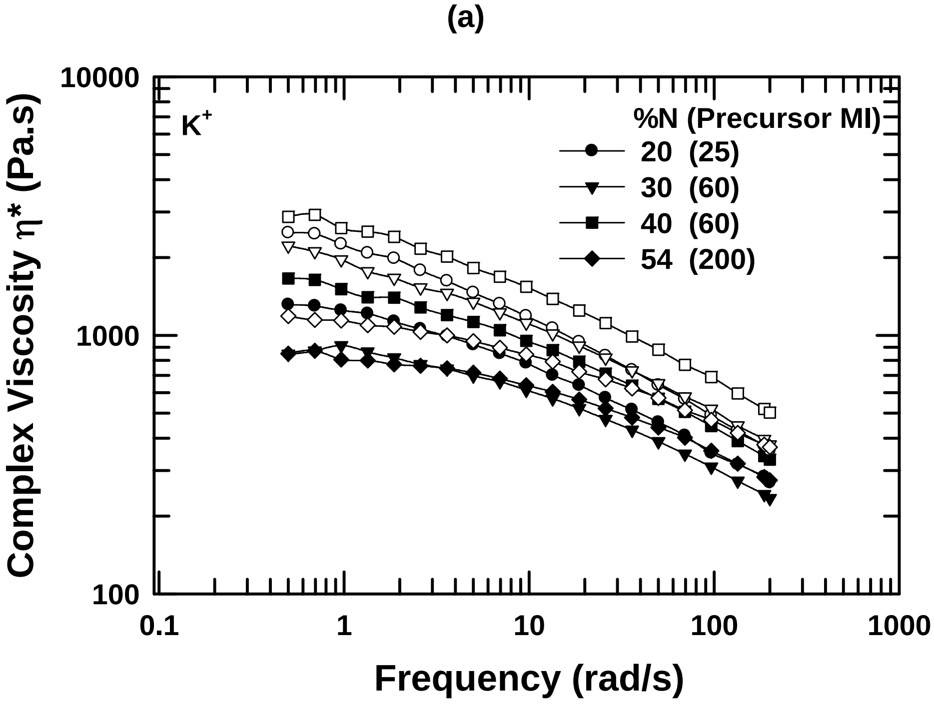

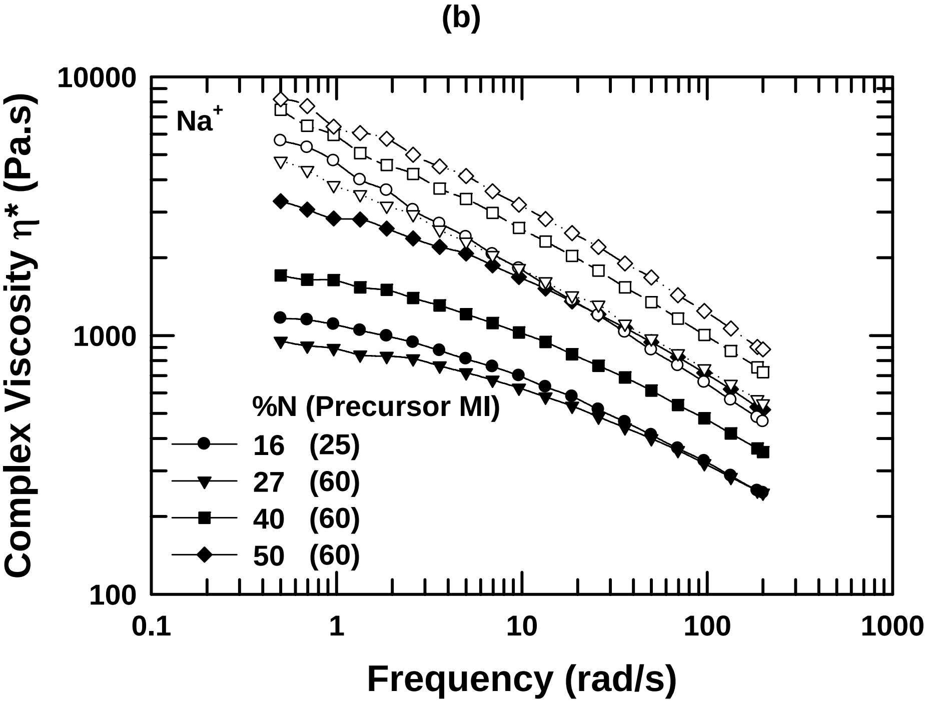

Figure 7.7: Complex viscosity for selected K$^+$ (a) and Na$^+$ (b) neat ionomers (filled) and ionomer nanocomposites with ~5 wt% MMT (unfilled) at 200 °C.

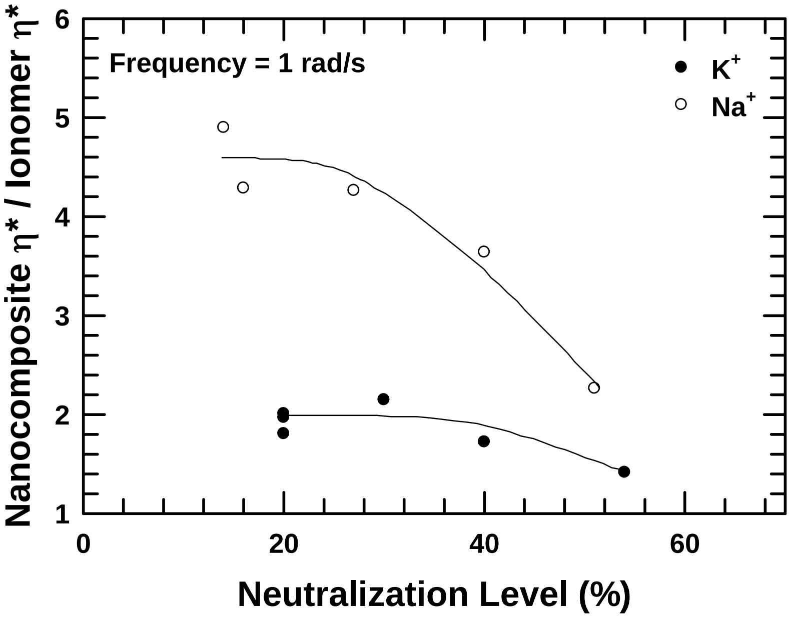

Figure 7.8: Ratio of the complex viscosity of nanocomposites with ~5 wt% MMT to that of the ionomer versus the neutralization level for selected K$^+$ (filled) and Na$^+$ (unfilled) ionomers at 200 °C.

Differential scanning calorimetry

Typical DSC thermograms of K^+ and Na^+ ionomer nanocomposites with ~5 wt% MMT measured 21 days after high temperature annealing (205-230 °C) are shown in Figure 7.9. The DSC scans reveal a low temperature (T_i) peak (42 – 50 °C) and a high temperature (T_m) peak (87 – 95 °C) associated with the melting of the secondary and primary crystallites, respectively. The T_i and the associated enthalpy (ΔH_i) increase for both ionomer types with increasing neutralization. The T_i of the Na^+ ionomer nanocomposites is typically higher than that of K^+ ionomer nanocomposites. The T_m, however, decreases with increasing neutralization level for both ionomer types. The enthalpy change for the T_m peak (ΔH_m) increases with increasing neutralization for K^+ ionomer nanocomposites; there is no clear trend for the Na^+ ionomer nanocomposites. These results indicate that the crystallization level increases with increasing neutralization level. These trends generally agree well with those found for the neat ionomers discussed in Chapter 6 [42].

(a)

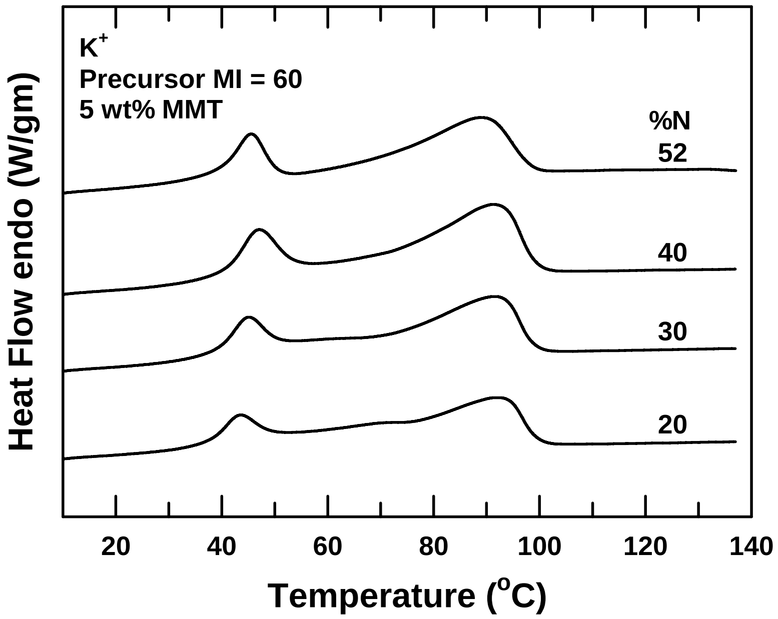

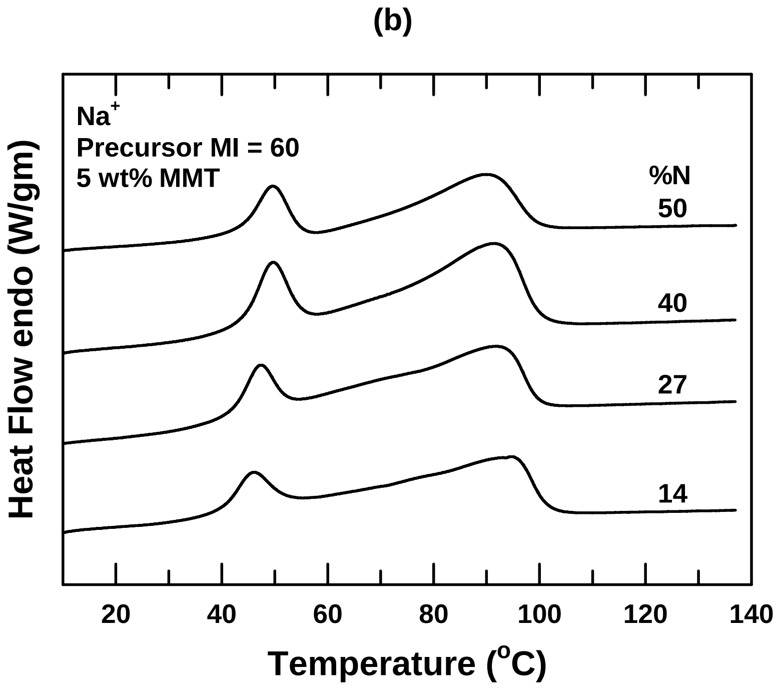

Figure 7.9: DSC thermograms of selected K^+ (a) and Na^+ (b) ionomer nanocomposites with ~5 wt% MMT, a precursor melt index of 60 g/10 min, and various levels of neutralization (%N) measured 21 days after high temperature annealing. The curves are vertically shifted for clarity.

The ratios of the ΔH_i and the ΔH_m of the nanocomposites with ~5 wt% MMT to that of the neat K^+ and Na^+ ionomers are shown in Figure 7.10. The Na^+ ionomer nanocomposites have larger increases or smaller decreases in the ΔH values as compared to the neat ionomers than the K^+ ionomer nanocomposites. The ΔH_m of the Na^+ ionomer nanocomposites increases by an average of 2.9 J/g upon addition of 5 wt% MMT, while that of the K^+ ionomer nanocomposites decreases by an average of 6.5 J/g, for example, indicating that the level of crystallinity in the Na^+ ionomers generally increases slightly with the addition of MMT, while the level of crystallinity in the K^+ ionomers decreases slightly with the addition of MMT. The organoclay may have opposing effects on crystallinity: clay particles may increase crystallization by acting as crystal nucleation sites, or clay platelets may impede crystal growth by imposing restrictions on the polymer chains [57, 58]. The clay generally appears to increase the crystallinity in the Na^+ ionomers and decrease the crystallinity in the K^+ ionomers. The decrease in crystallinity in the K^+ ionomers may also be related to a plasticization effect of the residual water not removed in the drying processes. The ΔH ratios generally decrease with increasing neutralization level, though the ΔH_m ratio of the K^+ ionomers increases with increasing neutralization level.

The differences between the peak temperatures of the nanocomposites with ~5 wt% MMT and the neat K^+ and Na^+ ionomers are shown in Figure 7.11. The T_i decreases upon MMT addition in almost all cases and decreases to a greater extent for the K^+ ionomers. This reduction in T_i may result from a decrease in crystallite size due to the increase in nucleation sites [57]. The T_m generally increases somewhat upon MMT addition and increases to a greater extent for the Na^+ ionomers. No clear trends are seen with increasing neutralization level or precursor melt index.

(a)

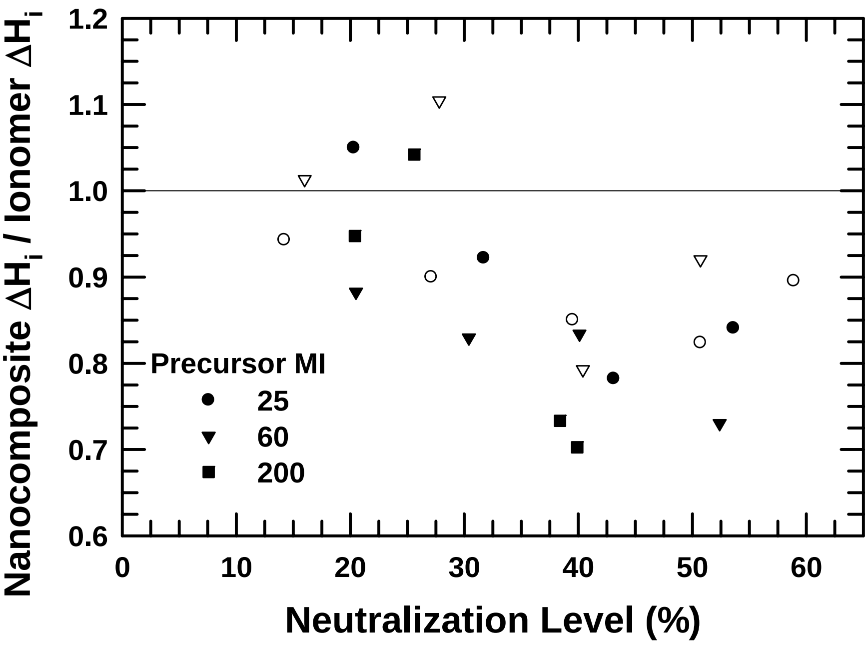

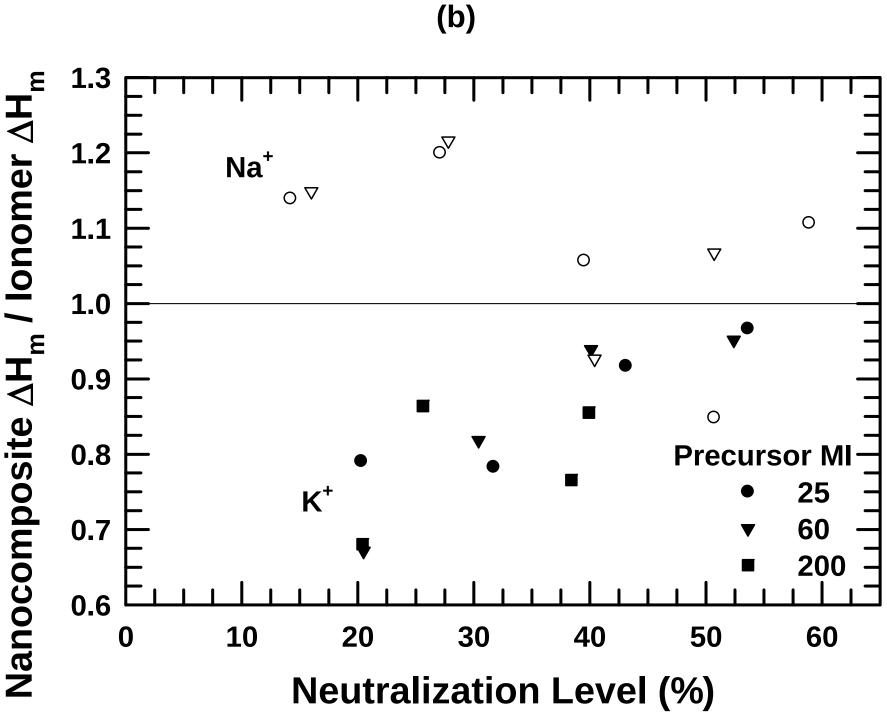

Figure 7.10: The ratios of the ΔH_i (a) and the ΔH_m (b) of the nanocomposites with ~5 wt% MMT to that of the neat K^+ (filled) and Na^+ (unfilled) ionomers.

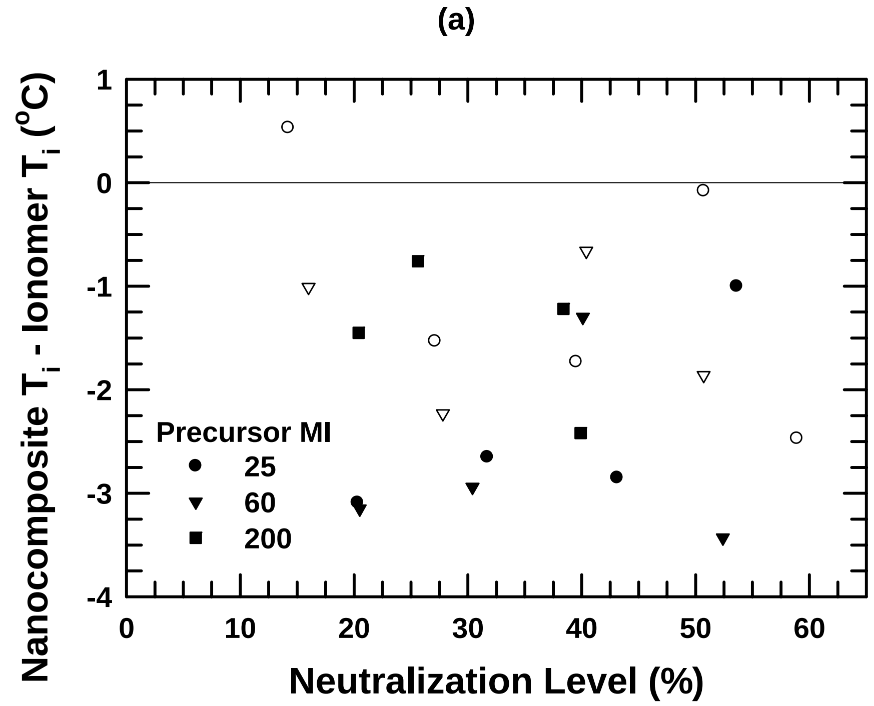

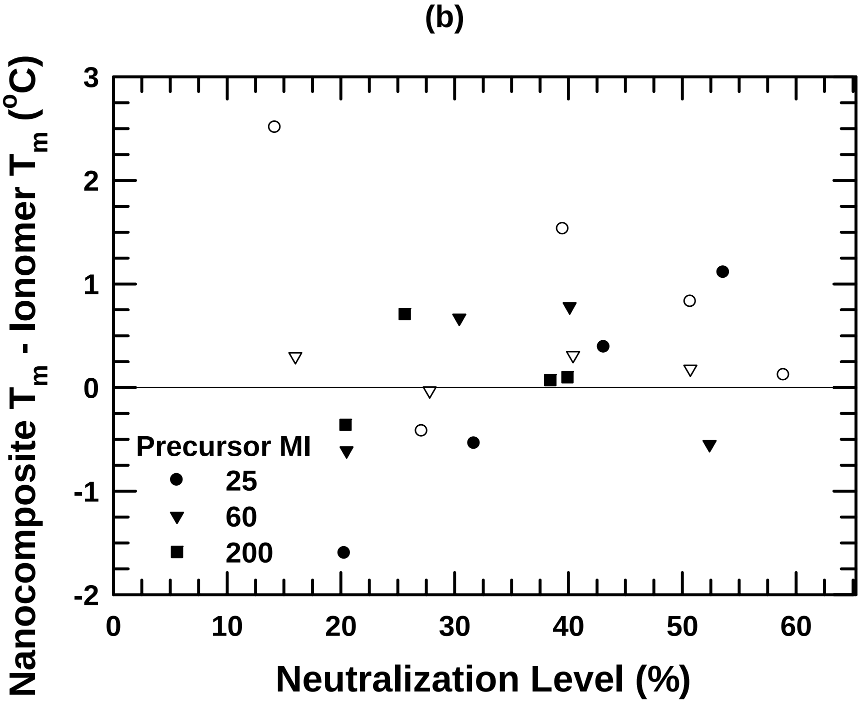

Figure 7.11: The differences between the T_i (a) and the T_m (b) of the nanocomposites with ~5 wt% MMT and the neat K^+ (filled) and Na^+ (unfilled) ionomers.

Mechanical properties

Figure 7.12 shows representative stress-strain curves for selected K^+ and Na^+ ionomer nanocomposites. The curves of both ionomer types show distinct yield points and strain hardening after yield for the neat ionomers and for some nanocomposites with < 5 wt% MMT. All the nanocomposites studied show high post-yield plastic deformation, though the extent of plastic deformation decreases as the MMT content increases in most cases. The stress at most strain levels increases with increasing MMT content for each series of ionomer nanocomposites.

(a)

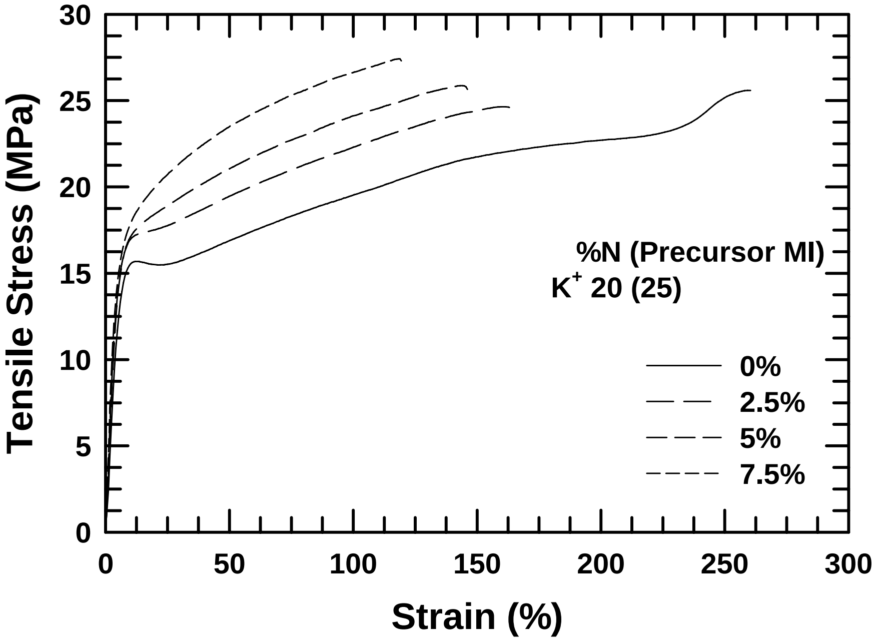
Tensile Stress (MPa)
0
5
10
15
20
25
30
Strain (%)
0
50
100
150
200
250
300
%N (Precursor MI)
K$^+$ 20 (25)
0%
2.5%
5%
7.5%

(b)

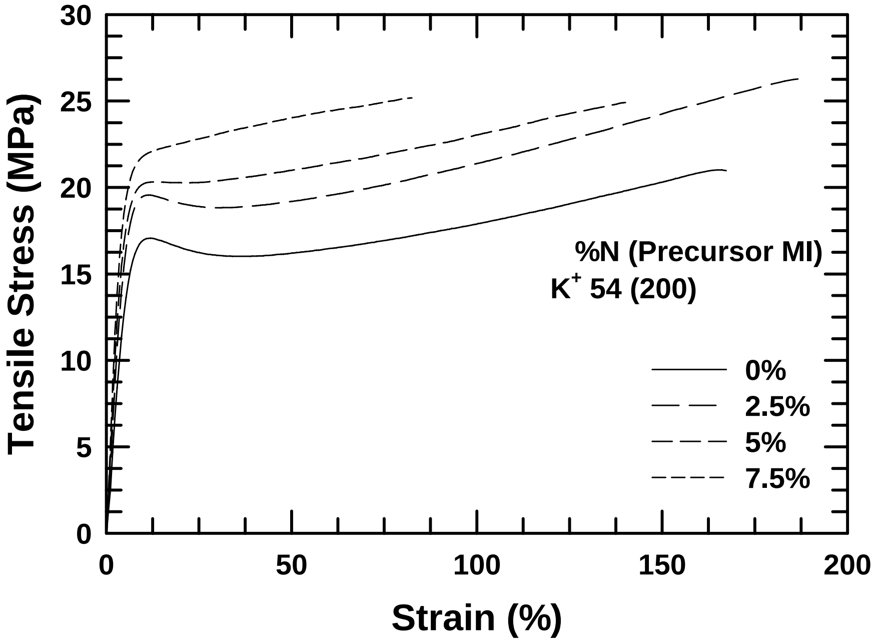
Tensile Stress (MPa)
0
5
10
15
20
25
30
Strain (%)
0
50
100
150
200
%N (Precursor MI)
K$^+$ 54 (200)
0%
2.5%
5%
7.5%

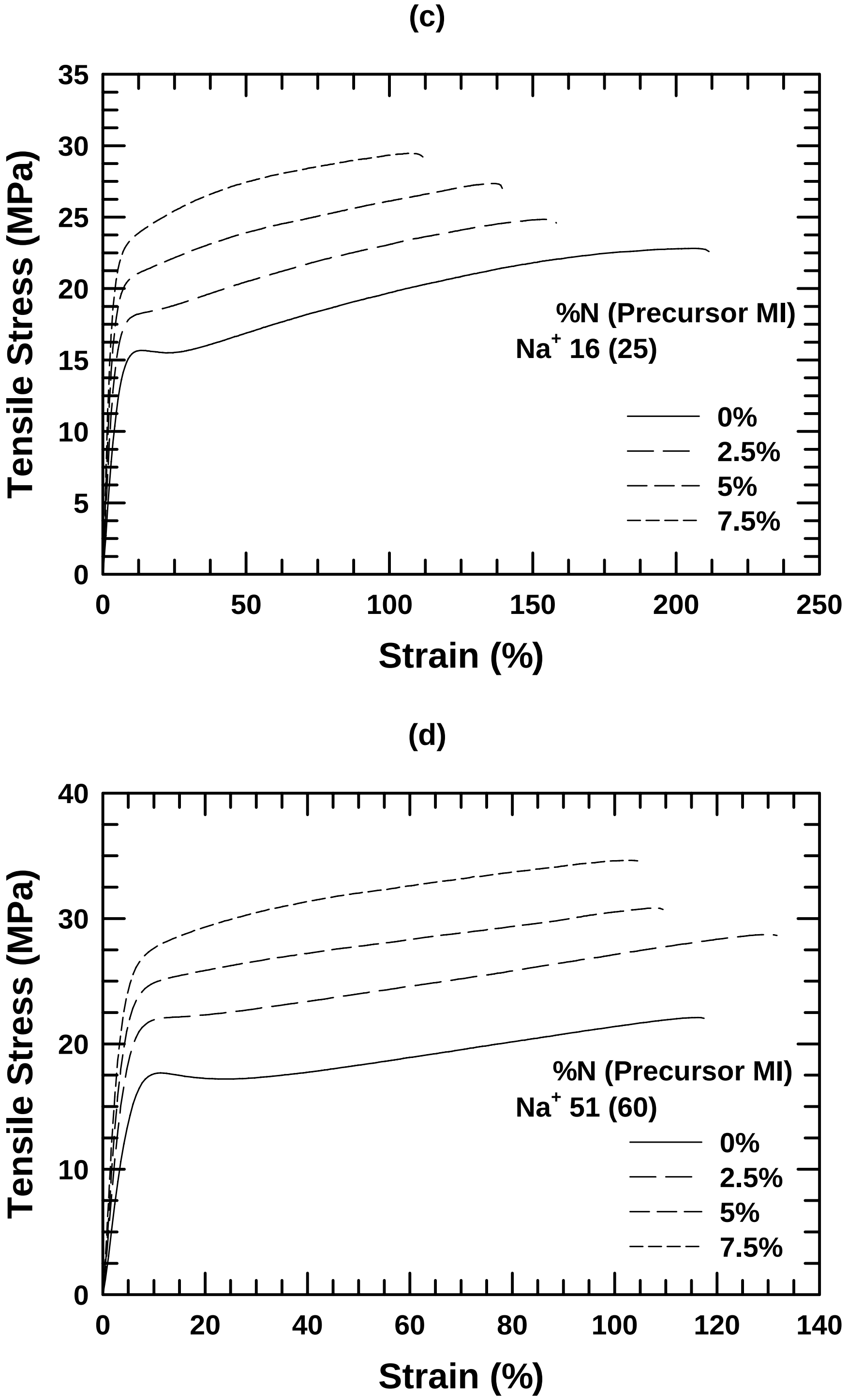

Figure 7.12: Stress-strain diagrams for nanocomposites based on selected neat K$^+$ (a) and (b) and Na$^+$ (c) and (d) ionomers at a crosshead speed of 5.1 cm/min.

Of the various mechanical properties, the tensile modulus provides the best indicator of organoclay exfoliation [1]. Because the moduli of the neat ionomers (E_m) with different degrees of neutralization and melt indices vary, examining the relative moduli (E/E_m) provides more useful comparisons. Figure 7.13 shows the effect of MMT concentration on the relative modulus of selected K^+ and Na^+ ionomer nanocomposites with various neutralization levels and a precursor melt index of 60 g/10 min. As expected, increasing the MMT content results in significantly increased relative moduli for all ionomers studied. The Na^+ ionomer nanocomposites have a significantly higher improvement in relative modulus with increasing MMT content than the K^+ ionomer nanocomposites. The improvement in relative modulus with increasing MMT content for K^+ ionomer nanocomposites increases as the neutralization level of the ionomer increases. The improvement in relative modulus with increasing MMT content for Na^+ ionomer nanocomposites, however, is higher for ionomers with neutralization levels < 30% than that of ionomers with neutralization levels > 30%.

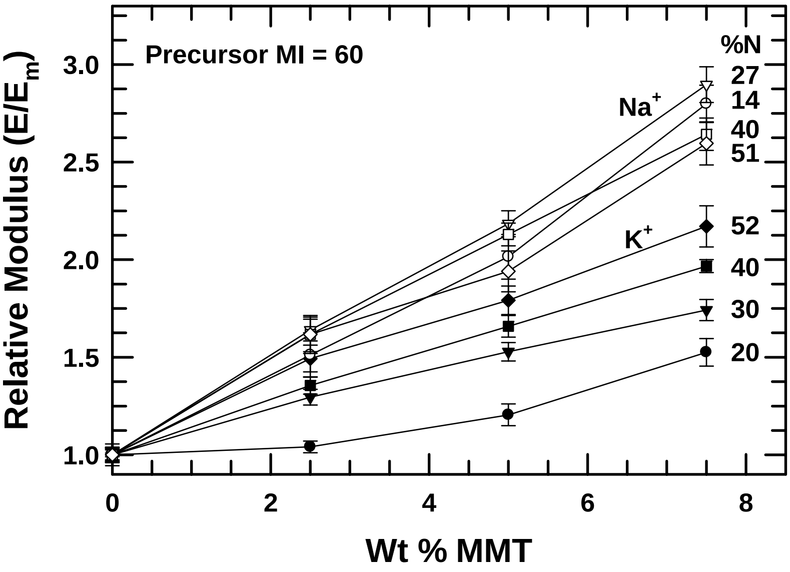

Figure 7.13: Relative modulus of selected K^+ and Na^+ ionomer nanocomposites as a function of MMT content.

To better understand the effect of the ionomer matrix, the relative modulus is plotted versus the neutralization level for K^+ and Na^+ ionomer nanocomposites with ~5 wt% MMT in Figure 7.14. Other clay loadings give similar trends. The relative modulus of K^+ ionomer nanocomposites increases as the degree of neutralization increases. Generally, the relative modulus also increases as the precursor melt index decreases at any given neutralization level. The relative moduli of Na^+ ionomer nanocomposites are higher than the relative modulus of K^+ ionomer nanocomposites at all neutralization levels and precursor melt indices. The higher exfoliation levels measured by the aspect ratios and the particle densities and the higher orientation indicated by TEM and WAXS partly explain the higher relative moduli of the Na^+ ionomer nanocomposites. The larger improvement in the Na^+ ionomer nanocomposites is also likely due, at least in part, to the increased crystallinity of the Na^+ ionomers and the decreased crystallinity of the K^+ ionomers upon addition of MMT.

(a)

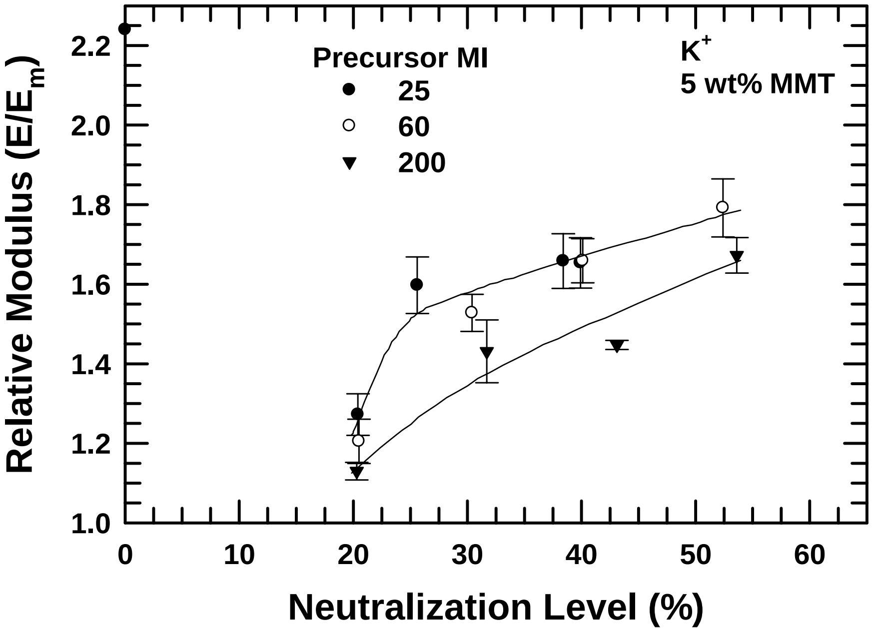

(b)

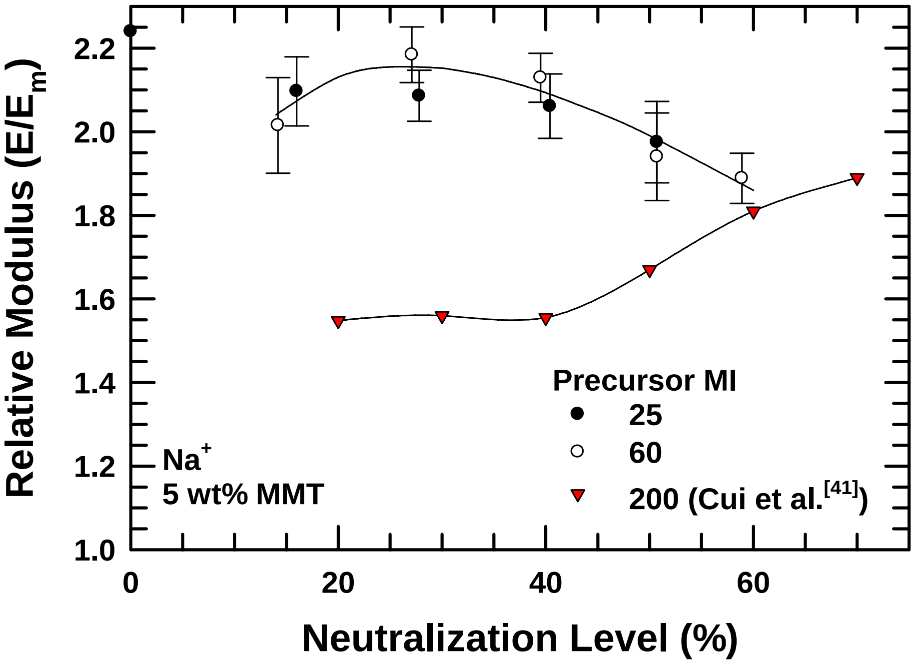

Figure 7.14: Effect of neutralization level on the relative modulus of K$^+$ (a) and Na$^+$ (b) ionomer nanocomposites used in this study and those reported by Cui et al. [41]. at a fixed MMT content of ~5 wt%. The relative modulus for the EMAA with a MI of 25 g/10 min [41] is shown for reference.

As the neutralization level increases, the relative modulus of Na$^+$ ionomer nanocomposites increases slightly at low degrees of neutralization and then decreases slightly at higher degrees of neutralization. The lower relative moduli for the Na$^+$ ionomer nanocomposites with neutralization levels > 50% is likely due to the lower aspect ratio of these nanocomposites. In addition, the moduli of the neat Na$^+$ ionomers are higher than those of the neat K$^+$ ionomers at neutralization levels > 50%. The precursor melt index does not appear to significantly affect the relative modulus at any given neutralization level, partly because of the narrower range of Na$^+$ ionomer melt indices as compared to that of the K$^+$ ionomers. The lower values reported by Cui et al. [41] can be attributed to the higher melt indices of the ionomers and the shorter time between molding and testing of the samples (minimum of 24 h versus 21 days) that causes significant morphological changes resulting from secondary crystallization as discussed in Chapter 6 [42]. The relative modulus of the EMAA, shown as a reference, is higher than that of the ionomer nanocomposites because the modulus of the neat EMAA is significantly lower than that of the neat ionomers [41].

Figure 7.15 shows the relative moduli for nanocomposites with ~5 wt% MMT plotted against the aspect ratios, $\langle l/t \rangle_n$, obtained from TEM images. In general, the relative modulus increases as the aspect ratio increases. The relative modulus of the K^+ ionomer nanocomposites increases at a higher rate than that of the Na^+ ionomer nanocomposites with increasing aspect ratio, while the Na^+ ionomer nanocomposites have significantly higher relative moduli than the K^+ ionomer nanocomposites at all aspect ratios. These trends are due likely in part to the differences in crystallinity, particle density, and particle orientation discussed above.

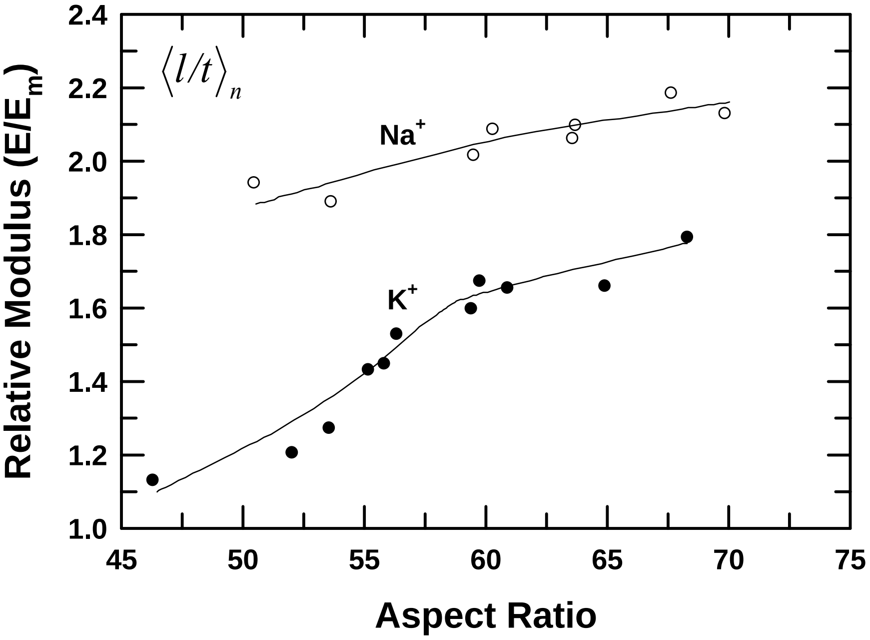

Figure 7.15: Relative modulus versus the number average aspect ratio for K^+ and Na^+ ionomer nanocomposites at a fixed MMT content of ~5 wt%.

Figure 7.16 shows the effect of MMT concentration on the elongation at break of selected K^+ and Na^+ ionomer nanocomposites with various precursor melt indices and neutralization levels. In general, the ductility decreases as the MMT content increases. However, the elongation at break of some ionomers with neutralization levels > 40% increases slightly with the addition of MMT, reaches a maximum between 2.5 and 5 wt% MMT, and then decreases upon further organoclay addition. All the nanocomposites remain very ductile (> 70% elongation at break). The elongation at break data of K^+ and Na^+ ionomer nanocomposites with ~5 wt% MMT are plotted versus the neutralization level in Figure 7.17. The elongation at break decreases as the neutralization level increases for both ionomer types, reflecting the increasing volumetric concentration of the ionic aggregates and the stronger interactions between the ionic groups. The elongation at break of the Na^+ ionomer nanocomposites is generally somewhat lower than that of the K^+ ionomer nanocomposites. Other clay loadings give similar trends. These trends mimic the results for the neat ionomers discussed in Chapter 6 [42].

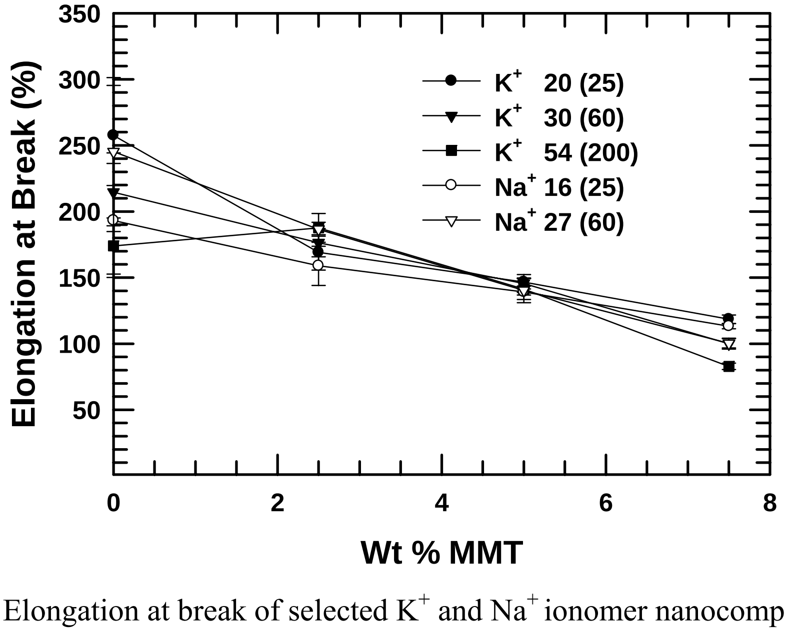

Figure 7.16: Elongation at break of selected K^+ and Na^+ ionomer nanocomposites as a function of MMT content.

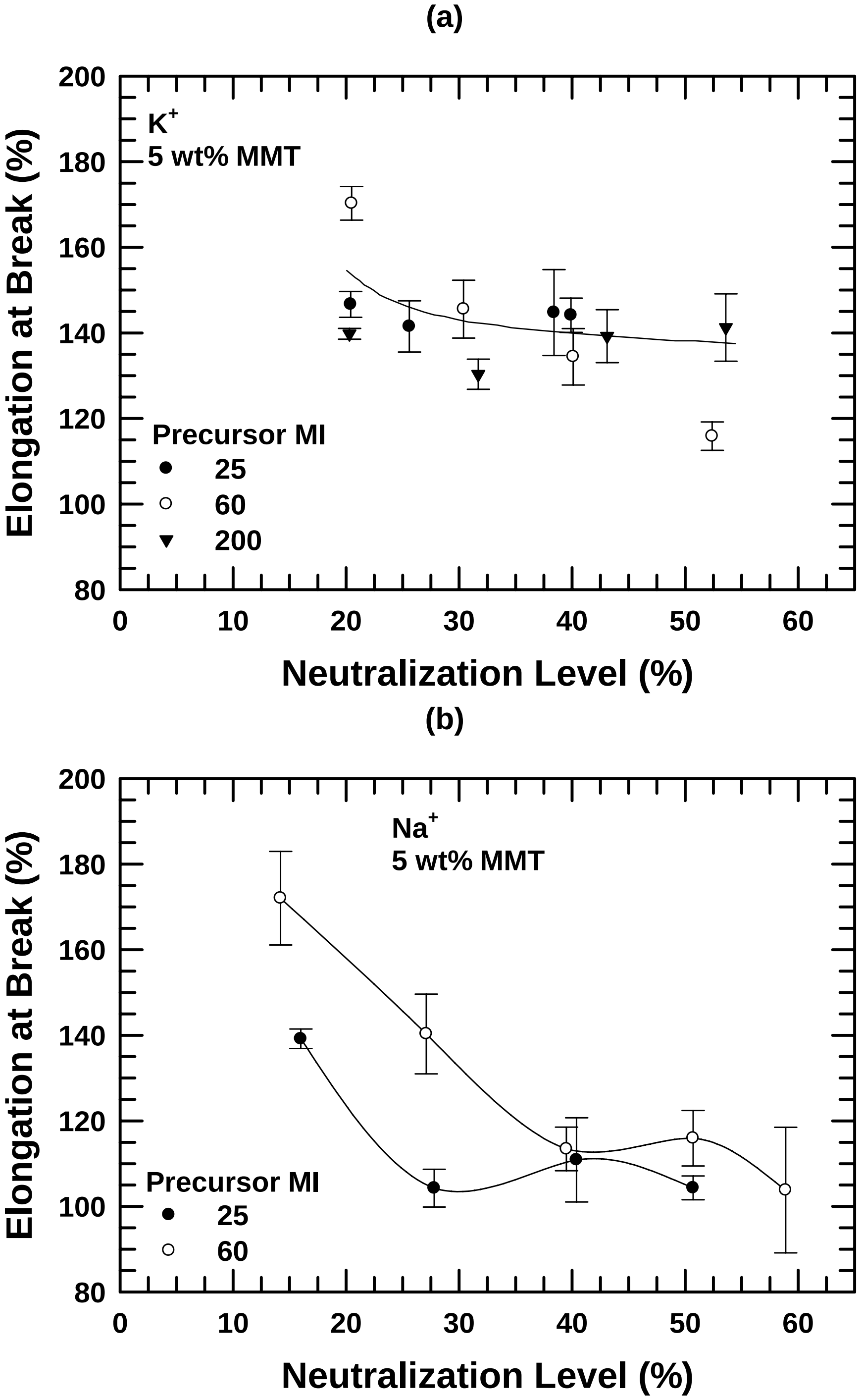

Figure 7.17: Effect of neutralization level on the elongation at break of K$^+$ (a) and Na$^+$ (b) ionomer nanocomposites used in this study at a fixed MMT content of ~5 wt%.

Fracture toughness measured by the Izod impact strength is an important property for some applications. Polymer nanocomposites based on polyolefins have been reported to have different impact values for the gate end and far end of injection-molded Izod bars [23, 31, 41, 59]. The Izod impact strength measured at the gate and far ends of selected K^+ and Na^+ ionomer nanocomposites with various precursor melt indices and neutralization levels is plotted versus the wt% MMT in Figure 7.18. For the neat polymer, the fracture energy of the gate end is generally lower than that of the far end as discussed in Chapter 6 [42]. Upon organoclay addition, however, the impact strength of the gate end tends to be higher than that of the far end. These trends may be explained by differences in the molecular orientation, crystal orientation, percent crystallinity, ion cluster morphology, and organoclay platelet orientation. The fracture energy of most of the ionomers increases with the addition of MMT, reaches a maximum between 2.5 and 5 wt% MMT, and then decreases upon further organoclay addition. This phenomena, consistent with previous reports [39, 41, 60], results from the opposing effects of increased stiffness (or yield stress) and reduced ductility.

The Izod impact strength data of K^+ and Na^+ ionomer nanocomposites with ~5 wt% MMT are plotted versus the neutralization level in Figure 7.19; the values from the gate and far ends are averaged together for simplicity. The impact strength of both ion types increases with decreasing melt index at any given neutralization level; there appears to be no significant trend with increasing neutralization level. The fracture energy of the Na^+ ionomer nanocomposites is generally higher than that of the K^+ ionomer nanocomposites due to the higher modulus of these materials. Other clay loadings give similar trends.

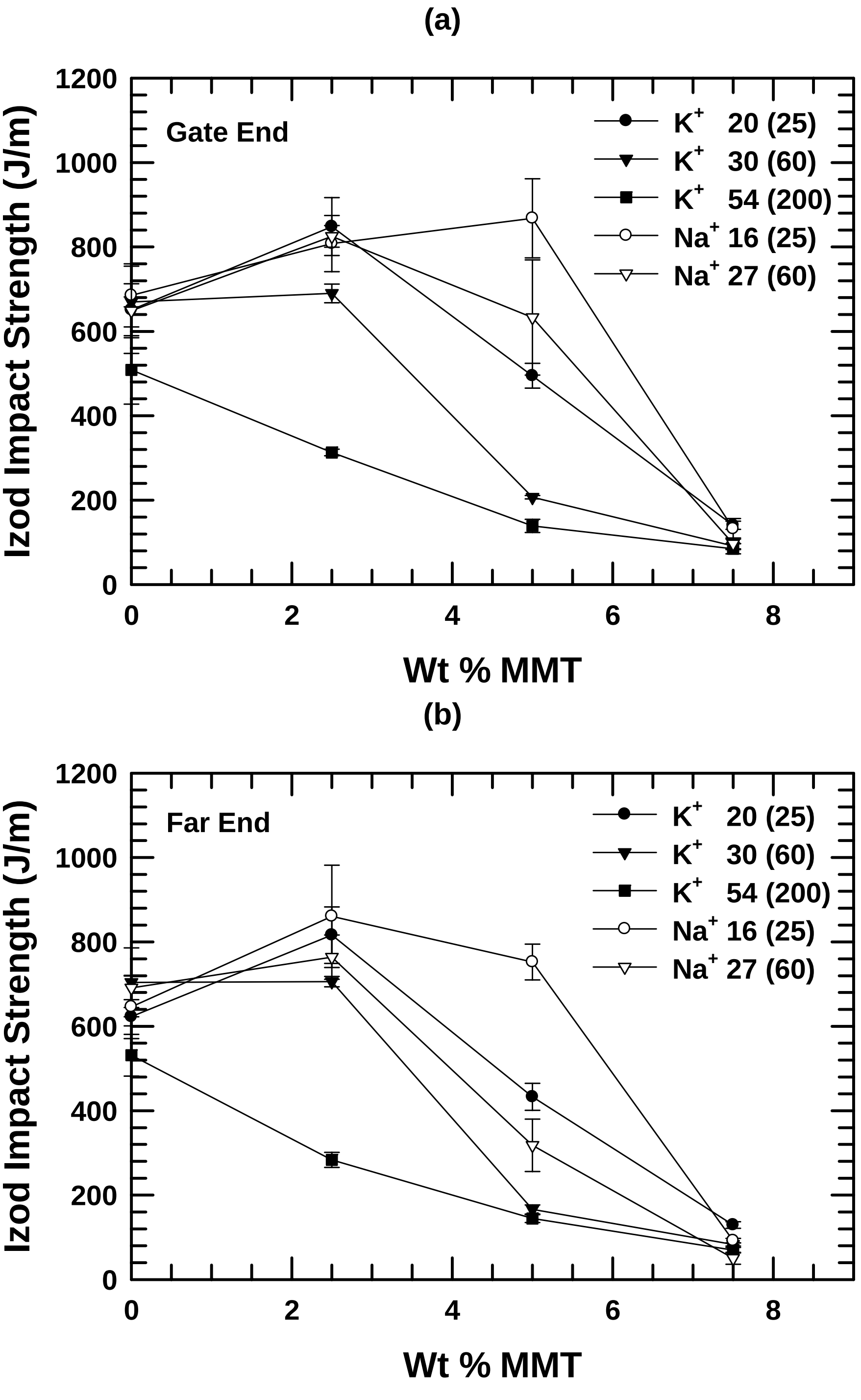

Figure 7.18: Izod impact strength of selected K^+ and Na^+ ionomer nanocomposites as a function of MMT content measured at the gate (a) and far (b) ends; the neutralization level and precursor melt index (in parentheses) are noted.

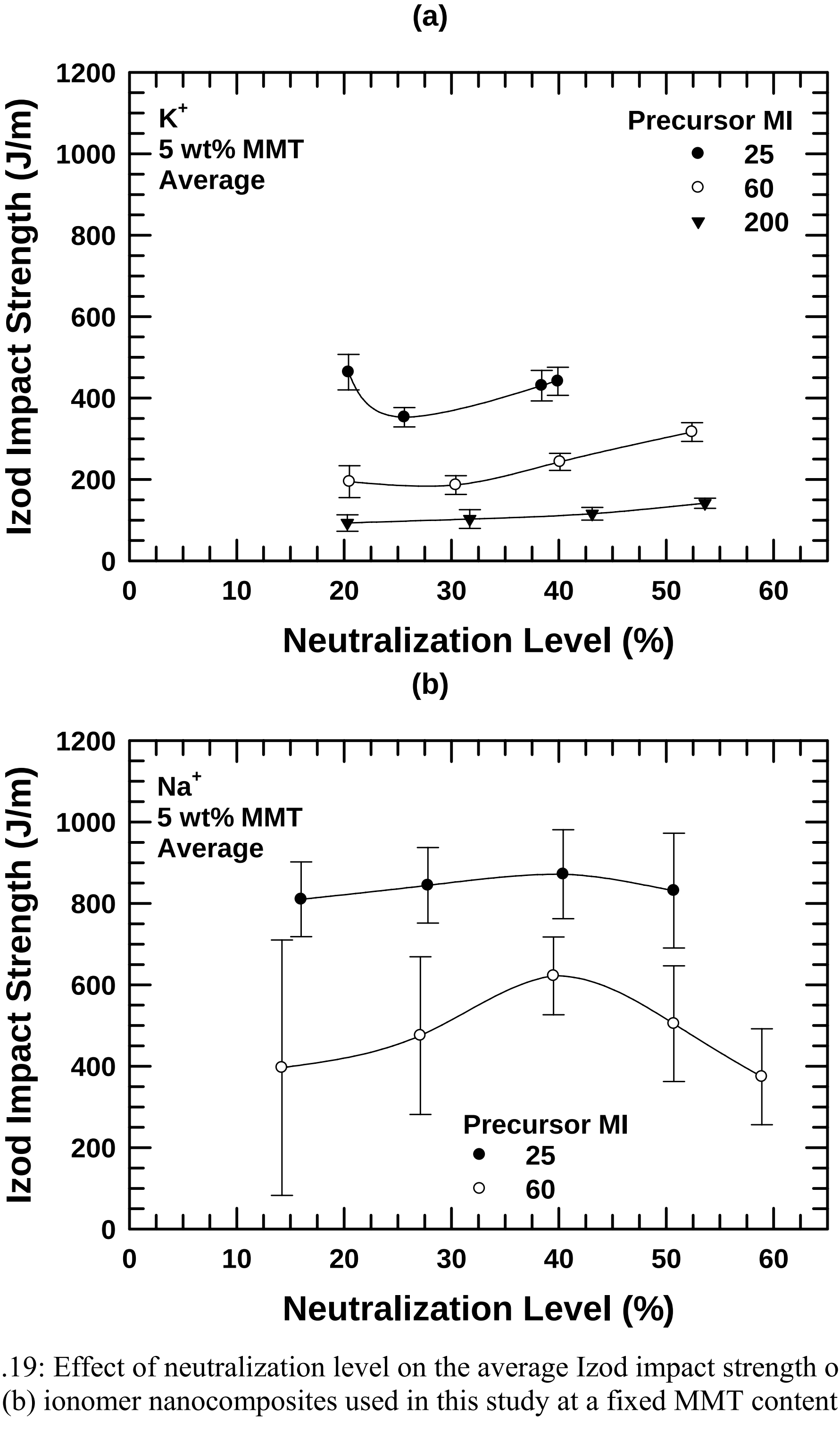

Figure 7.19: Effect of neutralization level on the average Izod impact strength of K$^+$ (a) and Na$^+$ (b) ionomer nanocomposites used in this study at a fixed MMT content of ~5 wt%.

Dynamic mechanical properties

Dynamic mechanical properties of K^+ and Na^+ ionomer nanocomposites with 40% neutralization are shown in Figures 7.20 and 7.21, respectively. The relaxation denoted by the decrease in E' and the peaks in E" and tan δ that occur in the vicinity of the T_i seen by DSC does not shift significantly as the degree of neutralization increases. The storage modulus, E', and the loss modulus, E", increase at all temperatures for both ionomer types with increasing MMT. The Na^+ ionomer nanocomposites show greater improvements in E' and E" with MMT addition than the K^+ ionomer nanocomposites. The tan δ peak that occurs in the vicinity of the T_i decreases in amplitude as the MMT content increases.

(a)

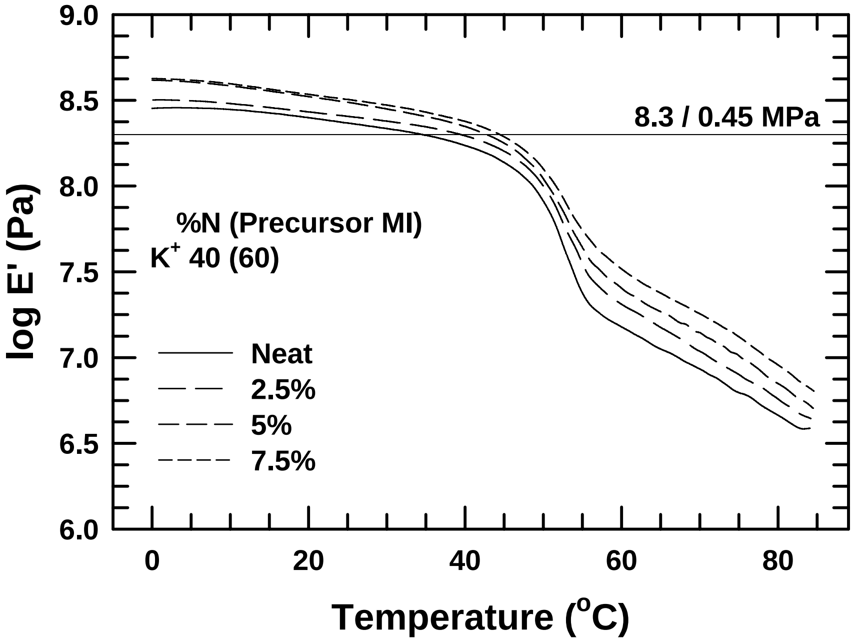

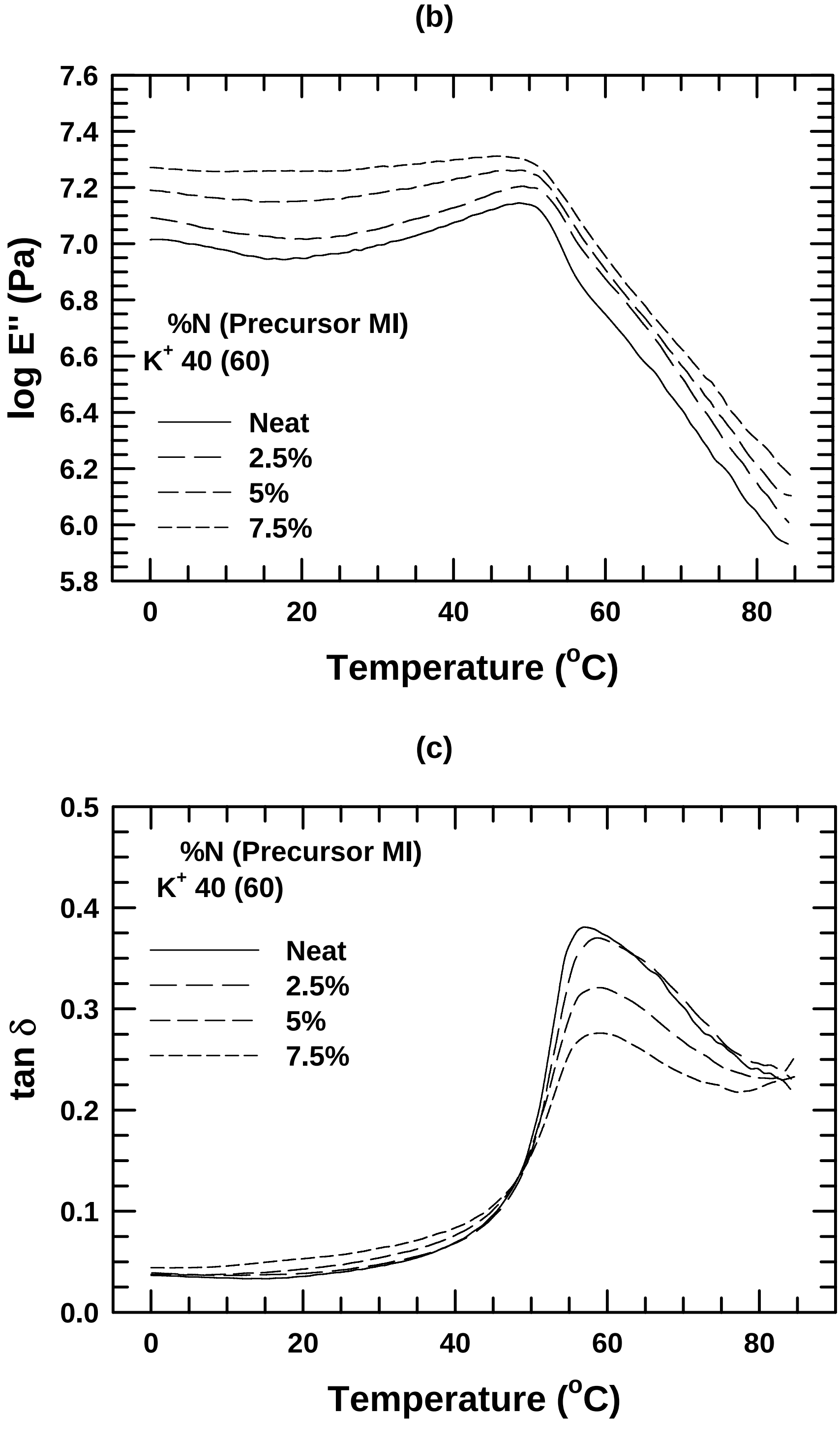

Figure 7.20: Storage modulus, *E′*, (a), loss modulus, *E″*, (b), and tan *δ* (c) for a selected K^+ ionomer nanocomposites.

(a)

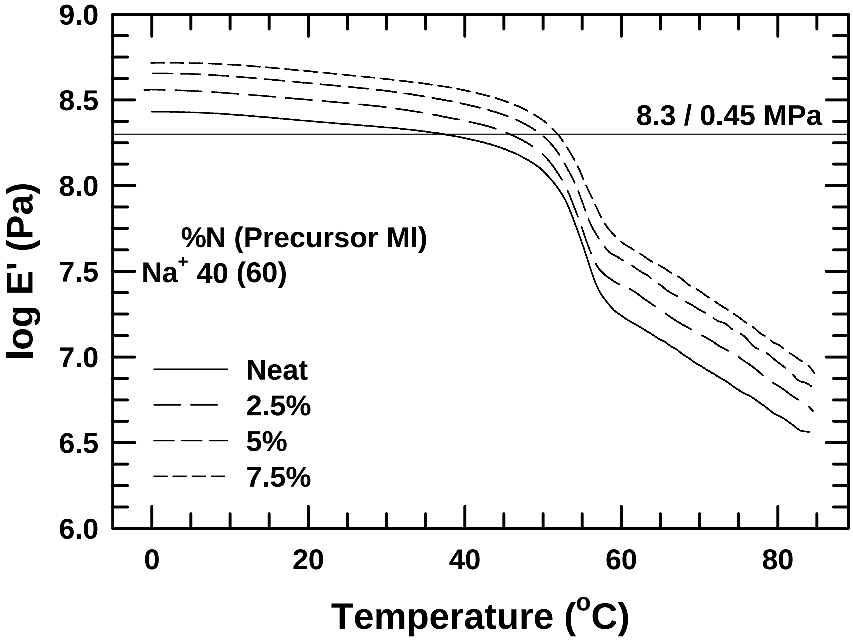
9.0
8.5
8.0
7.5
7.0
6.5
6.0
log E' (Pa)
0
20
40
60
80
Temperature (°C)
8.3 / 0.45 MPa
%N (Precursor MI)
Na+ 40 (60)
Neat
2.5%
5%
7.5%

(b)

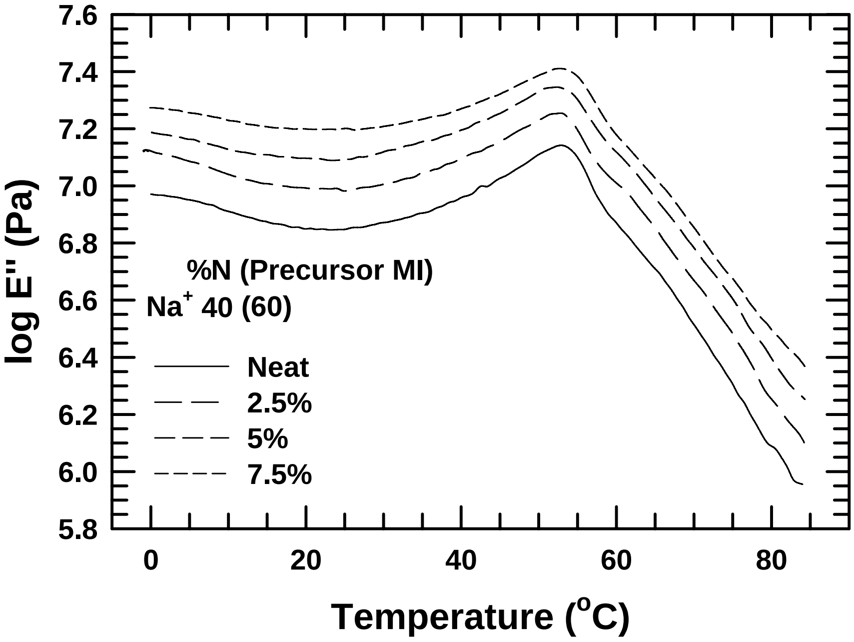
7.6
7.4
7.2
7.0
6.8
6.6
6.4
6.2
6.0
5.8
log E'' (Pa)
0
20
40
60
80
Temperature (°C)
%N (Precursor MI)
Na+ 40 (60)
Neat
2.5%
5%
7.5%

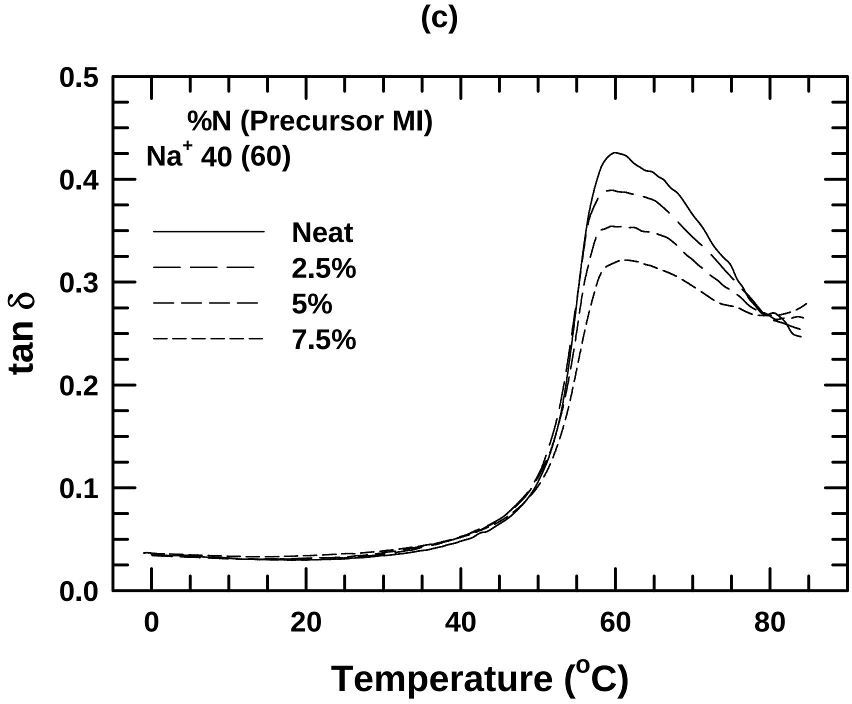

Figure 7.21: Storage modulus, *E*′, (a), loss modulus, *E*″, (b), and tan *δ* (c) for a selected Na^+ ionomer nanocomposites.

The heat distortion temperature (HDT) at a stress level of 8.3 MPa can be approximated as the temperature at which the log(E') = 8.3 (or E' = 0.45 MPa) [61-63]. The addition of MMT results in increased HTD in all cases. The HDT increases to a greater extent with MMT addition for Na^+ ionomer nanocomposites than for K^+ ionomer nanocomposites.

CONCLUSION

The effects of the degree of neutralization of the acid groups and, to some extent, the precursor melt index on the extent of organoclay exfoliation and the properties of nanocomposites based on Na^+ and K^+ EMAA ionomers are examined. WAXS and TEM coupled with detailed particle analysis show good, though incomplete, organoclay exfoliation. The aspect ratio generally increases as the neutralization level increases, except for Na^+ ionomer nanocomposites with neutralization levels > 50%. The particle density of Na^+ ionomer nanocomposites increases with increasing neutralization level and is generally higher than that of the K^+ ionomer nanocomposites. Considering both the aspect ratio and the particle density, it seems that the Na^+ ionomer nanocomposites have higher levels of exfoliation than K^+ ionomer nanocomposites. It appears from both WAXS and TEM analyses that the Na^+ ionomer nanocomposites have higher levels of particle orientation in the flow direction, possibly due to differences in the ionic group morphologies of the K^+ and Na^+ ionomers.

DSC results indicate that the T_i, ΔH_i, and ΔH_m generally increase, while the T_m decreases with increasing neutralization level. The Na^+ ionomer nanocomposites have larger increases or smaller decreases in the ΔH values as compared to the neat ionomers than the K^+ ionomer nanocomposites, indicating that the level of crystallinity in the Na^+ ionomers generally increases slightly with the addition of MMT, while the level of crystallinity in the K^+ ionomers decreases slightly with the addition of MMT. It appears that the crystal nucleation effect of the clay particles is dominant for the Na^+ ionomers, while the crystal growth retardation of the clay platelets is dominant for the K^+ ionomers.

The relative modulus significantly increases with increasing MMT content for all ionomers studied. The relative modulus of K^+ ionomer nanocomposites increases as the degree of neutralization increases. The relative moduli of Na^+ ionomer nanocomposites are higher than the relative modulus of K^+ ionomer nanocomposites, likely due to the higher exfoliation levels measured by the aspect ratios and the particle densities, the higher particle orientation indicated by TEM and WAXS, and the increased crystallinity of the Na^+ ionomers and the decreased crystallinity of the K^+ ionomers upon addition of MMT. In general, the relative modulus increases as the aspect ratio increases.

The elongation at break generally decreases as the MMT content increases and as the neutralization level increases for both ionomer types, but all the nanocomposites examined remain very ductile. The elongation at break of the Na^+ ionomer nanocomposites is generally somewhat lower than that of the K^+ ionomer nanocomposites. The fracture energy of most of the ionomers increases with the addition of MMT, reaches a maximum between 2.5 and 5 wt% MMT, and then decreases upon further organoclay addition. The impact strength increases with decreasing melt index at any given neutralization level for both ion types. The fracture energy of the Na^+ ionomer nanocomposites is generally higher than that of the K^+ ionomer nanocomposites. The complex viscosity, loss modulus, and storage modulus of the Na^+ ionomer nanocomposites increase more with MMT addition than the K^+ ionomer nanocomposites, indicating that Na^+ ionomer nanocomposites have higher levels of organoclay exfoliation.

REFERENCES

1. Fornes TD, Yoon PJ, Hunter DL, Keskkula H, and Paul DR. Polymer 2002;43(22):5915-5933.
2. Giannelis EP. Applied Organometallic Chemistry 1998;12(10-11):675-680.
3. Lee H-s, Fasulo PD, Rodgers WR, and Paul DR. Polymer 2005;46(25):11673-11689.
4. Bharadwaj RK. Macromolecules 2001;34(26):9189-9192.
5. Messersmith PB and Giannelis EP. Journal of Polymer Science Part A: Polymer Chemistry 1995;33(7):1047-1057.
6. Yano K, Usuki A, Okada A, Kurauchi T, and Kamigaito O. Journal of Polymer Science Part A: Polymer Chemistry 1993;31(10):2493-2498.
7. Lee H-s, Fasulo PD, Rodgers WR, and Paul DR. Polymer 2006;47(10):3528-3539.
8. Kim DH, Fasulo PD, Rodgers WR, and Paul DR. Polymer 2008;49(10):2492-2506.
9. Gilman JW. Applied Clay Science 1999;15(1-2):31-49.

10. Gilman JW, Kashiwagi T, Brown JET, Lomakin S, Giannelis EP, and Manias E. Int. SAMPE Symp. Exhibit. 1998;43:1053.
11. Bourbigot S, Le Bras M, Dabrowski F, Gilman JW, and Kashiwagi T. Fire and Materials 2000;24(4):201-208.
12. Hasegawa N, Kawasumi M, Kato M, Usuki A, and Okada A. Journal of Applied Polymer Science 1998;67(1):87-92.
13. Kawasumi M, Hasegawa N, Kato M, Usuki A, and Okada A. Macromolecules 1997;30:6333–6338.
14. Varela C, Rosales C, Perera R, Matos M, Poirier T, Blunda J, and Rojas H. Polymer Composites 2006;27(4):451-460.
15. López-Quintanilla ML, Sánchez-Valdés S, Ramos de Valle LF, and Guedea Miranda R. Polymer Bulletin 2006;57(3):385-393.
16. Galgali G, Ramesh C, and Lele A. Macromolecules 2001;34(4):852-858.
17. Reichert P, Nitz H, Klinke S, Brandsch R, Thomann R, and Mülhaupt R. Macromolecular Materials and Engineering 2000;275(1):8-17.
18. Cui L and Paul DR. Polymer 2007;48(6):1632-1640.
19. Lertwimolnun W and Vergnes B. Polymer 2005;46(10):3462-3471.
20. Hotta S and Paul DR. Polymer 2004;45(22):7639-7654.
21. Hasegawa N, Okamoto H, Kawasumi M, Kato M, Tsukigase A, and Usuki A. Macromolecular Materials and Engineering 2000;280-281(1):76-79.
22. Li X, Wang C-y, Fang L, and Liu L-z. Harbin Ligong Daxue Xuebao 2003;8(2):90-93.
23. Shah RK, Cui L, Williams KL, Bauman B, and Paul DR. Journal of Applied Polymer Science 2006;102(3):2980-2989.
24. Filippi S, Marazzato C, Magagnini P, Famulari A, Arosio P, and Meille SV. European Polymer Journal 2008;44(4):987-1002.
25. Wang KH, Choi MH, Koo CM, Choi YS, and Chung IJ. Polymer 2001;42(24):9819-9826.
26. Gopakumar TG, Lee JA, Kontopoulou M, and Parent JS. Polymer 2002;43(20):5483-5491.
27. Liang G, Xu J, Bao S, and Xu W. Journal of Applied Polymer Science 2004;91(6):3974-3980.
28. Morawiec J, Pawlak A, Slouf M, Galeski A, Piorkowska E, and Krasnikowa N. European Polymer Journal 2005;41(5):1115-1122.

29. Zhang M and Sundararaj U. Macromolecular Materials and Engineering 2006;291(6):697-706.

30. Mainil M, Alexandre M, Monteverde F, and Dubois P. Journal of Nanoscience and Nanotechnology 2006;6:337-344.

31. Spencer MW, Cui L, Yoo Y, and Paul DR. Polymer 2010;51(5):1056-1070.

32. Cui L, Ma X, and Paul DR. Polymer 2007;48(21):6325-6339.

33. Zanetti M, Camino G, Thomann R, and Mülhaupt R. Polymer 2001;42(10):4501-4507.

34. Cerezo FT, Preston CML, and Shanks RA. Composites Science and Technology 2007;67(1):79-91.

35. Shah RK, Kim DH, and Paul DR. Polymer 2007;48(4):1047-1057.

36. Filippi S, Marazzato C, Magagnini P, Minkova L, Tzankova N, Francesco D, and Mantia PL. Macromolecular Materials and Engineering 2006;291(10):1208-1225.

37. Huang Y, Ma X, Liang G, Wang S, and Zhang Q. Polymer 2008;49(8):2085-2094.

38. Shah RK, Krishnaswamy RK, Takahashi S, and Paul DR. Polymer 2006;47(17):6187-6201.

39. Shah RK, Hunter DL, and Paul DR. Polymer 2005;46(8):2646-2662.

40. Shah RK and Paul DR. Macromolecules 2006;39(9):3327-3336.

41. Cui L, Troeltzsch C, Yoon PJ, and Paul DR. Macromolecules 2009;42(7):2599-2608.

42. Spencer MW, Wetzel MD, Troeltzsch C, and Paul DR. Polymer 2011;52:Submitted. (Effects of Acid Neutralization on the Properties of K+ and Na+ Poly(ethylene-co-methacrylic acid) Ionomers).

43. Yoon PJ, Hunter DL, and Paul DR. Polymer 2003;44(18):5323-5339.

44. Fornes TD and Paul DR. Polimeros: Ciencia e Tecnologia 2003;13(4):212-217.

45. Stretz HA, Paul DR, Li R, Keskkula H, and Cassidy PE. Polymer 2005;46(8):2621-2637.

46. Yoon PJ, Fornes TD, and Paul DR. Polymer 2002;43(25):6727-6741.

47. Fornes TD and Paul DR. Macromolecules 2004;37(20):7698-7709.

48. Paul DR, Zeng QH, Yu AB, and Lu GQ. Journal of Colloid and Interface Science 2005;292(2):462-468.

49. Kim DH, Fasulo PD, Rodgers WR, and Paul DR. Polymer 2007;48(18):5308-5323.

50. Fornes TD, Hunter DL, and Paul DR. Macromolecules 2004;37(5):1793-1798.

51. Fornes TD, Yoon PJ, Keskkula H, and Paul DR. Polymer 2001;42(25):9929-9940.

52. Kim DH, Fasulo PD, Rodgers WR, and Paul DR. Polymer 2007;48(20):5960-5978.

53. Chavarria F and Paul DR. Polymer 2006;47(22):7760-7773.

54. Ren J, Silva AS, and Krishnamoorti R. Macromolecules 2000;33(10):3739-3746.

55. Krishnamoorti R and Yurekli K. Current Opinion in Colloid & Interface Science 2001;6(5-6):464-470.

56. Okamoto M, Nam PH, Maiti P, Kotaka T, Hasegawa N, and Usuki A. Nano Letters 2001;1(6):295-298.

57. Fornes TD and Paul DR. Polymer 2003;44(14):3945-3961.

58. Jimenez G, Ogata N, Kawai H, and Ogihara T. Journal of Applied Polymer Science 1997;64(11):2211-2220.

59. Cui L, Hunter DL, Yoon PJ, and Paul DR. Polymer 2008;49(17):3762-3769.

60. Yoo Y, Shah RK, and Paul DR. Polymer 2007;48(16):4867-4873.

61. Fornes TD and Paul DR. Polymer 2003;44(17):4993-5013.

62. Yoo Y and Paul DR. Polymer 2008;49(17):3795-3804.

63. Scobbo JJ. Thermomechanical performance of polymer blends. In: Paul DR and Bucknall CB, editors. Polymer blends, vol. 2. New York: Wiley, 2000. pp. 335-357.

Chapter 8: Conclusions and recommendations

CONCLUSIONS

This project addressed a number of fundamental issues associated with the melt processing of polymer nanocomposites to better understand the exfoliation process. The major focus of this project was to improve the organoclay exfoliation in non-polar polyolefin matrices. Various compatibilizers, such as maleated polyolefins, and various organoclay types were examined. Another major part of this dissertation was modeling these nanocomposites using novel approaches to improve the understanding of these systems.

Although polymer nanocomposites have been made from many polymers, few matrices, especially non-polar matrices, have achieved the high exfoliation levels seen with nylon 6. Considerable efforts have been made to improve organoclay exfoliation in hydrophobic polyolefins. Maleated polypropylene and maleated polyethylene have commonly been used as compatibilizers.

Nanocomposites formed from blends of HDPE and HDPE-*g*-MA and $M_2(HT)_2$ organoclay were melt processed to explore the extent of exfoliation and the mechanical properties over the entire range of matrix composition. WAXS and TEM show drastic improvements in exfoliation with initial amounts of HDPE-*g*-MA while further addition of HDPE-*g*-MA gives little visible change. Particle analysis, however, shows that the fraction of single platelets increases at a steady rate for nanocomposites with HDPE-*g*-MA contents $\geq$25%. As the HDPE-*g*-MA content increases, particle aspect ratio initially increases drastically, reaches a maximum, and slightly decreases, due to the particle thickness limit of a single platelet (0.94 nm).

Similarly, the relative modulus initially improves significantly with increased levels of HDPE-*g*-MA, while greater HDPE-*g*-MA content only gives a slight increase. The slight increase in relative modulus in spite of a slight decrease in aspect ratio might be due to the decreased modulus of the matrix, facilitating improvements in relative modulus. Modulus increases and Izod impact strength decreases as MMT levels increase, for all HDPE-*g*-MA levels. Fracture energy reaches a maximum at low HDPE-*g*-MA levels, decreases below the value for the pure HDPE nanocomposite, and levels off at higher HDPE-*g*-MA content. Initially, adding HDPE-*g*-MA to the matrix results in significantly improved exfoliation and properties. Further addition of HDPE-*g*-MA, however, lowers the matrix properties enough to offset the benefits of enhanced matrix/organoclay interactions.

Because of the different reinforcement effects of partially exfoliated organoclay tactoids and single platelets, particle analysis was also performed on these two populations separately. A composite model based on the Mori-Tanaka theory was developed to treat organoclay tactoids and single platelets as two separate types of fillers. This two population Mori-Tanaka model gives rather good quantitative agreement between the predicted values of modulus calculated from the TEM results and that measured experimentally.

Nanocomposites formed from PP and PP/PP-*g*-MA (mass PP-*g*-MA/mass organoclay = 1) and $M_2(HT)_2$ and s-$M_2(HT)_2$ organoclays were melt processed to explore the extent of exfoliation and the mechanical, rheological, and thermal expansion properties. WAXS and TEM coupled with detailed particle analysis were used to determine the effect of the organoclay used and the PP-*g*-MA compatibilizer on exfoliation. The PP/s-$M_2(HT)_2$ nanocomposites have higher particle densities than the PP/$M_2(HT)_2$ nanocomposites though the aspect ratio remains the same. The platelet dispersion is significantly improved by using PP-*g*-MA compatibilizer for both organoclays. Nanocomposites with s-$M_2(HT)_2$ have less agglomeration than $M_2(HT)_2$ nanocomposites. In general, nanocomposites produced with downstream organoclay feeding, with no turbine mixing elements in the screw design, and at high shear rates have lower agglomeration. The rheological properties and the relative modulus improve for the PP/s-$M_2(HT)_2$ nanocomposites but not to the same degree as either organoclay in a PP-*g*-MA compatibilized matrix. The elongation at break decreases with the addition of MMT and the addition of PP-*g*-MA accelerates this decrease for both organoclays. No meaningful trends were found for the Izod impact strength due to the brittle nature of the PP and the large standard deviations observed. The thermal expansion properties, however, are not improved by using the s-$M_2(HT)_2$ organoclay. The silanized organoclay nanocomposites show mostly improved properties compared to the non-silanized precursor nanocomposites, though the improvements were less than those observed for PP-*g*-MA compatibilized nanocomposites.

The Mori-Tanaka, Lee, and Chow composite models were used to predict the modulus and CTE of PP/PP-*g*-MA/MMT nanocomposites and PP/EOR blends. The Mori-Tanaka and Chow model predictions best match the experimental trends. Although the predictions for PP/PP-*g*-MA/MMT nanocomposites using a tactoid modulus of 70.6 GPa overestimate the modulus and underestimate the CTE in the FD, an adjusted E_{Tact} of 32 GPa matches the experimental data well. The predictions for PP/EOR blends overestimate the modulus and underestimate the CTE in the FD. In both systems, the predictions underestimate the CTE in the ND, suggesting the Chow model does not adequately capture the constraining effects of the MMT on the matrix and of the PP matrix on the EOR.

Various ternary-phase approaches were used to predict the modulus and CTE of PP/PP-*g*-MA/EOR/MMT nanocomposites. A *multiplicative* approach, wherein the contribution of the clay is calculated first and the nanocomposite is then considered to be the matrix for the elastomer blend, best matches the experimental trends. The models better capture the effects of the MMT than those of the EOR.

Models predicting the effect of the MMT tactoids on the experimental TPO or the effect of the EOR particles on the experimental nanocomposites were also used. The TPO/tactoid approach that predicts the effect of the MMT tactoids on the experimental TPO best matches the experimental trends. This TPO/tactoid model gives rather good quantitative agreement between the predicted values of modulus and CTE calculated using the experimentally determined aspect ratios and those measured experimentally for TPO nanocomposites.

The effects of the degree of neutralization of the acid groups and, to some extent, the precursor melt index on the properties of Na^+ and K^+ ethylene methacrylic acid (EMAA) ionomers were examined. DSC and modulus results indicate that the physical ageing effect due to secondary crystallization generally plateaus after 21 days after melt processing. K^+ ionomers absorb more water than Na^+ ionomers, and water absorption has a plasticization effect on the ionomers. DSC results indicate that the T_i, ΔH_i, and ΔH_m increase, while the T_m decreases with increasing neutralization level. These results indicate that crystallization increases with increased neutralization. The mechanical relaxation seen by DMA in the vicinity of the T_i shifts to higher temperatures as the neutralization level increases. The effects of precursor melt index are not as significant.

The complex viscosity, storage modulus, and loss modulus increase dramatically with decreasing precursor melt index. The rheological properties also increase as the neutralization level increases to a lesser extent. The Na^+ ionomers have somewhat higher rheological properties than the K^+ ionomers.

The ionomer modulus and yield strength increase with increasing neutralization level up to 40% neutralization and then plateau or slightly decrease with further neutralization. The plateaus/maxima may be the result of an optimal spacing of alkaline ions and carboxyl groups within ionic groups at neutralization levels near 33%. The elongation at break decreases with increasing neutralization. The precursor melt index and the neutralization level appear to affect both the elongation at break and the melt index of the ionomers similarly, resulting in a good correlation between the ionomer melt index and the elongation at break. The elongation at break of the K^+ ionomers is generally higher that that of the Na^+ ionomers. The impact strength decreases with increasing neutralization level. The modulus, yield stress, and impact strength are generally lowest for the ionomers with the highest precursor melt index.

The effects of the degree of neutralization of the acid groups and, to some extent, the precursor melt index on the extent of organoclay exfoliation and the properties of nanocomposites based on Na^+ and K^+ EMAA ionomers were also examined. WAXS and TEM coupled with detailed particle analysis show good, though incomplete, organoclay exfoliation. The aspect ratio generally increases as the neutralization level increases, except for Na^+ ionomer nanocomposites with neutralization levels > 50%. The particle density of Na^+ ionomer nanocomposites increases with increasing neutralization level and is generally higher than that of the K^+ ionomer nanocomposites. Considering both the aspect ratio and the particle density, it seems that the Na^+ ionomer nanocomposites have higher levels of exfoliation than K^+ ionomer nanocomposites. It appears from both WAXS and TEM analyses that the Na^+ ionomer nanocomposites have higher levels of particle orientation in the flow direction, possibly due to differences in the ionic group morphologies of the K^+ and Na^+ ionomers.

DSC results indicate that the T_i, ΔH_i, and ΔH_m generally increase, while the T_m decreases with increasing neutralization level. The Na^+ ionomer nanocomposites have larger increases or smaller decreases in the ΔH values as compared to the neat ionomers than the K^+ ionomer nanocomposites, indicating that the level of crystallinity in the Na^+ ionomers generally increases slightly with the addition of MMT, while the level of crystallinity in the K^+ ionomers decreases slightly with the addition of MMT. It appears that the crystal nucleation effect of the clay particles is dominant for the Na^+ ionomers, while the crystal growth retardation of the clay platelets is dominant for the K^+ ionomers.

The relative modulus significantly increases with increasing MMT content for all ionomers studied. The relative modulus of K^+ ionomer nanocomposites increases as the degree of neutralization increases. The relative moduli of Na^+ ionomer nanocomposites are higher than the relative modulus of K^+ ionomer nanocomposites, likely due to the higher exfoliation levels measured by the aspect ratios and the particle densities, the higher particle orientation indicated by TEM and WAXS, and the increased crystallinity of the Na^+ ionomers and the decreased crystallinity of the K^+ ionomers upon addition of MMT. In general, the relative modulus increases as the aspect ratio increases.

The elongation at break generally decreases as the MMT content increases and as the neutralization level increases for both ionomer types, but all the nanocomposites examined remain very ductile. The elongation at break of the Na^+ ionomer nanocomposites is generally somewhat lower than that of the K^+ ionomer nanocomposites. The fracture energy of most of the ionomers increases with the addition of MMT, reaches a maximum between 2.5 and 5 wt% MMT, and then decreases upon further organoclay addition. The impact strength of both ion types increases with decreasing melt index at any given neutralization level. The fracture energy of the Na^+ ionomer nanocomposites is generally higher than that of the K^+ ionomer nanocomposites. The complex viscosity, loss modulus, and storage modulus of the Na^+ ionomer nanocomposites increase more with MMT addition than the K^+ ionomer nanocomposites, indicating that Na^+ ionomer nanocomposites have higher levels of organoclay exfoliation.

RECOMMENDATIONS

Silane coupling agent optimization

The properties of silanized organoclay nanocomposites are mostly improved compared to those of the non-silanized precursor nanocomposites, though the improvements were less than those observed for PP-*g*-MA compatibilized nanocomposites. The trimethoxyphenyl silane coupling agent used is likely not optimal for this system. Other silane coupling agents might produce more significant improvements in exfoliation and, thus, reinforcement [1]. Silanes with a long alkyl group, such as octadecyltrimethoxy silane, likely interact more favorably with the hydrophobic PP matrix.

Ionic aggregate structure of potassium ionomers

The use of potassium-neutralized ethylene ionomers has been found to yield an ionomer with a high-surface conductivity, unlike those neutralized with sodium or zinc [2]. The authors hypothesized that the higher water absorption of the potassium-neutralized materials at constant relative humidity led to the higher surface conductivity. Although this explanation is consistent when comparing potassium and zinc ionomers; the difference between the water absorption of the potassium ionomer was only a factor of two higher than the sodium ionomer at a constant relative humidity while the surface conductivity was five orders of magnitude larger. In addition, at the same water content (different relative humidities), the potassium-neutralized material had substantial surface conductivity, while the sodium-neutralized material did not. Thus, the disparity in water content does not appear to explain the high surface conductivity of the potassium-neutralized materials.

It is possible that the morphology of the ionic groups plays a role in the surface conductivity of the potassium ionomers. Extended X-ray absorption fine structure (EXAFS) is a tool that can be used to probe the ionic group morphology. This technique has been used by Grady et al. for zinc-neutralized ethylene ionomers [3-7]. Although beset by experimental difficulties because of sodium's low atomic number (and hence low x-ray energies), Grady et al. also reported a poorly-ordered structure for sodium ionomers that depended highly on the neutralization level [8], though the data quality was extremely poor. The poor quality of the data may be the result of the inherent difficulties at working at the low x-ray energies required for the sodium-neutralized materials (due to the low atomic number of sodium) or of the high level of disorder in the arrangement of atoms around sodium.

Because potassium has a higher atomic number, EXAFS can be performed on these materials using a standard energy x-ray beam. Such experiments would enable the determination of the aggregate structure of potassium-neutralized ionomers as a function of neutralization level and water content. If the structure is well-ordered, then the structure of the aggregate can be determined both by comparison with computer models and via the measurement of small-molecule compounds (e.g. potassium acetate). Knowledge of the ionic aggregate structure would be useful in the study of potassium ionomer materials and may help explain their exceptional surface conductivity.

This technique may also be applied to potassium ionomer nanocomposites to help determine the role of the ionic groups in the exfoliation of the organoclay and the effect of the organoclay on the ionic aggregate structure.

Comparison of composite models with numerical simulations

Gusev et al. have developed numerical simulation tools (such as the PALMYRA software now sold by MatSim) for predicting the mechanical and thermal properties of composite systems possessing complex morphologies [9, 10]. These realistic numerical simulations provide quantitative predictions that can determine the optimum composite material and product designs. These simulations are more computationally intense, more time-intensive, and more expensive than the simple closed-form composite theory based models employed in this dissertation (Mori-Tanaka, Halpin-Tsai, Chow, etc.). Thus, such composite theory models enable the rapid examination of a wide range of parameter values to obtain qualitative and semi-quantitative predicted trends. The results can then focus subsequent more accurate numerical simulations.

The composite systems examined in this dissertation can be modeled using a numerical simulation tool (such as PALMYRA) that can realistically reflect the nanocomposite morphology. The morphological, mechanical, and thermal expansion results discussed in this dissertation can be used to set up the appropriate numerical simulations. Comparing the numerical simulation results with the modeling results presented herein may increase the understanding of the strengths and weaknesses of the composite theory models and offer insight into how these models can be improved.

REFERENCES

1. Joo JH, Shim JH, Choi JH, Choi C-H, Kim D-S, and Yoon J-S. Journal of Applied Polymer Science 2008;109(6):3645-3650.

2. Tachino H, Hara H, Hirasawa E, Kutsumizu S, and Yano S. Polymer Journal 1994;26(10):1170-1178.
3. Welty A, Ooi S, and Grady BP. Macromolecules 1999;32(9):2989-2995.
4. Grady BP, Goossens JGP, and Wouters MEL. Macromolecules 2004;37(23):8585-8591.
5. Grady BP. Polymer 2000;41(6):2325-2328.
6. Grady BP, Floyd JA, Genetti WB, Vanhoorne P, and Register RA. Polymer 1999;40(2):283-288.
7. Farrell KV and Grady BP. Macromolecules 2000;33(19):7122-7126.
8. Farrell V and Grady P. Macromolecules 2001;34(20):7108-7112.
9. Hine PJ, Rudolf Lusti H, and Gusev AA. Composites Science and Technology 2002;62(10-11):1445-1453.
10. Gusev AA and Slot JJM. Advanced Engineering Materials 2001;3(6):427-429.

Appendix A

Pertinent parameters used in the Mori-Tanaka and Lee models are

$$A_1 = D_1(B_4 + B_5) - 2B_2 \tag{1}$$

$$A_2 = (1 + D_1)B_2 - (B_4 + B_5) \tag{2}$$

$$A_3 = B_1 - D_1 B_3 \tag{3}$$

$$A_4 = (1 + D_1)B_1 - 2B_2 \tag{4}$$

$$A_5 = (1 - D_1)/(B_4 - B_5) \tag{5}$$

$$A = 2B_2 B_3 - B_1(B_4 + B_5) \tag{6}$$

and

$$B_1 = \phi D_1 + D_2 + (1-\phi)(D_1 S_{1111} + 2S_{2211}) \tag{7}$$

$$B_2 = \phi + D_3 + (1-\phi)(D_1 S_{1122} + S_{2222} + S_{2233}) \tag{8}$$

$$B_3 = \phi + D_3 + (1-\phi)[S_{1111} + (1 + D_1)S_{2211}] \tag{9}$$

$$B_4 = \phi D_1 + D_2 + (1-\phi)(S_{1122} + D_1 S_{2222} + S_{2233}) \tag{10}$$

$$B_5 = \phi + D_3 + (1-\phi)(S_{1122} + S_{2222} + D_1 S_{2233}) \tag{11}$$

and

$$D_1 = 1 + 2(\mu_f - \mu_m)/(\lambda_f - \lambda_m) \tag{12}$$

$$D_2 = (\lambda_m + 2\mu_m)/(\lambda_f - \lambda_m) \tag{13}$$

$$D_3 = \lambda_m/(\lambda_f - \lambda_m) \tag{14}$$

$$D_4 = -2(\mu_f - \mu_m)/(\lambda_f - \lambda_m) - 3 \tag{15}$$

where λ_m and μ_m and λ_f and μ_f are the *Lamé* constants of the matrix and the filler, respectively, and S is Eshelby's tensor (see Appendix B). The *Lamé* constants for isotropic materials are related to the Young's modulus and the Poisson's ratio by

$$\lambda = \frac{Ev}{(1+v)(1-2v)} \tag{16}$$

$$\mu = \frac{E}{2(1+v)} \tag{17}$$

Appendix B

The components of Eshelby's tensor, S_{ijkl}, are given below.

For spherical inclusions where $a = 1$,

$$S_{1111} = S_{2222} = S_{3333} = \frac{7-5v_m}{15(1-v_m)} \tag{18}$$

$$S_{1122} = S_{2233} = S_{3311} = \frac{5v_m - 1}{15(1-v_m)} \tag{19}$$

$$S_{1212} = S_{2323} = S_{3131} = \frac{4-5v_m}{15(1-v_m)}. \tag{20}$$

For ellipsoidal inclusions where $a \neq 1$,

$$S_{1111} = \frac{1}{2(1-v_m)}\left\{1-2v_m + \frac{3a^2-1}{a^2-1} - \left[1-2v_m + \frac{3a^2}{a^2-1}\right]g\right\} \tag{21}$$

$$S_{2222} = S_{3333} = \frac{3}{8(1-v_m)}\frac{a^2}{a^2-1} + \frac{1}{4(1-v_m)}\left[1-2v_m - \frac{9}{4(a^2-1)}\right]g \tag{22}$$

$$S_{2233} = S_{3322} = \frac{1}{4(1-v_m)}\left\{\frac{a^2}{2(a^2-1)} - \left[1-2v_m + \frac{3}{4(a^2-1)}\right]g\right\} \tag{23}$$

$$S_{2211} = S_{3311} = -\frac{1}{2(1-v_m)}\frac{a^2}{a^2-1} + \frac{1}{4(1-v_m)}\left[\frac{3a^2}{a^2-1} - (1-2v_m)\right]g \tag{24}$$

$$S_{1122} = S_{1133} = -\frac{1}{2(1-v_m)}\left[1-2v_m + \frac{1}{a^2-1}\right] + \frac{1}{2(1-v_m)}\left[1-2v_m + \frac{3}{2(a^2-1)}\right]g \tag{25}$$

$$S_{2323} = S_{3232} = \frac{1}{4(1-v_m)}\left\{\frac{a^2}{2(a^2-1)} + \left[1-2v_m - \frac{3}{4(a^2-1)}\right]g\right\} \tag{26}$$

$$S_{1212} = S_{1313} = \frac{1}{4(1-v_m)}\left\{1-2v_m - \frac{a^2+1}{a^2-1} - \frac{1}{2}\left[1-2v_m + \frac{3(a^2+1)}{a^2-1}\right]g\right\} \tag{27}$$

where

$$g = \frac{a}{(1-a^2)^{3/2}}\left[\cos^{-1} a - a(1-a^2)^{1/2}\right] \tag{28}$$

in the case of disks where $a < 1$ and

$$g = \frac{a}{(a^2-1)^{3/2}}\left[a(a^2-1)^{1/2} - \cosh^{-1} a\right] \tag{29}$$

in the case of fibers where $a > 1$.

Appendix C

The bulk and shear moduli for isotropic materials are related to the Young's modulus and the Poisson's ratio by

$$k = \frac{E}{3(1-2v)} \tag{30}$$

$$\mu = \frac{E}{2(1+v)} \tag{31}$$

The pertinent parameters related to Eshelby's tensor used in the Chow model are

$$\xi = \frac{K_1}{1 + 2(\mu_f / \mu_m - 1)(1-\phi)S_{2323}} \tag{32}$$

$$\zeta = \frac{1 + (\mu_f / \mu_m - 1)(1-\phi)(S_{3333} - S_{1133})}{1 + 2(\mu_f / \mu_m - 1)(1-\phi)S_{2323}} \tag{33}$$

$$K_i = 1 + (k_f / k_m - 1)(1-\phi)b_i \tag{34}$$

$$G_i = 1 + (\mu_f / \mu_m - 1)(1-\phi)c_i \tag{35}$$

$$\widetilde{K}_i = 1 + (k_f / k_m - 1)(1-\phi)b_i + \phi \tag{36}$$

$$\widetilde{G}_i = 1 + (\mu_f / \mu_m - 1)(1-\phi)c_i + \phi \tag{37}$$

where

$$b_1 = 2Q/3 - 2(1-I)R \tag{38}$$

$$b_3 = 2Q/3 - 2(2I-1)R \tag{39}$$

$$c_1 = \left(\frac{2}{3} - \frac{2-3I}{1-a^2}\right)Q - 4(I-1)R \tag{40}$$

$$c_3 = \left(\frac{2}{3} - \frac{(2-3I)a^2}{1-a^2}\right)Q + (2-I)R \tag{41}$$

$$2S_{2323} = \frac{2}{3}\left(\frac{1}{2} - \frac{(2-3I)}{4(1-a^2)}\right)Q + 2IR \tag{42}$$

$$S_{3333} - S_{1133} = \left(\frac{1}{2} - \frac{7}{12}\frac{(2-3I)}{1-a^2}\right)Q + (2-I)R \tag{43}$$

where

$$Q = \frac{3}{4}\frac{1}{1-\nu_m} \tag{44}$$

$$R = \frac{1}{4}\frac{1-2\nu_m}{1-\nu_m} \tag{45}$$

and

$$I = \frac{a}{(1-a^2)^{3/2}}\left[\cos^{-1} a - a(1-a^2)^{1/2}\right] \tag{46}$$

for $a < 1$ and

$$I = \frac{a}{(a^2-1)^{3/2}}\left[a(a^2-1)^{1/2} - \cosh^{-1} a\right] \tag{47}$$

for $a > 1$.

When $a \to 1$,

$$I = \frac{2}{3} \tag{48}$$

$$\frac{2-3I}{1-a^2} = \frac{2}{5} \tag{49}$$

we have

$$b_1 = b_3 = \frac{1}{3}\frac{1+\nu_m}{1-\nu_m} \tag{50}$$

$$c_1 = c_3 = S_{2323} = S_{3333} - S_{1133} = \frac{2}{15}\frac{4-5\nu_m}{1-\nu_m}\,. \tag{51}$$

Appendix D

Table D.1: Screw Configuration Descriptions

Configuration #	Configuration	# Kneading Blocks	# Reverses	# TME	# Eccentric Rings
209165	Low Shear	7	0	0	0
221134	High Shear-TME	13	2	1	0
221146	Medium Shear - TME	9	1	4	0
221122	Eccentric Ring - TME	4	2	4	6
221169	1 TME	1	1	4	0
221159	2 TME	1	2	8	0
221177	Low Shear	8	0	0	0
221186	Medium Shear	10	1	0	0
221191	High Shear	13	1	0	0
UT	Haake Extruder	4	2	0	0

Table D.2: Agglomeration particle count results for nanocomposites made on the Haake extruder with ~3 wt% MMT

Polymer Matrix	Organoclay	Feed Location [a]	Particle Count
PP	$M_2(HT)_2$	1	17
PP/PP-*g*-MA	$M_2(HT)_2$	1	14
PP	s-$M_2(HT)_2$	1	16
PP/PP-*g*-MA	s-$M_2(HT)_2$	1	28

[a] 1 = Upstream

Table D.3: Screw Configuration Descriptions

Configuration #	Configuration	Organoclay	Feed Location [a]	Particle Count
209165	Low Shear	s-$M_2(HT)_2$	1	15
209165	Low Shear	s-$M_2(HT)_2$	4	5
209165	Low Shear	$M_2(HT)_2$	1	50
209165	Low Shear	$M_2(HT)_2$	4	30
221134	High Shear-TME	s-$M_2(HT)_2$	1	19
221134	High Shear-TME	s-$M_2(HT)_2$	4	24
221134	High Shear-TME	$M_2(HT)_2$	1	286
221134	High Shear-TME	$M_2(HT)_2$	4	303

221146	Medium Shear - TME	s-$M_2(HT)_2$	1	47
221146	Medium Shear - TME	$M_2(HT)_2$	1	185
221146	Medium Shear - TME	$M_2(HT)_2$	4	89
221122	Eccentric Ring - TME	s-$M_2(HT)_2$	1	150
221122	Eccentric Ring - TME	s-$M_2(HT)_2$	4	62
221122	Eccentric Ring - TME	$M_2(HT)_2$	1	278
221122	Eccentric Ring - TME	$M_2(HT)_2$	4	550
221169	1 TME	$M_2(HT)_2$	1	286
221169	1 TME	$M_2(HT)_2$	4	386
221159	2 TME	$M_2(HT)_2$	1	378
221159	2 TME	$M_2(HT)_2$	4	373
221177	Low Shear	$M_2(HT)_2$	1	118
221177	Low Shear	$M_2(HT)_2$	4	89
221186	Medium Shear	$M_2(HT)_2$	1	63
221186	Medium Shear	$M_2(HT)_2$	4	28
221191	High Shear	$M_2(HT)_2$	1	24
221191	High Shear	$M_2(HT)_2$	4	11

[a] 1 = Upstream and 4 = Downstream Side Stuffer

Figure D.1: Screw designs

Low Shear 209165

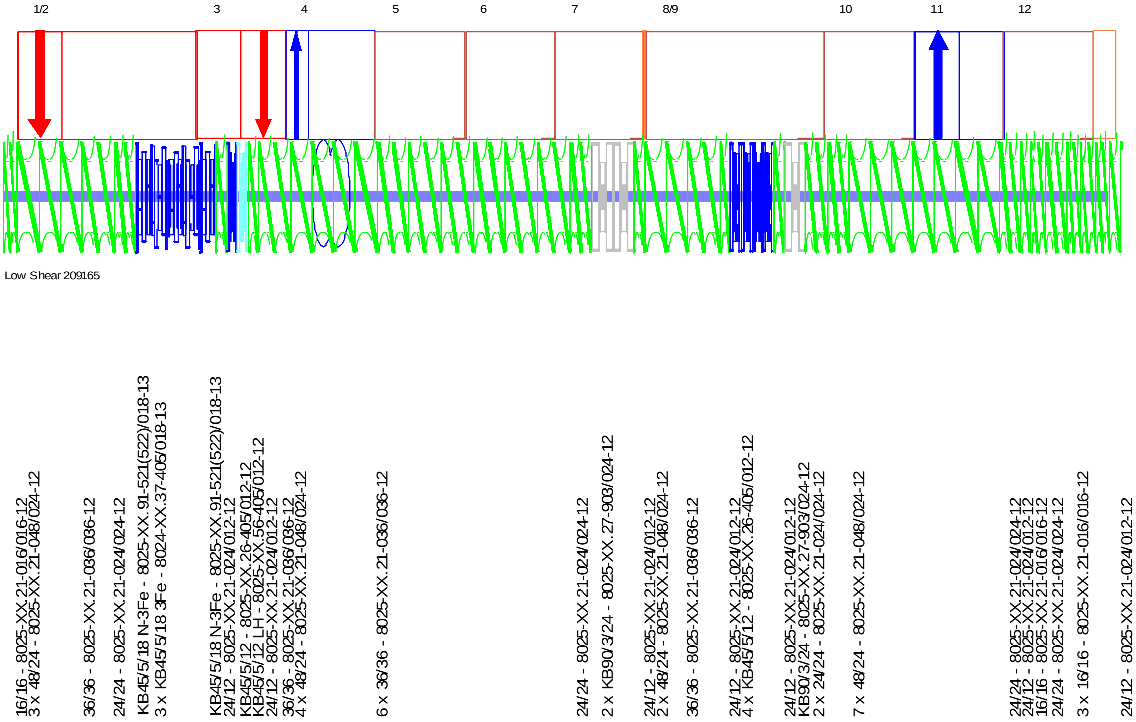

Medium Shear TME 221146

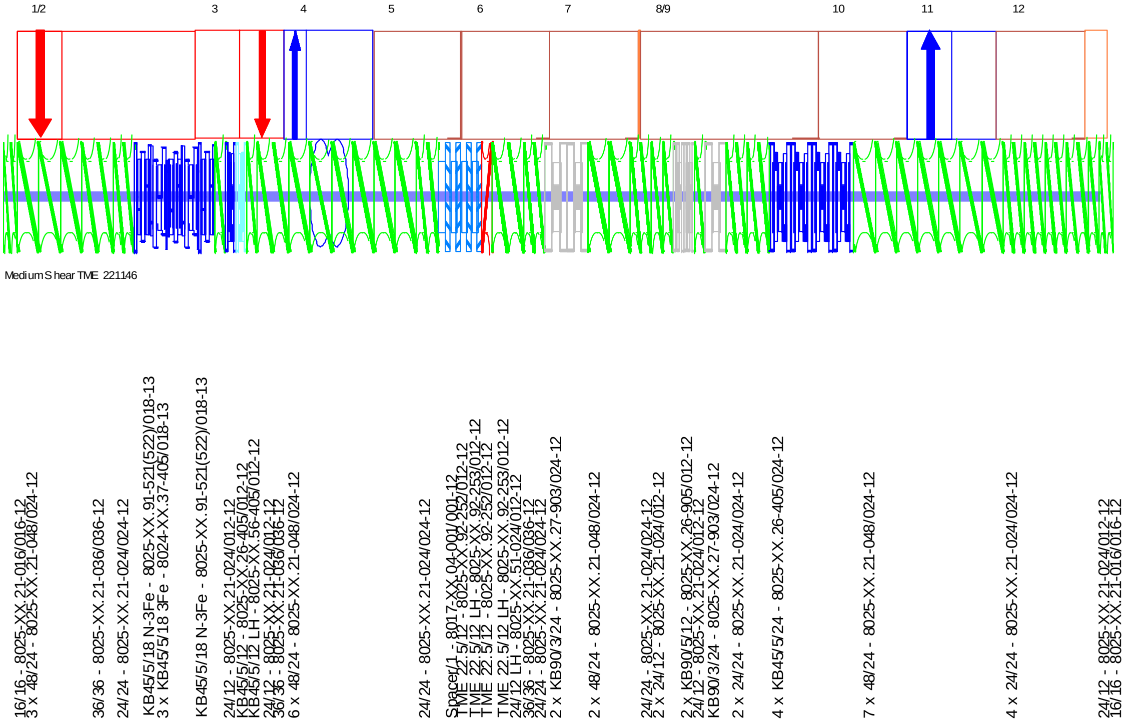

High Shear TME 221134

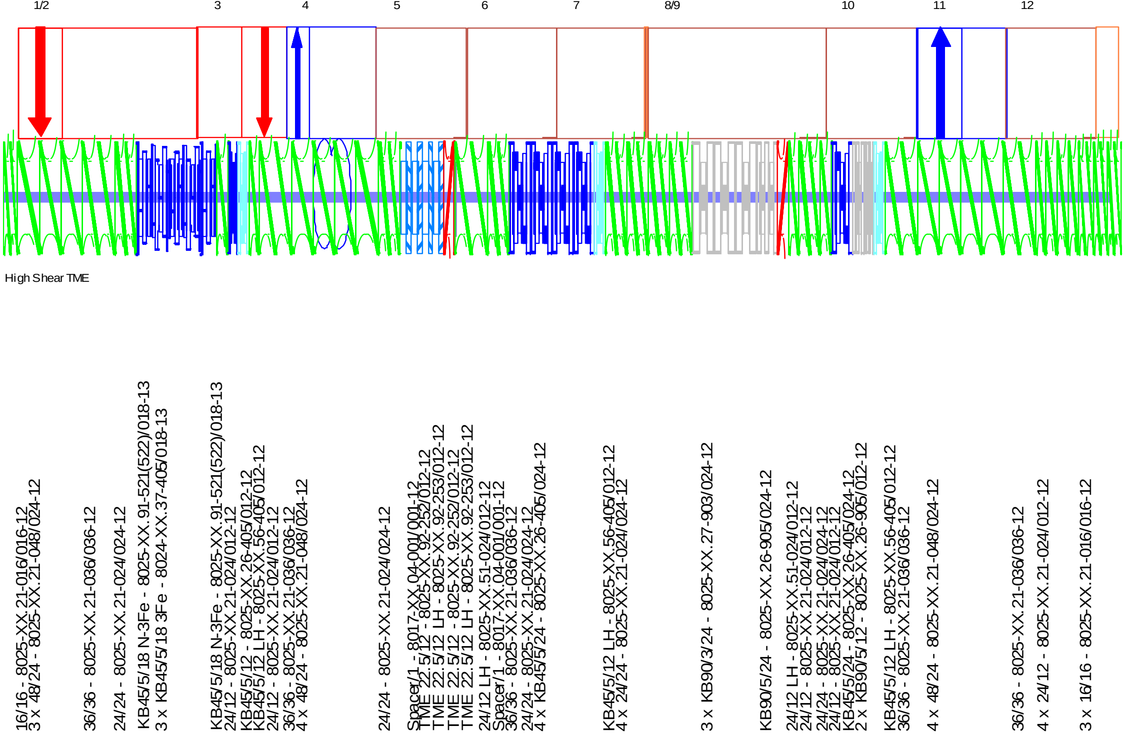

Eccentric Ring TME 221122

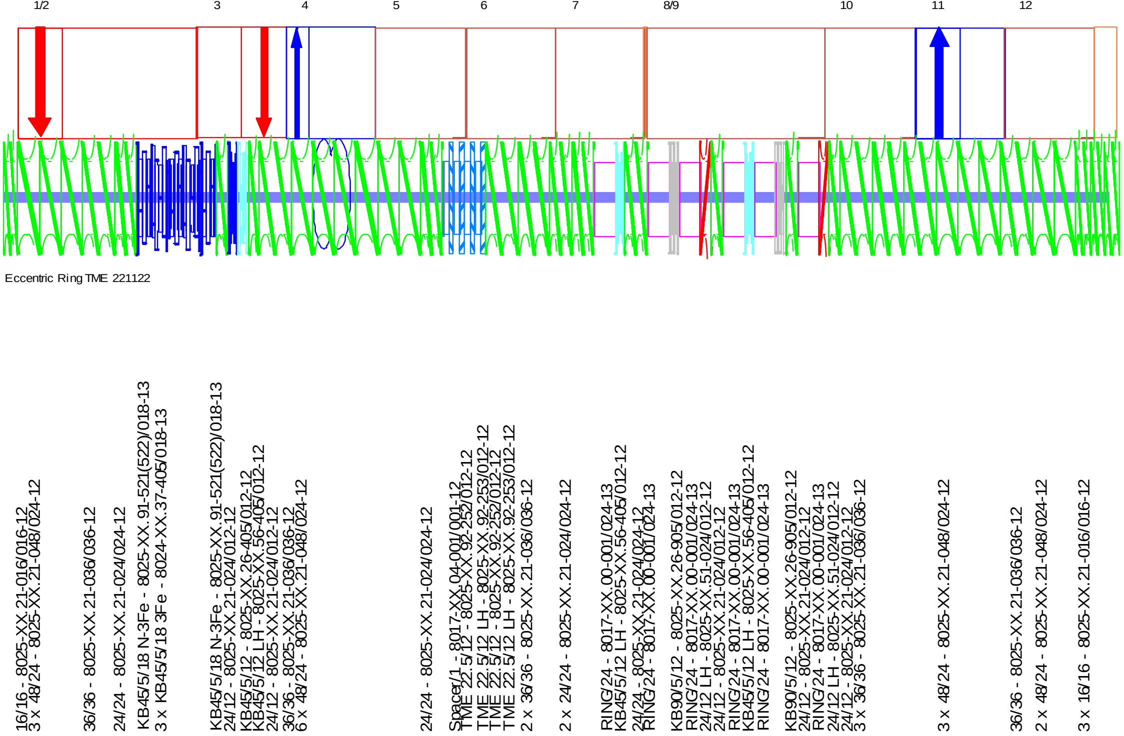

2 TME 221159

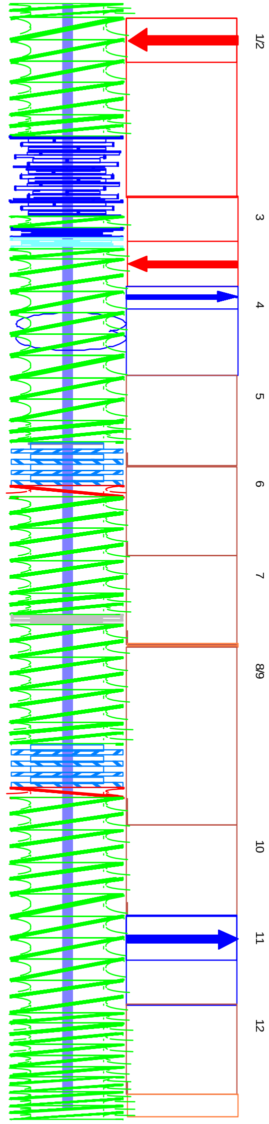

2 TME 221159

16/16 - 8025-XX.21-016/016-12
3 x 48/24 - 8025-XX.21-048/024-12

36/36 - 8025-XX.21-036/036-12

24/24 - 8025-XX.21-024/024-12

KB45/5/18 N-3Fe - 8025-XX.91-521(522)/018-13
3 x KB45/5/18 3Fe - 8024-XX.37-405/018-13

KB45/5/18 N-3Fe - 8025-XX.91-521(522)/018-13
24/12 - 8025-XX.21-024/012-12
KB45/5/12 - 8025-XX.26-405/012-12
KB45/5/12 LH - 8025-XX.56-405/012-12
24/12 - 8025-XX.21-024/012-12
36/36 - 8025-XX.21-036/036-12
6 x 48/24 - 8025-XX.21-048/024-12

24/24 - 8025-XX.21-024/024-12

Spacer/1 - 8017-XX.04-001/001-12
TME 22.5/12 - 8025-XX.92-252/012-12
TME 22.5/12 LH - 8025-XX.92-253/012-12
TME 22.5/12 - 8025-XX.92-252/012-12
TME 22.5/12 LH - 8025-XX.92-253/012-12
24/12 LH - 8025-XX.51-024/012-12
3 x 36/36 - 8025-XX.21-036/036-12

24/24 - 8025-XX.21-024/024-12
KB90/5/12 - 8025-XX.26-905/012-12
3 x 36/36 - 8025-XX.21-036/036-12

24/24 - 8025-XX.21-024/024-12
Spacer/1 - 8017-XX.04-001/001-12
TME 22.5/12 - 8025-XX.92-252/012-12
TME 22.5/12 LH - 8025-XX.92-253/012-12
TME 22.5/12 - 8025-XX.92-252/012-12
TME 22.5/12 LH - 8025-XX.92-253/012-12
24/12 LH - 8025-XX.51-024/012-12
3 x 36/36 - 8025-XX.21-036/036-12

4 x 48/24 - 8025-XX.21-048/024-12

36/36 - 8025-XX.21-036/036-12

24/12 - 8025-XX.21-024/012-12
24/24 - 8025-XX.21-024/024-12
3 x 24/12 - 8025-XX.21-024/012-12

3 x 16/16 - 8025-XX.21-016/016-12

1 TME 221169

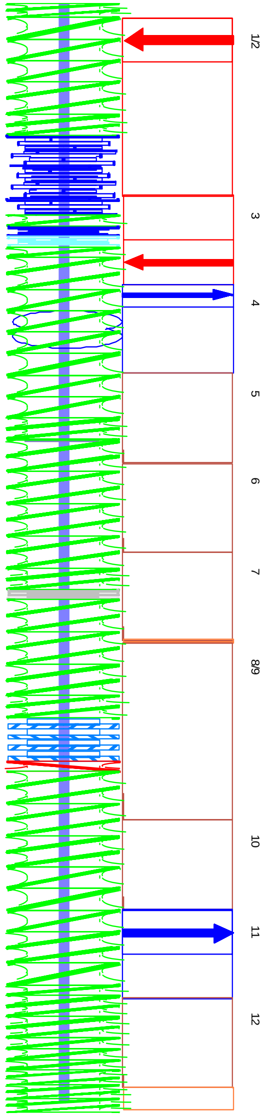

1 TME 221169

16/16 - 8025-XX.21-016/016-12
3 x 48/24 - 8025-XX.21-048/024-12

36/36 - 8025-XX.21-036/036-12

24/24 - 8025-XX.21-024/024-12

KB45/5/18 N-3Fe - 8025-XX.91-521(522)/018-13
3 x KB45/5/18 3Fe - 8024-XX.37-405/018-13

KB45/5/18 N-3Fe - 8025-XX.91-521(522)/018-13
24/12 - 8025-XX.21-024/012-12
KB45/5/12 - 8025-XX.26-405/012-12
KB45/5/12 LH - 8025-XX.56-405/012-12
24/12 - 8025-XX.21-024/012-12
36/36 - 8025-XX.21-036/036-12
6 x 48/24 - 8025-XX.21-048/024-12

24/24 - 8025-XX.21-024/024-12

Spacer/1 - 8017-XX.04-001/001-12
4 x 36/36 - 8025-XX.21-036/036-12

24/24 - 8025-XX.21-024/024-12

KB90/5/12 - 8025-XX.26-905/012-12
3 x 36/36 - 8025-XX.21-036/036-12

24/24 - 8025-XX.21-024/024-12

Spacer/1 - 8017-XX.04-001/001-12
TME 22.5/12 - 8025-XX.92-252/012-12
TME 22.5/12 LH - 8025-XX.92-253/012-12
TME 22.5/12 - 8025-XX.92-252/012-12
TME 22.5/12 LH - 8025-XX.92-253/012-12
24/12 LH - 8025-XX.51-024/012-12
3 x 36/36 - 8025-XX.21-036/036-12

3 x 48/24 - 8025-XX.21-048/024-12

36/36 - 8025-XX.21-036/036-12

48/24 - 8025-XX.21-048/024-12
24/12 - 8025-XX.21-024/012-12
2 x 24/24 - 8025-XX.21-024/024-12

3 x 24/12 - 8025-XX.21-024/012-12

3 x 16/16 - 8025-XX.21-016/016-12

Low Shear no TME 221177

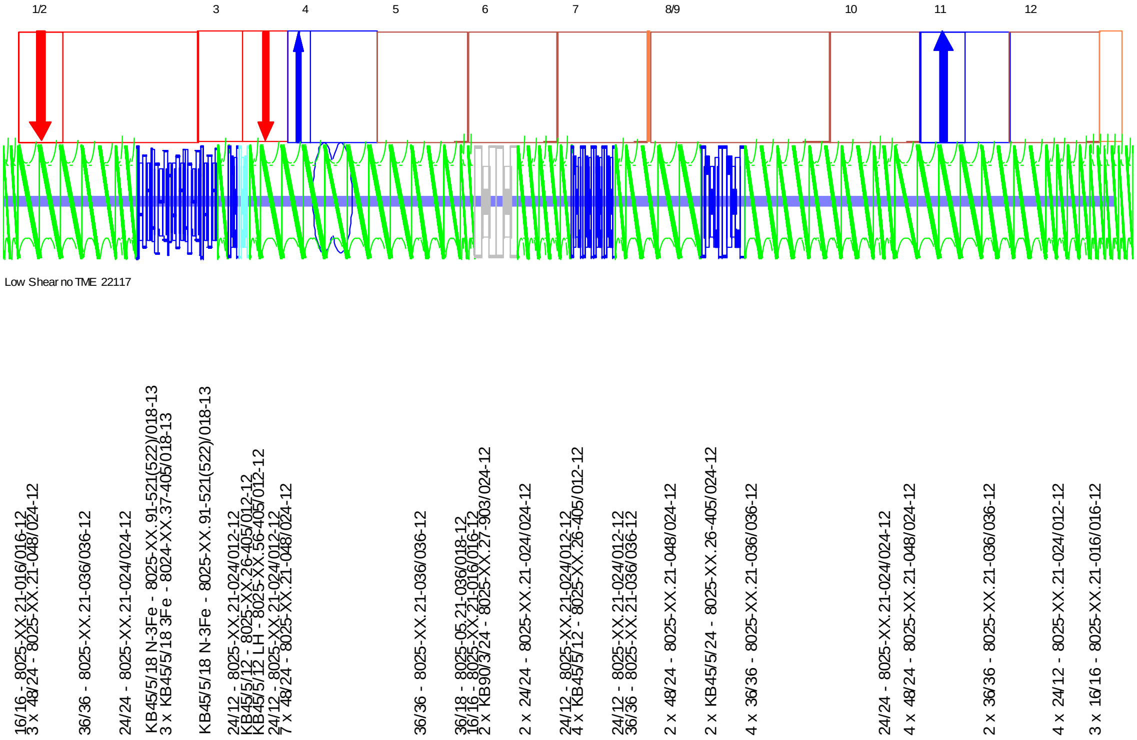

Medium Shear no TME 221186

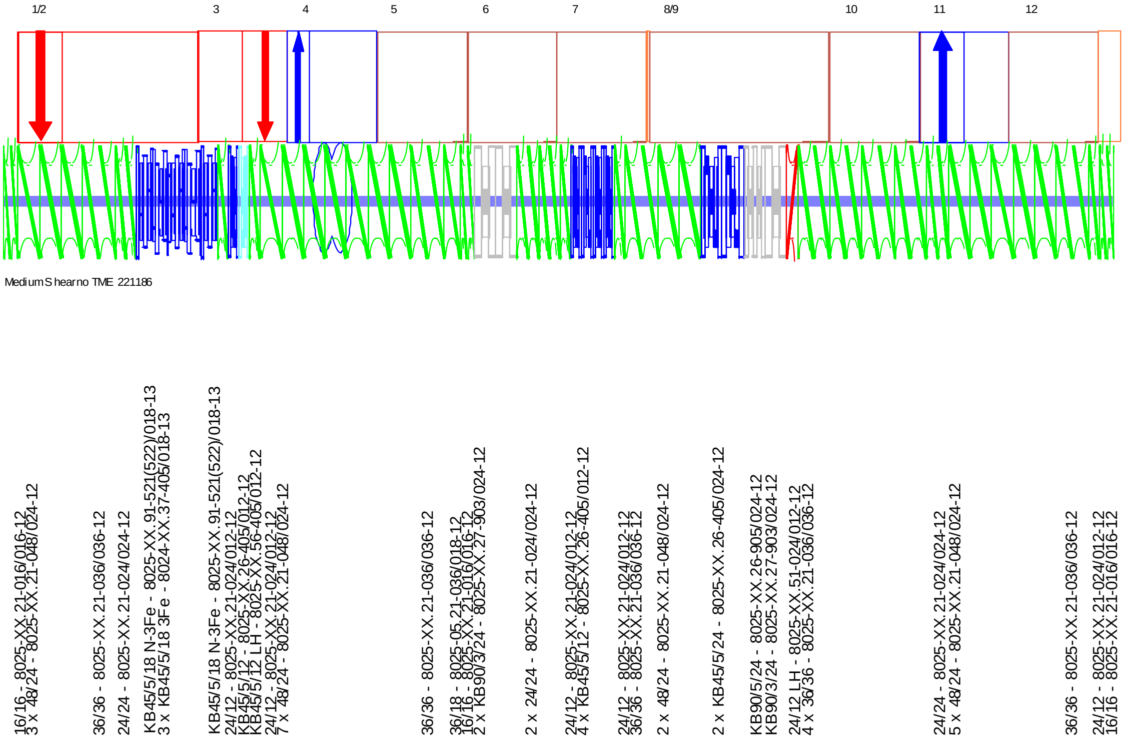

High Shear no TME 221191

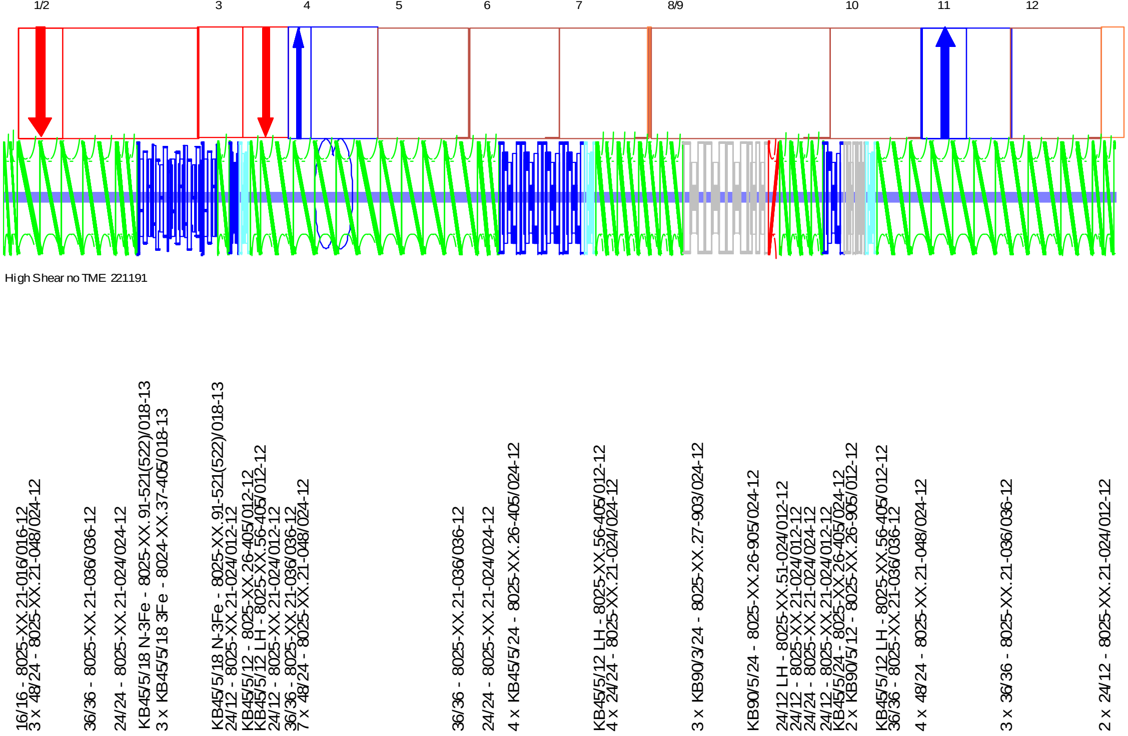

Figure D.2: Optical photomicrographs of nanocomposite films made by the ZSK extruder with ~3 wt% MMT

a. Upstream feeding and downstream feeding with a side stuffer using the Low Shear, no TME configuration

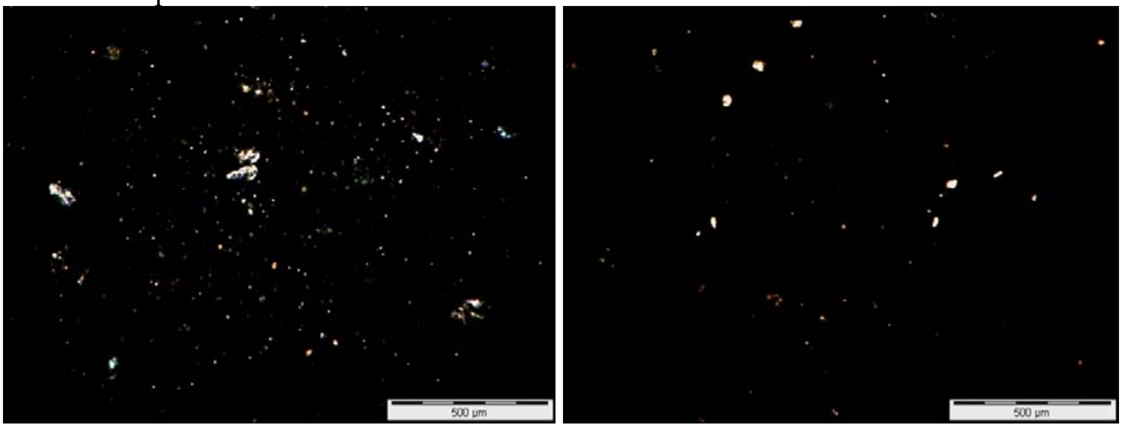
Upstream feed

Downstream with a side stuffer

b. TME Elements, configured with 4 elements to a set

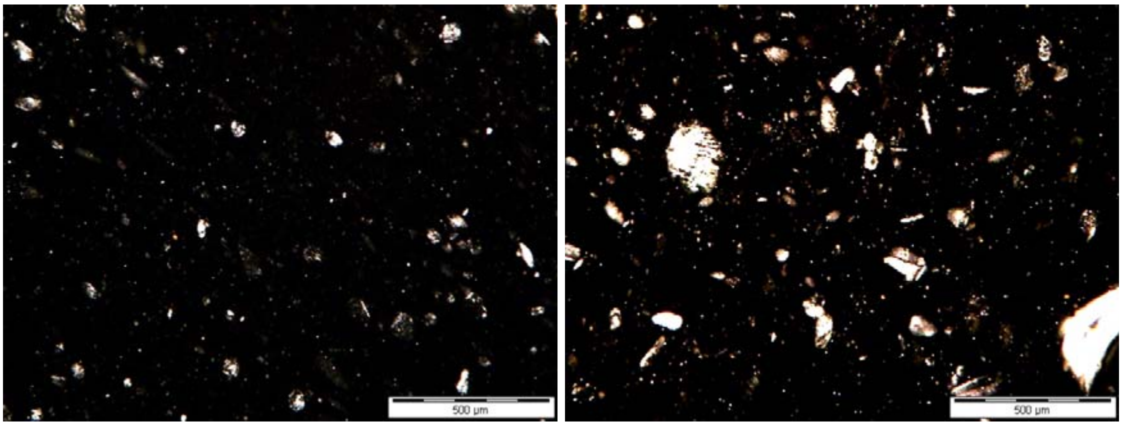
1 set TME elements

2 set TME elements

c. Low, medium, and high shear with no TME elements and fed at barrel 1

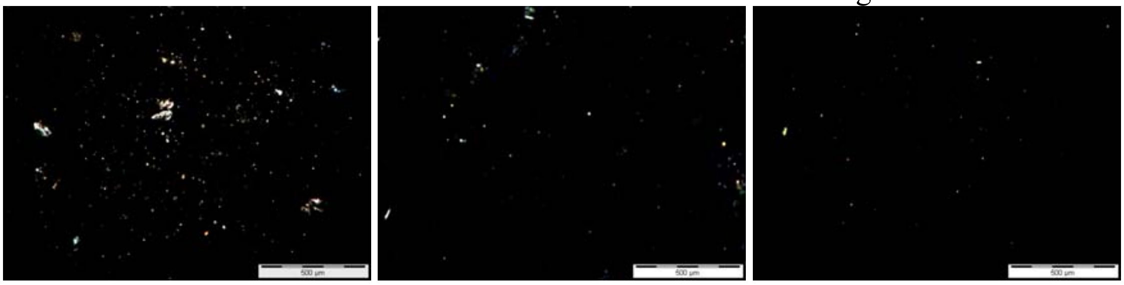
Low Shear

Medium Shear

High Shear

Bibliography

Akimoto, H, Kanazawa T, Yamada M, Matsuda S, Shonaike GO, and Murakami A. Journal of Applied Polymer Science 2001;81(7):1712-1720.

Bharadwaj, RK. Macromolecules 2001;34(26):9189-9192.

Bonotto, S and Bonner EF. Macromolecules 1968;1(6):510-515.

Borse, NK and Kamal MR. Polymer Engineering & Science 2009;49(4):641-650.

Bourbigot, S, Le Bras M, Dabrowski F, Gilman JW, and Kashiwagi T. Fire and Materials 2000;24(4):201-208.

Brune, DA and Bicerano J. Polymer 2002;43(2):369-387.

Carrado, KA and Xu L. Chemistry of Materials 1998;10(5):1440-1445.

Cerezo, FT, Preston CML, and Shanks RA. Composites Science and Technology 2007;67(1):79-91.

Chavarria, F and Paul DR. Polymer 2004;45(25):8501-8515.

Chavarria, F and Paul DR. Polymer 2006;47(22):7760-7773.

Chen, G-X, Choi JB, and Yoon JS. Macromolecular Rapid Communications 2005;26(3):183-187.

Chen, L, Wong S-C, Liu T, Lu X, and He C. Journal of Polymer Science: Part B: Polymer Physics 2004;42(14):2759-2768.

Chen, W, Xu Q, and Yuan RZ. Materials Science and Engineering B 2000;77(1):15-18.

Chen, W, Xu Q, and Yuan RZ. Composites Science and Technology 2001;61(7):935-939.

Cho, JW and Paul DR. Polymer 2001;42(3):1083-1094.

Chow, TS. Journal of Polymer Science: Polymer Physics Edition 1978;16(6):959-965.

Chow, TS. Journal of Polymer Science: Polymer Physics Edition 1978;16(6):967-970.

Corté, L and Leibler L. Polymer 2005;46(17):6360-6368.

Cui, L, Hunter DL, Yoon PJ, and Paul DR. Polymer 2008;49(17):3762-3769.

Cui, L, Ma X, and Paul DR. Polymer 2007;48(21):6325-6339.

Cui, L and Paul DR. Polymer 2007;48(6):1632-1640.

Cui, L, Troeltzsch C, Yoon PJ, and Paul DR. Macromolecules 2009;42(7):2599-2608.

Ding, Y, Zhang X, Xiong R, Wu S, Zha M, and Tang H. European Polymer Journal 2008;44(1):24-31.

Eisenberg, A and Kim J-S. Introduction to Ionomers. New York: Wiley, 1998.

Eshelby, JD. Proceedings of the Royal Society of London. Series A. Mathematical and Physical Sciences 1957;241(1226):376-396.

Farrell, KV and Grady BP. Macromolecules 2000;33(19):7122-7126.

Farrell, V and Grady P. Macromolecules 2001;34(20):7108-7112.

Fasulo, PD, Rodgers WR, Ottaviani RA, and Hunter DL. Polymer Engineering & Science 2004;44(6):1036-1045.

Filippi, S, Marazzato C, Magagnini P, Famulari A, Arosio P, and Meille SV. European Polymer Journal 2008;44(4):987-1002.

Filippi, S, Marazzato C, Magagnini P, Minkova L, Tzankova N, Francesco D, and Mantia PL. Macromolecular Materials and Engineering 2006;291(10):1208-1225.

Fordiani, F, Aubry T, and Grohens Y. Journal of Applied Polymer Science 2009;114(6):4011-4019.

Fornes, TD, Hunter DL, and Paul DR. Macromolecules 2004;37(5):1793-1798.

Fornes, TD, Hunter DL, and Paul DR. Macromolecules 2004;37(5):1793-1798.

Fornes, TD and Paul DR. Polymer 2003;44(14):3945-3961.

Fornes, TD and Paul DR. Polimeros: Ciencia e Tecnologia 2003;13(4):212-217.

Fornes, TD and Paul DR. Polymer 2003;44(17):4993-5013.

Fornes, TD and Paul DR. Macromolecules 2004;37(20):7698-7709.

Fornes, TD and Paul DR. Macromolecules 2004;37(20):7698-7709.

Fornes, TD, Yoon PJ, Hunter DL, Keskkula H, and Paul DR. Polymer 2002;43(22):5915-5933.

Fornes, TD, Yoon PJ, Keskkula H, and Paul DR. Polymer 2001;42(25):9929-9940.

Fornes, TD, Yoon PJ, Keskkula H, and Paul DR. Polymer 2002;43(7):2121-2122.

Galgali, G, Ramesh C, and Lele A. Macromolecules 2001;34(4):852-858.

Giannelis, EP. Applied Organometallic Chemistry 1998;12(10-11):675-680.

Gilman, JW. Applied Clay Science 1999;15(1-2):31-49.

Gilman, JW, Kashiwagi T, Brown JET, Lomakin S, Giannelis EP, and Manias E. Int. SAMPE Symp. Exhibit. 1998;43:1053.

González-Montiel, A, Keskkula H, and Paul DR. Journal of Polymer Science Part B: Polymer Physics 1995;33(12):1751-1767.

Gopakumar, TG, Lee JA, Kontopoulou M, and Parent JS. Polymer 2002;43(20):5483-5491.

Grady, BP. Polymer 2000;41(6):2325-2328.

Grady, BP. Polymer Engineering & Science 2008;48(6):1029-1051.

Grady, BP, Floyd JA, Genetti WB, Vanhoorne P, and Register RA. Polymer 1999;40(2):283-288.

Grady, BP, Goossens JGP, and Wouters MEL. Macromolecules 2004;37(23):8585-8591.

Gusev, AA and Slot JJM. Advanced Engineering Materials 2001;3(6):427-429.

Halpin, J. J. Compos. Mater. 1969;3:732.

Halpin, JC and Kardos JL. Polymer Engineering & Science 1976;16(5):344-352.

Hasegawa, N, Kawasumi M, Kato M, Usuki A, and Okada A. Journal of Applied Polymer Science 1998;67(1):87-92.

Hasegawa, N, Okamoto H, Kawasumi M, Kato M, Tsukigase A, and Usuki A. Macromolecular Materials and Engineering 2000;280-281(1):76-79.

He, H, Duchet J, Galy J, and Gerard J-F. Journal of Colloid and Interface Science 2005;288(1):171-176.

Herrera, NN, Letoffe J-M, Putaux J-L, David L, and Bourgeat-Lami E. Langmuir 2004;20(5):1564-1571.

Hill, R. Proc. Phys. Soc., London 1952;65A:349-354.

Hill, R. Journal of the Mechanics and Physics of Solids 1965;13(4):213-222.

Hine, PJ, Rudolf Lusti H, and Gusev AA. Composites Science and Technology 2002;62(10-11):1445-1453.

Hirasawa, E, Yamamoto Y, Tadano K, and Yano S. Journal of Applied Polymer Science 1991;42(2):351-362.

Ho, RM, Su AC, Wu CH, and Chen SI. Polymer 1993;34(15):3264-3269.

Hotta, S and Paul DR. Polymer 2004;45(22):7639-7654.

Hu, Y, Wang S, Ling Z, Zhuang Y, Chen Z, and Fan W. Macromolecular Materials and Engineering 2003;288(3):272-276.

Huang, JJ, Keskkula H, and Paul DR. Polymer 2006;47(2):624-638.

Huang, Y, Ma X, Liang G, Wang S, and Zhang Q. Polymer 2008;49(8):2085-2094.

Hui, CY and David S. Polymer Engineering & Science 1998;38(5):774-782.

Jang, BZ, Uhlmann DR, and Sande JBV. Journal of Applied Polymer Science 1985;30(6):2485-2504.

Jimenez, G, Ogata N, Kawai H, and Ogihara T. Journal of Applied Polymer Science 1997;64(11):2211-2220.

Joo, JH, Shim JH, Choi JH, Choi C-H, Kim D-S, and Yoon J-S. Journal of Applied Polymer Science 2008;109(6):3645-3650.

Kawasumi, M, Hasegawa N, Kato M, Usuki A, and Okada A. Macromolecules 1997;30:6333–6338.

Kim, DH, Fasulo PD, Rodgers WR, and Paul DR. Polymer 2007;48(20):5960-5978.

Kim, DH, Fasulo PD, Rodgers WR, and Paul DR. Polymer 2007;48(18):5308-5323.

Kim, DH, Fasulo PD, Rodgers WR, and Paul DR. Polymer 2008;49(10):2492-2506.

Kim, YK, Choi YS, Wang KH, and Chung IJ. Chemistry of Materials 2002;14(12):4990-4995.

Kohzaki, M, Tsujita Y, Takizawa A, and Kinoshita T. Journal of Applied Polymer Science 1987;33(7):2393-2402.

Kojima, Y, Usuki A, Kawasumi M, Okada A, Fukushima Y, Kurauchi T, and Kamigaito O. Journal of Materials Research 1993;8(5):1185–1189.

Kotoky, T and Dolui SK. Colloid & Polymer Science 2006;284(10):1163-1169.

Krishnamoorti, R and Yurekli K. Current Opinion in Colloid & Interface Science 2001;6(5-6):464-470.

Kulkarni, HP, Mogilevsky G, Mullins WM, and Wu Y. Journal of Materials Research 2009;24:1087-1092.

Kutsumizu, S, Goto M, and Yano S. Macromolecules 2004;37(13):4821-4829.

Kutsumizu, S, Tadano K, Matsuda Y, Goto M, Tachino H, Hara H, Hirasawa E, Tagawa H, Muroga Y, and Yano S. Macromolecules 2000;33(24):9044-9053.

Kuwabara, K and Horii F. Journal of Polymer Science Part B: Polymer Physics 2002;40(11):1142-1153.

Lan, T and Pinnavaia TJ. Chemistry of Materials 2002;6(12):2216-2219.

Lee, DC and Jang LW. Journal of Applied Polymer Science 1996;61(7):1117-1122.

Lee, DC and Jang LW. Journal of Applied Polymer Science 1998;68(12):1997-2005.

Lee, H-s, Fasulo PD, Rodgers WR, and Paul DR. Polymer 2005;46(25):11673-11689.

Lee, H-s, Fasulo PD, Rodgers WR, and Paul DR. Polymer 2006;47(10):3528-3539.

Lee, KY, Kim KH, Jeoung SK, Ju SI, Shim JH, Kim NH, Lee SG, Lee SM, Lee JK, and Paul DR. Polymer 2007;48(14):4174-4183.

Lertwimolnun, W and Vergnes B. Polymer 2005;46(10):3462-3471.

Li, B, Gong G, Xie B-H, Yang W, and Yang M-B. Journal of Applied Polymer Science 2008;109(2):1161-1167.

Li, X, Wang C-y, Fang L, and Liu L-z. Harbin Ligong Daxue Xuebao 2003;8(2):90-93.

Liang, G, Xu J, Bao S, and Xu W. Journal of Applied Polymer Science 2004;91(6):3974-3980.

Liu, L, Qi Z, and Zhu X. Journal of Applied Polymer Science 1999;71(7):1133-1138.

Long, Y and Shanks RA. Journal of Applied Polymer Science 1996;62(4):639-646.

Longworth, R and Vaughan DJ. Nature 1968;218(5136):85-87.

Loo, Y-L, Wakabayashi K, Huang YE, Register RA, and Hsiao BS. Polymer 2005;46(14):5118-5124.

López-Quintanilla, ML, Sánchez-Valdés S, Ramos de Valle LF, and Guedea Miranda R. Polymer Bulletin 2006;57(3):385-393.

MacKnight, WJ and Earnest TR, Jr. J. Polym. Sci., Macromol. Rev. 1981;16:41.

MacKnight, WJ, McKenna LW, and Read BE. Journal of Applied Physics 1967;38(11):4208-4212.

Mainil, M, Alexandre M, Monteverde F, and Dubois P. Journal of Nanoscience and Nanotechnology 2006;6:337-344.

Malwitz, MM, Lin-Gibson S, Hobbie EK, Butler PD, and Schmidt G. Journal of Polymer Science Part B: Polymer Physics 2003;41(24):3237-3248.

Marx, CL and Cooper SL. Journal of Macromolecular Science, Part B 1974;9(1):19 - 33.

Mehta, S, Mirabella FM, Rufener K, and Bafna A. Journal of Applied Polymer Science 2004;92(2):928-936.

Messersmith, PB and Giannelis EP. Journal of Polymer Science Part A: Polymer Chemistry 1995;33(7):1047-1057.

Morawiec, J, Pawlak A, Slouf M, Galeski A, Piorkowska E, and Krasnikowa N. European Polymer Journal 2005;41(5):1115-1122.

Mori, T and Tanaka K. Acta Metallurgica 1973;21(5):571-574.

Okada, A, Kawasumi M, Usuki A, Kojima Y, Kurauchi T, and Kamigaito O. Materials Research Society Symposium Proceedings 1990;171(Polym. Based Mol. Compos.):45-50.

Okamoto, M, Nam PH, Maiti P, Kotaka T, Hasegawa N, and Usuki A. Nano Letters 2001;1(6):295-298.

Oshinski, AJ, Keskkula H, and Paul DR. Polymer 1996;37(22):4891-4907.

Ou, Y-C, Guo T-T, Fang X-P, and Yu Z-Z. Journal of Applied Polymer Science 1999;74(10):2397-2403.

Pantani, R, Coccorullo I, Speranza V, and Titomanlio G. Progress in Polymer Science 2005;30(12):1185-1222.

Pantani, R, Coccorullo I, Speranza V, and Titomanlio G. Polymer 2007;48(9):2778-2790.

Park, M, Shim I-K, Jung E-Y, and Choy J-H. Journal of Physics and Chemistry of Solids 2004;65(2-3):499-501.

Paul, DR and Robeson LM. Polymer 2008;49(15):3187-3204.

Paul, DR, Zeng QH, Yu AB, and Lu GQ. Journal of Colloid and Interface Science 2005;292(2):462-468.

Ploehn, HJ and Liu C. Industrial & Engineering Chemistry Research 2006;45(21):7025-7034.

Premphet-Sirisinha, K and Preechachon I. Journal of Applied Polymer Science 2003;89(13):3557-3562.

Ray, AK. Journal of Thermal Analysis and Calorimetry 1996;46(6):1527-1539.

Rees, RW and Vaughan D. J. Polym. Prepr. (Am. Chem. Soc., Div. Polym. Chem.) 1965;6:296.

Rees, RW and Vaughan D. J. Polym. Prepr. (Am. Chem. Soc., Div. Polym. Chem.) 1965;6:287.

Register, RA and Cooper SL. Macromolecules 1990;23(1):318-323.

Reichert, P, Nitz H, Klinke S, Brandsch R, Thomann R, and Mülhaupt R. Macromolecular Materials and Engineering 2000;275(1):8-17.

Ren, J, Silva AS, and Krishnamoorti R. Macromolecules 2000;33(10):3739-3746.

Roover, BD, Sclavons M, Carlier V, Devaux J, Legras R, and Momtaz A. Journal of Polymer Science Part A: Polymer Chemistry 1995;33(5):829-842.

Schapery, RA. Journal of Composite Materials 1968;2(3):380-404.

Schlick, S. Ionomers: Characterization, Theory, and Applications. Boca Raton, FL: CRC Press, 1996.

Scobbo, JJ. Thermomechanical performance of polymer blends. In: Paul DR and Bucknall CB, editors. Polymer blends, vol. 2. New York: Wiley, 2000. pp. 335-357.

Shah, RK, Cui L, Williams KL, Bauman B, and Paul DR. Journal of Applied Polymer Science 2006;102(3):2980-2989.

Shah, RK, Hunter DL, and Paul DR. Polymer 2005;46(8):2646-2662.

Shah, RK, Kim DH, and Paul DR. Polymer 2007;48(4):1047-1057.

Shah, RK, Krishnaswamy RK, Takahashi S, and Paul DR. Polymer 2006;47(17):6187-6201.

Shah, RK and Paul DR. Polymer 2004;45(9):2991-3000.

Shah, RK and Paul DR. Macromolecules 2006;39(9):3327-3336.

Sheng, N, Boyce MC, Parks DM, Rutledge GC, Abes JI, and Cohen RE. Polymer 2004;45(2):487-506.

Sinha Ray, S, Yamada K, Okamoto M, and Ueda K. Polymer 2003;44(3):857-866.

Spencer, MW, Cui L, Yoo Y, and Paul DR. Polymer 2010;51(5):1056-1070.

Spencer MW, Wetzel MD, Troeltzsch C, and Paul DR. Polymer 2011;52:Submitted. (Effects of Acid Neutralization on the Properties of K+ and Na+ Poly(ethylene-co-methacrylic acid) Ionomers).

Stretz, HA and Paul DR. Polymer 2006;47(26):8527-8535.

Stretz, HA, Paul DR, and Cassidy PE. Polymer 2005;46(11):3818-3830.

Stretz, HA, Paul DR, Li R, Keskkula H, and Cassidy PE. Polymer 2005;46(8):2621-2637.

Tachino, H, Hara H, Hirasawa E, Kutsumizu S, Tadano K, and Yano S. Macromolecules 1993;26(4):752-757.

Tachino, H, Hara H, Hirasawa E, Kutsumizu S, and Yano S. Polymer Journal 1994;26(10):1170-1178.

Tachino, H, Hara H, Hirasawa E, Kutsumizu S, and Yano S. Journal of Applied Polymer Science 1995;55(1):131-138.

Tadano, K, Hirasawa E, Yamamoto H, and Yano S. Macromolecules 1989;22(1):226-233.

Tandon, GP and Weng GJ. Polymer Composites 1984;5(4):327-333.

Tant, MR, Mauritz KA, and Wilkes GL. Ionomers: Synthesis, Structure, Properties and Applications. London: Blackie Academic & Professional, 1997.

Tierney, NK and Register RA. Macromolecules 2002;35(6):2358-2364.

Tsujita, Y, Shibayama K, Takizawa A, Kinoshita T, and Uematsu I. Journal of Applied Polymer Science 1987;33(4):1307-1314.

Usuki, A, Koiwai A, Kojima Y, Kawasumi M, Okada A, Kurauchi T, and Kamigaito O. Journal of Applied Polymer Science 1995;55(1):119-123.

Usuki, A, Kojima Y, Kawasumi M, Okada A, Fukushima Y, Kurauchi T, and Kamigaito O. Journal of Materials Research 1993;8(5):1179-1184.

Utraki, LA. Clay-containing polymeric nanocomposites. Shawbury, Shrewsbury, Shropshire, SY4 4NR, UK, 2004.

Vaia, RA, Ishii H, and Giannelis EP. Chemistry of Materials 1993;5(12):1694-1696.

Vaia, RA, Ishii H, and Giannelis EP. Chemistry of Materials 2002;5(12):1694-1696.

van Es, M, Xiqiao F, van Turnhout J, and van der Giessen E. Comparing polymer–clay nanocomposites with conventional composites using composite modeling. In: Al-Malaika S, Golovoy A, and Wilkie C, editors. Specialty polymer additives: principles and applications. London: Blackwell Science, 2001. pp. Chapter 21.

Vanhoorne, P and Register RA. Macromolecules 1996;29(2):598-604.

Varela, C, Rosales C, Perera R, Matos M, Poirier T, Blunda J, and Rojas H. Polymer Composites 2006;27(4):451-460.

Voigt, W. Abh.Kgl.Ges.Wiss.Göttingen, Math.Kl. 1887;34: 3-51.

Wakabayashi, K and Register RA. Polymer 2005;46(20):8838-8845.

Wakabayashi, K and Register RA. Macromolecules 2006;39(3):1079-1086.

Wang, KH, Choi MH, Koo CM, Choi YS, and Chung IJ. Polymer 2001;42(24):9819-9826.

Wang, Z and Pinnavaia TJ. Chemistry of Materials 1998;10(12):3769-3771.

Weimer, MW, Chen H, Giannelis EP, and Sogah DY. Journal of the American Chemical Society 1999;121(7):1615-1616.

Welty, A, Ooi S, and Grady BP. Macromolecules 1999;32(9):2989-2995.

Wheeler, PA, Wang J, Baker J, and Mathias LJ. Chemistry of Materials 2005;17(11):3012-3018.

Wilson, FC, Longworth R, and Vaughan DJ. ACS Polym Prepr 1968;9(1):505−514.

Wunderlich, B and Czornyj G. Macromolecules 1977;10(5):906-913.

Xu, R, Manias E, Snyder AJ, and Runt J. Macromolecules 2001;34(2):337-339.

Yano, K, Usuki A, Okada A, Kurauchi T, and Kamigaito O. Journal of Polymer Science Part A: Polymer Chemistry 1993;31(10):2493-2498.

Yoo, Y and Paul DR. Polymer 2008;49(17):3795-3804.

Yoo, Y, Shah RK, and Paul DR. Polymer 2007;48(16):4867-4873.

Yoo, Y, Spencer MW, and Paul DR. Polymer 2011;52(1):180-190.

Yoon, PJ, Fornes TD, and Paul DR. Polymer 2002;43(25):6727-6741.

Yoon, PJ, Hunter DL, and Paul DR. Polymer 2003;44(18):5323-5339.

Yoon, PJ, Hunter DL, and Paul DR. Polymer 2003;44(18):5341-5354.

Zanetti, M, Camino G, Thomann R, and Mülhaupt R. Polymer 2001;42(10):4501-4507.

Zhang, M and Sundararaj U. Macromolecular Materials and Engineering 2006;291(6):697-706.

Zhang, R, Zhu Y, Zhang J, Jiang W, and Yin J. Journal of Polymer Science Part A: Polymer Chemistry 2005;43(22):5529-5534.

Vita

Matthew Walter Spencer was born in Salt Lake City, Utah on July 22, 1982 to Guy and Jody Spencer. After graduating from Davis High School in Kaysville, Utah in 2000, he attended Brigham Young University in Provo, Utah. After a two-year leave of absence for voluntary service, he graduated with a B.S. degree in Chemical Engineering in 2006. While pursuing his undergraduate degree, he worked for the Design Institute for Physical Properties. In August of 2006, he commenced his studies in the Chemical Engineering Graduate School of the University of Texas at Austin under the guidance of Professor Donald R. Paul and received his Master of Science Degree in 2009. After completing his doctorate, he will be employed as a Polymer Engineer by Green Source Energy.

Permanent address: 344 East 600 North
Kaysville, UT 84037

This dissertation was typed by the author.